Expanding the Attosecond Toolbox:

Demonstration of Novel Experiments, New Light Sources and Detectors

Cover: Unlike the measurements presented in this thesis, the image on the cover was recorded with shutter times of several seconds while moving a bright light source behind cut out paper letters. The result is an image which does not allow the extraction of any timing information on the performed motion such as speed, direction or shape of the lightsource.

Flip Book: Eadweard Muybridge in 1877 took the first photos of a horse in motion, to settle the question whether at a certain moment in time all four hooves of a galloping horse are off the ground at the same time. His photographs thus present the first time-resolved measurement of a fast motion, which takes place on time scales that the human eye can not resolve, and are often used images in the femtosecond and attosecond spectroscopy community.

Isbn: 978-90-77209-57-8

An electronic copy of this thesis is available at www.amolf.nl/publications.

Expanding the Attosecond Toolbox:

Demonstration of Novel Experiments, New Light Sources and Detectors

Een Wetenschappelijke Proeve Op Het Gebied Van
De Natuurwetenschappen, Wiskunde En Informatica

Proefschrift

ter verkrijging van de graad van Doctor
aan de Radboud Universiteit Nijmegen,
op gezag van de rector magnificus
Prof. mr. S.J.J. Kortmann,
volgens besluit van het college van decanen
in het openbaar te verdedigen op maandag 12 december 2011
om 15.30 uur precies

door

Georg Gademann

Geboren op 18 januari 1983
te Heidelberg, Duitsland

Promotor:	Prof. dr. M. J. J. Vrakking
Manuscriptcommissie:	Prof. dr. W. J. van der Zande Prof. dr. H. J. Bakker (Universiteit van Amsterdam) dr. G. Steinmeyer (Max Born Institute, Berlin)

The work described in this thesis was performed at the FOM Institute for Atomic and Molecular Physics (AMOLF), Science Park 104, 1098 XG Amsterdam, The Netherlands.
This work is part of the research programme of the 'Stichting voor Fundamenteel Onderzoek der Materie (FOM)', which is financially supported by the 'Nederlandse Organisatie voor Wetenschappelijk Onderzoek (NWO)'.
The work presented in Chapter 6 was carried out as part of the EU Industry-Academia Partnership Program FLUX (PIAPP-GA-2008-218053).

Time flies like an arrow, fruit flies like a banana.

(Groucho Marx)

Contents

1 Introduction

NATURE has been defined as a 'principle of motion and change', and it is the subject of our inquiry. We must therefore see that we understand the meaning of 'motion' for if it were unknown, the meaning of 'nature' too would be unknown.

Aristotle, Physics Book III, 1

Aristotle defined motion and change as the fundamental concept in physics and understanding motion as the key to understanding the nature of things around us. This is the approach that science follows to a large extent until today. However, when Aristotle and his contemporaries thought about motion they would have mainly considered the movement of the sun over the sky or the phases of the moon, allowing them to measure change and motion on timescales of months, days or hours. In this sense the measurement of motion or dynamics in general has taken an unbelievable evolution with respect to the timescales that can be measured today.

To quantify motion, however, a second concept is necessary first: time. According to Aristotle *'time is the measure of motion'* [1]. He thus defines time as being deduced from motion. Since then the concept of time has changed over centuries. In contrast to the Aristotelian idea, Newton defined time as fundamental and motion as a derived concept. With the beginning of the modern age, the Newtonian view has been widely accepted. Yet this introduction will stick with Aristotle for a little while longer, as it provides an intuitive understanding that in order to measure motion one needs to define a relevant reference in time first.

To improve such time references has been one of the most continuously pursued tasks in physics over the last centuries or even millennia. At the beginning of human perception of time, the periodic motion of the sun, the moon or the earth was used to clock time, whereas artificial sources such as water clocks or hour glasses usually allowed the measurement also of shorter time intervals, although only on a rudimentary scale. Only the invention of mechanical clocks, which were based on pendulums and springs, by Christiaan Huygens and Robert Hooke in the 17th century (the oldest pendulum clock constructed by Huygens in 1657 can still be seen in the Museum Boerhaave in Leiden, Netherlands), allowed the precise measurement of time, as was for

example necessary in naval navigation. Mechanical clocks stayed the measurement technique of choice for over 250 years until the development of Quartz based clocks in the 1930s and finally of atomic clocks another 30 years later brought huge leaps in the precision measurement of time. (It is interesting to note that the second as a base unit of the SI system was defined by astronomic motion until 1967, when it was replaced by the atomic clock standard.)

For time is just this-number of motion in respect of 'before' and 'after'.

Aristotle, Physics Book IV, 11

'This-number' Aristotle meant in the sense of an infinitely divisible entity. In order to measure ever shorter time intervals, it consequently requires a time source that allows the division of the "before" and "after" into ever smaller sub-intervals, i.e., in the limiting case, the precise measurement of motion needs a timing source, which supplies a temporal reference that is comparable to the timescales of the motion itself. In the last five to six decades science has made tremendous advances in measuring motion, which takes place on timescales never accessible before. Nowadays commonly available electronics can measure timescales in the nano-[1] to picosecond[2] range. The SI base unit of the second today is defined by a microwave frequency standard, whose cycle period lies in the tens of picoseconds.

Since the early 1990s researchers have moved to a new era of measuring ultrafast dynamics. This, however, only became possible with the invention of the laser [2, 3] and especially pulsed laser sources [4–7], which established the foundation from which for the first time optical timescales can be accessed. Considering the cycle time of visible light, optical timescales lie within a few femtoseconds[3]. The development of laser pulses with pulse durations of only a few femtoseconds [8] enabled experimental researchers to follow chemical reactions, i.e., nuclear motion leading to the molecular transition from the "before" to the "after", on time intervals consisting of only a few tens of femtosecond (acknowledged by the Nobel prize for Ahmed Zewail in 1999 [9]).

The corresponding experiments are usually performed in a pump-probe scheme. Pump-probe experiments use a first ultrashort laser pulse to initiate dynamics in the system of interest (defining the moment of 'before'), which is followed by a second ultrashort laser pulse that probes the system after a certain time interval (defining the moment of 'after'). When this measurement is repeated multiple times while successively changing the delay between the two pulses, the individual measurements can be composed to form a "movie" of the motion under investigation. Analogue to the duration of the shutter time of a camera, the duration of the laser pulses dictates if a sharp or a blurred image of the process will be taken. The laser pulse duration hence ultimately dictates the temporal resolution of the experiment.

[1] $1\ \text{ns} = 1 \cdot 10^{-9}\text{s} = 0.000000001\text{s}$
[2] $1\ \text{ps} = 1 \cdot 10^{-12}\text{s} = 0.000000000001\text{s}$
[3] $1\ \text{fs} = 1 \cdot 10^{-15}\text{s} = 0.000000000000001\text{s}$

The minimally attainable pulse duration, however, is restricted by the cycle time of the light that the pulses are composed of. Conventional femtosecond laser pulses are based on wavelengths in the near infrared (IR) wavelength region, which sets the limit for the pulse duration to 2 - 3 femtoseconds - and thus also the time resolution of pump-probe experiments employing these laser pulses. Using conventional pump-probe techniques, it would therefore be impossible to resolve the dynamics of electrons in atoms, molecules or solid-state systems which take place on the timescale of a few hundred attoseconds[4].

Chemical reactions as well as the interaction of atoms and molecules with light are governed by the ultrafast electronic response of the system. In the Aristotelian sense understanding and controlling this motion, will therefore yield the ultimate understanding of the complete system and its behavior. Thus, one of the foremost interests in time-resolved spectroscopy today is to follow precisely these electronic dynamics. Accordingly even shorter pulse durations are required to perform successful pump-probe experiments on attosecond timescales.

The generation of light pulses with attosecond pulse durations was finally achieved in 2001. High harmonic generation (HHG) of a fundamental laser field with wavelengths in the IR range was used to produce radiation in the extreme ultraviolet (XUV) range of the electro-magnetic spectrum. The application and generation of attosecond pulses, either in the form of attosecond pulse trains (APT) [10] or isolated attosecond pulses (IAP) [11], established the field of attosecond physics and forms the context that this thesis was conducted in. (As a matter of fact this very year 2011 marks the 10 year anniversary of the establishment of the attosecond era.)

The goal of this thesis was to improve the available techniques to perform measurements on electron dynamics and particularly pave the way towards pump-probe experiments where both pump and probe pulse are made up of attosecond pulses. Such experiments would open up the gate to reach the ultimate time-resolution possible in attosecond pulse experiments. This goal was approached from different directions including both the development of new technologies as well as testing novel experimental techniques. The range of topics that the presented work covers therefore is very broad and touches on almost every aspect of the field of attosecond science both in the sense of application, presented in Part I of this thesis, and technical innovations presented in Part II.

Chapter 2 puts all parts of the presented work in the context of the current developments of the field. After a brief historical and technical introduction of HHG and the generation of attosecond pulses (Section 2.1), it focuses mainly on the application of APT and IAP (Section 2.2) in two-color experiments to explore electron dynamics in a range of systems. For completeness other time-resolved techniques that achieve attosecond resolution without the use of attosecond pulses are introduced briefly.

To further put the technical developments presented in Part II in the correct context of their intended use, the attoscience review section further includes a

[4] $1\text{ as} = 1 \cdot 10^{-18}\text{s} = 0.000000000000000001\text{s}$

section on the recent developments in non-linear XUV and particularly XUV-pump-XUV-probe experiments (Section 2.4). As a guideline for future PhD students, different techniques for the generation of IAPs and especially their scalability to high driving energies are further laid out along with the necessary phase-matching considerations that such a setup would require.

In connection with this overview four novel experiments were performed at the AMOLF XUV laboratory. The results are presented in Chapter 3. The first two experiments (Section 3.1) explore the attosecond control of photoionization of small molecules such as H_2, D_2, and O_2. The results on O_2 allow insight into the application of the control mechanism also to more complex molecules. The experiments further mark a first step towards using attosecond pulses as a probe to study electron dynamics in molecules and investigate possible new observables such as photo-electron yield and angular distributions. The third experiment (Section 3.2) investigates photoelectron angular distributions recorded from aligned CO_2 molecules, which reveal the influence of molecular structure. In the future, the presented experimental approach could be extended to make possible the time-resolved study of molecular structure in femtosecond chemical reactions. All three experiments are presented in the form of short overviews, briefly explaining experimental technique and results and are covered in detail in the thesis works of Freek Kelkensberg [12] and Wing Kiu Siu [13].

The focus of the chapter lies on the fourth experiment (Section 3.3) which is presented in detail. HHG is controlled in time by launching electron wave packets (EWPs) in the continuum by an APT. Those wave packets are subsequently accelerated and recombined by a coincident IR field, which is synchronized to the APT. By changing the delay between the two fields, the precise instant with respect to the IR field when the EWPs are launched can be controlled on attosecond time scales. The mechanism is investigated using an all-optical setup, where the physical observable is the generated high harmonic radiation yield. As such, the experiment offers new ways to control electron-ion recollision in a number of potential experiments, such as high harmonic or tomographic imaging or maybe even electron diffraction experiments using ponderomotively accelerated electrons among others.

The discussed experiments were the very first series of experiments conducted with the new attosecond setup in our laboratory. Seeing the great performance of the complete system and the ability to produce large amounts of high quality data after an extended optimization period was one of the greatest successes that I was allowed shearing in close collaboration with my colleagues.

The technical innovations presented in Part II aim at overcoming some inherent limitations, which attosecond experiments as presented in Part I suffer from. When generating APTs, conversion efficiencies from IR photons to XUV photons are rarely better than 10^{-5} and even lower in the case of IAP generation. The single shot signal in such cases therefore is extremely low, e.g., one can estimate that for common IAPs and a maximum background pressure inside the interaction chamber of $\sim 10^{-5}$mbar only ~ 1 in 10^4 photons

is absorbed in the gas target. As the amount of signal produced in an experiment depends on the product of the number of XUV photons contained in the attosecond pulses and the number of gas atoms inside the target volume, there are two ways to address the problem. Either one can increase the number of photons in the attosecond pulse, and / or increase the density of atoms in the target gas jet. The results presented in this part of the thesis aim at improving both of these aspects and thus also pave the way towards applying attosecond pulses with considerably higher photon energies (e.g., hundreds of electron-volts) in attosecond experiments.

Generally increasing the gas density is technically straight forward, however, the use of conventional charged particle detection, e.g., by means of a stack of micro-channel plates (MCP) and a phosphor screen, restricts the operating background pressure to below 10^{-5} mbar. Assuming a constant pumping speed of the vacuum pumps, thus also the pressure in the gas target is limited by these restrictions.

In Chapter 4 a new pixel detector for use in velocity map imaging and coincidence measurements is proposed and compared to different conventional detection systems. Among several other advantages this new type of detector can be operated even at atmospheric pressures, thus overcoming the pressure limitations imposed by most conventional detection schemes. The results of several first proof-of-principle experiments and systematic detector studies are presented. In the meantime this project has evolved into a dedicated PhD position working with the next generation of these detectors. A short outlook section briefly summarizes the most important changes and advances that have accumulated since the time that the presented work was performed.

Increasing the photon numbers in attosecond pulses was the goal of the work presented in Chapter 5 and 6. As mentioned before, a higher photon flux will lead to improved signal rates in general attosecond experiments, however, the low photon fluxes in current APT or IAP sources in combination with extremely small cross-sections for non-linear processes in the XUV spectral range pose a second, even more severe limitation to attosecond science. To induce a non-linear process, XUV intensities of at least 10^{13} W/cm^2 would be necessary. XUV-pump-XUV-probe experiments, however, necessarily rely on at least a two-photon process, i.e., at least a one-photon process or higher is needed for the pump event and a second one for the probe-pulse. The small conversion efficiencies allowing pulse energies of IAPs only in the pico- to nanojoule range have up to now prevented the demonstration of such attosecond XUV-pump-XUV-probe experiments.

To overcome this limitation and with the declared goal to perform XUV-pump-XUV-probe experiments in the future, a terawatt (TW) femtosecond amplifier for the production of intense IAPs has been designed and set up. After a thorough introduction to short pulse lasers and especially the concepts of carrier-envelope phase-stabilization, Chapter 6 describes design, implementation and performance as well as the necessary stabilization of the carrier-envelope-phase (CEP) of the TW-amplifier. As such, this amplifier presents for the first time the demonstration of CEP-stable pulses with energies up

to 50 mJ. Developing and building up my own amplifier system was a welcome technical playground, which yielded great satisfaction for me, both in the prospect of contributing to the realization of a completely new form of attosecond pump-probe experiments as well as in the personal achievement of the goal formulated at the very beginning of my thesis work.

As one will see clearly from this outline, the performed PhD work has been extremely versatile in the fields that have been addressed. It gave me the opportunity to experience attosecond science from every related aspect ranging from fundamental research on atomic and molecular systems to detector physics and laser development. I perceived this fact as a great pleasure, since:

> *'...Change in all things is sweet', as the poet says,...*
>
> Aristotle, NICOMACHEAN ETHICS Book VII, 14

Part I

Attosecond Science

2 Introduction to attosecond science

2.1 High harmonic generation

The field of non-linear optics was established when the first frequency-doubling in a crystal was successfully demonstrated [14] shortly after the invention of the laser in 1960 [2, 3]. Since then, experimental researchers have strived to create ever shorter wavelengths using multiple consecutive low-order conversion processes [15, 16]. With the development of pulsed laser sources [4–7] reaching high peak powers and the coming of age of strong field physics, the next steps towards high harmonic generation (HHG) were taken. It took however until 1987 that the first high harmonic radiation was observed [17, 18]. Already in these early studies researchers realized the now well known division of conversion efficiencies into three different regions: The decrease at low harmonic orders, followed by an extended plateau with constant conversion efficiencies and an abrupt cut-off (see Figure 2.1). The extended plateau was quickly attributed to the non-perturbative action on the target atoms by the high intensity laser pulses exceeding several 10^{13} W/cm^2 [18]. As a result of different semiclassical [19, 20] and quantum-mechanical [21, 22] calculations, it was finally possible to predict the cut-off position by the universal rule $E_{\text{cutoff}} = I_P + 3.17\ U_P$. I_P is the ionization potential of the target gas and U_P is the ponderomotive energy (the mean kinetic energy that an electron acquires in an oscillating electric field) described by $U_P = I_{\text{laser}}/4\omega^2$. This discovery also explained the surprising fact that higher cut-off energies were only reached with longer wavelengths.

Among these theoretical works, the semi-classical description by Corkum [20], introduced the frequently used "Three-Step-Model" of HHG, which is depicted in Figure 2.2(a). This model describes the interaction of the laser field with the target atoms in terms of only two states: the electronic groundstate and the continuum state. Excited bound states are neglected. In the first step the electron tunnels through the potential barrier, which is modified by the presence of the intense IR field, and launches the electron into the continuum with zero initial velocity. The probability of this step is the highest around the crests of the electric field. While the first step is treated quantum-mechanically, the second step, in which the continuum electron is accelerated away from the ion core and, as the IR field reverses its direction, returns to the mother ion,

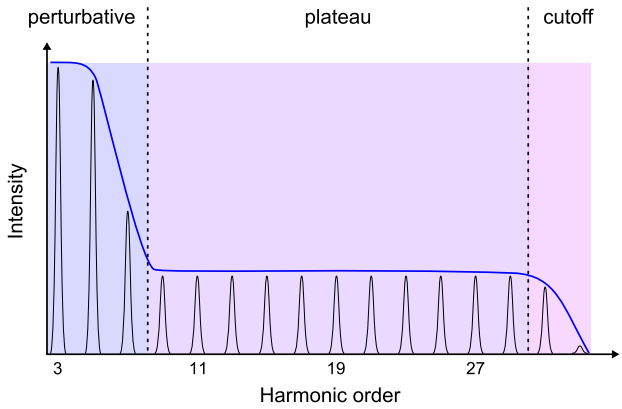

Figure 2.1: Illustration of the three different regimes in the high harmonic spectrum, characterized by a quick decrease in conversion efficiency for low harmonic orders which is followed by an extended plateau region and ends in a sharp cut-off at high photon energies.

is treated in the classical sense. According to the strong field approximation (SFA) [23, 24], the influence of the Coulomb potential can be neglected during the time that the electron spends in the continuum and hence moves only under the influence of the electric field of the laser pulse. In step three, as the electron returns to the ion core it can recombine and emit the potential energy plus the kinetic energy it has acquired from the laser electric field in form of a single photon with XUV frequencies. Depending on the time t during the IR cycle T, when the electron is released into the continuum, it can follow different trajectories or quantum paths. However, only those quantum paths initiated approximately during $t = T/4$ to $T/2$, where $t = 0$ signifies the moment where the electric field is zero, will efficiently generate harmonic radiation. Due to the inversion symmetry of the process, this emitted radiation is only produced in odd order harmonics of the fundamental light field.

The Three-Step-Model was subsequently tested by studying the dependence of HHG on the ellipticity of the driving field [25–27]. The measurements proved that the HHG process reacted very sensitively on the polarization of the driver field, hence supporting the image created in the three-step model. In a field with a polarization deviating from linear, the free electron will return to the ion core with a strongly reduced probability.

The so far described mechanism, however, applies to individual atoms only. In order to describe harmonic radiation emitted from a macroscopic sample of atoms, the electric fields generated from the individual atoms have to be added up coherently. Efficient generation of high harmonic radiation will therefore only be realized if phase matching is achieved, meaning that for a certain quantum path, every microscopic field emitted from a single atom has to oscillate in phase with the fields stemming from atoms distributed over the complete length of the non-linear medium [28, 29]. This mechanism is illustrated in Figure 2.2(c) and is only realized if the generating field and the harmonic field

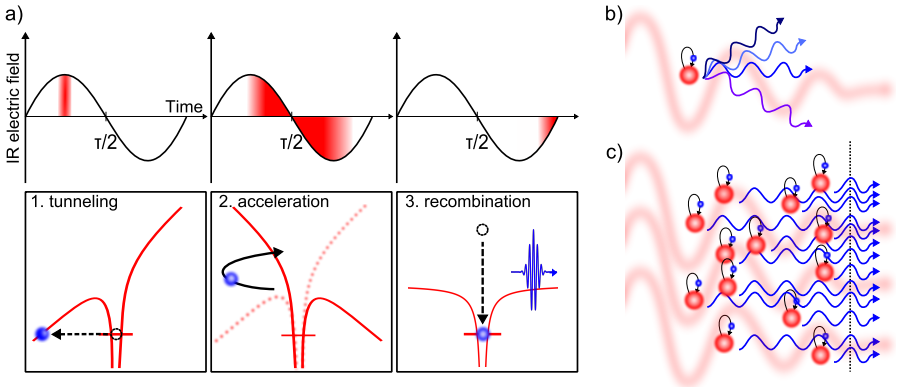

Figure 2.2: (a) Illustration of the three-step-model (bottom) together with the time interval (shaded in red) relative to the laser cycle of the driving IR field during which each step takes place (top). (b) High harmonic generation from a single molecule resulting from different quantum paths with different return times in contrast to (c) HHG in a macroscopic gas sample, where phase-matching is achieved, i.e., contributions of a single quantum path interfere constructively, resulting in efficient HHG.

have a fixed phase relation during propagation in the non-linear medium. If no phase-matching is achieved the radiation from different quantum paths (case of a single atom, see Figure 2.2(b)) interfere destructively, which results in poor conversion efficiencies from the fundamental to high harmonic radiation.

There are several contributions that can cause phase-mismatch between the fundamental field and the generated field, such as positive dispersion from free electrons in the medium (caused by ionization by the fundamental field), the dipole phase of the microscopic oscillators, geometric dispersion described by the Gouy-phase as well as normal dispersion by the medium itself (for more information on dispersion see also Section 5.2.3). These different effects can be controlled in a number of ways, including the gas pressure in the target, focusing conditions and position of the gas target with respect to the laser focus [29]. One common way of compensating for example the material dispersion by the Gouy-phase is to place the gas medium behind the focus position of the driving field [30]. In this approach it is possible to compensate geometric and free electron dispersion against material dispersion. Phase-matching in hollow core fibers [29, 31, 32] often allows for longer coherence lengths, as geometrical and dipole phases are strongly suppressed and, due to the single mode propagation, a constant intensity can be maintained over a long interaction region. A rule of thumb for efficient phase matching conditions in the absorption limit, i.e., when absorption becomes the limitation instead of coherence lengths, has been derived by Constant *et al.* [33]. (See also Section 2.5.2 for more details on phase-matching.)

Together with a series of experiments, optimizing the HHG processes [34] and investigating the spatial [35, 36] and temporal [37] structure of the produced radiation, the existence of an attosecond structure in the emitted radiation in the form of an APT was proposed [38–40], if the harmonics were locked

in phase. First proposals for the generation of IAPs were presented by Corkum *et al.* [41] and Ivanov*et al.* [42], which already had remarkable similarities to the technique of polarization gating (see also Section 2.5.1), demonstrated over ten years later by Sola and Sansone [43–45].

2.1.1 Generation of attosecond pulses

Attosecond pulses can be produced in two possible fashions. Either HHG from multi-cycle laser pulses is directly used to produce a train of attosecond pulses or an isolated attosecond pulses can be produced using one of several technically more demanding techniques. The principles and implications of either approach are laid out in the following paragraphs.

Attosecond pulse trains

The periodicity of the three-step process already implies that high harmonic emission of a single atom should take place at discrete intervals, separated by half-cycles of the fundamental field (see Figures 2.3 (a+b). XUV-photon emission can however result from a large number of different trajectories, with always two trajectories (short and long with respect to their time in the continuum) leading to the same photon energy. Antoine and coworkers [27] calculated that harmonic emission from a single atom therefore takes place at multiple times during a half-cycle of the laser field, attributed to recombination of electrons from the long and short trajectories. Long trajectories, however, have a larger spatial divergence than contributions originating from short trajectories [46]. Spatially filtering these different contributions by placing of a small aperture in the far-field allows the extraction of clean attosecond pulses, timed near the zero crossings of the driving IR field.

The first conclusive evidence of an APT resulting from HHG was presented by Paul and coworkers [10] in 2001. In their experiment, they observed the modulation of sidebands in photoelectron spectra as a function of the XUV-IR delay. The sidebands are caused by absorption and emission of additional IR photons relative to the photon energy of the individual harmonics. Each sideband can therefore be accessed from two consecutive harmonics, e.g., either from the lower harmonic by absorption of an additional IR photon or from the next higher harmonic by emission of an additional IR photon from the coincident IR field. The phase of the modulation of the respective sidebands then depends sensitively on the phase between the contributing harmonics and can subsequently be extracted. With this information, the temporal evolution of the attosecond pulses can be reconstructed. These measurements became known as "Reconstruction of Attosecond harmonic Beating by Interference of Two-photon Transitions" (RABITT) [47].

The results of such measurements show that the attosecond pulses resulting from HHG have a so called attochirp, i.e., the different optical frequencies inside the attosecond pulse are temporally delayed with respect to each other (see also Section 5.2.3). This behavior stems from the different recollision times during the generation process and limits the achievable pulse duration.

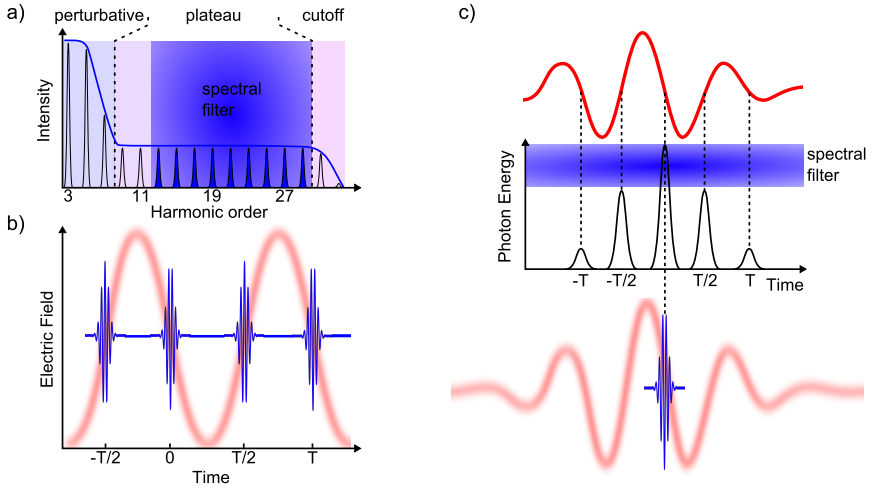

Figure 2.3: (a) Typical harmonic spectrum of odd harmonic orders. The shaded area symbolizes a spectral filter, which is often used to select harmonics of the plateau region, to generate an APT as depicted in (b). The attosecond pulses in an APT are synchronized to the zero crossing of the electric field of the driving IR field. In contrast to APTs, IAPs can, among other approaches (see Section 2.5.1), be formed from the cut-off region, as illustrated in the top of (c). Even though harmonics can be generated for multiple cycles in the IR field, the highest energy harmonics are only produced by the center half-cycle of the IR field. When those harmonics are spectrally selected (blue shaded area), they can form an IAP as depicted in the bottom of the illustration.

Spectral filtering with thin aluminum or other metallic filters can function as means of dispersion compensation, making pulse durations well below 200 as possible. Additionally such metallic filters are used to spectrally filter out lower harmonics which are experimentally uninteresting and block the fundamental laser light from disturbing the experiment. The shortest demonstrated pulse duration for pulses in an APT is currently 63 as [48].

Isolated attosecond pulses

Soon after the discovery of HHG in gases, it was proposed that under certain conditions the temporal structure of the emitted XUV radiation might make possible the generation of IAPs with pulse durations of ∼100 as [41, 49–51]. Finally in 2001 "X-ray pulses approaching the attosecond frontier" [52] were for the first time experimentally demonstrated in attosecond streaking experiments [53] yielding a time duration of 1.8 fs, i.e., shorter than the cycle time of the driving Ti:Sa laser.

Compared to generating APTs, which is relatively simple in terms of required experimental techniques, the generation of IAPs involves some experimental challenges that have to be mastered. It is intuitively clear that a driving pulse consisting of fewer field oscillations will produce an APT with fewer pulses. If this reduction is pushed to the extreme, the generation of

the highest order harmonics can be restricted to the most intense half-cycle of the driving laser field. This is, however, only possible if the pulses are short enough, such that the maximum field strength of consecutive half-cycles varies significantly. By spectrally selecting the highest energy region with appropriate spectral filters, one can generate isolated attosecond pulses. This experimental principle, illustrated in Figure 2.3(c), was also the approach used in the first IAP generation experiments and is still widely applied today. One of the advantages of the approach is that the attochirp in harmonic emission, as described in the last paragraph, is negligible in the cut-off region of the harmonic spectrum compared to harmonics in the plateau region [54]. The produced IAPs therefore often feature pulse durations which are close to their transform limit.

However, to produce the necessary laser pulses with few-cycle pulse duration, multi-cycle pulses from a femtosecond amplifier, containing one or a few millijoules of energy, have to be post-compressed in hollow-core fibre or filamentation setups.

Once few-cycle pulses have been achieved the maximum electric field strength varies strongly from cycle to cycle. Generally one describes the electric field evolution of such laser pulses $E(t)$ by an envelope function $A(t)$, which defines the temporal shape and duration of the laser pulse, and a carrier wave, which oscillates at the laser frequency ω beneath the pulse envelope.

$$E(t) = A(t) \cdot cos(\omega \cdot t + \phi_0) \tag{2.1}$$

In this case, ϕ_0 defines the phase of the carrier wave with respect to the envelope function and is consequently called the carrier-envelope phase (CEP). A value of $\phi_0 = 0$ would consequently describe a pulse in which an electric field maximum of the carrier wave coincides with the maximum of the pulse envelope. Under these conditions the highest possible instantaneous intensity is reached. In the case of $\phi_0 = \pi/2$ on the other hand, a so-called sine-pulse would be generated, characterized by two equally strong electric field maxima though oriented in opposite direction. For a more elaborated discussion of CEP effects the reader is referred to Section 5.3. In the same chapter an intuitive illustration of the CEP in few-cycle laser pulses can also be found in Figure 5.6.

Due to their double peak field evolution, sine-pulses can generate an APT consisting of two attosecond pulses or even no pulses at all if the instantaneous intensity of the two respective field cycles does not reach the threshold for energetic electron recollision; isolated attosecond pulses are, however, only produced for a cosine shaped driving field, i.e., when the CEP equals zero.

The conditions for IAP generation therefore depend strongly on the value of the CEP of the driving laser pulse. Even though experiments with IAPs were already performed earlier [11], the controlled generation of IAPs required the development of laser sources that could provide femtosecond pulses with a stabilized wave form and pulse energies in the millijoule range. This major technical advancement for attoscience was achieved in 2003 by Baltuska *et al.* [55].

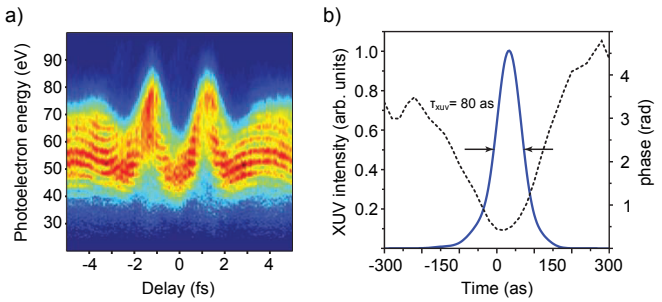

Figure 2.4: (a) Streaking spectrogram of the shortest demonstrated IAPs [56]. The duration of the streaking IR field is 3.3 fs, consisting of less than 1.5 cycles of the fundamental field at 720 nm. (b) The retrieved intensity profile and spectral phase of the attosecond pulse indicate a pulse duration of 80 as and an almost perfectly compensated spectral phase. Taken from ref. [56].

The first characterization measurements of attosecond pulses relied on a cross-correlation with the cycle-averaged intensity profile of the driving IR pulse [52]. In a second, more advanced cross-correlation measurement (streaking measurement [53]) the oscillating electric field of the driving pulse was employed to achieve an improved temporal resolution of <150 as [11]. This allowed the demonstration of the first real attosecond pulses with a duration of 650 as [11]. In the following years further improvements in the generation and characterization of IAPs were demonstrated, concentrating mostly on pulse characteristics such as duration [57–59], synchronization with the IR field [60] and tempo-spectral properties [61]. Using the same streaking techniques attosecond pulses were also used to measure the precise field evolution of IR pulses [62–64]. The current world-record for the shortest IAP was demonstrated by Goulielmakis and coworkers [56]. Employing driver pulses with a duration of only 3.3 fs the generated IAPs had a duration of only 80 as (their results are depicted in Figure 2.4).

In the meantime multiple alternative generation methods have been developed, which allow the generation of IAPs also from multi-cycle laser. These techniques will be described in the context of non-linear XUV and XUV-pump-XUV-probe experiments in Section 2.5 of this overview. The fundamentals of ultrashort laser pulses, CEP and the development of a CEP-stabilized laser systems will be covered thoroughly in Chapter 6.

2.2 Measuring electron dynamics in attosecond experiments

Many atomic and chemical processes as well as ultrafast phenomena in solid state systems, nano-scale structures or large bio-molecules are steered by electronic motion. In chemistry, the outcome of chemical reactions is determined by the electrons forming and breaking chemical bonds between the different reactants. In biology on the molecular scale, systems are influenced by electron

motion. This can be in the sense of electron motion responsible for the processing of bio-information or electronic motion governing changes in the chemical composition and functioning of biological systems [54]. In engineering, the control of ever faster switching of electron currents in nano-scale circuitry holds the promise to achieve still increasing rates of information processing. It is thus clear that the detailed understanding as well as the control of electron dynamics in any of these systems is a great experimental challenge and of fundamental importance for natural scientists and society in general.

The timescales of electron motion, however, escapes most conventional measurement techniques. Even though the Bohr model of atoms has for a long time been replaced by the quantum-mechanical description of atomic systems, it still allows to give a dynamical significance to the atomic unit of time [65], which is defined as

$$\tau_{\text{a.u.}} = \frac{\hbar}{2Ry} \ . \tag{2.2}$$

Ry is the Rydberg constant equal to 13.6 eV, the ionization potential of hydrogen. Qualitatively, the atomic unit of time describes the time that an electron in the ground state of a Bohr hydrogen atom needs to complete 1 rad of its path around the nucleus: $\sim$ 24 as. Electron motion hence takes place on an attosecond timescale.

Obviously the Bohr model does not correctly describe the quantum-mechanical situation in the sense that electrons do not physically orbit around the nucleus. In quantum mechanics, the electron in its energetic groundstate is described by its electronic wave-function, which in this case is stationary and the expectation values for the electron's position and momentum do not evolve. This is different if the electron absorbs energy and is excited. The electron wavefunction is then described by a superposition of multiple states. Assuming a superposition of only two states separated by an energy difference ΔE, the expectation values of the wavefunction will oscillate with a period $T = h/\Delta E$. For common electronic states the energy splitting is on the order of a few electronvolts, e.g., for H_2^+ the splitting between the lowest two electronic states is 11.9 eV, which consequently results in an oscillation period of 350 as.

Until a decade ago, it was only possible to measure processes on such timescales indirectly, usually by determining the line-widths of certain decay processes, which inferred the corresponding lifetimes via the uncertainty principle. However, to reveal more details of the process, especially in complex systems, direct observation becomes necessary.

IAPs and APTs are the ideal tools to perform such measurements. Which of the two attosecond sources is chosen to perform a measurement depends on several restrictions and / or benefits that make either method attractive for different kinds of experimental approaches as will be laid out in the course of this section.

Ultrafast dynamics are usually measured in a pump-probe approach, where a first pulse of coherent light initiates a dynamic process in the system to be studied. The dynmamic is subsequently probed by a second pulse. Pump-probe experiments therefore always rely on a multi-photon process. As the

achievable pulse energies of available attosecond sources are rather low (several pJ - nJ, see Section 2.5.1), this scheme up to now has only been realized as a two-color experiment, i.e., with one of the pulses being a femtosecond IR pulse. To achieve the necessary attosecond resolution, one uses the dependence of the investigated process on the sub-cycle time evolution of the IR field rather than on the much slower evolution of its femtosecond pulse envelope. Developments in the area of non-linear XUV experiments and XUV-pump-XUV-probe experiments are discussed separately in Section 2.4.

The first attosecond experiments have focused on characterizing the temporal evolution of the attosecond pulses themselves [10, 52, 57, 58, 64, 66] as well as on their generation process [60, 67, 68]. Nonetheless, the technical routine to produce attosecond pulses achieved in second half of the last decade has finally allowed to perform attosecond experiments that concentrate on the application of these pulses to the measurement and control of electron dynamic phenomena.

An overview of the so far performed experiments will be given in this section while several selected experiments will be discussed in more detail in the following Section 2.2.1. Experiments on the characterization of attosecond pulses will be omitted in this introduction as they have extensively been treated in a number of excellent reviews [54, 69, 70].

As pointed out in the beginning of this section, the electron dynamics of interest encompass a large number of different host systems, ranging from atoms to molecules or solid bodies and including both individual and collective motion of electrons as well as their interaction with each other. The experimental techniques that have been developed to investigate these dynamics are therefore just as numerous and span both measurement as well as control schemes. Measurement and control in the presented experiments are nevertheless closely connected as any measurement process also controls the appearance of the observed signal [54], e.g., the controlled and reproducible change of photo-electron spectra as a function of the delay between the pump and the probe pulse.

To create a structure for the presented overview, the discussed experiments have been divided into rough categories of probing electron dynamics in the continuum, of bound electron dynamics and experiments that focus on multi-electron dynamics and electron-electron correlation. For easy reference of the different experiments [71–90], they are also summarized in Table 2.1, which arranges the relevant experiments according to the dynamics that they probe and the experimental approach that was implemented.

Photo-ionization is one of the most fundamental processes in the interaction of light with matter and therefore has been studied by a number of experiments. Uiberacker *et al.* [71] probed the sub-cycle evolution of strong-field ionization using so-called "Attosecond tunneling spectroscopy". Neon atoms were ionized by an energetic IAP leaving the singly charged ions with electrons populating excited states, which lie close to the ionization potential. These excited states were subsequently tunnel-ionized by an intense IR field. By changing the delay between the IAP and the IR field the temporal evolution of these excited bound states can be probed. In the experiment of Uiberacker and coworkers [71] the

amount of doubly charged neon atoms as a function of the XUV-IR delay revealed a step-like increase for each additional sub-cycle that participates in the tunneling process. It was thus proven that strong-field ionization depended with attosecond resolution on the instantaneous electric field strength of the probe pulse.

Photo-ionization from solid state systems on the other hand was probed by Cavalieri and coworkers [73]. Employing "Attosecond streaking spectroscopy" [53], the different ionization times of electrons stemming either from localized core-states or delocalized conduction-band states were probed with IAPs. In such streaking experiments the time of emergence of electrons in the continuum is mapped to the final kinetic energy on the detector by the instantaneous field strength of a coincident IR laser field. A temporal shift in the two resulting streaking traces corresponding to each ionization channel revealed their relative delay. The same approach was chosen by Schultze *et al.* [74] to probe the ionization of electrons from the 2s and the 2p orbitals of neon atoms.

Using yet another technique, namely "Attosecond electron wavepacket (EWP) interferometry", allowed Klünder and coworkers [83] to extract emission times of 20 - 140 as for single-photon ionization from argon atoms. Attosecond EWP interferometry was, however, first demonstrated by Remetter *et al.* [85] in a pioneering work on continuum electron dynamics. Employing an APT in combination with a multi-cycle IR field, the multiple EWPs created by the APT can interfere at the detection plane, which allows interferometric measurements not only on the electron dynamics involved, but especially also enables the extraction of the phase accumulated by the EWPs during their interaction with the IR field. Such interferometric measurements have the great advantage that due to the interference of multiple events the signal to noise ration can be greatly enhanced.

In the hope to perform a tunneling spectroscopy measurement using APTs, Johnsson and coworkers [81] used APTs with a central energy lying below the ionization potential of the target helium atoms to populate weakly bound states. These subsequently were to be probed by an intense IR field through tunnel-ionization. Calculations solving the time-dependent Schrödinger equation, however, revealed that the eventually measured ion yield oscillations could not be reproduced with IAPs. This, however, would have been the case if tunnel-ionization had really been the cause for the measured modulation. It was consequently concluded that interference of transiently bound EWPs, resulting from different attosecond pulses of the train, caused a modulation of the absorption probability in the ground state and thus effectively also influenced the amount of ionized electrons. The experiment therefore signified the first interferometric measurement of bound EWPs and their dynamics.

While in recent works Ranitovic and coworkers [82] performed a systematic study of the dependence of EWP interferometry on the properties of the exciting APT, Holler *et al.* [78] concentrated on the residual 30 - 40 % of the electrons which remain in the excited states despite of the IR field. Since in the original experiment by Johnsson *et al.* [81] only charged particles could be detected, the information of the electrons remaining in the excited states was

*Table 2.1: Overview of attosecond experiments studying various electron dynamics in different systems. Experiments marked by * are treated in detail in Section 2.2.1 and Chapter 3.*

Experimental Technique	Dynamics of interest: Bound Electron Dynamics	Continuum Electron Dynamics	Multi-electron Dynamics
Tunneling Spectroscopy	Uiberacker 2007 Attosecond real-time observation of electron tunneling in atoms [71] (IAP) Mauritsson 2010 Attosecond electron spectroscopy using a novel interferometric pump - probe technique [72] (IAP) *		
Streaking Spectroscopy	Cavalieri 2007 Attosecond spectroscopy in condensed matter [73] (IAP) Schultze 2010 Delay in photo-ionization [74 (IAP)		Drescher 2002 Time resolved inner shell spectroscopy [75] (IAP) Gilbertson 2010 Monitoring and controlling the electron dynamics in helium with isolated attosecond pulses [76] (IAP) *
Transient Absorption Spectroscopy and Harmonic Seeding	Goulielmakis 2010 Real time observation of valence electron motion [77] (IAP) * Holler 2011 Attosecond electron wave-packet interference observed by transient absorption [78] (APT)	Gademann 2011 Attosecond control of electron-ion recollision in high harmonic generation [79] (APT) *	Wang 2010 Attosecond time-resolved autoionization of argon [80] (IAP) *
Photo-electron Spectroscopy	Johnsson 2007 Attosecond control of ionization by wavepacket interference [81] (APT) Ranitovic 2010 IR-assisted ionization of helium by attosecond extreme ultraviolet radiation [82] (APT) Klünder 2011 Probing single-photon ionization on the attosecond time scale [83] (APT)	Johnsson 2005 Attosecond electron wave packet dynamics in strong laser fields [84] (APT) Remetter 2006 Attosecond electron wavepacket interferometry [85] (APT) Mauritsson 2008 Coherent electron scattering captured by an attosecond quantum stroboscope [86] (APT)	
Photo-fragment Spectroscopy	Sansone 2010 electron localization following attosecond molecular photoionization [87] (IAP) * Singh 2010 Control of electron localization in deuterium molecular ions using an attosecond pulse train and a many-cycle infrared pulse [88] (APT) Kelkensberg 2011 Attosecond control of dissociative photo-ioniozation in D_2 [89] (APT) *		Siu 2011 Attosecond ionization of O_2 molecules in the presence of an IR field [90] (APT) *

effectively lost. Using "Transient absorption spectroscopy", however, allowed Holler and his coworkers to access also this information. Instead of measuring

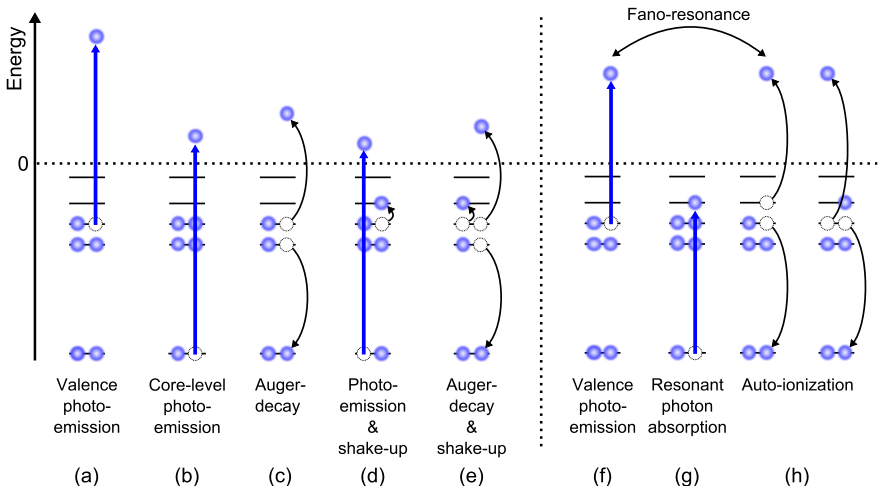

Figure 2.5: Illustration of the different possible direct or indirect ionization processes. Direct ionization from either a core state (a+f) or a valence state (b) is illustrated. After ionization (b) or excitation (g) from a core state a number of relaxation processes (c-f) relying on multi-electron interaction can occur. In the right half of the illustration, processes are depicted that ultimately can lead to the occurrence of Fano resonances, i.e., direct photo-emission from a valence state (f) in combination with resonant XUV or x-ray absorption followed by participant or spectator decay (h), usually summarized under the name of auto-ionization.

only the resultant charged particles after absorption of the XUV photons, transient absorption spectroscopy measures the optical absorption of the original XUV photons themselves. The residually transmitted XUV light is recorded as a function of the XUV-IR delay, allowing the measurement of the spectrally resolved absorption process with attosecond resolution. In most cases, this approach is experimentally easier as it is an all-optical approach. Additionally, it can lead to a higher acquisition efficiency, which in return results in shorter measurement intervals.

The same technique allowed Goulielmakis *et al.* [77] to follow the motion of bound valence electrons in krypton ions in real-time over a time interval of several femtoseconds. This experiment is explained in detail also in Section 2.2.1. The demonstrated results are also interesting since the experiment was performed in a fashion where part of the information is lost in the form of an undetected electron. It is thus dealing with an open system, which allows testing the coherence between the specimens of the ensemble.

Multi-electron dynamics and electron-electron correlations [91] are at the base of most physical processes, while only in simple prototypical systems and processes the assumption of a single active electron can be applied. Ways to measure and control such dynamics are therefore of great interest for the attosecond research community. Core excitation of atoms, commonly encountered during excitation with high energy attosecond pulses, can cause a number

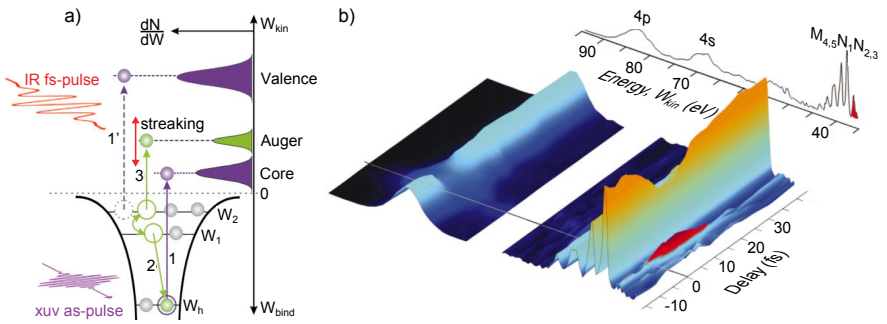

Figure 2.6: Schematic (a) and result (b) of the first application of attosecond pulses to investigate electron dynamics in atoms [75]. (a) The Auger process is a response to the photo-ionization via an XUV pulse. Direct ionization (from an inner or outer shell, 1 and 1' respectively) are instant responses of the atom (see also Figure 2.5). The inner shell vacancy with energy W_h is filled with an electron from an outer shell (2). The excess energy of this process is transferred to another electron in an outer shell which is subsequently emitted from the atom (3). The time evolution of this last process traces the decay of the inner shell vacancy. (b) Experimental electron spectra as a function XUV-IR delay. The delay where strongest broadening of the 4p photo-electron signal takes place indicates time zero. The contribution of the lowest energy channel of the Auger decay group (indicated in red), characterizes the delayed decay dynamics of the M-shell vacancy in krypton. Taken from ref. [75].

of multi-electron dynamics such as (sequential) multi-electron ionization and / or shake-up of one or several electrons, which are subsequently followed by relaxation processes such as the Auger-decay. An overview of different such ionization and excitation processes is illustrated in Figure 2.5.

Concentrating on multi-electron processes, the attosecond streaking measurements by Drescher and co-workers [75] signified the first real-time observation of the decay of an inner-shell vacancy by measuring the time-evolution of the resulting Auger electrons. The experimental principle and results are plotted in Figure 2.6. A similar approach was also used by Gilbertson *et al.* [76] to study and control auto-ionization of helium following the two-electron excitation through an IAP and the resultant Fano-resonances (see Figure 2.5). Wang and coworkers at the same time performed time-resolved measurement on auto-ionization of argon atoms using the transient absorption technique described above. For a more detailed discussion of the latter two experiments the reader is referred to Section 2.2.1.

Some of the most complex but also most relevant systems to investigate electron dynamics are molecules. In molecules there exists a correlation between the motion of the electrons and the nuclei. According to the Born-Oppenheimer approximation, these two motions take place at such different timescales that they can be considered independently when looking for solutions of the quantum mechanical equations of motion for the molecular system. There are, however, moments in chemical reactions where this approximation breaks down. For example this happens at the intersection of different poten-

tial energy surfaces, so-called conical intersection. When a molecule during its dynamics encounters one of these points, the ultrafast electron motion can have an effect on the dynamics of the complete molecular system. Therefore these are points which are of extreme interest for the further application of attosecond experiments.

Additionally, recent calculations have shown that even though molecular dynamics are usually related to femtosecond timescales, the charge rearrangement following ultrafast excitation or ionization of an electron unfolds on attosecond timescales [92, 93]. These results motivated the first experiment recently performed by Sansone and coworkers [87] to apply IAPs to the study of molecular electron dynamics. They observed the localization of an electron on one of the hydrogen cores during dissociative photo-ionization of molecular hydrogen ions. The localization process could be controlled by the relative phase of an intense few-cycle IR field with respect to the IAP (for a more detailed discussion of the experiment see also Section 2.2.1). In order to observe the electron localization, the asymmetry of ion fragment distributions was recorded in a velocity map imaging spectrometer (see also Section 3.1.2 and 4.1). Similar results were also achieved using APT with one attosecond pulse per full cycle of the probing IR field in a follow-upexperiment by Singh and coworkers [89].

These two experiments stand in close relation to two experiments which were performed at the AMOLF XUV laboratory during the course of this thesis. These experiments and the interpretation of the results are presented separately in Chapter 3. Dissociative photo-ionization of H_2, D_2 [88] and O_2 [90] molecules in the presence of an IR field was probed using a APTs. Both the angular distribution as well as the yield of ion-fragments proved to be effective observables to study attosecond processes in molecular systems. The results of the O_2 measurements further tested the application of the experimental approach on more complex molecular systems.

Another versatile approach to investigate multi-electron dynamics [94–97], as well as imaging molecular orbitals [94, 98–100] and probing related attosecond dynamics [101–103] is "High harmonic spectroscopy" which was first demonstrated by the pioneering work of Itatani *et al.* [98]. In these experiments not photon pulses in the sense of IAP or APT are used to probe the system of interest (These experiments are therefore also not listed in Table 2.1). Instead the process of HHG itself constitutes the measurement principle in the sense that the recolliding electrons act as attosecond probe to the generating medium. For completeness of this introductory chapter, a more detailed description and overview of experiments achieving attosecond resolution without the need for attosecond light pulses, such as High Harmonic Spectroscopy, can be found in Section 2.3.

In this context, however, it is interesting to investigate more closely the motion of the continuum EWPs. Continuum electron motion and the interaction with an intense IR field has first been investigated by Johnsson and coworkers [84] performing photo-electron spectroscopy measurements using regular APTs. In so-called "Attosecond Quantum Stroboscope" measurements on the

other hand Mauritsson *et al.* [86] released a sequence of identical EWPs into an intense IR field. The APT that was used in this experiment consisted of only one pulse per full optical cycle. These EWP are then identical in the sense of their relation to the driving IR field, assuming a slowly varying envelope of the femtosecond pulse. Thanks to these identical EWPs, a single ionization event could be studied stroboscopically by changing the delay between the EWP generating APT and the IR field and simultaneously measuring the resulting electron momentum distribution. In this first pioneering experiment, Mauritsson and coworkers studied the coherent scattering of electrons from their parent ions after their initial direction had been reversed by the intense IR field.

An experiment that allows the precise control over the available quantum paths and thus also control over the recolliding EWPs was performed in the course of this thesis [79]. EWP are launched into an IR field by use of an APT. The control over the subsequent recollision process was monitored by measuring the yield of high harmonic generation as a function of the delay between the APT and the multi-cycle IR pulse. A detailed discussion of this experiment is presented in Section 3.3.

The advantages and disadvantages related to the use of either IAPs or APTs is probably difficult to extract from the presented experiments. For reasons of clarity a number of reasons which speak either for or against the choice of one technique over the other is therefore summarized in the list on the following page. It becomes clear that depending on the dynamics of interest and the host system of these dynamics either IAPs or APTs can be more suitable. For a detailed overview of the different experimental techniques mentioned in this Section, the reader is also referred to the very good review of Krausz and Ivanov [54].

The number of experiments investigating electron dynamics has been growing exponentially over the last years. As the necessary technology becomes available at an increasing number of research facilities and the technical demands are lowered (see also Section 2.5.1), also the use of IAPs has seen a steady growth. Particularly the use of attosecond technology to investigate electron dynamics in molecules shows that the development towards systems of biological and technical relevance is starting to pick up pace, which promises a large number of further intriguing results in the near future.

Attosecond Pulse Trains	**Isolated Attosecond Pulses**
⊕ relatively simple experimental implementation	⊖ higher technical demands on the driving laser pulses such as few-cycle duration and CEP-stability
⊕ high single pulse energies as well as high integrated photon numbers ⇒ higher signal rates	⊖ low single pulse energies due to low conversion efficiencies (depending on generation technique: see Sections 2.1.1 and 2.5.1)
⊕ extraction of EWP phase via attosecond interferometry [81, 85]	⊕ implementation of classical pump-probe schemes using a single pump and a single probe pulse
⊕ in interference measurements using APT consisting of N pulses the investigated process is repeated N times and thus yield interference fringes which are N^2 times brighter ⇒ better signal to noise ratio [86]	⊕ large bandwidth allows coherent excitation of states spanning a large bandwidth [72]
⊕ allow simultaneously high spectral and temporal resolution	⊕ excellent temporal resolution
⊕ spectral and temporal properties of the pulse train can be tailored to the experiment and the system under investigation	⊖ spectral resolution is limited due to large bandwidth (see above)
⊖ duration of investigated dynamics is limited to a half period of the fundamental light otherwise multiple pumping and probing occur (can be extended to a full cycle when generating APT with two color field [86])	⊕ measurement of dynamics with attosecond resolution over time-spans much longer than the pulse duration of the fundamental field [72]
⊖ more complicated interpretation and analysis of resultant data	⊕ straightforward interpretation of experimental results

2.2.1 Recent attosecond experiments

In the following short paragraphs a selection of the most recent experimental results from a number of interesting attosecond experiments is presented. These papers have been picked to some extent based on personal liking, however, all of them present either new developments in experimental techniques such as transient absorption spectroscopy or interferometric measurements using IAPs and / or stand out because of the new physics that they have been able to explore. All of the presented experiments in this chapter are also listed in Table 2.1, where they are marked by a * - sign.

Attosecond control in auto-ionization [76, 80]

Using similar approaches as in the first IAP experiment by Drescher *et al.* [75], Gilbertson *et al.* [76] and Wang *et al.* [80] studied Fano resonances and the accompanying auto-ionization decay mechanisms in helium and argon, respectively. Such experiments are particularly interesting since they allow investigation of electron-electron correlations. In addition to extracting the decay time, both were able to demonstrate dynamical control on an attosecond time scale. In Gilbertson's experiment [76], helium atoms were ionized with IAPs. This ionization can take place via two channels, e.g., direct photo-ionization or double excitation to the 2s2p state through 1-photon absorption followed by auto-ionization (see Figure 2.7(a) and Figure 2.5).

Quantum interference between these two pathways causes the characteristic Fano resonance in the spectral domain (see also Figure 2.5). When an additional IR field is introduced, the electron dynamics can be monitored via streaking measurements allowing the extraction of the auto-ionization decay time. At the same time the IR field can modify the interference between the two ionization pathways by manipulating the amount of electrons stemming either from double excitation or direct ionization. An example of such control is plotted in Figure 2.7(b), showing that the peak amplitude of the Fano resonance oscillates with a period equal to that of the IR field, when scanning the XUV-IR delay with attosecond resolution.

Wang *et al.* [80] studied the auto-ionization of argon using transient absorption spectroscopy. This all optical technique yields can yield a higher data collection efficiency compared to conventional observables (In IAP experiments this is particularly helpful, considering the low pulse energies of available IAPs sources) and better energy resolution (50 meV) compared to photo-electron spectroscopy while allowing a much simpler experimental setup. Additionally, also absorption processes which do not result in charged particles can be monitored.

Contributions from the 4p, 5p and 6p states belonging to the $3s3p^6np^1$ P Fano resonance series were revealed in the recorded absorption spectra. When adding an additional IR field and measuring the transmitted harmonic radiation as a function of delay (see Figure 2.7(c)), the resonance peaks shifted to higher energies and became broader and weaker as they got closer to the temporal overlap of the two pulses. For high enough intensities of the IR, the 4p

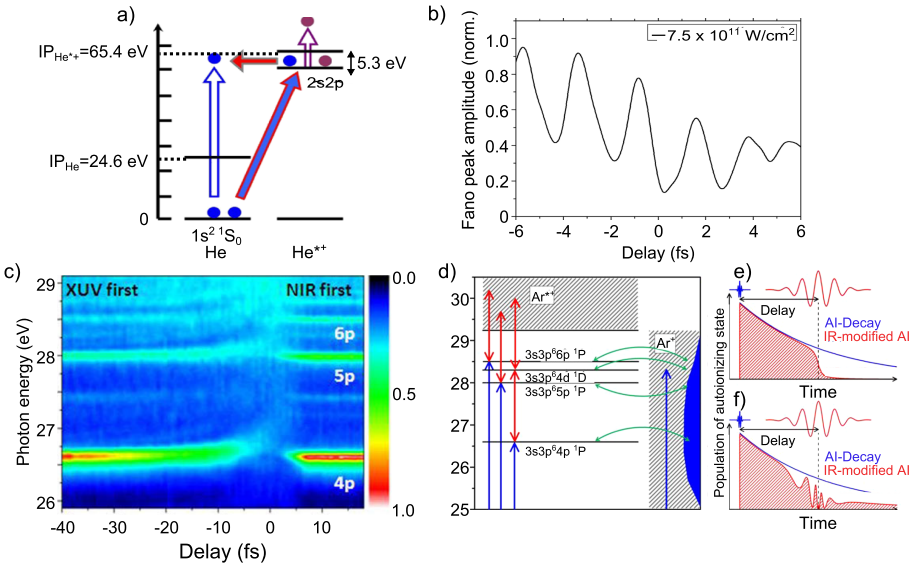

Figure 2.7: Experimental principle and results by the experiments of Gilbertson et al. (a+b) [76] and Wang et al. (c+d) [80].(a) Principle of the experiment by Gilbertson et al. showing the two ionization pathways (direct and auto-ionization) that are responsible for the appearance of the Fano resonances. In (b) the experimental result show the attosecond control over the Fano interference by manipulating the two pathways via the coincident IR field. Taken from ref. [76]. The results of Wang's experiment (c) show the transmitted XUV radiation as a function of delay and photon energy resulting from absorption in argon in the presence of a strong IR field. (d) Illustration of the auto-ionizing states in argon. Blue errors depict XUV excitation and / or ionization while red arrows symbolize either non-resonant coupling to the Ar^{*+} continuum or resonant coupling between different auto-ionizing states. Green arrows stand for configuration interaction couplings of auto-ionizing states to the Ar^{+} continuum. The resultant auto-ionizing decay evolution for non-resonant and resonant IR coupling are plotted in (e) and (f), respectively. Non-resonant coupling results in a broadening of the resonance, while resonant coupling causes a splitting of the resonance. Both effects can be recognized in the measured data (c). Taken from ref. [80].

state is additionally split asymmetrically with respect to the zero delay. This suggests an IR facilitated control over the auto-ionizing states via IR induced coupling to the ionization continuum. As is illustrated in Figure 2.7(d), this coupling can either happen non resonantly between auto-ionizing states and continuum states, or resonantly between different auto-ionizing states themselves, when they fall within the spectral bandwidth of the IR pulse (EIR = 1.3-2.1 eV). The latter is the case for the 4p and 4d auto-ionizing states (ΔE_{4p-4d}=1.7 eV).

The result of the two kinds of couplings on the evolution of the population in the auto-ionizing states is illustrated in Figures 2.7(e) and 2.7(f). While in the XUV-only case the auto-ionizing states will decay exponentially, the

non-resonant couplings will speed up this decay, leading to a broadening and shifting of the resonances as observed in the experiment (Figure 2.7(c+e)). In the case of a strong resonant coupling on the other hand, Rabi-oscillations between the two states involved (Figure 2.7(f) can cause a Stark like splitting of the resonance curve, which in summary explains the features observed in the measured data (see Figure 2.7(e)).

Attosecond interferometry using IAPs [72]

The goal of the experiment presented by Mauritsson *et al.* [72] is to characterize attosecond wavepackets by interfering them with respective free electron reference wavepackets. This makes it the first experiment to demonstrate attosecond EWP interferometry using IAPs. As described in Section 2.2, attosecond EWP interferometry had so far been exclusively used in experiments employing APT. The adapted experimental principle is illustrated in Figure 2.8(a). (I) Using IAPs with a broad spectral profile centered close to the ionization threshold of helium results in the simultaneous creation of a bound excited wavepacket near the ionization threshold as well as a free electron wavepacket in the continuum. (II) The bound wavepackets can evolve in a field free case for a certain delay before (III) they are ionized by a few-cycle IR pulse. Once the evolved bound state wavepackets are born into the continuum they can interfere with the free electron wavepackets, creating a interference pattern that includes both (i) quantum beat signals stemming from interference between quantum paths leading from the different excited states to the same final energy and (ii) interference with the free electron. As the results plotted in Figure 2.8(b) show, the latter interference (ii) depends on the observation energy, the quantum beat (i) on the other hand is independent of observation energy and therefore leads to vertical stripes in the delay dependent photoelectron spectrum. The different components of the excited wavepacket can easily be extracted by 2D Fourier analysis revealing both, which states are excited by the IAP, as well as the relative population of each of those states.

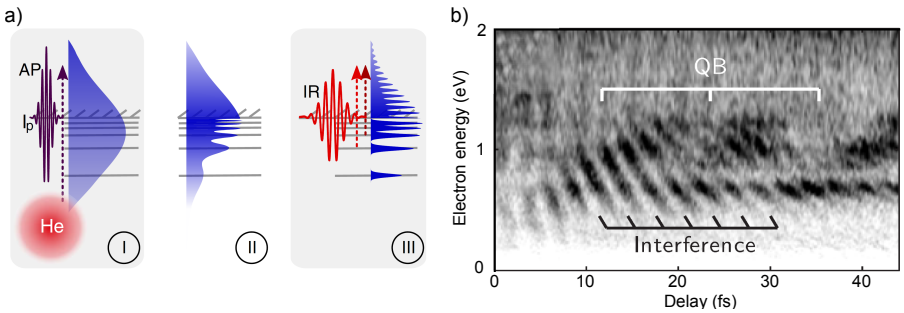

Figure 2.8: (a) Schematic illustration of the attosecond interferometry measurement by Mauritsson et al. [72] using IAPs as described in the text. In (b) a photo-electron spectrum in helium is plotted as a function of XUV-IR delay, revealing multi-path interference and quantum beats (QB). Adapted from ref. [80].

There are two distinct advantages of such a measurement compared to the known experimental approaches such as streaking for example. When IAPs are used in an experiment, the spectral resolution is usually limited by the spectral bandwidth of the exciting pulse, i.e., spectral resolution is only achievable at the expense of temporal resolution. In the case of the newly presented technique the spectral resolution, however, is dictated by the inverse of the delay between the two pulses, which can easily reach a factor of 100 better than the Fourier limit of the exciting IAP when using delays of ~ 10 fs.

Additionally, whereas in streaking or tunneling spectroscopy the IR field coincides with the IAP, in attosecond interferometry only delays without temporal overlap between the two pulses are considered in the analysis. In contrast to most other measurement techniques, this makes measurement of the excitation process in the unperturbed case possible, i.e., without the perturbing influence of a superposed IR field.

Molecular attosecond experiment with IAPs [87]

Even though the atomic motion related to chemical reactions takes place on a femtosecond timescale, it has been predicted that charge rearrangement in bio-molecules, following ultrafast excitation or ionization, happens on an attosecond timescale [92, 104]. Following these predictions and experiments performed with few-cycle IR pulses [105], Sansone *et al.* [87] performed the first experiment applying IAPs to investigate electron dynamics in molecules. These measurements revealed intramolecular electron rearrangements on an attosecond timescale.

H_2 and D_2 molecules were dissociatively ionized by a two color field consisting of an XUV-IAP and an IR few-cycle laser pulse. Measured angular asymmetries in the momentum distribution of the resulting fragment ions were used as observables. The results, which are plotted in Figure 2.9(a), revealed a modulation that depended with attosecond resolution on the pump-probe delay, inferring electron localization within the molecule to take place on attosecond timescales. Two IR-field induced mechanisms causing electron localization by breaking the symmetry of the two-electron wavefunction were described. Mechanism 1, depicted in Figure 2.9(b), changes the wavefunction of the continuum electron, i.e., describes an influence of the few-cycle IR field during the photo-excitation process. This mechanism occurs only at temporal overlap of the pump and the probe pulse. Mechanism 2, illustrated in Figure 2.9(c) changes the wavefunction of the molecular ion, i.e., describes an influence of the IR field on the molecular ion during the dissociation process, causing a population transfer between a wavepacket dissociating in the $2p\sigma_u$ and $1s\sigma_g$ states. This second process is mainly active after the temporal overlap of the two pulses.

Measurements on electron localization in H_2 in a comparable experiment using APTs yielded similar results [89]. In this case the APT was generated from both even and odd harmonics, thus breaking the symmetry of the wavefunction and making the use of a multi-cycle IR probe pulse possible. In Section 3.1 two more molecular attosecond experiments are presented applying

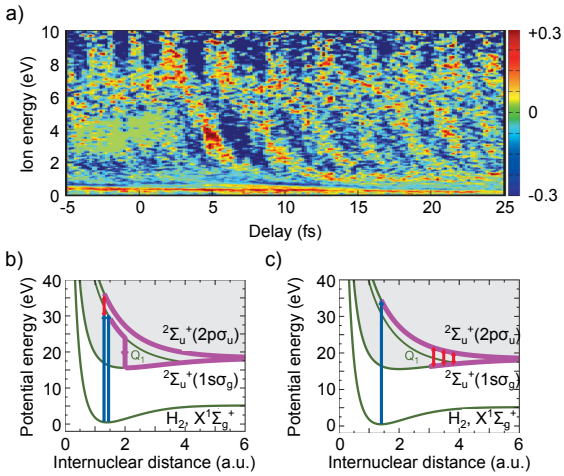

Figure 2.9: Molecular attosecond experiments by Sansone and coworkers [87]. In (a) the asymmetry parameter as a function of delay and ion fragment energy is plotted. The plot reveals a localization of the electron wavepacket in one of the outgoing ions, which depends with attosecond resolution on the XUV-IR delay. In (b) and (c) the two active mechanisms are illustrated. Blue arrows indicate ionization by the IAP, red arrows symbolize interaction with the IR field and purple lines describe pathways of the excited wave packet. (b) Mechanism 1 causes asymmetry by interference between two wavepackets. One EWP can be promoted to the $2p\sigma_u$ state by direct XUV ionization, the other resulting from auto-ionization of the Q1 state to the $1s\sigma_g$ state. The two states can, however, be coupled via absorption of an IR photon from the Q1 state before auto-ionization takes place. (c) Mechanism 2 describes interference between a wavepacket launched in the $2p\sigma_u$ state and coupling of this state to the $1s\sigma_g$ via stimulated emission of IR-photons during the dissociation process. Taken from ref. [87].

APT to H_2, D_2 and O_2.

These pioneering results will most likely attract the attention of many experimental scientist and motivate a quick increase in the number of molecular attosecond experiments. Especially the promise of attosecond technology to also investigate electron dynamics in multi-electron systems will further challenge the scientific community.

Real-time measurement of valence electron motion [77]

Only recently Goulielmakis *et al.* were able to demonstrate for the first time measurements resolving electron motion in real time using transient absorption spectroscopy. The experimental principle is illustrated in Figure 2.10(a). An infrared few-cycle pump pulse was used to generate krypton ions in a superposition of the two lowest energy states ($4p^{-1}_{J=1/2}$ and $4p^{-1}_{J=3/2}$ with J being the total angular momentum). The two states are split by 0.67 eV due to spin-orbit interaction, suggesting an electron beat time of 6.2 fs. The superposition is then probed by an IAP exciting the electrons mainly to the higher

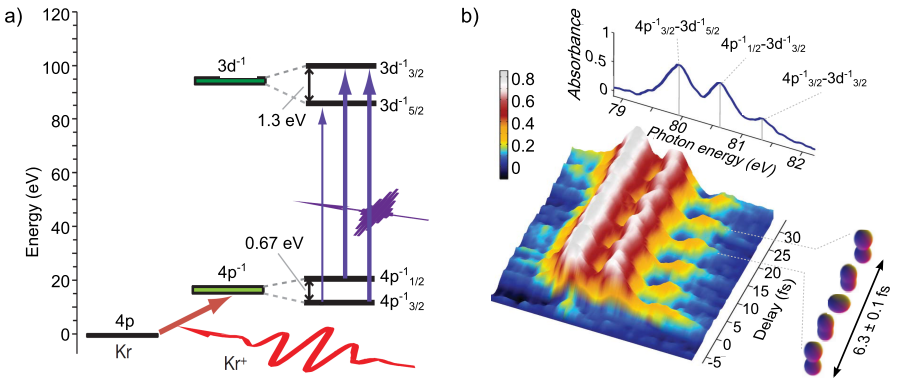

Figure 2.10: (a) Energy diagram of the krypton ion illustrating the experimental principle of the experiment by Goulielmakis [77]. The few cycle IR pulse ionizes the 4p subshell of krypton and generates a coherent superposition of the two spin orbit states $4p^{-1}_{3/2}$ *and* $4p^{-1}_{1/2}$*. From there the ion is excited to the* $3d^{-1}_{3/2}$ *state. Excitation to the* $3d^{-1}_{5/2}$ *state is only allowed from the* $4p^{-1}_{3/2}$ *state, but not from the* $4p^{-1}_{3/2}$ *state. This explains the experimental results plotted in (b). Interference between the two quantum-paths leading to the* $3d^{-1}_{3/2}$ *state is revealed by the characteristic modulation in the channels at ∼80.5 eV and ∼81.5 eV photon energy. The channel at ∼80 eV is attributed to excitation to the* $3d^{-1}_{5/2}$ *state via a single quantum path, and therefore shows no sign of an interference effect. Adapted from ref. [77].*

lying $3d^{-1}_{J=3/2}$ state. The different pathways leading to the excited state can either add up constructively if they are in phase, causing a strong population of the excited ion state and therefore a strong absorption of the incident XUV light in the specific transition energies. Or if the pathways are out of phase they add up destructively leading only to a small population of the excited ion state and accordingly to weak absorption of the XUV light. When the delay between the IR pump and XUV probe pulse were varied, the absorption was modulated with a period of 6.3 fs in very good agreement with the expected value, indicating the evolution of the phase and therefore the electron/hole dynamics.

(Interestingly, Goulielmakis and coworkers also present the stepwise formation of Kr^+, Kr^{2+}, and Kr^{3+}, with a half-cycle delay separating the appearance of each new charge state. This side result en passant confirms the sub-cycle dependence of tunneling ionization first demonstrated in the afore mentioned experiment by Uiberacker *et al.* [71].)

Another very important aspect elaborated by the author and further illuminated by Smirnova [106] is the inherent measurement of the entanglement between the continuum electron and the ion, which is left behind. As one electron is lost on the way to producing Kr^+ the authors are measuring an open system, which is a source of decoherence in the measured part of the system. The degree of the coherence of this sub-system, more specifically the coherence of the spin-orbit dynamics in the Kr^+, is encoded in the visibility of the interference features, i.e., the modulation depths in the absorption lines

of the delay scans. In the measurements, a high coherence - good modulation depths in the measurement - indicated that the quantum states of the removed electron were only weakly entangled and hence could be treated independently. This high degree of coherence was ensured by the few cycle laser pulse (with a duration of 3.3 fs), which built up the final population of the $4p^{-1}$ state within a single half cycle of the wavepacket (lasting 3.1 fs).

As Smirnova points out [106], this result has important implications especially to attosecond molecular experiments. As has been mentioned in the last presented molecular attosecond experiment, hole migration in large molecules can take place at sub-femtosecond timescales, during which the hole can travel over many Ångström [92, 107–109]. In the concept of charge-directed reactivity [110] - the notion that molecular bonds break at places where the hole has traveled to - such early stage hole dynamics might have a strong influence on the subsequent femtosecond scale nuclear dynamics.

Theoretical work aiming in the same direction has been done by Pabst and coworkers [111], who investigated entanglement between a photoelectron ionized by an IAP and the remaining ion. So far, theoretical calculations [112, 113] have often neglected this interaction, i.e., assumed a perfectly coherent hole wavepacket. From their results Pabst and coworkers, however, concluded that the interaction greatly enhances the entanglement between the two systems, and therefore cannot be neglected. The theoretical analysis of the results of Sansone and coworkers [87] in the last paragraph is an example where this interaction was not neglected.

Attosecond transient absorption spectroscopy could test the key assumption of this concept, namely coherence of the hole wavepacket during its preparation. Further the ability to probe coherences could allow investigating the coupling of hole dynamics to other electronic and vibrational modes in molecules, as this can be seen as a de-coherence evolving over time [106].

2.3 Other attosecond experimental techniques

Experiments with attosecond pulses, either in the form of APT or IAP, have been complemented by a number of experimental techniques, which achieve attosecond resolution without relying on attosecond pulse durations. For completeness of this overview three of these techniques will be described briefly.

The most well known approach probably is the use of waveform controlled laser pulses, which was first demonstrated in the pioneering work of Baltuska *et al.* [55]. One of the first applications to investigate and control sub-femtosecond dynamics in molecules was demonstrated by Kling and coworkers [105], and relates strongly to the earlier described molecular experiments by Sansone *et al.* [87] (See also Section 2.2.1). Using CEP-control, Zherebtsov and coworkers [114] recently demonstrated attosecond control over the collective electron motion and directional emission from dielectric SiO_2 nano-particles by manipulating the CEP-phase of the driving few-cycle laser pulses.

Attosecond angular streaking, also termed atto-clock experiments [115, 116], employs close to circularly polarized CEP-stable few-cycle laser pulses to achieve attosecond resolution. In this case the rotating electric field vector maps the instant of ionization of the investigated system to the emission angle of the photo-electrons. Using this technique, Eckle and coworkers were able to put an upper limit of 34 as on the tunneling delay time in helium atoms [117]. In contrast to common streaking experiments with linearly polarized light, where the ionization time is streaked to energy by use of an attosecond pulse (only possible during a quarter cycle of the IR field), in angular streaking the full cycle of the laser field can be used to study attosecond dynamics. This advantage was exploited this year (2011) by Pfeiffer *et al.* [118], when they measured ionization times related to sequential double ionization of argon in coincidence experiments. Using multi-cycle laser pulses, they were able to get fine and coarse timing information. Fine timing information was contained in the measured streaking angle, while the magnitude of the electron momenta as they reach the detector is dictated by the envelope of the laser pulse, thus supplying coarse timing information. In the images of the atto-clock one can think of a minute and an hour hand of the clock-face. Using this technique attosecond resolution even over large delays can be obtained.

Another very successful development in attosecond experiments is the use of the recolliding electron in HHG as a probe of the system under investigation. When the recolliding EWP interferes with the bound electronic wave function, the harmonic radiation produced can carry information on molecular structure as well as dynamics. The research field applying this concept has been dubbed high harmonic spectroscopy or attosecond high harmonic imaging [54]. In the experiment establishing this new field, Itatani and coworkers [98] were able to tomographically reconstruct the highest occupied molecular orbital (HOMO) of N_2, after recording a series of high harmonic spectra taken at different alignment angles of the molecule. Haessler *et al.* extended this work and imaged the HOMO and HOMO-1 [119]. Following experiments used the attochirp of the recolliding EWP to achieve a temporal resolution of 100 as. This technique was

used to investigate nuclear dynamics in H_2^+, CH_4 and CD_4 [101, 103] as well as to control attosecond EWP emission enabling pulse shaping in the attosecond regime [120]. Other experiments have been looking at multi-electron processes [95, 97]. In conclusion attosecond high harmonic imaging is an interesting field that promises experimental researchers to perform experiments, which simultaneously achieve Ångström spatial and attosecond temporal resolution.

2.4 XUV non-linear optics and XUV-pump-XUV-probe experiments

A majority of the just described two-color measurements can be seen as cross correlations of the attosecond pulse (or pulses) with the intense IR pulse, in which the electric field cycle acts as a watch that the electronic, atomic or molecular dynamics are measured against. However, due to its high intensity the IR pulse can often have a non-negligible influence on the investigated system. As a matter of fact, the influence of the IR field is many times turned into the actual objective of the investigation (which then is usually described as a control mechanism). Thus one of the greatest promises that attoscience holds is the demonstration of pump-probe experiments, in which both pump and probe pulse are made up of IAPs. This would allow measurements where both pulses are short compared to the timescales of the investigated dynamics and hence eliminate the just described drawbacks of IR pump or probe pulses. Even though there have been multiple theoretical proposals for XUV-pump-XUV-probe experiments [121–123], a number of prohibitive factors exists that for a long time have not allowed such experiments. First, in most of today's attosecond setups, the conversion efficiency from IR photons to XUV photons is rarely better than 10^{-5} - 10^{-6} for APT and even less for IAPs, which hence have been limited to pulse energies of pJ - nJ level. Considering the low cross-section for non-linear processes in the XUV spectral region (10^{-49} - 10^{-52} cm^4s for two photon XUV ionization), the XUV intensities would have to exceed $10^{13}W/cm^2$, in order to produce a measurable two-photon signal.

2.4.1 First steps in XUV non-linear experiments

While for a long time, due to the already mentioned restrictions, XUV-pump-XUV-probe experiments have been a distant dream of experimental physicists in attosecond science; thanks to the development of high energy laser sources and new techniques in HHG, such experiments are on the verge to become a reality. The evolution of XUV-pump-XUV-probe experiments has taken a similar evolution to XUV-IR pump-probe experiments as described earlier in the chapter. First non-linear processes such as two-photon ionization [124, 125], two-photon double-ionization [126, 127], or two-photon above-threshold ionization [128] were used mainly to investigate the temporal structure of the radiation produced by HHG in autocorrelation measurements. Recently however, the very first XUV-pump-XUV-probe experiments were performed at the FEL facility FLASH. The first XUV-pump-XUV-probe experiment using

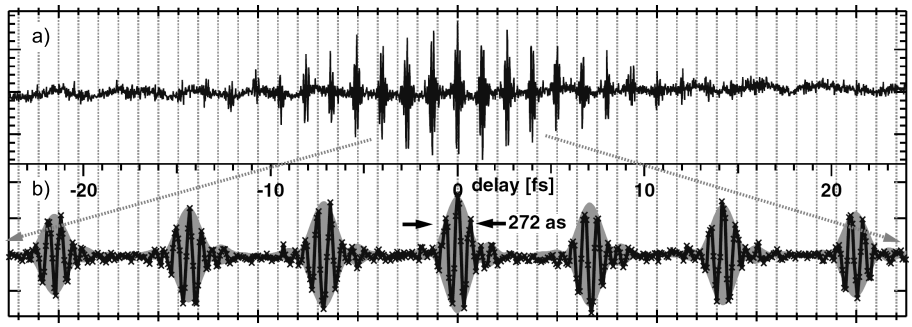

Figure 2.11: (a) Interferometric autocorrelation trace of a complete APT measured by Nabekawa et al. [130]. (b) Zooming in on the measurement in (a), reveals the relative CEP between consecutive attosecond pulses. Cross marks correspond to the actual measurement points, taken at a step size of 16.7 as, i.e., 5 measurement points per full cycle of the XUV radiation. Taken from ref. [130].

XUV sources based on HHG has only been presented this year (2011) [129]. Even though none of these experiments have yet succeeded to achieve attosecond resolution, the experimental principles are in all cases easily adaptable to IAPs and delay scans with attosecond resolution. An overview of the recent evolution will be given in this section.

XUV non-linear autocorrelation

The most straight forward way of characterizing attosecond pulses, either in the form of IAPs or APTs, is autocorrelation. However, autocorrelation needs a non-linear process, which, as mentioned above, is hard to achieve in the XUV spectral region. Nevertheless, there have been a number of publications characterizing either isolated XUV pulses composed of single harmonics with pulse durations in the femtosecond regime [131, 132] and APTs [125, 128, 133, 134] by using two-photon single-ionization mostly of helium. The singly charged ions are then detected as a function of the delay between the two pulses. By extending this scheme to detect doubly charged helium ions the energy range of this measurement technique was extended to 79 eV [126]. More refined techniques allowing the extraction of the spectral phase of the pulses, like Frequency Resolved Optical Gating (FROG) [135], have been demonstrated [136, 137] as well as Spectral Phase Interferometry for Direct Electric field Reconstruction (SPIDER) [138] in the XUV spectral region [139, 140]. XUV non-linear processes in atomic and molecular gas targets are two-photon single-ionization [124], two-photon double-ionization [126, 127], two-photon above-threshold-ionization [128, 141], and two-photon Coulomb-explosion [134, 142] and have mostly been applied in the context of XUV autocorrelation.

The probably most beautiful data from these measurements has been achieved by interferometric auto-correlation of APTs measured by Nabekawa and coworkers [130] and is shown in Figure 2.11. The plot shows an auto-correlation trace, which visualizes in a directly understandable way that pulses in an APT are

generally locked in CEP with a π phase shift between consecutive pulses, stemming from the inverted electric field of the driving laser pulse.

The first XUV-pump-XUV-probe experiments using a Free Electron Laser

Overcoming the intensity restrictions of IAPs, the recent advent of free electron lasers (FEL) such as FLASH in Hamburg or LCLS (Stanford) provides facilities where tremendous intensities in the XUV spectral region can be reached (though at much longer pulse duration). Jiang and coworkers performed two experiments at FLASH, where they exploited the huge flux of up to 10^{12} photons / pulse centered at 38 eV and concentrated in a time interval of $\sim$ 30 fs (determined by non-linear autocorrelation in N_2 [143]), to reach intensities in the range of 10^{13} - 10^{14} W/cm^2 [144, 145]. In a split mirror setup they were able to perform XUV-pump-XUV-probe experiments on molecular samples and detect the resultant ion fragments in a cold target recoil ion momentum spectrometer (COLTRIMS: Additional information can be found in Chapter 4).

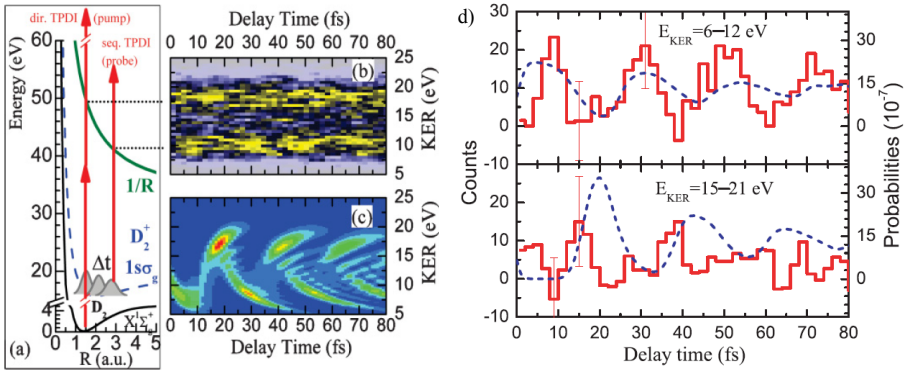

Figure 2.12: Results of the first XUV-pump-XUV-probe experiments performed by Jiang et al. [144] using XUV radiation of an FEL. In (a) the two pathways of either direct XUV two-photon double-ionization or sequential two-photon double-ionization of D_2 are illustrated. The latter is used to trace the motion of the molecular wavepacket. (b) and (c) show the experimental and a theoretical KER spectra for coincident D^+ + D^+ fragments as a function of pulse delay, respectively. (d) Delay dependence of the ion yields in two different energy regions of the experimental KER spectrum. Experimental results are plotted in red solid lines, theoretically calculated ionization probabilities are plotted in blue dashed lines. Taken from ref. [144].

The first experiment used two photon sequential double-ionization of D_2 to trace the femtosecond nuclear wavepacket dynamics in the $1s\sigma_g$ state of the molecular ion. The principle of the experiment is mapped out in Figure 2.12(a). The XUV pump pulse either populates the ground state of the D_2^+ molecular ion or directly double-ionizes the molecule by two-photon ionization, projecting it onto the repulsive (D^+ + D^+) Coulomb potential resulting in ionic fragments with E_{kin} = 18 eV. In the former case, dynamics of the evolving

wavepacket are probed by the time delayed second XUV pulse, sequentially ionizing the D_2^+ ion. Depending on the time delay between the two pulses, the moving wavepacket is projected to different energies of the Coulomb exploding potential curve and the kinetic energy release (KER) ($\propto 1/R$, with R being the internuclear distance of deuterium atoms at the moment of sequential ionization) of the fragments is detected in the COLTRIMS. The result of this measurement is plotted in Figure 2.12(b+d). Depending on whether the second ionization step happens at the inner or outer turning point of the wavepacket motion, the KER is either 10 eV or 18 eV. Summations over the signal in the two-dimensional data around these two energy regions (see Figures 2.12(d)) reveal the wavepacket motion in the lower energy channel, while oscillations in the higher energy channel are barely visible. This is due to a large time-independent signal stemming from the two-photon direct ionization channel.

The second experiment investigated XUV induced isomerization from acetylene to vinylidene cations [145], but will not be described in detail. The isomerization process involves at least one breaking of a CH bond and one forming of a new CH bond as one hydrogen atom moves from one end to the other end of the CC core. This process was mapped in real time by measuring CH_2^+ and C^+ in coincidence as a function of the delay between the two XUV pulses, with the CH_2^+ isomer fragment being a unique signature for H-atom transfer. The effective isomerization time in these measurements was found to be 52 ± 15 fs.

Both of these proof-of-principle experiments demonstrate that XUV-pump-XUV-probe approach are feasible and allow investigation of time evolution in nuclear wavepackets, structure dynamics in molecules and charge transfer processes. Nevertheless both experiments relied on large scale facilities using a technique for XUV pulse generation differing completely from the table top approach in HHG. Even though these two measurements allow conclusions about the general feasibility of XUV-pump-XUV-probe experiments, they leave the question unanswered if such experiments can already be accomplished with available HHG techniques. In the group of Charalambidis this question has been answered positively, which is proven by two further experiments, relying solely on XUV pulses produced via HHG in gas targets as laid in the next paragraphs.

The first XUV-pump-XUV-probe experiments using a HHG source

Even though auto-correlation measurements (relying on higher-order processes) with attosecond pulses and femtosecond XUV-pulses, produced with HHG, have already been demonstrated (see Figure 2.11), the first applied pump-probe-experiments using such pulses have only been demonstrated recently. Two examples including the first demonstration of an pump-probe experiment using IAPs will be presented in this section.

Probing molecular decay times Peralta Conde and coworkers [146] performed time resolved studies on the characteristic decay times of an excited electronic wavepacket in ethylene, decaying to the groundstate via a sequence

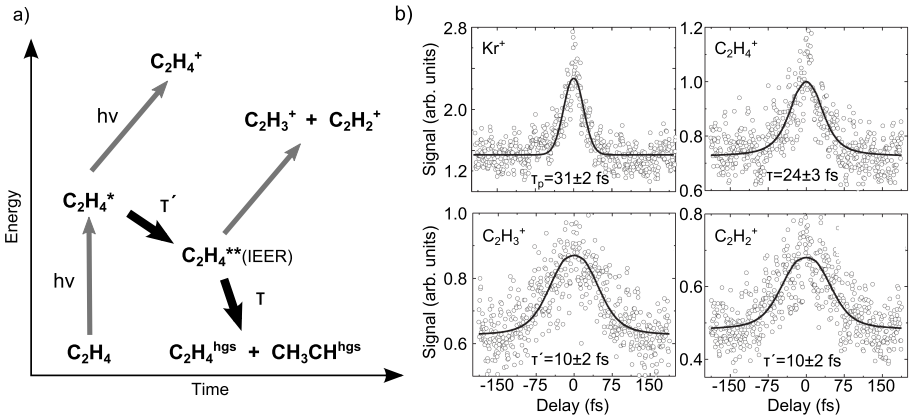

Figure 2.13: XUV pump-probe measurements on the excitation dynamics of Ethylene performed by Peralta-Conde and coworkers [146]. (a) Schematic of the excitation loop that Ethylene molecules undergo after excitation by a deep UV pulse. The different indicator channels for the measurement of the decay time are depicted as well. (b) Autocorrelation traces for these different channels and krypton. Krypton was mixed in the target gas to measure the duration of the VUV pulse, which was subsequently incorporated in the theoretical model. The decay times of the relevant states are encoded in the width of the autocorrelation traces of the respective ion fragments and were retrieved by fitting the result of a theoretical model to the experimental data (plotted in solid lines). The resultant lifetimes τ and τ' are printed in the measurement graph in (b). Adapted from ref. [146].

of quantum paths. The majority of the ethylene molecules is excited by the fifth harmonic of a Ti:sapphire femtosecond laser (produced in a xenon gas jet with subsequent spectral filtering) to an excited valence state as depicted in Figure 2.13(a). From this state the exited ethylene can either absorb another VUV photon, producing exclusively $C_2H_4^+$ ions, or it can reach an intermediate electronically excited region (IEER), where multi-dimensional dynamics occur and which is assumed to have a lower energy than the simple excited state. This decay is related to the decay time τ. When the ethylene molecule absorbs a second VUV photon while it is in the IEER, photo-fragmentation results in $C_2H_3^+$ and $C_2H_2^+$ molecular ion fragments, acting as a marker for the IEER state. If no photon is absorbed, the molecule reaches a conical intersection with the groundstate producing hot groundstate (hgs) ethylene and ethylidene. This decay is related to the time-constant τ'.

Figure 2.13(b) shows the dependence of the resonant two-photon ionization signal in the three ion fragment channels on the delay between the two VUV pulses. It also includes an intensity autocorrelation trace in krypton, which was mixed into the target gas to extract the pulse duration. The traces attributed to the three different ion fragments is modified by the characteristic decay times τ and τ', which were extracted by fitting parameters in a theoretical model (drawn as solid lines in the plots). This experiment marks the first non-linear deep UV experiment using radiation from HHG in a gas target.

Even though the pulses used are on the order of 30 fs and far away from the reachable photon energies in the XUV spectral region, the experimental principal is straight forward to apply to IAPs.

Revealing auto-ionizing wavepacket dynamics with IAPs All three experiments described so far in this section have not yet reached the ultimate goal in attosecond science, namely a pump-probe experiments, where a first IAP initiates electron dynamics, which are subsequently probed with a second IAP. Such an experiment has finally been demonstrated by Tzallas and coworkers [129] who investigated the dynamics in a coherently excited superposition of auto-ionizing manifolds in xenon. For this, IAPs spanning the spectral region of 50-80 eV were generated in xenon with a pulse energy of ∼100 nJ and subsequently focused by a split mirror setup in a second xenon target.

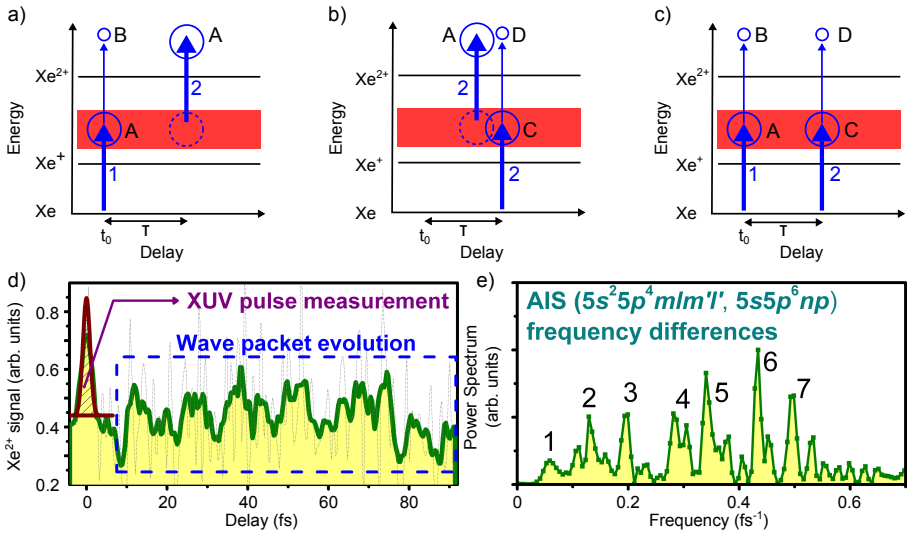

Figure 2.14: Experimental principle and results of the measurements of Tzallas and coworkers [129]. (a-c) Illustrated are state diagrams showing the ionization energies of Xe, Xe^+, and Xe^{2+}. The red area indicates the existence of an auto-ionizing manifold. XUV-pulses (blue arrows indicating (1) pump and (2) probe pulse) can excite wavepackets (circles) in both the auto-ionizing manifold and the continuum. The measured modulation of the Xe^{2+} yield can be caused by interference between two wavepackets from different origins. For the analysis, interference between wavepackets A and D resulting from process (b) in the continuum is considered to be most prominent, even though all processes take place simultaneously. (d) The experimentally measured Xe^{2+} yield is plotted as a function of the delay. Two delay regions are highlighted: In the first the two pulses overlap in time therefore the Xe^{2+} yield corresponds to a second order autocorrelation trace of the XUV pulses. In the second region the dynamics of the wavepackets in the auto-ionizing states are probed. In (e) the Fourier analysis of this region is plotted. Contributions from beat frequencies between different states in the auto-ionizing manifold can clearly be discerned. Adapted from ref. [129].

The estimated intensity reached between $3.2 \cdot 10^{13}$ and $2.5 \cdot 10^{14}$ W/cm^2. At these intensities the production of doubly-ionized xenon ions via two-photon absorption becomes more efficient than its one-photon counterpart.

The first pulse resonantly excites xenon atom to an auto-ionizing manifold. A small fraction of these states are further ionized by photons of the same pulse to produce Xe^{2+}. The second pulse can act in different ways, which are illustrated in Figure 2.14(a-c). Most interesting is the case when the second pulse performs the same steps as the first pulse, but additionally ionizes the evolved wavepacket in the auto-ionizing manifolds (see Figure 2.14(b)). When the delay is changed, the temporal evolution of the first excited wavepacket can be probed. The evolution of such wavepackets involving a large number of different states is rather complicated and produces a superposition of multiple beat signals at frequencies $\omega_i - \omega_j = \Delta E_{ij}/\hbar$, where ω_i and ω_j are the frequencies related to states i and j of the involved auto-ionizing manifolds [147].

This evolution was revealed by Tzallas *et al.* by measuring the yield of Xe^{2+} ions as a function of the delay between the two pulses and is plotted in Figure 2.14(d). Subsequently the beat frequencies were extracted by Fourier-analysis (see. Figure 2.14(e)), and could then be attributed to state transitions in the auto-ionizing manifold. Depending on the measured delay range, the energy resolution can be extended to arbitrary precision revealing beat periods that lie well below 1 fs. (This experiment follows a similar approach as demonstrated by Skantzakis and coworkers [147], who, however, used only two XUV single-photon process in combination with spatial confinement in the interaction volume to detect a beat signal).

With this experiment the era of XUV-pump-XUV-probe experiments using IAPs has been established, however, the necessary equipment is still missing in many laboratories. Even in the just presented experiment, there is an uncertainty with respect to the temporal structure of the IAPs, as the driver laser was not CEP stabilized. The result was the uncontrolled generation of either single or double pulse structures, which leaves an experimental uncertainty in the measured data. To create IAPs in a controlled fashion with the necessary intensities for non-linear optics in the XUV spectral region calls for technical developments in multiple parts of the generation process, which will be considered in the following section.

2.5 Technical considerations to set up a non-linear XUV experiment

This Section is closely related to the development of a terawatt amplifier system described in Chapter 6 supplying femtosecond pulses with a stable CEP. The intended use of this laser system is to be used for the generation of intense IAPs to perform attosecond-pump-attosecond-probe experiments as described in the last section.

To achieve the mandatory XUV intensities from HHG, one cannot rely on the conventional techniques described in Section 2.1. The use of energetic driver pulses therefore brings with it changes relating particularly to two aspects of the subsequent IAP or APT generation process. First, techniques for generating IAPs must be scalable to the increased driver energy, which excludes most of the traditional methods. Second, many of currently available phase-matching techniques are restricted to pulse energies of the driver pulse below a few millijoules. In the last few years there have, however, been a number of developments which potentially allow the production of intense IAPs from energetic driver sources.

2.5.1 Production of IAPs from multi-cycle pulses

The traditional way of producing IAPs is using few-cycle driver pulses from chirped pulse amplification (CPA) systems compressed in hollow core fibres [148] or filamentation [149] stages and spectral filtering of the cut-off harmonics generated via HHG in a gas target. Even though pulse durations as short as 80 as have been demonstrated using this technique [56], scaling to higher driving pulse energies is experimentally extremely demanding. Post-compression techniques to achieve intense few-cycle laser pulses are limited to input energies below 10 mJ. Additionally the strong drop of harmonic intensity in the cut-off region leads to very low conversion efficiencies from IR photons to XUV photons. Consequently the resulting XUV photon flux is only on the order of 10^5 photons / pulse (for $\sim$80 eV photons) [56]. Another technique that uses few-cycle laser pulses for the generation of IAPs is polarization gating (PG)[43–45] which uses two co-propagating pulse replicas with counter rotating circular polarization that have a small temporal overlap. In the region of overlap the electric fields of the two replicas add up to a linearly polarized gate. If the gate width is restricted to a single half cycle of the driving field, IAPs can be produced. Sansone et. al. [45] demonstrated pulses with 130 as duration and a photon flux of $1.25 \cdot 10^7$ photons / pulse (39 eV photons) using this technique.

At the same time PG lays the groundwork for a number of techniques that try to circumvent the need for few-cycle driving pulses opening up the possibility of generating IAPs directly from multi-cycle driver pulses. Such systems with pulse durations up to 30 fs are nowadays widely available and can reach energies even in the multi-Joule level.

The first advancement towards using longer driver pulses was made with double optical gating (DOG) [150], which additionally exploits the asymme-

try in the driving laser field introduced by adding a small fraction of second harmonic radiation to the fundamental PG light field. The asymmetry in the driver field limits attosecond pulse production to every full cycle of the field, allows the use of a larger gate width and additionally suppresses ionization from the leading edge of the driving pulse. Thus the use of laser pulses with durations of up to 12 fs has been demonstrated. IAPs generated from DOG have reached pulse energies of 6.5 nJ at 39 eV in argon and 170 pJ at 50 eV in neon corresponding to photon fluxes of approximately 10^9 photons / pulse and $2 \cdot 10^7$ photons / pulse respectively [151] before filtering with an aluminum mirror. The DOG technique was further refined by introducing its generalized form (GDOG) [152] which uses elliptically polarized light instead of circularly polarized lightfields as in PG and DOG. In this way ionization from the leading edge of the driving laser pulse could further be reduced, allowing for the first time the use of laser pulses directly from a laser amplifier (pulse duration: 28 fs) to produce IAPs from argon with a duration of 160 as and a pulse energy of 170 pJ at 40 eV ($2.6 \cdot 10^7$ photons / pulse) [153]. Nevertheless at higher driver energies one will still have to deal with the increased ionization which calls for further development of new phase-matching techniques.

Another approach to generating IAPs from multi-cycle driver pulses is the heterodyne mixing of two laser fields which was proposed for the first time by Siedschlag and coworkers [154], who predicted the production of isolated attosecond pulses from driving pulses with a duration of up to 30 fs. They further investigated phase-matching conditions and the necessity of a stabilized CEP for efficient IAP generation. Similar results were also presented in [155]. Experimental results from combining 800 nm, 30 fs laser pulses with weak 1300 nm, 40 fs pulses show the generation of continuous spectra in the XUV region, that can lead to the formation of IAPs [156]. This scheme further reduces the ionization in the leading edge of the pulse by two orders of magnitude compared to DOG and GDOG. Conversion efficiencies of 10^{-5} are expected. Using appropriate driving laser sources and phase-matching techniques, as described in Section 2.5.2, this approach eventually could lead to IAPs from HHG in gas with energies in the microjoule range [157, 158].

All of the so far demonstrated techniques for IAP production rely on HHG in gaseous media. However, when using plasmas generated from solid targets as a non-linear medium [159], conversion efficiencies of up to ten percent are expected [160]. In this case ionization changes from being a limitation in the process of HHG to being an inherent necessity for the process. At intensities when the magnetic field of the laser electromagnetic field becomes relevant, the plasma surface generated by the leading edge of the pulse begins to oscillate parallel to the laser propagation direction acting as a mirror for the incoming radiation that moves with relativistic velocities. This can lead to HHG and attosecond bunching of the reflected radiation [161–163]. Multiple experiments have been performed recently that demonstrate the conversion from IR light to XUV radiation by HHG from surfaces [164–168]. In 2008 it was demonstrated that the phases of harmonics emitted from surfaces are indeed locked and thus form an APT with individual pulses spaced by the laser period [169] as

opposed to APT from gaseous targets, where attosecond pulses are generated at each half-cycle of the driving field. This year (2011) Bom and coworkers were able to characterize pulses of an APT generated from a Chromium plasma [170]. The reconstructed pulse duration from RABBITT scans was an almost Fourier-limited 300 as. There have also been a number of schemes proposed for the production of IAPs, most of which require the use of few-cycle laser pulses. Nonetheless the use of polarization gating techniques seem feasible, even when multi-cycle driver pulses are used [171, 172]. Recent measurements [173] support this notion.

For all mentioned techniques of IAP production the stabilization of the CEP is mandatory if one wants to produce attosecond pulses with consistent temporal shape and photon flux for all laser pulses. When scaling CPA systems to higher pulse energies, the repetition rate of the laser system is usually limited to a few tens of Hertz. However, all of today's commercially available CEP-stabilized laser systems are operated at pulse repetition rates in the kHz range and pulse energies of not more than 20 mJ. In Chapter 6 the development and setup of a CEP stabilized TW amplifier running at 50 Hz repetition is presented. With achievable pulse energies of 50 mJ at a pulse duration of 32 fs, it is the ideal source to drive production of intense IAPs as described in this chapter.

2.5.2 Phase-matching for high energy driver pulses

Unlike in conventional high harmonic generation, where usually a relatively tight focusing geometry is used to achieve saturation intensities in the gas target, higher driving pulse energies require a somewhat different approach. Formerly used hollow core fibres for phase-matched HHG [29, 31, 33, 174, 175] can suffer damage at the fibre entrance, when irradiated with laser pulses exceeding an energy of a few millijoules. The same holds true for filamentation techniques, where high driving pulse energies cause the necessary single filament to break up into multiple filaments. Also in tight focusing conditions, the extremely high intensities would make phase-matching impossible due to plasma generation.

The outline of this paragraph will follow the most conclusive description of phase-matching techniques appropriate for the use of high energy driving pulses, which can be found in refs. [157, 176]. In order to increase the harmonic yield, they demonstrated the use of high energy driving lasers in combination with a loose focusing geometry. In the long focusing limit, this geometry becomes equivalent to the guided beam geometries mentioned before [177].

The focal length has to be chosen such that the intensities reached in the focal spot remain below the ionization threshold of the target gas. This allows neglecting the phase mismatch caused by free electrons. Thus phase-matching conditions can be satisfied purely by compensating the phase mismatch induced by the neutral medium's dispersion with an opposing mismatch by the geometrical dispersion resulting from the Gouy phase-shift.

The formula derived by Constant [33] estimates the photon number N_q of the q-th harmonic per unit of time and area as:

$$N_q \propto N_0^2 |d(q\omega_0)|^2 \frac{4(l_{abs}L_{coh})^2}{L_{coh}^2 + (2\pi L_{abs})^2} \cdot \left[1 + exp\left(-\frac{L_{med}}{L_{abs}}\right) - 2cos\left(\frac{\pi L_{med}}{L_{coh}}\right) exp\left(-\frac{L_{med}}{2L_{abs}}\right)\right] , \quad (2.3)$$

where $d(q\omega_0)$ is the atomic dipole moment induced by the laser pulse, N_0 is the neutral gas density, and ω_0 is the frequency of the laser pulse. L_{med}, L_{coh}, and L_{abs} denote the length of the medium, the coherence length and the absorption length of the q-th harmonic.

The formula implies that the photon yield N_q saturates, when the coherence length L_{coh} becomes comparable to the absorption length L_{abs}. Accordingly, the coherence length should considerably exceed the absorption length. When additionally the medium length is longer than the absorption length, but still smaller than the coherence length, the harmonic photon yield follows the proportionality [178]

$$N_q \propto |d_q|^2 \, z_0 \, (NL_{med})^2 \propto A(PL_{med})^2 , \quad (2.4)$$

where z_0 is the Rayleigh length, A is the spot area of the driving laser at the interaction region and P is the gas pressure of the target gas. There are several restriction imposed with respect to usable values of these parameters, e.g., the intensity of the laser is restricted to values below the ionization threshold of the target gas, and the product PL_{med} is limited by the self-absorption of the harmonic radiation in the gas target itself. Thus increasing the spot size with increasing driving pulse energy seems to be the sensible solution. However, a larger spot size, assuming a Gaussian beam, implies a decrease in the Gouy-phase, which is described by

$$\Delta k_{gouy} = \frac{q}{z_0 + \frac{z^2}{z_0}} . \quad (2.5)$$

Consequently, the gas pressure must be decreased to lower material dispersion, which in return is compensated by proportionally increasing the medium length to regain the lost energy in the emitted harmonics. As a rule of thumb, the product PL_{med} is kept constant. In conclusion the increase in XUV photon yield is achieved via an increase in active area contributing to the HHG process. A systematic study [157] using laser pulses with a duration of 35 fs and an adjustable pulse energy of 5 - 20 mJ, however, showed that an increase in the driving energy by a factor of four and simultaneously optimizing the focal waist radius (60 µm to 200 µm), medium lengths (1 cm to 10 cm) and gas pressure (20 torr to 2 torr) led to a rise in the achieved photon yield by a factor of 10. The conversion efficiency thus increased by a factor of two to 1.5 x 10^{-5}. This

was attributed to a lower re-absorption of the generated harmonics outside the generation gas cell due to the improved background pressure [178], which is an additional benefit of the low pressure / long medium length geometry.

Total harmonic energies achieved with such a setup are as high as 11.5 µJ in xenon spanning harmonic orders 11 - 19, and 0.7 µJ in argon spanning harmonic orders 23 - 31 [158]. Similar results were also demonstrated by Hergott and coworkers using a comparable phase-matching geometry [179].

2.5.3 Quick note on the filtering of the fundamental

In conventional low energy HHG sources driven by few mJ femtosecond lasers, the residual IR light after the HHG cell is filtered out by thin metal foils of several hundred nanometers thickness, such as aluminum or zirconium. In case of a high energy pump beams, such thin foils can easily be damaged due to the thermal load.

The solution lies in silicon or silicon carbide plates which are set at the Brewster angle of 70° for the fundamental IR light [180]. At this angle the XUV light around the 27th harmonic sees a reflectivity of ∼70 %. Appropriate substrates with sufficiently low surface roughness (<1 nm) and high damage threshold are commonly used in the semiconductor field. Efficiencies of such harmonic separators can reach values exceeding those of their thin metal foil counterparts.

3 Attosecond experiments at AMOLF

In this chapter four experiments are discussed that have been performed in the course of this thesis at the AMOLF XUV laboratory. In the context of the introductory chapter 2, the first two experiments are a continuation of the work started by Sansone *et al.* [87] (see also Section 2.2.1) to apply attosecond pulses to the investigation of electron dynamics in molecules. Since the two experiments are closely related they are presented in the same section.

The third experiment exploits the high photon energies inherent to attosecond pulses. Electron diffraction of electrons stemming from within a molecule could allow the direct observation of structural dynamics with higher spatial and temporal resolution than possible with conventional femto-chemistry methods. In such common spectroscopic measurements, a pre-existing knowledge of the molecular structure is often required to interpret the measured results, whereas the presented experimental technique might allow the direct measurement of the molecular structure and the dynamics related to it. This was achieved by measuring photo-electron angular distributions originating from XUV-ionization of aligned molecules and comparing them to theoretical simulations.

The third experiment can be seen in the context of high harmonic spectroscopy [98] (see Sections 2.2 and 2.3), where, unlike in conventional pump-probe techniques, the recolliding electrons are used to probe structure and dynamics of molecules. In the presented experiment, an APT was used to launch EWP into the continuum at well defined points in time with respect to a coincident IR field. The IR field subsequently reverses their initial velocity, leading to recollision with the parent ions in a well-controlled manner. The functioning of this principle is observed by recording the high-harmonic yield stemming from the process of electron-ion recollision as a function of the delay between the APT and the multi-cycle IR pulse.

3.1 Attosecond control of dissociative photo-ionization of small molecules

3.1.1 Introduction

Since the first realization of laser pulses with attosecond duration [10, 11], scientists have engaged in applying the new possibilities that these pulses offer to observe and control ultrafast electron dynamics in different systems such as atoms [71, 75] and solid state systems [73]. Chemical transformations of molecules and the related atomic motion happens on timescales of femtoseconds, however, also an electronic timescale is relevant and was predicted for ultrafast charge re-arrangement following the sudden removal or excitation of electrons [92, 93]. This motivated the first time-resolved measurements applying isolated attosecond pulses to molecules [87]. In a pump-probe experiment H_2 and D_2 molecules were dissociatively ionized by a sequence of an isolated attosecond pulse and a few-cycle phase-stabilized infrared (IR) pulse. The angular asymmetry in the momentum distribution of the ejected ion fragments depended with attosecond resolution on the relative delay between the two pulses, implying that electron localization in one of the ejected nuclei happened on an attosecond timescale.

However, in this experiment it was not yet possible to trace the motion of the electron during the process of localization and only the final result could be observed. The attosecond pulse acted as a pump, which initiated the investigated electron dynamics, which were subsequently addressed by the IR pulse, whereas using attosecond pulses as a probe might allow the real time measurement and control of molecular systems. Since current attosecond light sources do not yet provide sufficient intensity to conduct attosecond pump - attosecond probe experiments, current schemes of such an experiment would have to be two-color experiments, involving at least one pulse with femtosecond duration.

Two experiments that test this approach were performed at AMOLF. In the first experiment dissociative photo-ionization (DPI) of H_2 and D_2 molecules was controlled using attosecond extreme ultraviolet (XUV) pulses in the presence of an IR-field. In the second experiment the measurement was extended to O_2 molecules to test the feasibility of such a control scheme on larger molecules where the response of the system is multi-electron in nature and can involve coupling of nuclear and electronic degrees of freedom. Results for both measurements will be presented and differences in results and interpretation highlighted.

3.1.2 Experimental setup for H_2, D_2, and O_2 measurements

The experimental setup used to measure the presented data is shown in Figure 3.1 and described in detail in the corresponding caption. The XUV attosecond pulse train (APT) was produced via high harmonic generation (HHG) in kryp-

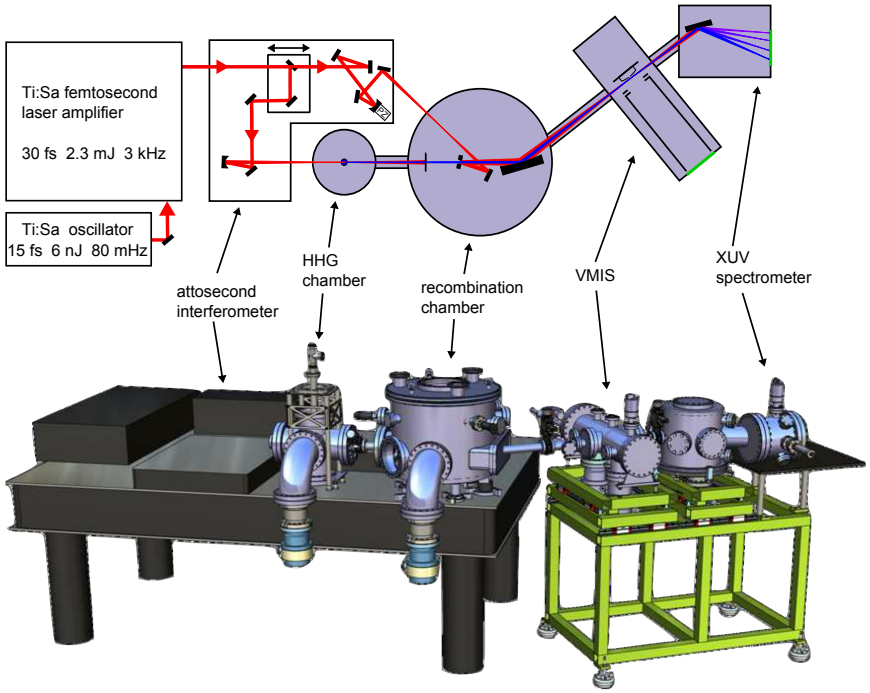

Figure 3.1: ***top:*** *Schematic of the attosecond pump-probe setup at the AMOLF XUV laboratory. Ultrashort IR laser pulses (30 fs, 2 mJ, 780 nm, 3kHz) of a Ti:Sa laser system are equally split into the two arms of a Mach-Zehnder interferometer. The first arm includes a gas cell with static gas pressures for generation of the attosecond pulse train (APT) via high harmonic generation. The residual IR light and lower order harmonics after the gas cell are filtered out using a 200 nm thick aluminum filter. The second arm includes additional focusing optics to match the laser beam divergence of both arms and two delay stages for coarse and fine adjustment of the relative delay between the APT and the IR pulse. The delay between the two arms is actively stabilized using a copropagating HeNe-laser beam. In this way a residual timing jitter of less than 50 as root-mean-square is achieved. The XUV and IR beams are recombined on a drilled mirror and collinearly focused into the interaction region of the velocity map imaging spectrometer (VMIS) using a platinum coated toroidal mirror. To achieve a high target gas density in the interaction region the gas is introduced by a pulsed valve that is integrated into the repeller electrode of the VMIS [181]. Charged particles formed through interaction with the combined light fields are registered on a two-dimensional position sensitive detector. An electrostatic lens assembly projects the original 3D momentum distribution of the particles on the 2D detector such that particles with the same velocity are mapped to the same spatial coordinate of the detector, hence the name of the technique. A 200 ns gate is applied to the detector to select either electrons or ion fragments of interest. The remaining XUV light after the VMIS is monitored with an XUV flat-field spectrometer.* ***bottom:*** *A realistic rendering of the attosecond pump-probe setup.*

ton for the H_2 and D_2 measurements and in xenon for the O_2 measurement. The XUV spectra consisted of the odd harmonic orders 11-27 (17.5 eV - 42.9 eV) and 11 - 21 (17.5 eV - 33.4 eV) respectively. The femtosecond IR pulses in the second interferometer arm had a pulse duration of 30 fs and were centered at a wavelength of 785 nm. The XUV and IR beams were subsequently recombined on a drilled mirror and focused into the target gas. The three-dimensional velocity distributions of the fragment ions H^+, D^+ and O^+ were projected onto a position-sensitive two-dimensional detector and the original velocity distributions were retrieved using a numerical inversion algorithm. The intensity of the IR field in both cases was chosen to be low enough to not cause any dissociation by itself. Momentum distributions of the H^+, D^+ and O^+ fragment ions were recorded while scanning the XUV-IR delay with a step size of 200 as over the central time overlap of the XUV and IR pulses.

3.1.3 Results for D_2

All results presented in this section refer to measurements on D_2 molecules. Results from measurements with H_2 show an analogous behavior. The kinetic energy spectrum of D^+ resulting from XUV-only ionization by the APT is plotted in Figure 3.2(a) in black solid lines for emission along the laser polarization and in Figure 3.2(b) for ejection perpendicular to the laser polarization. To obtain these spectra the ion yield was angularly integrated over an acceptance angle of $\pm$ 20° along the respective emission direction. This distinction is made since different ionic states appear at different angles of the momentum map.

Contributions to the ion fragment signal from different channels can be discerned and related to the potential energy curves plotted in Figure 3.2(c). Ion fragments with small kinetic energies (E_{kin} <1 eV) originate from a weak dissociative channel after direct ionization to the primarily stable ionic groundstate $1s\sigma_g$ of D_2^+. Fragments ejected mainly along the laser polarization in the kinetic energy region from 1 eV to 5 eV stem from auto-ionization of the $1\Sigma_u^+Q_1$ doubly excited states depicted as red curves in Figure 3.2(c). Contributions from the $2p\pi_u$ at 5 eV are barely discernable as ionization to this continuum and excitation to even higher lying states was restricted as much as possible by tuning the XUV spectrum accordingly. This section will focus primarily on the channels at 7 - 8 eV, which originate mainly from direct ionization to the $2p\sigma_u$ continuum for molecules aligned parallel to the laser polarization, and from excitation to the Q_2 auto-ionizing doubly excited states (blue curves in Figure 3.2(d) for perpendicularly aligned molecules.

When introducing an additional IR field to the interaction, significant changes in the photo-ion kinetic energy spectrum become visible. The red dashed lines in Figures 3.2(a+b) show the photo-ion spectrum that results from averaging over a range of delays spanning one complete cycle of the IR field. The ion yield along both emission directions is enhanced over the full kinetic energy range, while the enhancement around the 7-8 eV channel is particularly pronounced.

Figure 3.3 shows kinetic energy spectra as a function of the XUV-IR delay for ion emission parallel (a) and perpendicular (b) to the laser polarization.

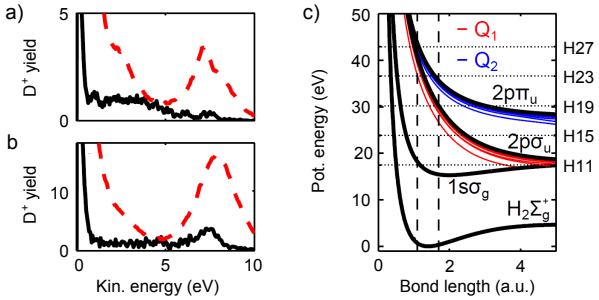

Figure 3.2: Kinetic energy spectra for D^+ fragments emitted along (a) and perpendicular (b) to the laser polarization in case of APT-only ionization (black solid lines) and in the presence of the IR field (cycle averaged)(red dashed lines). Neutral states are marked in red and blue, ionic states as well as the neutral groundstate in black. The Franck-Condon region is indicated with vertical dashed lines. The horizontal dashed lines mark the energies of harmonic orders present in the experiment.

Different parts of the spectrum oscillate with half the period of the IR laser field, indicating a direct influence of the instantaneous IR electric field strength on the process under investigation. The ion yield of the high energy channels (E_{kin} = 7-8 eV) at parallel and perpendicular emission to the laser polarization oscillate out of phase, as can be seen by channel specifically integrated ion yield plots in Figures 3.2(c+d)(black curves). For parallel ion emission (Figure 3.2(c)) the yield from the channel at lower kinetic energies (E_{kin} <5 eV) (red line) additionally oscillates out of phase with the channel at high kinetic energies (E_{kin} = 7 eV)(black line).

Calculations solving the time dependent Schrödinger equation (TDSE) by a close-coupling method for D_2 interacting with a combined XUV and IR field [87, 182] reproduced the channels prominent in the experiment as well as the oscillations at low and high energies (results not shown here). They further reinforce the notion that high energy fragments (E_{kin} = 7-8 eV) mainly stem from the $2p\sigma_u$ continuum, whereas fragments with low kinetic energy (E_{kin} = 1-5 eV) are the result of auto-ionization from the $^1\Sigma_u^+ Q_1$ state to the $1s\sigma_g$ continuum. Additionally the calculations showed that such oscillations appear for both APT and isolated attosecond pulses. Therefore they cannot be attributed to an interference effect from consecutive attosecond pulses as occurred in the afore-mentioned He experiment by Johnsson *et al.*, (see Section 2.2) [81]. Even though these calculations allow reproduction of the measured data with great detail, they do not allow a good insight into the physical processes, and thus the development of a qualitative understanding is difficult.

In order to develop such a qualitative picture, a simple model, schematically illustrated in Figure 3.4(a), was developed. In this model the complete system was described only by the neutral groundstate and the two ion continua $1s\sigma_g$ and $2p\sigma_u$ responsible for producing high energy fragments. Nuclear degrees of freedom were neglected. Both continuum states can be accessed from the groundstate only via ionization by the high harmonic radiation (depicted as blue arrows). The effect of the IR field is described as a coupling in the ion

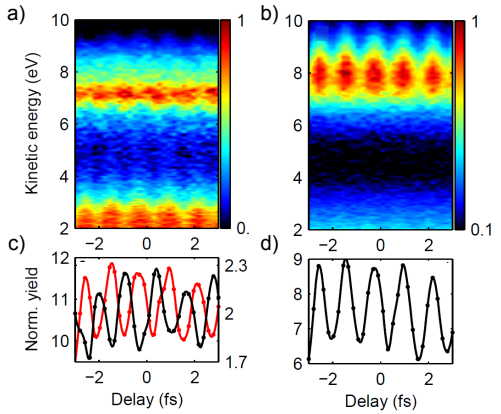

Figure 3.3: Kinetic energy spectra of fragments emitted parallel (a) and perpendicular (b) to the laser polarization as a function of the relative XUV-IR delay. Corresponding time dependent ion yields normalized to the APT only yields are plotted in (c) and (d). In (c) the ion yield at 3 eV (red) oscillated out of phase to the ion yield of the 7 eV channel (black). In (d) only fragments around 8 eV are considered. The channels for parallel and perpendicular emission for E_{kin} = 7-8 eV oscillate out of phase.

continuum states by emission or absorption of a single IR photon. For the rest of this section, couplings between the two continua will be referred to as diagonal couplings (diagonal red arrows in Figure 3.4(a)) while coupling within the same continuum will be referred to as vertical coupling (vertical red arrows). In the calculation the different coupling mechanisms can selectively be switched on or off.

In Figure 3.4(b) the total probability for ionization to the $2p\sigma_u$ continuum, corresponding to the formation ion fragments with E_{kin} = 7-8 eV, is plotted for different coupling configurations as described in the simple model. The blue dashed line considers only vertical coupling within the $2p\sigma_u$ continuum. In a corresponding photoelectron spectrum this would lead to oscillating sidebands (similar to those known from RABITT measurements [10]), which, however, do not lead to a significant change in the total ion yield from this continuum. The result of the calculation, in which only diagonal couplings between the $1s\sigma_g$ and the $2p\sigma_u$ continuum were taken into account, is depicted by the red line. This configuration leads to large oscillations in the total ionization probability (a corresponding calculated photoelectron energy spectrum as a function of delay is shown in Figure 3.4(c)). In this case high harmonic radiation populates mostly the $1s\sigma_g$ state from which the sidebands in the $2p\sigma_u$ continuum are accessed via absorption or emission of an IR photon. Thus there are two pathways to each sideband in the $2p\sigma_u$ continuum. Constructive and destructive interference between these two channels, depending on the relative phase of the XUV and IR fields, therefore leads to the oscillation of the total ionization yield with half the IR period.

The grey and black curves in Figure 3.4(b) show the result of the simple

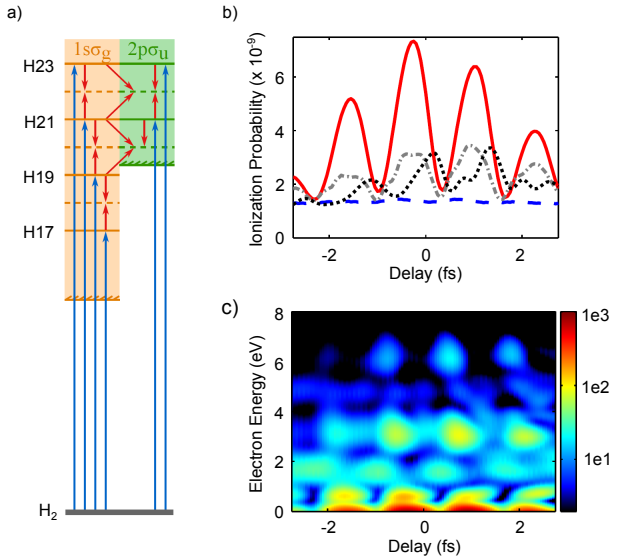

Figure 3.4: (a) Schematic illustration of the simple model used to calculate the results in (b) which show the ionization probability to the $2p\sigma_u$ continuum for the various curves coupling configurations of the IR. The diagram in (a) and different curves in (b) are discussed in detail in the text. (c) Photoelectron spectra calculated by the simple model as a function of the XUV-IR delay calculated corresponding to the red line in (b).

model when both vertical and diagonal couplings are switched on and the result of the full TDSE calculation, respectively. Apart from a phaseshift which is due to the limitations of the simple model, in which only one internal nuclear distance is considered, the grey curve resembles the results off the full calculation closely.

In summary, in this experiment it was possible to show that the ion yield from different dissociative ionization channels could be controlled by carefully adjusting the relative delay between the APT and the IR field. Considering the simplicity of the electronic states in molecular hydrogen and its ion, the observed behavior could be explained in terms of interference between different ionization pathways propagated by absorption or emission of IR photons in the molecular ion only.

3.1.4 Results for O_2

In Figure 3.5(a), the angle-integrated kinetic energy spectra of O^+ ion fragments in the case of XUV ionization only (red dashed line) and for XUV ionization in the presence of the IR field (black solid line) are plotted. In the XUV-only spectrum four main contributions can be attributed to different ionization pathways. A potential energy diagram of O_2^+ is shown in Figure 3.5(b). Most relevant for the discussion in this section are the channels at $E_{kin} = 1.9$ eV

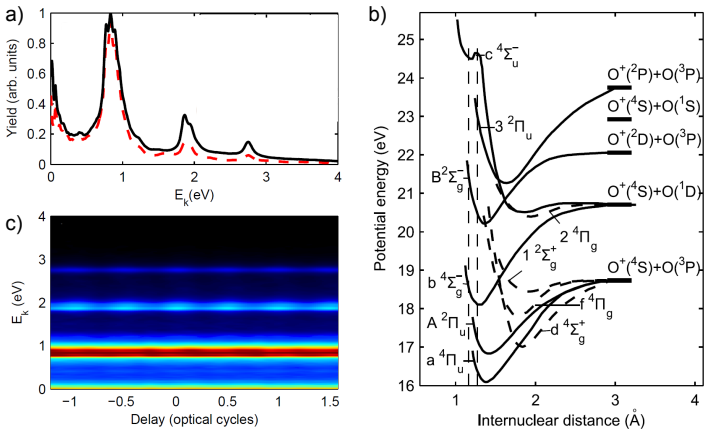

Figure 3.5: (a) Kinetic energy spectra for O^+ fragments in the case of APT only ionization (red dashed line) and in the presence of the IR field (cycle averaged)(black solid line). Potential energy curves of relevant states of the O_2^+ ion are shown in (b) where the energy scale is relative to the O_2 ground state. The Franck-Condon region is indicated with vertical dashed lines (data taken from [184]). In (c) the angle-integrated kinetic energy spectra are plotted as a function of XUV-IR delay.

and 2.9 eV, which stem from dissociation following ionization to the different vibrational levels (ν =0,1) of the c $^4\Sigma_u^-$ state [183, 184], as well as the channel at E_{kin} = 0.9 eV from DPI after formation of the B $^2\Sigma_g^-$ (ν =0-3) state.

Similar to the results in the D_2 measurements, the IR field causes significant changes in the ion kinetic energy spectrum. The corresponding curve in Figure 3.5(a) (solid black line) is the result of averaging spectra taken at different delays spanning one complete cycle of the IR field. An enhancement that covers the full energy range of the spectrum is visible. The enhancement of the E_{kin} = 1.9 eV and 2.9 eV channels is particularly pronounced. In Figure 3.5(c), the ion kinetic energy spectra are plotted as a function of time, which reveals an oscillation in the channels with half the period of the IR field. In Figures 3.6(a-c) the angle-integrated ion yields for the main channels are plotted as a function of XUV-IR delay. These oscillation take place on top of a delay-independent enhancement compared to yield measurements from XUV-only ionization (comparison not shown here).

The question arises if the measured attosecond delay can be interpreted with the same simple model used to explain the D_2 results, i.e., by purely electronic coupling in the ion continuum states. Given the more complicated and closely spaced electronic states in O_2 and its molecular ion, a (additional) coupling of electronic states in the neutral molecule, or even a coupling between electronic and nuclear degrees of freedom during the fragmentation process, could be plausible.

Indications for both descriptions can be found. In a quasistatic model the ionization or excitation of the neutral molecule by the APT happens in the presence of a static electric field given by the instantaneous field of the IR

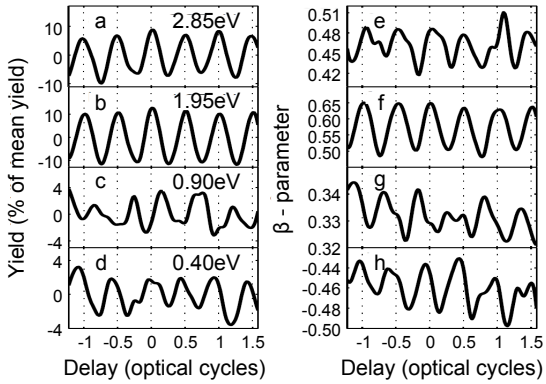

Figure 3.6: Ion yields obtained from Figure 3.5(c) by summing over an energy range of 0.2 eV around the maxima of the channels indicated in (a-d). The corresponding delay dependence of the β-parameters describing the angular distribution of the ion fragments is plotted in (e-h).

pulse. In this case, however, we would expect that at zero crossings of the IR field the kinetic energy spectra resemble spectra taken with XUV-only ionization. This is in contradiction to the measurement of a delay-independent yield enhancement as well as yield oscillations that do not show a clear phase relation (see Figures 3.6(a-d)), i.e., suggesting the existence of IR-induced sequential excitation processes leading to a time-delayed dissociation. An analytical model, including both coupled electronic and nuclear motion, would be required to interpret the experimental results in its completeness. Such a theoretical description is, however, not available at the moment.

At the same time the good synchronization of yield oscillations in the E_{kin} = 1.9 eV and 2.9 eV channels (see Figures 3.6(a+b)), both attributed to the formation of the c $^4\Sigma_u^-$ state, can be taken as signs for a purely electronic effect mediated by the IR field, without the involvement of any nuclear dynamics. Further, the absence of yield oscillations in the O_2^+ ion fragments, which would indicate the occurrence of IR-induced admixtures in the neutral molecule [185], and the presence of yield oscillations in specific fragmentation channels, as expected from couplings in the ion states, indicate that couplings predominantly occur in the ionic states.

In such a quasistatic picture, where XUV ionization happens from a neutral state to a system, in which combined molecular ion + continuum electron states are coupled to each other by an IR field, the angular distribution of the ion fragments allows conclusions about the character of the transitions facilitating the couplings in between the different ion states (e.g., diagonal couplings in Figure 3.4(a)). The angular distribution of the ion fragments is related to the β-parameter as described in the Legendre-polynomial $P(E, \cos(\theta), t) \sim 1 + \beta(E, t)P_2(\cos(\theta))$, e.g., an increase of the β-parameter describes a sharpening of the angular distribution along the laser polarization and vice versa.

In our constellation, the rising of a channel specific β-parameter coinciding with a rise in the respective ion yield signifies a parallel transition, i.e., ionic

couplings are favored for molecules aligned parallel to the laser polarization if the associated ionic transition is also parallel and vice versa. A decrease in β-parameter in combination with an increase in ion yield therefore indicates a perpendicular ionic transition.

In Figure 3.6(e-h) channel specific β-parameters are plotted as a function of time. Taking into account spin selection rules while assuming that couplings in which molecular ion and continuum electron both change in electronic state can be neglected, the phase between the respective β-parameter oscillations and the corresponding yield oscillations for each channel allow conclusions about which states are involved in the coupling. The in-phase oscillations for the E_{kin} = 1.9 eV and 2.9 eV (Figures 3.6(a+e), (b+f)) channels, attributed to the c $^4\Sigma_u^-$ states, imply a coupling to the b $^4\Sigma_u^-$ state. The out-of-phase modulation of the E_{kin} = 0.9 eV channel, attributed to the B $^2\Sigma_g^-$ state, on the other hand would indicate a perpendicular transition and therefore a possible coupling to the bound X $^2\Pi_g$ or A $^2\Pi_u$ state.

3.1.5 Conclusion

In the two presented experiments it was shown that DPI of small molecules induced by a two-color XUV-IR field can efficiently be controlled by tuning the delay between the XUV and the IR fields. For H_2 and D_2 measurements a simple description was used, wherein the IR field couples two XUV ionization continua via different pathways involving the absorption or emission of one IR photon. Interference between these two pathways depending on the relative delay between XUV and IR field leads to large ion yield oscillations and periodic changes in the angular distribution of the ion fragments. The application of the same model was investigated for O_2 molecules, which, however, due to the more complex potential structure, shows that nuclear degrees of freedom as well as non sequential electronic processes might play a role. Nonetheless the experiments show that the result of a photochemical reaction, in this case yield and angular distribution of ion fragments following dissociative two-color photo-ionization, can actively be controlled, even for multi-electron systems.

3.2 XUV ionization of aligned molecules

3.2.1 Introduction

Probing the temporal evolution of molecular structure in chemical processes, such as dissociation or isomerization, is usually done by observing the photo-absorption spectrum of the investigated system as a function of time [9]. However, this approach relies on a pre-existing understanding of the spectroscopy of the molecule involved. A more direct measurement instead can be performed by diffracting electrons or light waves directly from the molecular structure and observing the diffraction pattern. Using short electron bunches, structural changes in chemical reactions [186], in crystals [187], and phase transitions [188] have been resolved. In order to achieve the necessary sub-nanometer spatial resolution, the de Broglie-wavelength ($\lambda_{\mathrm{deBroglie}} = \pi \cdot (2/\mathrm{E_{kin}})^{1/2}$) of the electrons has to be small relative to the interatomic distances of the investigated structure [189, 190]. To achieve such a resolution, electron kinetic energies of above 50 eV can already be sufficient. A comparable resolution with light waves can only be achieved, if the photon energy lies in the x-ray regime. Suitable light sources in the desirable wavelength region are nowadays available from free electron laser (FEL) facilities such as FLASH or LCLS. One of the advantages of these light sources are the ultrashort pulse durations well below 100 fs, which have the potential to make time-resolved x-ray diffraction experiments possible [191, 192]. This is in contrast to conventional electron bunches which are very difficult to produce with pulse durations below 100 fs. An alternative method that can combine the advantages of both previously mentioned techniques is to use photo-electrons generated within the molecule by single photon ionization from an XUV- or X-ray pulse. On their way to the detector, the outgoing electrons then diffract on the atomic centers of the parent molecule [193]. The time duration of the electron bunch is dictated solely by the duration of the ionizing light pulse, which can be generated via HHG reaching pulse durations as short as 80 as [56]. Nonetheless, also FEL pulses with very high photon fluxes [194, 195] could be used.

Additionally to the information on molecular structure encoded in the photo-electron angular distribution (PAD) [193], the outgoing electron also contains information on the molecular orbital from which it originated. The extraction of this structural and orbital information is, however, only possible if the PAD is measured in a coordinate system that is defined by the molecular axis. This can either be achieved by coincidence measurements or using molecular alignment and orientation techniques [196]. In the current experiment we impulsively aligned CO_2 molecules such that at the moment of ionization by an XUV pulse the molecules are aligned relative to the laboratory frame [196–199]. This technique makes possible the measurement of molecular frame photo-electron angular distributions (MFPADs). Information on the orbitals accessed by the harmonics could be extracted and an onset of the influence of the molecular structure on the MFPADs could be observed.

3.2.2 Experiment

In this experiment the same setup as presented in Figure 3.1 and described in section 3.1.2 was used. XUV pulses were generated by HHG in argon. The spectrum consisted of the odd harmonic orders from 11 (17.5 eV) to 31 (49.3 eV). In the second interferometer arm a 2 cm thick piece of SF11 glass was inserted into the beam path, stretching the respective IR pulses to a duration of 300 fs. The stretched IR pulses were used to induce a time-dependent alignment of the CO_2 molecules. The intensity of the alignment pulses was kept at values around 10 TW/cm^2 to limit ionization while achieving a reasonable degree of alignment. In the VMIS the two beams were collinearly focused into an effusive beam of CO_2 molecules and photo-electron angular distributions were recorded for different alignment degrees controlled by the XUV-IR delay.

Impulsive alignment of CO_2 When moderately intense laser pulses interact with an ensemble of molecules, whose rotational period (42.7 ps for CO_2) is much longer than the laser pulse duration, a rotational wavepacket is created, which de-phases and re-phases with a periodicity that is related to the rotational period of the molecule. At a fixed time after the laser interaction, this leads to a revival of alignment in which the angular distribution of the molecules rapidly switches between a case of alignment parallel to the laser polarization to a case of anti-alignment. In the latter case the molecular axes are lying in a plane perpendicular to the laser polarization. The degree of alignment is described by the expectation value $\langle\cos^2(\theta_{\mathrm{CO_2}})\rangle$, where θ_{CO_2} describes the angle between the molecular axis and the polarization direction of the laser field. For an isotropic distribution of molecules, $\langle\cos^2(\theta_{\mathrm{CO_2}})\rangle$ yields a value of 1/3. Perfect (anti-)alignment is given when $\langle\cos^2(\theta_{\mathrm{CO_2}})\rangle = 1$ (0). $\langle\cos^2(\theta_{\mathrm{O^+}})\rangle$ describes the measurable expectation value of the fragment angular distribution of O^+ ions, which in the axial recoil approximation is related to expectation value $\langle\cos^2(\theta_{\mathrm{CO_2}})\rangle$. Higher values of $\langle\cos^2(\theta_{\mathrm{O^+}})\rangle$ compared to the isotropic distribution signify a degree of higher alignment whereas lower values indicate a higher degree of anti-alignment.

3.2.3 Results

In Figure 3.7(a) a slice through the 3D electron momentum distribution for XUV ionization from randomly aligned molecules is shown. Photo-electron spectra (PES) extracted from this measurement for electron emission along ($\theta_{e^-} = 0^\circ \pm 20^\circ$) and perpendicular ($\theta_{e^-} = 90^\circ \pm 20^\circ$) to the laser polarization are plotted in Figure 3.7(b). Each harmonic can produce several ionic states that each have a different ionization potential. The series of peaks, which can be seen in the PES, can be attributed to four different ionization channels. As indicated by the harmonic ladders above, they originate from the highest occupied molecular orbital (HOMO) ($X^2\Pi_g$; IP=13.8 eV), HOMO-1 ($A^2\Pi_u$; IP=17.6 eV), HOMO-2 ($B^2\Sigma_u^+$; IP=18.1 eV), and HOMO-3 ($C^2\Sigma_g^+$; IP=19.4 eV). The angular distributions of the HOMO-1 and HOMO-3 are peaked parallel to the laser polarization while emission of electrons from the HOMO and

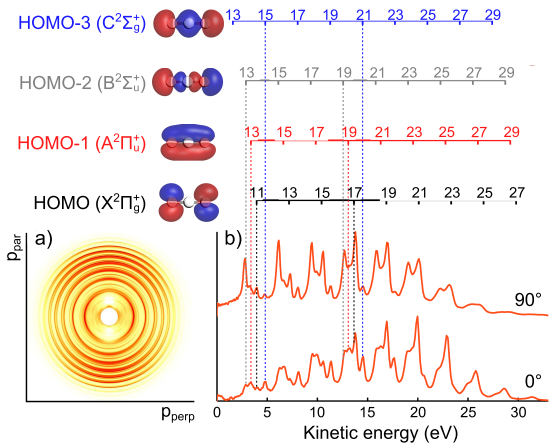

Figure 3.7: (a) Slice through the 3D photo-electron momentum distribution for ionization by an XUV pulse from randomly aligned CO_2 molecules. (b) Photoelectron spectra for electrons emitted parallel ($\theta_{e^-} = 0^\circ$) and perpendicular ($\theta_{e^-} = 90^\circ$) to the laser polarization, obtained by integrating over an acceptance angle of $\pm 20^\circ$with respect to the laser polarization axis. The series of peaks is due to four ionization channels corresponding to the HOMO, HOMO-1, HOMO-2, and HOMO-3 orbitals of CO_2, which can each be accessed by multiple harmonic orders, as indicated by the harmonic ladders in the top part of the figure. The corresponding orbitals are plotted to the left of the ladders along with the electronic state they correspond to.

HOMO-2 occurs predominantly perpendicular to the laser polarization.

This behavior becomes even more prominent when photo-ionizing from an ensemble of aligned molecules. In Figure 3.8(a) the expectation value $\langle \cos^2(\theta_{O^+}) \rangle$ of O^+ ions, signifying the degree of alignment for the CO_2 molecules, is plotted around the alignment revival at 21 ps as a function of delay between alignment pulse and XUV-pulse. Around the revival time, identified by an increase and following decrease of $\langle \cos^2(\theta_{O^+}) \rangle$, significant changes in both yield (plotted in Figure 3.8(b)) and β-parameter (plotted in Figure 3.8(c)) are revealed. The enhancement or suppression of the photo-ionization yield depending on the alignment is evidence for the symmetry of the transition from the molecular groundstate to the final combined molecular ion + continuum electron state. Consequently, ionization from HOMO and HOMO-1 involve perpendicular transitions while ionization from HOMO-2 and HOMO-3 should involve parallel transitions.

To accentuate changes in the PADs for the different alignment configurations the difference between PADs at maximum alignment and anti-alignment was taken. The resulting differential PAD is plotted in Figure 3.9(a), which shows a comparison of an experimentally measured differential PAD (right) as a function of electron kinetic energy and electron emission angle (θ_{e^-}) and a PAD calculated from theory (left). For the theoretical results, an electron-molecule quantum scattering method was used, which previously has been successfully applied to calculating MFPADs from synchrotron radiation [200–202]. The

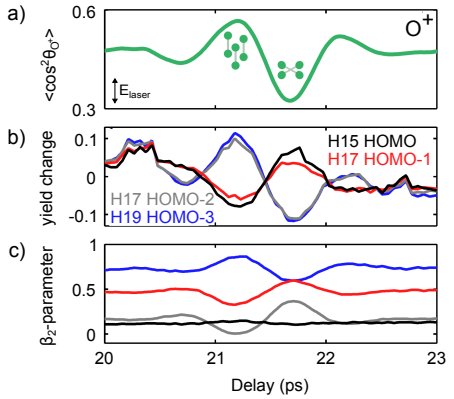

Figure 3.8: (a) The expectation value $\langle\cos^2(\theta_{O+})\rangle$ of O^+ fragments characterizing the alignment of the CO_2 molecules as a function of the delay between XUV and IR pulses around the second alignment revival. High (low) values of $\langle\cos^2(\theta_{O+})\rangle$ identify alignment of the CO_2 molecules parallel (perpendicular) to the laser polarization axis. The temporal evolution of the fragment photo-electron yield (b) and β-parameter of the photo-electron angular distribution (c) for the four different channels reveal significant channel specific changes around the revival time.

conditions for the calculation were chosen to fit the experimental conditions in terms of involved ionic states, relative intensities of the HHG spectrum and angular distribution of the aligned molecules. Depending on the character of the underlying transition (parallel or perpendicular), the contributions in the PAD are either positive (red/yellow) or negative (blue).

In Figures 3.9(b-e) experimental (dotted lines) and calculated (solid lines) differential PADs for selected harmonic orders are plotted for the four channels individually. The sign of the contributions in the HOMO, HOMO-1 and HOMO-3 reinforce the earlier statement concerning the symmetry of the transition involved, e.g., enhanced photo-electron yield for anti-aligned molecules indicates perpendicular transitions for the HOMO and HOMO-1, whereas yield enhancement of photo-electrons for aligned molecules signifies a parallel transition for the HOMO-3. However, the state specific PADs are able to reveal additional features, difficult to extract otherwise. This is especially obvious for the HOMO-2 (Figure 3.9(d)), where a dramatic change at photo-electron kinetic energies of 15 eV is exposed. At low energies only positive values are observed, whereas at higher photo-electron energies also negative values emerge. This speaks for a symmetry change of the final state from Σ_u to Π_u implying a accompanying change in the symmetry of the outgoing electron.

Additional changes in the PADs that evolve with photo-electron kinetic energy can be observed also for the rest of the channels. For example, the differential PAD from ionization by harmonic 13 from the HOMO leading to photo-electrons with $E_{kin} = 7.2$ eV (Figure 3.9(b)) shows dips at $\theta_{e^-} = 45^\circ$, which move to $\theta_{e^-} = 0^\circ$ and $\theta_{e^-} = 180^\circ$ for higher electron kinetic energies caused by higher harmonic orders. Similar changes can be observed for PADs from all involved orbitals. Influences from shape resonances [193, 200, 203]

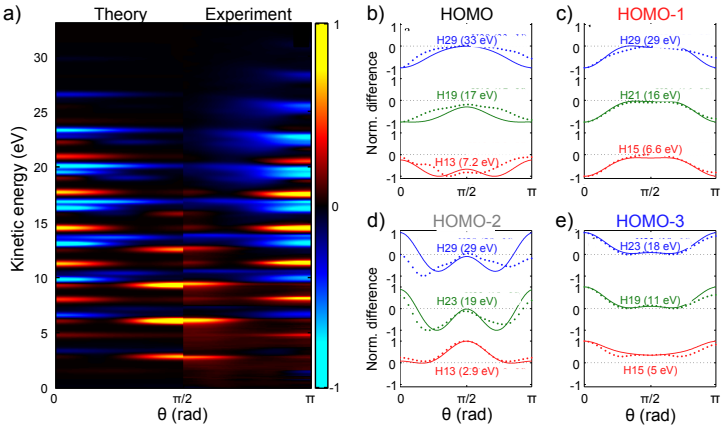

Figure 3.9: (a) Comparison between experimental and calculated differential PADs as a function of the photo-electron kinetic energy and emission angle θ_{e^-} relative to the laser polarization. In (b-e) the comparison is further elaborated. Experimental (solid lines) and calculated (dotted lines) differential PADs are plotted separately for the four channels and selected sets of harmonics. The evolution of the angular distributions with kinetic energy is caused by interaction of the outgoing electrons with the molecular structure.

could be ruled out by suppressing inter-channel couplings in the calculations, which in return did not show any significant differences. For this reason the changes in the angular distribution of the photo-electrons can rather be interpreted as a fingerprint of the molecular structure at the moment of ionization. As mentioned before, the electrons emerging from within the molecule experience the atoms in the molecular environment as scattering centers. The interaction of the electrons with the Coulomb-field of these atoms would have a strongly kinetic energy dependent effect on their trajectories, which in return could lead to the energy dependence which was resolved in the presented experimental data and reproduced by the theoretical calculations.

3.2.4 Conclusion

The successful reproduction of the experimental results by theoretical calculations allowed the extraction of information on the molecular orbitals. Further the experimental data showed a dependence on photo-electron kinetic energy, which could be interpreted as the onset of structural information in MFPADs. These results show that an extension of this type of experiments towards time resolved measurements of structural and electronic dynamics in photo-chemical reactions is feasible. In this sense, the introduction of a third pulse initiating a photo-chemical reaction in the aligned molecules, which is subsequently probed by an XUV attosecond pulse, could be a logical next step. While these types of experiments are likely to be heavily pursued at XUV and X-ray FEL facilities, they also hold great promise for further application from HHG based laser sources. New phase-matching techniques [29] will enable the extension of

these experiments to higher photon energies while the inherent synchronization of the involved laser pulses when deduced from a single source will allow investigation of dynamics with attosecond resolution.

3.3 Attosecond control of electron-ion recollision in high harmonic generation

3.3.1 Introduction

High harmonic generation (HHG) is prominently known for the production of attosecond pulse trains (APTs) and individual attosecond pulses [10, 58]. In the language of the semi-classical three-step model of harmonic generation an electron is released into the continuum via tunnel ionization, gains kinetic energy via acceleration in the laser field, and upon rescattering with the parent ion can recombine and give rise to emission of high-frequency radiation [19, 20]. The recolliding electron wave packet (EWP) can be viewed as a probe of the generating system, offering the possibility for four-dimensional imaging with Angstrom spatial and attosecond temporal resolution [94, 101, 119, 204, 205]. Up to now the only temporal control over the HHG process has come via shaping of the strong IR laser field which drives all three steps in the process [206], with the constraint that the peak intensity must be high enough to drive the initial ionization step.

By generating harmonics with an APT in combination with an IR pulse, the IR-driven tunnel ionization step in the three-step model can be replaced by APT-driven one-photon ionization. The technique of using an APT to control the initial EWP in harmonic generation was first proposed in theoretical works in 2004 [207]. The short duration and high photon energy of the individual pulses in the APT allows the ionization to be fixed to a certain time during the IR cycle which can be controlled via the relative delay between the two pulses. The APT ionization allows direct control over the initial EWP, and the IR field will subsequently control the acceleration and potential recollision of the EWP. A similar APT-IR control scheme was used experimentally in [81, 86] to create and control below-threshold EWPs in helium to study time-dependent coherent electron rescattering on the parent ion. Biegert *et al.* demonstrated strong enhancement of harmonics generated in helium in a two-color IR-APT experiment in which the relative delay between the IR and the APT was not controlled [208].

In this section we demonstrate for the first time that it is possible to temporally control HHG by forming the initial EWP with an APT. To do this we first synthesize an APT via harmonic generation in xenon using a strong IR laser pulse. The APT is inherently synchronized to this IR field [38]. We then use the APT and a copy of the IR pulse, which is independently delayed relative to the APT, to generate harmonics in helium in a separate gas jet. We show that the helium harmonics are enhanced periodically as a function of the APT-IR delay, with a maximum in the efficiency occurring once every half-optical cycle of the IR field. The enhancement occurs when the XUV ionization launches the EWP on a trajectory which can return to the core [207]. Moreover, under our experimental conditions the kinetic energy of the APT-initiated returning EWPs is in a range that is not accessible in EWPs launched by IR tunnel ionization. We show that the experimental results are in good agreement with

calculations including both the single atom and macroscopic response. Our results demonstrate that it is possible to decouple the ionization step from the acceleration and re-scattering steps in the three-step harmonic generation process, offering a new degree of control over initial and rescattering electron wave packets.

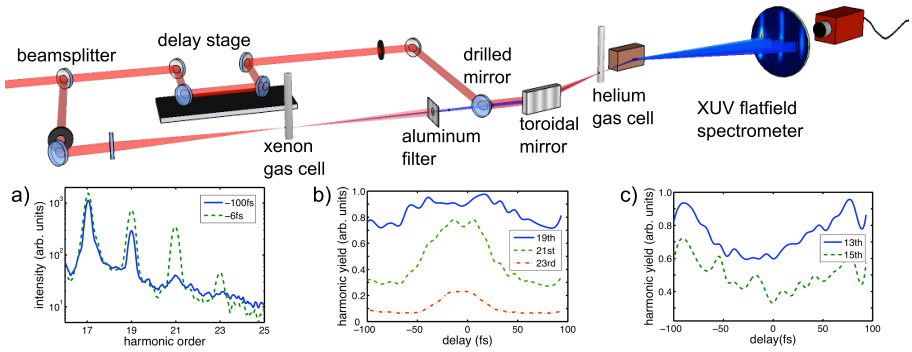

Figure 3.10: ***top)*** *Schematic drawing of the experimental setup* ***bottom)*** *Raw data of measurements scanning over a large delay range. (a) Two individual spectra taken far away and close to temporal APT-IR overlap. The background at large delays and high energies is due to scattered XUV light from blocked out lower harmonic orders. At temporal overlap these orders will be depleted by enhanced absorption as seen in Figure 3.10 (c), thus reducing the background for measurements at temporal overlap. (b) Coarse delay scan of the yield of harmonics 19, 21 and 23 showing strong enhancement. (c) Harmonics 13 and 15 as a function of the APT-IR delay, revealing absorption when the two pulses overlap.*

3.3.2 Experimental setup

The experiments were conducted with a 780 nm IR laser system that delivered 30 fs laser pulses with a pulse energy of 2 mJ at a repetition rate of 3 kHz. 50% of the beam was used to generate the initial APT in a 3mm long gas cell filled with xenon. The low order harmonics and the remaining IR after the first gas cell were filtered out with a 200 nm Al filter. The resulting APT comprised of harmonics 11 to 21 was propagated to a second 3 mm long gas cell filled with helium (15-25 mbar), where it was collinearly recombined with the remaining IR beam from the other interferometer arm. The focusing conditions of the two beams were adjusted such that the beams focused slightly before the second gas cell to favor phase matching of the short electron trajectories [31]. The relative APT-IR delay could be adjusted over several hundred femtoseconds with a resolution of less than 100 as (see Figures 3.10 and 3.11) by actively stabilizing the interferometer arms. In the absence of temporal overlap between the IR and APT pulses, the helium gas is observed to absorb only harmonics 17-21 of the APT which are above the He ionization threshold. When the XUV and IR pulses are overlapped we also observe strong absorption of harmonics 13 and 15, indicating that the APT-driven ionization of the laser dressed atom

is due to the simultaneous absorption of several harmonics and therefore of short duration (see Figure 3.10(c)).

3.3.3 Experimental Results

The spectra in Figure 3.10(a) show the harmonic yield for harmonics 17-23 for two different APT-IR delays. Negative delays indicate that the IR pulse precedes the APT. For large time delays, when there is no temporal overlap, only harmonic orders of the original APT are detected behind the second gas cell. The IR pulses by themselves are too weak to produce harmonics. At temporal overlap of the APT and the IR pulse, however, new harmonics 23-27 can be observed (see Figures 3.10(a) and 3.12(a)). In addition, the yield of existing harmonics 17-21 is significantly enhanced.

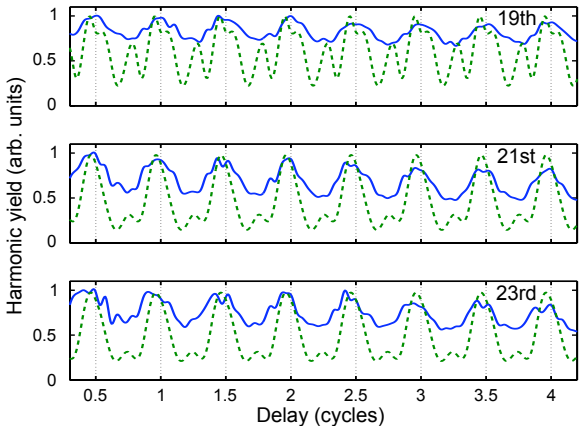

Figure 3.11: High resolution delay scan of the yield of harmonics 19, 21, and 23, with the delay given in units of the IR cycle. The experimental (blue solid line) and the theoretical results (green dashed line) agree well.

Figure 3.11 shows a sub-cycle delay scan of the yield of harmonics 19-23, performed around zero temporal APT-IR overlap. All three harmonics clearly exhibit periodic enhancement once per half-cycle of the IR field. At these delays, the APT not only increases the probability for one-photon ionization as compared to IR tunnel ionization, but moreover launches the EWP onto a returning trajectory, thereby enhancing the yield of these harmonic orders. In the semi-classical model the release times that lead to returning electrons are controlled by the IR field and are directly related to the electron's energy upon return [68, 207]. By fitting sine functions to the experimental data and extracting the respective phase, we observe a clear delay between the optimal release times of harmonics 19 and 21 (120 as delayed from H19) and 23 (270 as delayed from H19). Also shown in the figure is a calculated delay scan which will be discussed in further detail below.

Figure 3.12 shows a spectrum and a delay scan measured in an experimental configuration where the IR focus was moved 6 mm toward the gas jet, which in

general leads to improved phase matching of the long trajectory contribution to the harmonic spectrum [31]. The spectrum in Figure 3.12(a) has a higher cutoff energy than the measurements of Figure 3.10 because of the increase in IR intensity in the gas jet. In addition, a new spectral feature has appeared in harmonics 23-27 on the low energy side of each harmonic. In Figure 3.12(b) we separate the time dependence of the two features by showing a delay scan of each of the two spectral features for harmonic 25 (highlighted in different colors in Figure 3.12(a)), obtained by spectral integration over each region separately for each delay-dependent spectrum. We attribute the blue contribution as coming from short trajectory returns, and the red contribution, which is observed predominantly off-axis and is only visible in this phase matching configuration, as coming from long trajectory returns. Figure 3.12(b) shows that the long trajectory contribution is shifted by 350 as with respect to the short trajectory contribution, consistent with the expectation from the semi-classical model in which long trajectories are released earlier than short trajectories [207, 209]. This behavior is also reproduced in calculations described in more details below (theoretical results not plotted in Figure 3.12(b)).

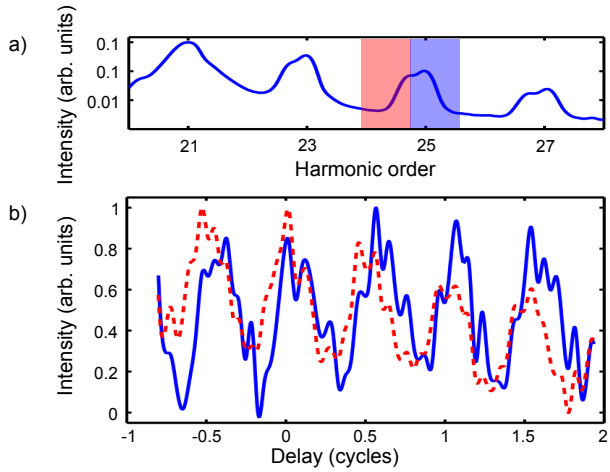

Figure 3.12: (a) Typical harmonic spectrum at a harmonic yield maximum for phase matching with long trajectory contributions. Sidebands (red area) below the short trajectory (blue area) signal appear and are enhanced for certain delays. (b) The delay dependence for short (blue solid line) and long (red dashed line) trajectories are shown using the example of harmonic 25. The two contributions are out of phase by 350as. The two signals have been normalized to their respective maximum and minimum values to emphasize their relative temporal shift.

3.3.4 Theoretical modeling

To gain a more complete understanding of our experimental results, we have performed a series of calculations including the combined microscopic and macroscopic response of the helium gas to the combined IR-APT fields. We

solve the coupled Maxwell wave equation and time-dependent Schrödinger equation (TDSE) for all frequencies ω of the combined electric field $E_{tot}(\omega)$, composed of the IR-probe, the seeding APT and the generated harmonics:

$$\nabla_{\perp}^2 E_{tot}(\omega) + \frac{2i\omega}{c}\frac{\partial E_{tot}(\omega)}{\partial z} = -\omega^2\mu_0(P(\omega) + P_{ion}(\omega)).$$

E_{tot} and the P terms are also functions of the cylindrical coordinates r and z. We solve this equation by space-marching through the helium gas, at each plane z in the propagation direction calculating the response $P(\omega)$ as the Fourier transform of the time-dependent dipole moment (times the atomic density) driven by the evolving electric field $E_{tot}(t)$. The dipole moment is calculated via numerical integration of the TDSE within the single active electron (SAE) approximation. The source term is then used to propagate to the next plane in z, thereby coupling the harmonics generated in one step back into the full electric field so that they will contribute to the driving electric field in the next step. In this way we obtain a very complete description of both the single-atom harmonic generation, and the macroscopic phase matching, absorption, and dispersion imprinted on the harmonics in the gas medium. The term $P_{ion}(\omega)$ is due to the free-electron plasma current and is also calculated within the TDSE-SAE, see [30]. This term is very small in our experimental configuration.

The green curves in Figure 3.11 show the calculated delay dependence of harmonics 19-23 in conditions similar to the experiment. The peak intensity of the IR (APT) pulse is 5×10^{13} W/cm^2 (5×10^9 W/cm^2), with a duration of 26 fs (13 fs). The beam focal diameters are 100 µm (40 µm). The APT is synthesized from harmonics 11 through 19, with relative strengths obtained from the experiment and with relative phases consistent with the semi-classical model [68]. The individual bursts in the APT are thus strongly chirped with a duration of approximately 430 as. The 3 mm long He jet is placed 4 mm downstream from both laser foci. In Figure 3.11, delays of 0.0, 0.5, etc mean that the attosecond bursts overlap the peaks of the IR electric field in the common focus of the two beams. Because of the different Gouy phase shifts of the two beams, the overlap in the generation medium of the APT and the peak IR field is shifted to -0.06, +0.44, +0.94, etc. In Figure 3.11, the experimental results have been shifted in time for best overlap with the calculations. The theoretical and experimental results match well, exhibiting one enhancement peak per IR half-cycle, although the contrast is significantly higher in the theory results. The smaller secondary enhancement of H19 in the calculation is due to interference between the initial H19 radiation, included in the APT, and the newly generated H19. In the calculation the secondary peak goes away when we decrease the relative amount of H19 in the APT.

One of the most striking features of our experimental and theoretical results is that the harmonics are enhanced just once during each half cycle of delay between the IR and APT fields. This differs from an earlier theoretical

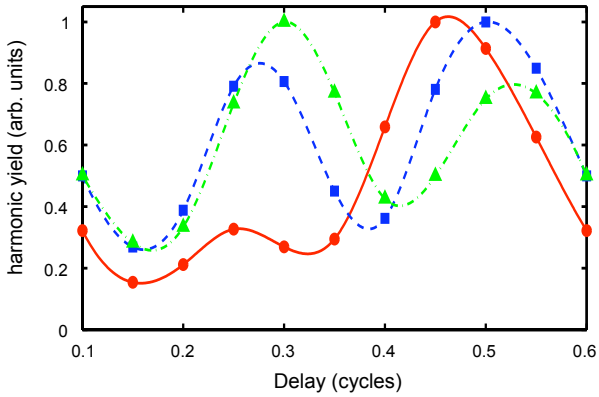

Figure 3.13: Calculated delay dependence of H21 yield for IR intensities of $5{\cdot}10^{13}\,W/cm^2$ (red solid line), $6.5{\cdot}10^{13}\,W/cm^2$ (blue dashed line), and $7.5{\cdot}10^{13}\,W/cm^2$ (green dash-dotted line). As the intensity increases the yield is enhanced twice per half-cycle, as opposed to once per half-cycle at low intensities.

prediction of a twice-per-half-cycle enhancement of the harmonic signal in [207] , corresponding to the release of the EWP initially moving uphill or downhill with respect to the IR laser force at the time of release. Our calculations show that the once-per-cycle enhancement is a consequence of the relatively low IR intensity used in our experimental conditions. Figure 3.13 shows that as the IR intensity is increased slightly, to 6.5 and then 7.5×10^{13} W/cm^2, the calculated delay dependence of harmonic 21 starts to exhibit two peaks per IR half-cycle as predicted by the simple model in [209]. We have performed extensive calculations on the effect of experimental uncertainties on the signal-to-noise ratio in Figure 3.11. We have in particular investigated whether imperfect spatial APT-IR overlap, or very long and/or chirped individual APT bursts, could lead to the appearance of just one enhancement peak per half-cycle. While these effects certainly do decrease the signal-to-noise ratio, it is only at the lowest IR intensities that we observe the suppression of one of these enhancements. We attribute the observation of a once-per half cycle modulation to the enhanced role played by the atomic potential at low IR intensity. At low intensity the barrier formed by the combined laser and atomic potential is only weakly suppressed which means that the electrons are released into the continuum with relatively low velocity [207]. In a separate study of classical trajectory dynamics in the combined laser and atomic potentials, we have found that uphill trajectories in particular are sensitive to the atomic potential and can rescatter many times on the core [210], suggesting that they may become trapped and not contribute to harmonic generation. Such trapping of uphill trajectories has been previously observed when photoelectrons are launched near the ionization threshold in the presence of a DC electric field [211]. We note that without the APT it would not be possible to study harmonic generation in helium at these low intensities, since the ionization rate in helium due to the IR laser alone is prohibitively small.

3.3.5 Conclusion

The use of APT-created electron wave packets affords new avenues for the study and application of harmonic generation in atomic and molecular systems. For example, the study of multichannel dynamics in molecular systems could be advanced by using the large bandwidth of the APT to create an EWP which is a coherent superposition of contributions from multiple orbitals. In addition, decoupling of the ionization and acceleration/recombination steps allows for the use of flexible polarization geometries, which, in combination with molecular alignment techniques, could significantly extend tomographic imaging of the (time-evolving) electronic orbitals [100].

Part II

Technical innovations for attosecond experiments

4 Velocity map imaging using an in-vacuum pixel detector

4.1 Introduction

Scientific interest in the interaction of atoms and molecules with other atoms, ions or electromagnetic radiation has led to the development of a wide range of imaging detectors. By detecting the spatial and temporal coordinates of charged particles, and thus their velocities, detailed conclusions about the processes leading to the formation of the charged particles can be drawn. The most prevalent methods include Velocity Map Imaging (VMI) spectrometers and Cold Target Recoil Ion Momentum (COLTRIM) spectrometers, today in a broader understanding also referred to as Reaction Microscopes. Both techniques are based on similar working principles. Physical or chemical processes in a target are triggered either by particle impact or by the interaction with a light field, which results in charged fragments. The processes involved can include any form of direct or indirect ionization, dissociation or - even - a chemical reaction. The charged fragments (ions and / or electrons) are accelerated in a DC electric field onto a two-dimensional detector where they are registered as events. Their positions and / or arrival times are recorded, giving insight into the angular and kinetic energy distribution.

VMI (see Figure 4.1) is a high resolution ion or electron imaging technique. Here electrostatic optics, usually consisting of a flat repeller plate, a flat apertured extractor plate and a flight tube with another flat and apertured ground plate are used. The geometry of these parts and the applied voltages determine the fragments' path of flight towards the detector. Their lateral displacement on the detector upon arrival is defined by the initial velocity vectors perpendicular to the detector axis [212–214]. A unique feature of VMI lies in decoupling the position of creation of the fragments from their impact position on the detector by using an electrostatic lens. In this way, spatial blurring of the image is minimized and a velocity resolution of less than 1 % can be achieved [215]. At the same time, VMI maintains a linear mapping of the fragments' velocities across the detector. Under typical VMI conditions, the spectrometer is operated at a point which is close to the Wiley-McLaren time-of-flight focusing condition, decreasing the effects of the position of creation on the arrival time and thus creating a two-dimensional projection of the original three dimensional velocity distribution on the detector surface. By choosing the axis

of symmetry in the interaction region parallel to the plane of the detector, the original three-dimensional distribution can be retrieved with appropriate numerical algorithms. In VMI measurements, several thousand events per laser shot can usually be recorded, before detrimental effects such as changes to the detected velocities as a result of space charge set in. An image is composed of many individual hits and forms the final measurement.

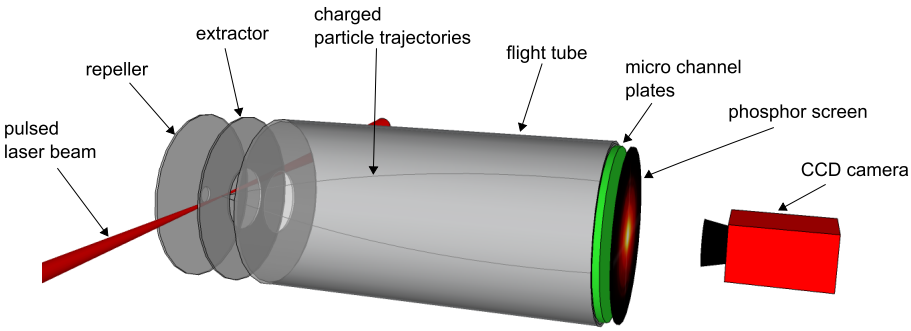

Figure 4.1: Schematic of a VMI setup showing the repeller and extractor electrodes for applying the acceleration voltages which project the charged particles onto the MCP detector.

VMI experiments typically only yield velocity components of a single - either negatively or positively charged - fragment at a time. Thus, they offer only an incomplete view of the reactants' full momentum distribution. In order to retrieve the full information from an experiment, the momentum vectors of all participating fragments - negatively as well as positively charged - have to be measured in coincidence. Such kinematically complete experiments can be accomplished by using Reaction Microscopes [216, 217]. Positively charged fragments are mapped by a weak homogeneous electric field onto a position- and time-sensitive detector. The time and place of incidence then allows reconstructing the initial momentum of these fragments. Electrons are accelerated by the same electric field in the opposite direction. The electron velocities are much higher than those of the ions due to their smaller mass. To account for this difference, an additional weak magnetic field is often applied which guides them on a spiral-shaped track onto a second detector. The retrieval of the initial momentum components of all fragments over a solid angle of almost 4π is possible. The signal rates in Reaction Microscope measurements have to be small enough to allow unambiguous coincidence recognition. Hence, the use of a detector with high quantum efficiency is crucial.

In both cases, VMI and Reaction Microscopes, the conventional charged particle detectors consist of multiple micro-channel plates (MCP) for signal amplification. They are followed by either phosphor screens in combination with charge coupled device (CCD) cameras, delay line anodes or wedge-and-strip anodes [218]. Due to the active open surface of MCPs, the quantum efficiencies of such setups are limited to around 60 %.

In the case of phosphor/CCD setups, the electron cloud leaving the MCPs

hits the phosphor screen and locally creates photons, which then are optically registered by the CCD camera, where they are transformed into an electronic signal. It follows that this is a rather indirect detection process. These photons again create electron-hole pairs which finally lead to the detected signal. CCD cameras produce good spatial resolution, especially when using centroiding algorithms [219], and are available for reasonable prices. A drawback is that there is no sub-microsecond timing information available, which can only be obtained by using expensive and complicated pulsed gates.

When using wedge-and-strip or delay line anodes, the position can be reconstructed by measuring the relative charge distribution in the former and relative timing signals in the latter case. Commercially available detector setups allow spatial resolutions down to 50 µm [220], while timing information extracted directly from the MCPs can reach < 300 ps [221]. The dead time of delay line anodes of ~ 20 ns is short compared to that of charge integrating anodes, which cannot spatially resolve events with a time difference below several hundred nanoseconds [222]. Both reconstructions nevertheless require involved electronic processing as well as a slow event-by-event transfer to the computer, which limits the event acquisition rate to maximally 200 kHz [221]. The above mentioned numbers apply to the most commonly used setups in experimental laboratories. Better results have been obtained at the cost of extremely dedicated and complex setups. For further Reference see [223, 224].

A problem that we encountered in our own research are restrictions imposed by the maximum tolerable operating pressure of an MCP. MCPs cannot be operated at pressures higher than 10^{-5} mbar. In many experiments such a maximum pressure is perfectly tolerable, however, exceeding this value may become desirable in experiments where the collision rate is very low due to cross-sections and/or the flux of incoming particles (photons, ions) being very small. Here, one would like to increase the target gas densities, which, at a constant pumping speed, can increase the background pressure above the tolerable limit. For this reason, we have started investigating the possibility to use alternative detector types in VMI and/or Reaction Microscopy setups.

Here we propose a new concept, moving to an in-vacuum pixel detector, which has the potential to circumvent most of the above-mentioned limitations. After an introduction to this new detector type, a range of possible applications will be described. Subsequently first experimental results achieved using this detector will be presented.

4.2 The MEDIPIX / TIMEPIX chips

The Medipix2 detector is a pixel detector, which was designed by the CERN electronics department on behalf of the MEDIPIX collaboration [225]. It was originally designed for counting X-ray photons, without noise or dark current, at high fluxes (several Giga photons per cm^2 per second). At the same time good position resolution is achieved using 256×256 pixels with a pitch of 55 µm. The Medipix2 detector is the successor of the earlier Medipix1 chip, consisting of 64×64 pixels with a pixel size of 170×170 μm^2. In its normal operation

mode, the Medipix2 detector uses a pixilated array of reverse-biased semiconducting diodes as a sensor layer, which is bump-bonded to the Medipix2 read-out ASIA (application specific integrated circuit) [226, 227], as seen in Figure 4.2.

In our case a 300 µm thick array of reverse-biased photo diodes is used as the sensor. It is made from slightly n-doped high-resistivity silicon, with a p-type implantation in every pixel. The entrance window on the n-side is an ohmic contact of 150 nm thick Aluminum, where the bias voltage is applied. In the sensor layer every impinging particle creates one electron-hole pair per 3.6 eV of deposited energy. When a positive voltage is applied to the unsegmented n+ contact the generated holes drift towards the pixilated p+ contacts for collection. The amount of charge that the pixel electronics will detect is therefore proportional to the energy deposited in the detector layer by the impinging particle. With the sensor layer described above, photons and electrons can efficiently be detected, provided that the photon, respectively electron kinetic energy, exceeds the 4 keV detection threshold. For electrons detected in a VMI, this requirement can easily be met. With the sensor layer described above ions cannot be detected, since ions will not penetrate the Aluminum entrance layer. Therefore, for ion detection one has to rely on different means of charge amplification, as described in a later paragraph of this paper. We note that so far detection efficiencies of $\sim$ 85 % have been demonstrated [228].

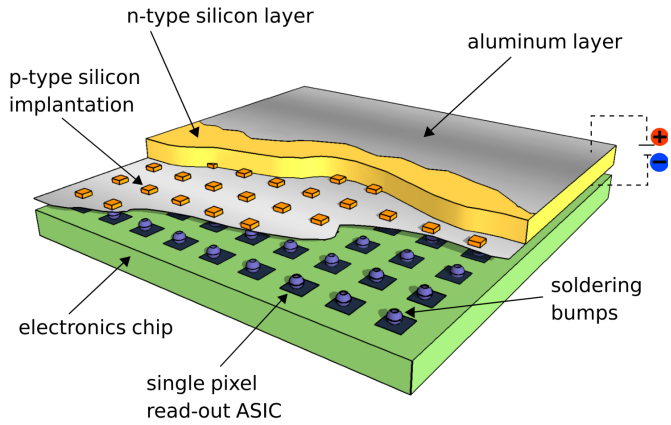

Figure 4.2: Schematic illustration of the Medipix2 detector. Visible are the sensor layer for electron-hole pair creation and the applied bias voltage as well as the bump-bonded read-out ASIC.

The ASIC contains in each individual pixel an analog input stage, an electronic shutter, two individually tunable energy discriminators as well as a 14-bit pseudo-random counter (see Figure 4.3). By making use of the two discriminator levels, one can define an energy window such that only incident particles

within this window will lead to a registered event. Since the threshold energies that can be chosen for the discriminator levels lie well above the noise level of the pixels ($\sim$ 100 e^-), almost noise free measurements are possible [229]. There are three further adjustment bits available for every pixel, which are used to equalize the detector response over the full pixel array. This feature is easily accessible via a software routine from the openly available control program Pixelman [230, 231], which is run on a PC. Connection to the chip is established either via an USB interface [232, 233] or a serial interface [234, 235].

The parameters, such as acquisition time and number of acquisitions, can easily be controlled by the same software. Here the acquisition window can be selected ranging from tenths of a second to several minutes or hours. The maximum single pixel acquisition rate for consecutive events lies at approximately 100 kHz per pixel. This means that during the chosen acquisition window events arriving on a single pixel with temporal distance larger than 10 µs will be separately counted. For separate pixels, parallel detection over the complete chip surface is possible. Therefore a maximum of 65536 separate events can be registered at the same time, assuming they are detected on separate pixels. This is an obvious advantage over wedge-and-strip or delay-line anodes, where at most one or a few incoming particles can be tolerated on the entire detector in one read-out cycle. [222].

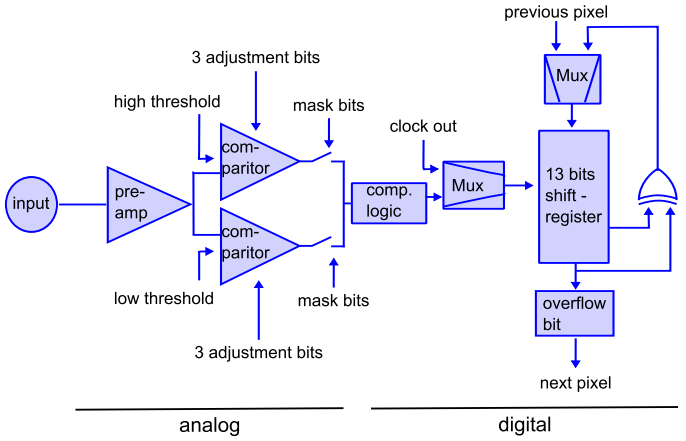

Figure 4.3: Schematic of the read-out electronics. Every pixel consists of an analog amplifier part and a digital part containing threshold discrimination, individual adjustment bits as well as the counter. Using the adjustment bits, a uniform detector response over the complete chip is ensured. This equalization can be automatically performed using the available read-out software.

The Timepix chip was conceived as a small modification of the Medipix2 read-out chip [235, 236] and is based on the same technological principles. In addition to the normal event-counting mode of the Medipix2 chip, it is especially adapted to measure not only the position but also the arrival time of the incoming particle. Each Timepix pixel can be programmed in one of three

modes: single particle counting (like Medipix2), arrival time (counting clock ticks from the moment the particle arrives until the shutter closes), or Time over Threshold (counting clock ticks as long as the discriminator threshold is exceeded). The Timepix pixels have only one energy discrimination threshold, thereby still allowing noise free detection. The Time over Threshold output is directly proportional to the amount of charge deposited on the particular pixel, i.e., to the energy of the detected particle. This is an important option, when centroiding algorithms are applied to achieve sub-pixel spatial resolution for events that lead to a detectable signal over a range of pixels. An example for such events are signals stemming from electron clouds after an initial electron or ion impact on a MCP detector placed in front of the Timepix detector [237, 238], as will be further explained in a later paragraph.

The general idea of Timepix is to distribute an external clock to the full 256×256 pixel matrix. The pixel logic is changed such that the counting of clock-pulses in the pseudo-random register is enabled by the first hit after the shutter opens and continues until the shutter closes. The nominal clock frequency for Medipix2 using the so-called Muros interface [234] is 160 MHz. This clock signal is an external input to the chip, and can be varied at will. In this way every pixel gets a "common-stop TDC" with 6.25 ns resolution. Due to the pseudo random counter approach in the 14 bit shift register, the highest possible clock-cycle that can be counted is 11810. The resultant dynamic range therefore is $11810 \cdot 6.25$ ns $= 74$ µs. Only a small number of pixels will typically be "hit" during an exposure, so most of the counters will have a zero value during read-out. After the acquisition is completed, all the $\sim$ 65000 pixel counter contents are serially shifted out in 5 to 10 milliseconds. By using the 32-bit parallel read-out bus of the chip one can obtain frame rates of $\sim$ 1 kHz [238, 239].

Both Timepix and Medipix2 chip[1] are buttable from three sides without creating any dead spaces in between the single chips. One edge is reserved for electronic read-out via wire bonds. In this way, detector arrays of 2×n chips can be created. For the presented experiments an array of 2×2 chips was used, creating an active detection area of 28×28 mm^2, which will be referred to as the Medipix2 Quad detector. In the framework of the RELAXD project, the development of electronic read-out using vias through the chip, and 1 gigabit/s bandwidth, will facilitate the production of even larger detector arrays [240]. As a follow-up to the Medipix2 detector, the Medipix3 chip has already been designed at CERN and is currently being tested [241]. A successor for the Timepix chip is still in the design phase.

In applications like VMI, the Medipix2 or Timepix chip in combination with a suitable sensor layer can easily be implemented. Without further optimization, it can be used to image electrons with high efficiency and good spatial resolution. The data is immediately available in ASCII or binary formats. MCP detectors offer efficiencies of around 60 %, corresponding to the active

[1] Research licenses to obtain the Medipix2 and/or Timepix chip, with a corresponding USB read-out system, and Pixelman software package, can be obtained via the chairperson of the Medipix2 Collaboration, Michael CAMPBELL from PH/ESE, CERN, Geneva, Switzerland; Tel: +41 22 76 74866; email: Michael.Campbell@cern.ch.

surface, whereas Medipix2 detectors have been shown to reach efficiencies up to at least 85 % and are expected to achieve even unit detection efficiency. At the same time Medipix2 chips offer an even efficiency distribution over the whole active surface.

4.3 Envisioned range of application

Velocity Map Imaging

As mentioned above, the first considerations to use Medipix2 chips in our research were initiated by the pressure limitations imposed by MCP based detectors. So far there are no such limitations known for Medipix2 chips other than the effects of electrical breakdown as described by the Paschen curve. In two-dimensional VMI, high signal rates are desirable, since typically one would like to record a projected image with $10^5 - 10^6$ events in order to be able to perform the extraction of the 3D velocity distribution with high accuracy. Depending on the available light source or projectile that is used in the collision experiment, achieving this number in a reasonable time can be challenging. In our own attosecond experiments, where photon numbers can be as low as 10^5 per shot, and experimental conditions rigorously have to be kept stable, this can be hard to do. Therefore efficient use of the available photons has to be made, for example by increasing the target gas density. However, this also increases the background pressure in the apparatus. This approach fails for MCPs, whereas Medipix2 can be operated over a large pressure range reaching from high vacuum to atmosphere (see Section 4.4).

The Medipix2 chip is thus expected to allow an increase in signal rate by as much as one to two orders of magnitude, thus decreasing the acquisition time by the same factor. In the remainder of this paper we will present a successful demonstration of this concept. First however, we describe a few other applications of the Medipix2/Timepix chip in VMI and/or Reaction Microscopy, which we regard as very promising and soon hope to develop.

3D Measurements

Time as the third dimension in imaging experiments can be accessed by using the Timepix instead of the Medipix2 chip. This will permit ion time-of-flight measurements simultaneously to VMI measurements. Nowadays in VMI, such measurements are already performed by applying slice imaging [215, 242]. Gating the detector and recording a series of two dimensional velocity distributions, the original three dimensional distribution of the particles can be retrieved. This, however, requires sophisticated timing and gating electronics to operate the detector. The application of the Timepix chip allows direct measurements with an arrival time resolution down to 10 ns. First tests of this capability, by measuring the difference in arrival time of backward and forward emitted ion fragments with respect to the detector, are in progress in our laboratory (see Section 4.6).

High position resolution measurements

High resolution photon counting using the Timepix chip has been performed and described by Vallerga and coworkers [237]. The sensor diode matrix above the read-out ASIC was replaced by an MCP, this way also allowing the detection of positively charged ions. The resulting charge cloud behind the MCP is detected on the pixel input pad of the bare Medipix2/Timepix read-out ASIC. Depending on the distance and extraction voltage between the MCP and the Timepix ASICc, the charge cloud coming from the MCP will cover multiple pixels. Using the above mentioned ability to determine the amount of charge deposited per pixel, a weighted centroiding algorithm can be used to achieve spatial resolution well below 10 µm [238]. In this case, the size of the MCP pores becomes the limiting factor. A similar technique has been known and applied also in VMI measurements for quite some time. Centroiding pixel counts on CCD cameras also leads to improvement of spatial resolution with current MCP-phosphor combinations [219].

Coincidence measurements

In combination with Reaction Microscopes, the Timepix detectors promise experiments with considerable less technological effort. Higher spatial accuracy as well as faster read-out can be achieved combining techniques described above. Precise timing information still has to be obtained from the fast MCP signal, whereas the Timepix temporal information can deliver a time stamp for the recorded event to unambiguously recognize coincidences on multiple detectors. In this way, coincidence measurements at increased count rates are feasible (see also Section 4.6).

4.4 First tests using the Medipix2 chip

In this section we report the first application of a Medipix2 chip assembly to VMI. The following measurements show that the detector is capable of replacing the commonly used 2D MCP-based charged particle detectors in such experiments. The most important aspects of the new detector, such as spatial resolution, quantum efficiency and behavior for different background pressures, have been tested. As a first experiment, we recorded multi-photon ionization signals from xenon (see Figure 4.4). The third harmonic at 355 nm (3.49 eV) of a flash lamp pumped YAG-laser was used as the pulsed laser source. The intensity of the laser pulses is estimated to reach 10^{12} W/cm^2 at a repetition rate of 10 Hz. The acquisition window of the Medipix2 chip was chosen to be 0.1 seconds to ensure that for each acquisition only the signal of one laser pulse was recorded. Depending on the signal strength, 100 - 1000 acquisitions were summed up to produce the final image. We were able to observe the signal from two different four-photon ionization processes corresponding to the $^2P_{3/2}$ (12.13 eV) and $^2P_{1/2}$ (13.44 eV) ionization thresholds of Xe [243]. The kinetic energies of the detected electrons were therefore 1.83 eV and 0.52 eV. These

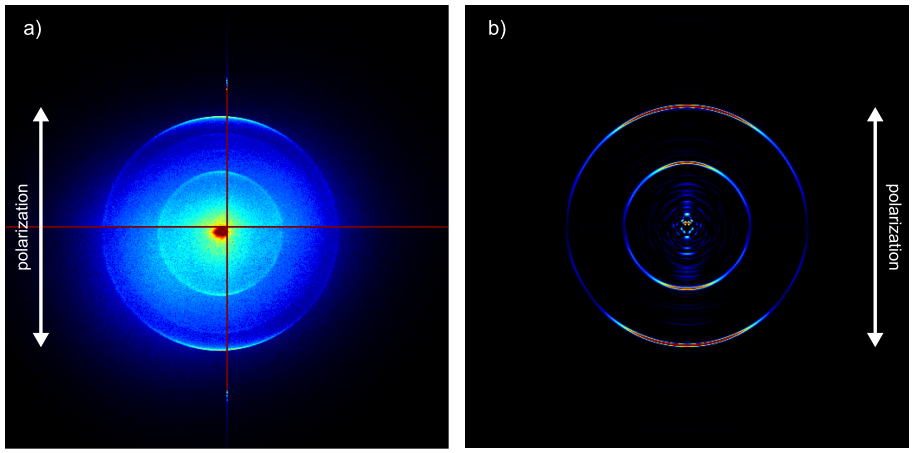

Figure 4.4: (a) Photoelectron image for four-photon ionization of Xe by a 355 nm Nd:YAG laser, recorded by the Medipix2 chip. Considerable signal due to ionization of background gas is also visible. The inner- and outermost ring are due to the xenon signal, which selectively was obtained by background subtraction. Since the images were recorded using a Medipix2 Quad detector, a bright cross is visible, which is caused by the larger surface pixels at the joining sides of the four read-out ASICs that read the Quad sensor. These pixels can either be masked or adjusted for the increased size after the measurement; (b After background subtraction an inversion algorithm allows extraction of a slice through the original three dimensional distribution, thereby revealing the velocity- and angular distribution of the ejected photo-electrons.

kinetic energies were measured with an energy resolution $\Delta E/E$ better than 0.07 and 0.03 respectively (see Figure 4.6).

We will discuss the individual measurements and results in detail in the following paragraphs. The most important aspect of this work was to test the capability of Medipix2 to increase the signal rate of VMI experiments. Therefore the quantum efficiency and the ability to operate the detector at elevated background pressures were investigated.

Quantum Efficiency

The efficiency of the Medipix2 detector will mainly depend on the kinetic energy of the particles to be detected and on the energy thresholds chosen in the discriminator logic. We expect to see a rise of detected signal as a function of the acceleration voltage of the electrons. This acceleration voltage can be chosen by applying a higher voltage to the repeller and extractor plates of the VMI setup, while maintaining electron focusing conditions at the detector surface. As described above, the detection threshold lies at approximately 4 keV. This level may vary depending on the amount of leakage current in the detector, which itself depends on temperature as well as on the amount of scattered light hitting the detector surface. In the present experiments, where a large flux of ultra-violet 355 nm photons was used to create an electron signal,

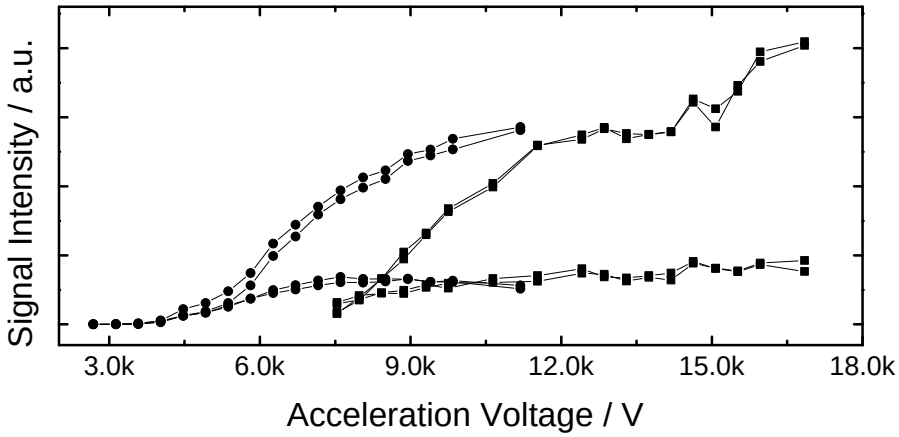

Figure 4.5: Voltage dependence of the signal rate for two different setups (red and black curves). The shift between the two curves is due to different threshold settings in both cases and can be explained by the amount of scattered light reaching the detector in the two measurements. However, the appearance of the same qualitative features should be noted. At voltages around 10 kV a plateau region becomes apparent. The subsequent rise is due to charge sharing effects.

the latter was definitely an issue and grounds for further improvements in the future.

Two measurements were conducted, varying the voltage of the VMI-setup from 4 kV to almost 17 kV, as shown in Figure 4.5. There is a shift of the two curves in voltage dependence. This shift is due to different threshold levels used in the two measurements, i.e., the threshold necessary to suppress noise stemming from scattered UV-light hitting the detector (see above). In the second experiment, more light hit the detector and therefore increased the dark counts. Consequently, a higher threshold level had to be chosen.

The curves nevertheless show the same qualitative features. At acceleration voltages of around 10 kV, a plateau region becomes apparent, which we interpret as a sign that unit detection efficiency has been achieved. In the second experiment the voltage range was increased to investigate the extent of this plateau region. Eventually a second increase in signal was observed at even higher acceleration voltages. At such high impact energies impinging particles create very large charge clouds that laterally spread on their path through the sensor layer, leading to detection on multiple adjacent pixels. This effect is known as charge-sharing leading to higher signal counts [244, 245]. Charge-sharing can readily be recognized in single-shot acquisitions where multiple adjacent pixels show counts simultaneously. Depending on the thickness of the sensor layer and the applied bias voltage, this behavior can be influenced. As discussed above, in the case of using MCPs in combination with bare Medipix2 / Timepix chips, this effect can even be desirable and exploited for centroiding.

In conclusion, measurements were performed suggesting that unit quantum

efficiency can be achieved and the necessary range of acceleration voltages was identified. This range is expected to extend to lower acceleration voltages as we move to other laser sources, such as femtosecond and/or XUV light sources. Here the required light intensities can be reached at much lower single pulse energies thus decreasing the amount of scattered light hitting the detector surface. Accordingly, adjusting the detection threshold levels will lead to unit quantum efficiency at considerably lower impact energies.

Operation at increased background pressure

A second test was performed to investigate the pressure operating range for Medipix2. As mentioned above, the expectation is to be able to perform VMI measurements with a 10-100 times increased target gas density. The base pressure in the experimental setup was in the range of 10^{-7} mbar, in the presence of the target gas jet. To increase the background pressure to the required testing levels, a leak valve was installed through which the chamber pressure could be precisely controlled. Helium was chosen as leak gas to increase the background pressure without affecting the signal level. In this way, it was possible to separate the influence of high pressure on the electron generation process and the subsequent detection.

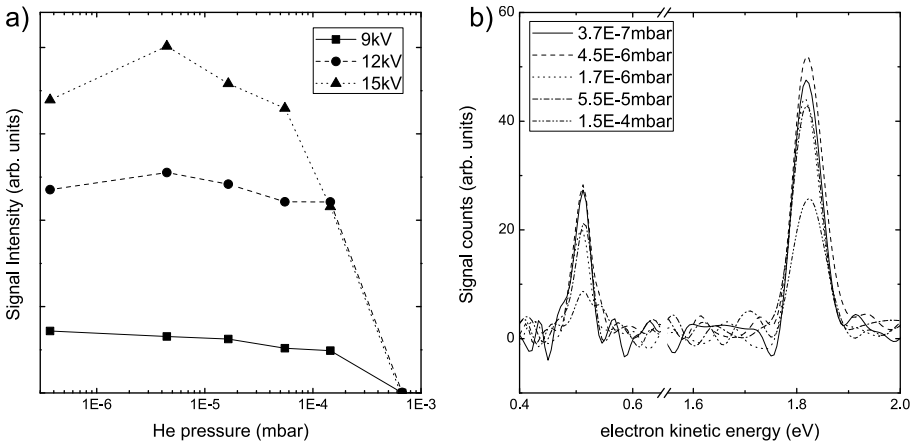

Figure 4.6: In (a) the pressure dependence of the signal intensity is shown for different acceleration voltages. A clear decrease in signal with increasing background pressure is visible. For pressures above 10^{-3} mbar the mean free pathlength for electrons in the extraction region of the VMI (see Figure 4.1) becomes too small for a reliable measurement. (b) Even though we see a reduction in signal due to the decreasing mean free path length, the kinetic energy resolution of the detector is maintained over the full pressure range.

The pressure was increased in steps to $\sim 10^{-3}$ mbar. Above this pressure the operation becomes restricted by the turbo molecular pumps. Another restriction that has to be respected is the electric breakdown of gasses as described by the Paschen curve. In order to protect the chip assembly and pre-

vent electronic breakdown over the sensor layer, gas pressures exceeding 10^{-3} mbar were avoided. The Xe target gas densities were held at a constant level throughout the tests. Therefore any drop in signal stems solely from the increased background pressure. Of course, in a real application of the detector at elevated pressure, the target gas density would be increased to the maximum tolerable amount.

In Figure 4.6 a moderate decrease of signal for pressures above 10^{-5} mbar followed by a much more rapid drop above a background pressure of 10^{-4} mbar can be seen. Above pressures of 10^{-3} mbar the signal becomes too weak for decent measurements. At the same time, the original spatial resolution is maintained throughout the complete tested pressure range. This behavior is attributed to the reduced mean free pathlength especially for slow electrons during acceleration. As electrons are liberated in the laser focus, their initial velocity is on the order of a couple of eV. In the tested pressure range the mean free path for such slow electrons lies between 0.5 and 500 mm. This is about four orders of magnitude lower than the mean free path for electrons traveling with a kinetic energy of 5 keV [246]. Collisions of slow electrons with the background helium atoms will lead to a strong deviation from their original path, preventing them from reaching the detector. After acceleration, the electrons will travel with less disturbance. Therefore no spreading or blurring of the signal is visible.

4.5 Conclusion

In conclusion, we have reported in this paper a first example of the use of pixel detectors for position-sensitive ion/electron detection. Given the prevalence of these types of detectors in chemistry and physics research, and given the large, as yet unexplored potential of these detectors, we foresee widespread use of these detectors in the coming years, where the results presented here merely serve as a first illustration.

4.6 Update and Outlook

Since conducting the afore mentioned experiments, about two years have passed. Due to the promises that the new detector technology holds a new PhD position was dedicated to investigate further application of the Medipix / Timepix chips to VMI and coincidence measurements. The responsible person for the results summarized in this brief update and outlook is Julia Jungmann.

In the framework of this newly created PhD position and in the continuation of the proposed use of Timepix, the slice imaging approach (see Section 4.3) has successfully been demonstrated in photo-dissociation of NO_2 [247]. These experiments were conducted using an MCP in combination with the bare Timepix detector, i.e., without a sensor layer. The demonstrated time resolution lies at around 10 ns. This resolution was achieved with a maximum possible clock frequency of 100 MHz when using Quad detectors, which is con-

trary to single detectors where up to 160 MHz clock frequencies are possible. The resultant dynamic range for the charged particle incidence time in the case of the Timepix Quad detector was $\sim$ 120 µs.

Using an MCP in combination with a bare Timepix / Medipix chip allowed the detection of positively charged ions as well as the detection of electrons and ions also with lower kinetic energies than the before mentioned 4 keV. Further experiments investigated spatial resolution of this setup in the context of imaging mass spectrometry [248].

In the course of these measurements more precise specifications of Medipix and Timepix chips such as read-out rates, temporal resolution and the performance of different read-out interfaces have been further evaluated. The three main read-out systems are the USB and Muros interface described in the previous sections. A new read-out system developed by John Vallerga and coworkers allows substantially higher read-out rates by accessing the data of each separate Quad chip in parallel as well as also reading out 32 groups of eight lines of pixels for each chip in parallel. Thus, they can fetch the data off the chip with a 1 kHz rate. In comparison, using the RELAXd board in combination with the Pixelman software only 10-15 Hz are achievable and in combination with a new acquisition software around 60 Hz have been reached. A good overview over the different read-out hardware and software can be found in Reference [249].

Experiments for ion-ion coincidence experiments are planned using the new 1kHz read-out system. For this, a 400 kHz femtosecond OPCPA laser system [12] will induce Coulomb-explosion in molecules. The acquisition time of the Timepix detector will be set to $\sim$ 100 µs, which is the maximum achievable dynamic range, and thus will acquire images of 40 consecutive laser shots. Including the read-out time of 1 ms, the effective repetition rate at which the experiment is run will be around 36 kHz. Even though this means a $\sim$ 90 % downtime, such high repetition rates are nevertheless hard to achieve in conventional approaches. If this proof-of-principle experiment will be successful, a second flight tube for the detection of coincident electrons will be added to the system.

Additionally, a convenient feed-through for the use of the detectors in vacuum now eliminates the former problem of contamination introduced by the read-out interface, originally soldered directly to the chip itself. The Medipix / Timepix detectors thus have proven to be very useful for the application to photo-electron / ion spectroscopy and imaging mass spectrometry measurements and the development which was started in this PhD thesis continues to yield great results.

5 Ultrashort laser pulses and carrier envelope phase

5.1 Introduction

In the following sections the development of a terawatt (TW) amplifier system will be presented. In order to perform non-linear XUV and attosecond-pump-attosecond-probe experiments, one needs XUV sources with higher photon fluxes than currently available, as was pointed out in Section 2.4. The presented terawatt amplifier was designed to create a femtosecond source, which allows the generation of IAPs with sufficient intensity to create non-linear processes in the XUV spectral range. While femtosecond amplifiers that generate peak powers in the terawatt regime are not a major technical challenge anymore, their main shortcoming for the application to attosecond science has been the missing carrier-envelope phase (CEP) stability. CEP-stabilization has been demonstrated for a wide range of amplifier systems operating with a few millijoules of pulse energy and repetition rates in the kHz range [55, 250–254]. The TW amplifier, which was designed and set up in this thesis, therefore presents the first source of femtosecond laser pulses with a stabilized CEP reaching pulse energies of up to 50 mJ.

To introduce the reader to the principles involved in femtosecond laser development and CEP-stabilization, the first part of this chapter will lay out the concepts of ultrashort laser pulses generation and amplification, carrier-envelope phase and the different technical aspects of its stabilization. Afterwards, the design, implementation and performance of the TW-amplifier will be described in detail.

5.2 Fundamentals on ultrashort laser pulses

Laser radiation shows multiple characteristics that predestine lasers as a source of high intensity radiation. Their high degree of spatial coherence allows focusing to extremely small spot sizes, concentrating the optical energy contained in the laser beam to a very small area. In order to increase the intensity incident on this area, further laser sources have been developed that additionally concentrate the energy in time to very short intervals. This is of particular interest in the case of non-linear spectroscopy, since the probability of processes that involve N photons relates to the intensity I of the light sources as I^N. As

was further pointed out in Chapter 2, the temporal resolution in time-resolved spectroscopy depends to a great extent on the time duration of the exciting laser pulses making generation of ever shorter laser pulses an important branch in laser physics.

Although the first demonstrated laser relied on flashlamp pumping of a ruby crystal and therefore the laser radiation was already then emitted in discrete pulses, today there are many techniques available that allow the generation of laser pulses with tremendously shorter pulse duration. The shortest possible laser pulses directly from a laser oscillator are nowadays produced by Kerr-lens modelocking [255]. The pulse envelope of such pulses contains only a few-cycles of the carrier wave, hence these pulses are usually referred to as few-cycle pulses. In the following sections, the concepts of these techniques will be introduced as well as propagation of such short laser pulses through dispersive material and the related effects on the pulse properties. In addition, techniques which are commonly used to compensate these effects will be presented. In the end the technique of chirped pulse amplification (CPA) will make the connection to the presented experimental work.

5.2.1 Generation of ultrashort laser pulses

The concept of the laser is assumed to be known to the reader, the basic laser principle will thus only be laid out briefly. Strongly simplified, a laser oscillator consists of only two parts: an optical resonator and an optical amplifier. Optical amplification is achieved by stimulated emission from an atomic or molecular systems, which is operated in population inversion with respect to the relevant laser energy levels. The spectral bandwidth of the gain is determined by the linewidth of the involved laser transition.

Emitted radiation from the gain medium is coupled back into the gain medium by the optical resonator, which leads to an avalanche like amplification of the light inside the resonator cavity. This process reaches an equilibrium, when the optical amplification in the gain medium balances the losses experienced in the resonator. When assuming an ideal (dispersion-free) Fabry-Perot resonator, consisting of two parallel flat mirrors separated by a distance d, this resonator supports only longitudinal modes whose phase shift per round-trip equals an integer multiple of 2π:

$$2 \cdot k \cdot d = \frac{4\pi\nu d}{c} \stackrel{!}{=} 2\pi \cdot q \ , \qquad q = 1, 2, 3 \ldots \tag{5.1}$$

with k denoting the wavenumber, ν the optical frequency and c the speed of light. The frequency spacing between adjacent modes in such a resonator hence is

$$\nu_{rep} = \frac{c}{2d} \ . \tag{5.2}$$

The spectral position of each mode ν_q in this case is given by:

$$\nu_q = \nu_{CE} + q \cdot \nu_{rep} \ , \qquad q = 1, 2, 3 \ldots \ . \tag{5.3}$$

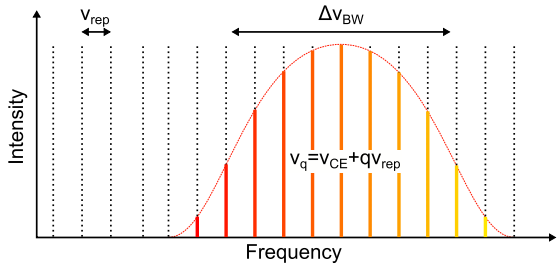

Figure 5.1: Schematic plot of the distribution of longitudinal modes of a laser resonator in the frequency domain. Indicated in the plot are the spacing of individual modes as well as their spectral position. For illustration purposes the spectral spacing is, however, strongly exaggerated. In a realistic cavity q is on the order of $10^5 - 10^6$ *and the gain bandwidth of Ti:Sapphire can support* $\sim$ *250.000 modes.*

This is illustrated also in Figure 5.1. One should note, however, that these relations, with $\nu_{CE} = 0$, only hold in the absence of dispersion inside the cavity, i.e., neglecting dispersion, which is generally introduced by the gain medium. Dispersive materials inside the cavity will lead to a non-zero offset by ν_{CE}, which is caused by second order dispersion leading to a departure of the longitudinal modes from their previously equidistantly spaced positions (see also Section 5.2.4).

The emitted laser radiation, which is coupled out through one of the resonator mirrors, is composed of all frequencies that simultaneously fulfill the necessary frequency relation and experience enough gain to compensate the losses in the resonator.

In usual laser resonators, the frequency separation between the modes is much smaller than the spectral bandwidth of the gain profile, hence a large number of modes will be supported and oscillate at the same time. In the free-running case, the phases of the different modes fluctuate statistically and time independently, leading to the emission of series of bursts of incoherent light, spaced by $T_{rep} = 1/\nu_{rep} = 2d/c$, as illustrated in Figure 5.2. If, however, the individual modes can be phase locked, meaning that the phase difference between consecutive modes is constant, they will interfere constructively at one place inside the laser cavity, forming a single ultrashort laser pulse. This process is called mode-locking and is also illustrated in Figure 5.2. This individual pulse will then circulate inside the laser cavity and part of it will leak through the output coupler. T_{rep} is therefore the time that the pulse travels inside the cavity before it comes back to the output coupler and it is thus clear that the repetition rate of the emitted pulse train is equivalent to the inverse of the round-trip time.

The derivation of the modelocking process can also be obtained when starting from the temporal image of an infinitely long pulse train. The Fourier transform of such a pulse train into the frequency domain spectrum would result in a number of frequency spikes separated by ν_{rep}, while the pulse duration would translate into the number of existing frequency modes. This is

equivalent to the image constructed above.

Depending on the spectral bandwidth of the oscillating modes $\Delta\nu_{BW}$, the minimum achievable pulse duration, also called the Fourier- or transform-limited pulse duration τ_{FL}, is given by

$$\tau_{FL} \geq \frac{\alpha}{\Delta\nu_{BW}} = \frac{\alpha \cdot \lambda_1 \cdot \lambda_2}{c \cdot \Delta\lambda} \ , \tag{5.4}$$

where $\Delta\nu_{BW}$ and $\Delta\lambda$ are the full-width at half-maximum (FWHM) of the spectral bandwidth (either in terms of frequency or wavelength), λ_1 and λ_2 are the respective wavelengths values corresponding to lower and higher bound of $\Delta\lambda$, respectively, and α is a constant which takes into account the temporal pulse shape (Gaussian: $\alpha_{\text{gaussian}} = 0.441$, Secant: $\alpha_{\text{sech}} = 0.315$, Lorentzian: $\alpha_{\text{lorentz}} = 0.142$). As pointed out earlier, equation 5.4 describes the fact that a greater spectral bandwidth is usually related to a shorter time duration. For a pulse propagating in vacuum this is easily the case. However, during propagation of light pulses inside optical material, the refractive index of the material is usually frequency-dependent, which can lead to a distortion of the temporal structure of the pulse. The pulse duration will therefore exceed the bandwidth-limited minimum value, if a frequency chirp exists, i.e., non-zero phase-structure within the pulse. Propagation of ultrashort laser pulses will be described in detail in Section 5.2.3.

The most common technique today to achieve modelocking is to introduce an intensity dependent loss mechanism in the laser cavity. This can for example be a saturable absorber [256], which reach lowest absorption, and therefore lowest losses, only at high incident intensities. This is usually the case if the laser runs in a mode where the energy is concentrated in short bursts, i.e. when the laser is modelocked. The shortest femtosecond laser pulses nowadays are commonly realized using the so-called Kerr-lens modelocking, which was first introduced by Sibbett and coworkers [257]. This approach uses the effect that high intensities change the refractive index of the gain material according to

$$n = n_0 + n_2 \cdot I \ . \tag{5.5}$$

A Gaussian spatial distribution of the intensity in the laser beam profile thus results in a higher refractive index at the center of the beam. This in turn causes the gain medium to act like a weakly converging lens. If the laser resonator is designed accordingly, low losses are only achieved for a Kerr-lens focused beam using either hard or soft apertures, which again is only the case in a pulsed mode.

Especially in solid state gain media, the spectral bandwidth of the gain profile can be large, which leads consequently to shorter achievable pulse durations and thereby higher peak intensities. To produce the shortest laser pulses the common gain material nowadays is Titanium doped Sapphire (Ti:Sapphire), for which the center of the gain profile lies around 800 nm [258], while the lasing transition is best pumped around 500 nm. Ti:Sapphire has several other properties such as high saturation fluences and good thermal conductivity,

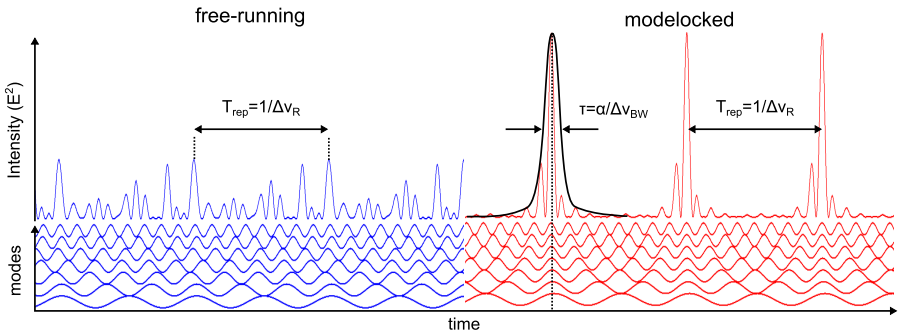

Figure 5.2: Illustration of the radiation emitted by a resonator in the free-running (blue) and the modelocked (red) case. Considered are seven spectrally equidistant longitudinal modes with constant amplitude (bottom). For the free running case the waves are summed with random phases whereas for the modelocked case a constant phase is assumed. In the former case incoherent radiation is emitted in bursts, which repeat at the oscillator repetition rate, while in the latter case, coherent radiation in the form of short pulses is emitted. The duration of the emitted pulses is then inversely proportional to the number of oscillating modes described by $\Delta\nu_{BW}$.

which make it by far the most popular gain material for ultrashort laser pulse generation and for their amplification.

5.2.2 Description in the time and frequency domain

A linearly polarized light beam consisting of multiple frequencies centered around the frequency ω_0 and traveling along the propagation direction z can best be described by its electric fields:

$$\boldsymbol{E}(\boldsymbol{r},t) = \hat{\boldsymbol{u}} \cdot \mathrm{Re} \int_{-\infty}^{\infty} A(z,\omega-\omega_0) \cdot u_\omega(\boldsymbol{r}) \cdot e^{i(\omega \cdot t - k(\omega)\cdot z)}\, d\omega \ . \tag{5.6}$$

The electric field in this case is decomposed into the unit vector $\hat{\boldsymbol{u}}$ defining the polarization direction perpendicular to the propagation direction, a complex amplitude $A(z,\omega-\omega_0)$, where ω is the angular frequency related to ν by a factor of 2π, and the transversal beam-profile $u_\omega(\boldsymbol{r})$. $k(\omega)$ is the frequency-dependent wavenumber.

Assuming an even distribution of the frequencies over the beam profile is usually justified for not too broad optical spectra. For most laser beams the approximation of a Gaussian intensity distribution in the beam profile can also be applied. The propagation principles of such a beam are well described with the formulas of Gaussian optics, which will not be further discussed here, but can be found in any optics textbook [259–261].

In the following, we will, however, use a simpler approach and start out with an electric field wavepacket which is described by a slowly varying field envelope $f(t)$ and a carrier wave oscillating with the center frequency ω_0 (a

more detailed description of this approach can also be found in [261]):

$$E(t) = f(t) \cdot e^{-i\omega_0 t} = \frac{1}{\sqrt{2\pi}} \int_{-\infty}^{\infty} a(\omega) e^{-i\omega t} d\omega \ , \tag{5.7}$$

where $a(\omega)$ is the amplitude of each frequency contributing to the final wavepacket and $I(\omega) := |a(\omega)|^2$ is called the spectrum of the wavepacket. $a(\omega)$ can consequently also be described by the inverse Fourier transform of the electric field. Including the definition $\omega' = \omega - \omega_0$, this leads to

$$a(\omega_0 + \omega') = \frac{1}{\sqrt{2\pi}} \int_{-\infty}^{\infty} f(t) e^{i\omega' t} \ . \tag{5.8}$$

In the Fourier limited case, the shape and position of the spectrum is therefore defined by the temporal pulse envelope and vice versa. However, if the pulse is propagated through a dispersive optical system, each frequency will have a different speed of light, contributing to the wavepacket at the output of the system with a spectral phase $\phi(\omega)$. The final wavepacket can therefore be described as

$$E_{fin}(t) = e^{-i\omega_0 t} \ \cdot \ \frac{1}{\sqrt{2\pi}} \int_{-\infty}^{\infty} \left[a(\omega_0 + \omega') e^{i\phi(\omega_0 + \omega')} \right] e^{-i\omega' t} d\omega' \ , \tag{5.9}$$

where the first term again gives the carrier wave and the integral term gives the temporal pulse envelope defined by the spectrum and the spectral phase accumulated in the optical system. The precise influence of an optical system on the spectral phase and therefore on the temporal properties of the pulse will be described in the following section.

5.2.3 Dispersion

In optical materials the phase velocity changes for different light frequencies, which is generally called dispersion and is described by a frequency-dependent refractive index $n(\omega)$. In this section, the interest lies, however, on the phases for different frequencies acquired when traveling through a dispersive medium. This is often easier described by the frequency-dependent wavenumber $k(\omega) = \omega n(\omega)/c$. The accumulated spectral phase of each frequency within a light pulse after traveling a distance z can then be written as

$$\phi(\omega) = \frac{\omega}{c} n(\omega) \cdot z = k(\omega) \cdot z \ . \tag{5.10}$$

A constant phase term describing the absolute phase at the entrance into the dispersive material has been omitted as for the following description only changes in the phase are of interest.

To study the impact of the accumulated spectral phase on the pulse shape, one can develop the spectral phase $\phi(\omega)$ around the central frequency in a Taylor expansion:

$$\phi(\omega) = \phi_0 + \phi_1 \cdot \frac{\omega - \omega_0}{1} + \phi_2 \cdot \frac{(\omega - \omega_0)^2}{2} + \ldots + \phi_n \cdot \frac{(\omega - \omega_0)^n}{n!} \ . \tag{5.11}$$

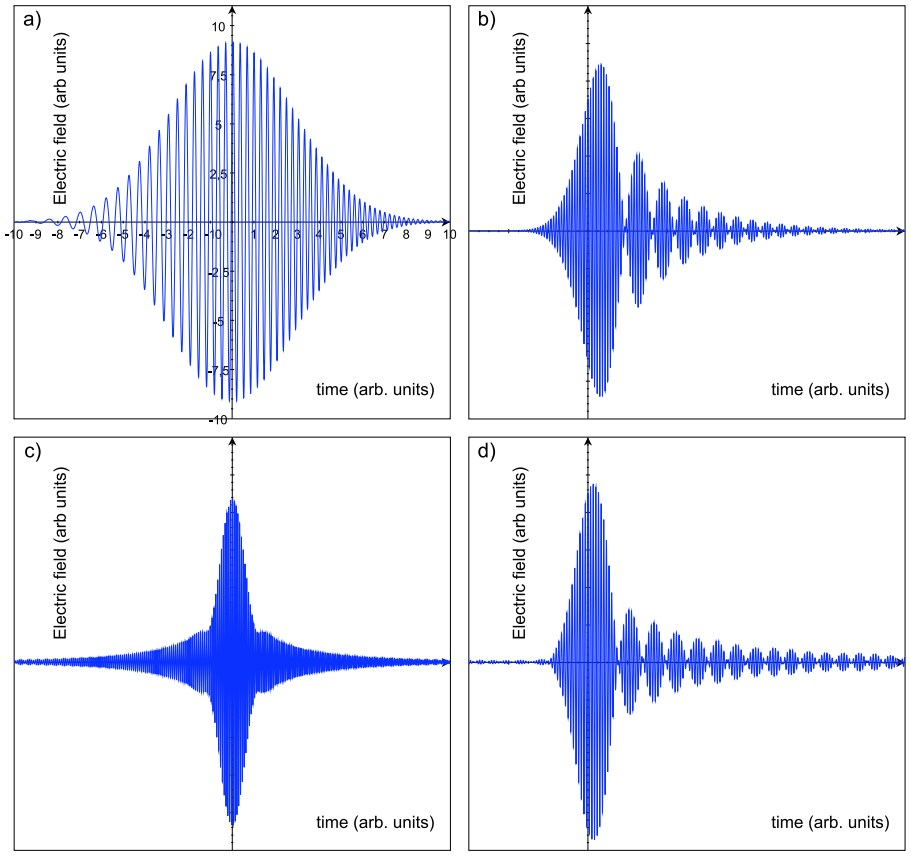

Figure 5.3: The effect of a linear frequency chirp described by ϕ_2 on a the electric field evolution of a short laser pulse is shown in (a). The following graphs (b-d) show the individual influence of positive higher order dispersion terms on a laser pulse: (b) $\phi_3 > 0$, (c) $\phi_4 > 0$, (d) $\phi_5 > 0$.

Here ϕ_0 denotes the carrier envelope phase which will be introduced in detail in Section 5.3. ϕ_1, defined by

$$\phi_1 = \left.\frac{d\phi(\omega)}{d\omega}\right|_{\omega=\omega_0} = \frac{dk}{d\omega}\cdot z = \frac{z}{v_G} = GD(\omega)\ , \tag{5.12}$$

is called the group delay (GD) and describes the time it takes the pulse envelope traveling at the group velocity v_G (see Figure 5.6) to pass through the dispersive material. The GD has no influence on the pulse profile and only reflects a delay of the pulse maximum compared to free space propagation. The unit of the GD is fs.

The term ϕ_2 denotes a quadratic spectral phase and is called the group delay dispersion (GDD).

$$\phi_2 = \left.\frac{d^2\phi(\omega)}{d\omega^2}\right|_{\omega=\omega_0} = \frac{dGD(\omega)}{d\omega} = \frac{d^2k(\omega)}{d\omega^2}z = GDD(\omega) \tag{5.13}$$

This term causes a broadening of the temporal profile due to a linear time dependence of the frequencies within the pulse envelope, usually referred to as linear chirp. The unit is fs^2. Higher terms ϕ_n deform the temporal structure of the pulse as plotted in Figure 5.3.

In order to achieve a perfectly compressed and thus most intense pulses at the place of experiment, dispersion of second and higher orders have to be efficiently compensated. Techniques to do this will be briefly introduced in the following section.

5.2.4 Dispersion management in laser systems

There are two important reasons to control the dispersion introduced in a laser system. Intuitively, it is clear that if the shortest possible pulses are supposed to be delivered at an experiment, all dispersion introduced by optical elements lying on the beam path to the experimental setup has to be compensated. Both linear and non-linear dispersion would otherwise lead to a stretched and distorted temporal pulse profile (see Figure 5.3). The resultant pre- or post-pulses, shoulders and the reduced peak intensity are undesirable in most high-intensity experiments.

Secondly, the resonator for production of ultrashort pulses described in Section 5.2.1 was assumed to be dispersion-free. In reality, this is commonly not the case. Taking dispersion of the gain material or other optical components inside the resonator into account would lead to unevenly spaced modes, i.e., contradicting the frequency conditions (given by Equation 5.3) of a modelocked laser. In order to re-establish the phase conditions expressed in equation 5.1, it is important to control the dispersion already inside the oscillator cavity. The better a constant spectral phase is achieved, the larger will be the bandwidth at which the phase conditions given by equations 5.1 and 5.3 are fulfilled and hence the shorter the achievable pulse durations.

In conclusion, managing these higher order terms of dispersion is thus mandatory when working with ultrashort pulses. This is the case both in oscillators but also for dispersion introduced in amplifiers or on the way to the experiment.

Most optical materials show a positive dispersion, meaning that longer wavelengths see a lower refractive index, e.g., after a pulse has traveled through normal dispersive material, the red wavelengths of the pulse spectrum will be traveling in the front of the pulse envelope, whereas blue frequencies will be traveling in the trailing edge of the pulse. Optical devices have therefore been developed introducing controlled negative dispersion into the beam path. The most important techniques will be discussed briefly. The exact derivation of dispersion terms introduced by the different methods can be found in the respective literature. The treatment in this section will only be of qualitative nature, while necessary references to the precise mathematical expressions will be given accordingly.

The common approach to gain control over dispersion is by spatially dispersing the different spectral components of a light pulse and propagating them through an optical setup in which the optical pathlength is different for

each frequency component. This is called geometric dispersion. Subsequently, the separate frequency components are recombined to form a pulse with an optimized amount of dispersion.

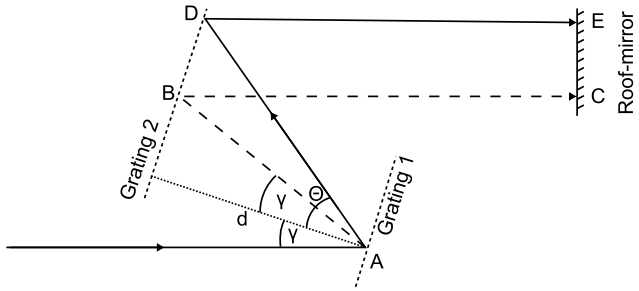

Figure 5.4: Geometric setup of a grating compressor. The incidence angle is given by γ and the diffraction angle is given by θ. The path ABC, gives the beam path of the un-diffracted beam.

Grating stretcher and compressor

The most important tool for managing large amounts of dispersion is the grating compressor, introduced by Treacy in 1969 [262]. The principle is illustrated in Figure 5.4. The incident laser pulse is diffracted on a first grating and the different frequency components are spatially dispersed. After reflection of a second grating positioned parallel to the first, the different wavelengths propagate parallel. Subsequent reflection of a roof-mirror sends the light back through the same setup, which recombines the before spatially separated wavelengths to reconstitute the original laser pulse, however, with altered dispersion.

It is easy to see qualitatively that the introduced GDD must have a negative value, when taking the position of the roof-mirror as a reference plane and comparing two optical paths from point A to this plane. The dashed beampath (ABC) in Figure 5.4 illustrates an un-deflected beam, i.e. the same path light would take if the gratings were replaced by mirrors. This path must naturally be a minimum in pathlengths according to Fermat's principle. Any other path must inherently be longer.

According to the grating equation

$$m\lambda = d\,(sin\,\theta - sin\,\gamma)\ , \qquad m = 0, \pm1, \pm2, \dots\ , \tag{5.14}$$

the diffraction angle θ increases with wavelength. The generated GD must therefore be smaller for shorter wavelengths, or equivalently for higher optical frequencies. The resulting GDD hence is negative. The value of the GDD then depends linearly on the distance d between the two gratings. When the beam is passed back through the grating pair to recombine the different wavelengths, the acquired GDD is multiplied by a factor of two.

The advantage of a grating compressor is its reflective nature, which allows the compression also of very energetic beams. The maximum energetic throughput of grating compressors, however, is rarely better than 70 %, owing

to an effective reflectivity of not much more than 90 % for typical reflection gratings.

The amount of dispersion in grating compressors is usually much higher than the dispersion accumulated from optical materials in common beam-paths. Grating compressors are therefore commonly used in chirped pulse amplification (CPA) setups in combination with a grating stretcher (see also Section 5.2.5), introducing and compensating very large amounts of dispersion.

For the precise derivation of the dispersion terms introduced by grating compressors the reader is referred to references [262–264].

Other techniques

There are a number of other techniques to introduce controlled amounts of negative dispersion, which are less relevant for the work described in this thesis, however, should be mentioned for completeness.

Often used inside ultrashort laser oscillators and amplifiers are **prism sequences** [265, 266]. The working principle is generally similar to the mechanism introducing geometric dispersion in case of the grating compressor. The material dispersion of the prisms, however, also introduces positive GDD. By changing the insertion of the prisms, the amount of total GDD can thereby be controlled. By using different prism materials, the shape of the introduced GDD can be matched very precisely to the needs of the laser system. Also, the losses introduced by prism compressors are significantly smaller than grating compressor, which makes them in particular suitable for the use inside laser cavities.

Chirped mirrors [267] are the tool of choice to compress few-cycle pulses with an extremely broad spectral bandwidth. Similar to highly reflective Bragg mirrors, chirped mirrors are built from coating layers with alternating high and low refractive index. The layer thickness, however, changes as a function of layer depths with respect to the surface of the mirror. This function is chosen such that the Bragg condition for different wavelengths is fulfilled at different depths of the mirror coatings. Optimization algorithms have been developed that are able to design layer progressions to compensate almost any shape of higher order dispersion. The introduced amount of negative dispersion of such mirrors is generally small, which makes multiple bounces on the mirrors necessary. Since the layer progressions have to be designed specifically for every application, the use of chirped mirrors is, however, rather inflexible and it is difficult to react to changes in the experimental setup.

To meet the demand for a more flexible dispersion compensation, a number of adaptive techniques have been developed. One approach is to use either **liquid crystal displays** (LCDs) [268] or **deformable mirrors** [269] set in the center of a refractive 4-f setup. In this case, the pulse is spatially dispersed into its different frequency components using either gratings or prisms. The LCD is then placed in the center of the 4-f setup and can modulate the phase and / or amplitude of each frequency independently per pixel of the display. Alternatively the LCD can be replaced by a deformable mirror, folding the 4-f setup at its axis of symmetry. Piezo-elements then deform the mirror surface

which leads to different geometric pathlengths for neighboring wavelengths.

Another approach, which has gained a lot of attention in the last years is the use of **acousto-optic programmable dispersive filters** (AOPDFs) [270]. If an acoustic wave is propagated through an acousto-optic crystal, the lattice expansion and compression at the crests and troughs of the acoustic wave cause a slight change of the refractive index of the crystal at periodic distances. An optical wave can partially diffract on this lattice if the Bragg condition is satisfied. If a chirped acoustic wave is used, which travels coaxially with the optical wave, each frequency component of the optical wave will be diffracted only at the point in the crystal where the Bragg condition is fulfilled. Diffraction then projects a part of the wave into a different mode, which subsequently will form the output pulse. Since the acousto-optic crystal is birefringent, the diffracted wavelengths will experience a different refractive index, making the total accumulated phase of each frequency dependent on the pathlength traveled in the second mode, and thus frequency-dependent on the position inside the crystal where the Bragg condition is satisfied.

AOPDFs have so far been used to optimize the phase in CPA systems, however, recently they have successfully been applied to control the CEP of both amplifiers and oscillators (see Sections 5.4.1 and 5.4.2).

5.2.5 Amplification of ultrashort laser pulses

The pulse energies supplied by common ultrashort pulse laser oscillators lies on the order of 5 - 10 nJ. Despite the short pulse durations, this is usually too low to meet the requirements of high intensity applications and hence further amplification of the pulses is needed.

Ti:Sapphire has evolved into the most popular gain material for both ultrashort laser oscillators but also for femtosecond amplifiers because of its high saturation fluence

$$J_s = \frac{\hbar\omega_0}{\sigma_e(\omega)} = 0.9\ \frac{J}{cm^2}\ , \tag{5.15}$$

allowing the extraction of high energies, as well as because of the bandwidth of its gain profile and its high damage threshold. Additionally, there are a number of widely available lasers types which emit radiation at a wavelength around 500 nm (Nd:YAG 532nm, Nd:YLF 527 nm), and hence can be used to pump the Ti:Sapphire crystal.

However, there are two limitations in amplifying ultrashort laser pulses in general. First, in order to achieve good energy extraction, the pulse to be amplified has to have an energy fluence inside the gain medium which is close to the saturation fluence of the gain material. In the case of a 30 fs pulse and the above mentioned saturation fluence of Ti:Sapphire the intensity in this case would lie on the order of $3 \cdot 10^{13}$ W/cm^2, i.e., above the damage threshold of most optical materials.

Second, the B-integral described by

$$B = \frac{2\pi}{\lambda} \int n_2 I(z) dz \tag{5.16}$$

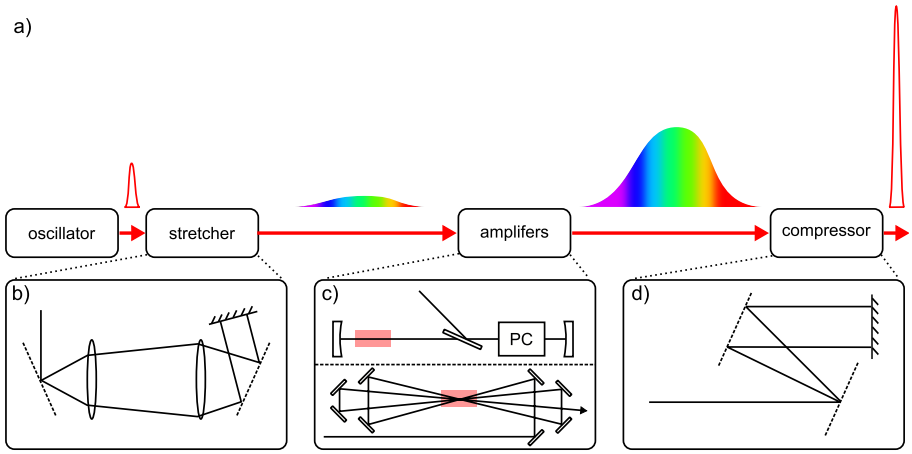

Figure 5.5: (a) Schematic of the CPA principle. (b) shows the geometric setup of a grating stretcher used to expand the pulse duration and thus decrease the peak intensity. (c) gives an impression of the two types of common amplifiers, e.g., regenerative amplifier (top) and multipass amplifier (bottom). (d) illustrates the common grating compressor setup.

gives a number for the total amount of non-linear phase acquired in the optical material during amplification (see also equation 5.5). Values of B larger than $\sim$ 3 - 5 mark the border where self-focusing and other non-linear effects start to play a non negligible role. These values should therefore not be exceeded in ultrashort laser pulse amplification. A 30 fs pulse at saturation fluence propagated through 10 mm of Ti:Sapphire ($n_2 \approx 3 \cdot 10^{-16}$ cm^2/W [271]) would, however, acquire a B-integral value in the range of $\sim 10^3$.

To solve these problems, chirped pulse amplification (CPA) was invented [272], which makes possible the amplification of ultrashort laser pulses to much higher pulse energies. To reach this goal CPA employs a three step approach, as illustrated in Figure 5.5a).

In the first stage, the pulses are stretched in time, usually by introducing large amounts of positive dispersion. The common optical setup to achieve this are grating stretchers or dispersive glass blocks. Grating stretchers work on the same principles as grating compressors (Section 5.2.4), but by introducing an inverting telescope in the setup, the effective distance between the two gratings becomes negative (see Figure 5.5(b)) and hence the introduced GDD takes positive values (see also Section 5.2.4). The amount of higher order dispersion introduced is, however, precisely the same as an equivalent grating compressor. The usual stretching ratio is on the order of $10^3 - 10^5$.

In the second stage the pulses are amplified. The achievable pulse energies are approximately by a factor, which is equivalent to the stretching factor, higher compared to the maximum pulse energies achievable with compressed pulses. For Ti:Sapphire the high saturation fluence, however, stems from a rather small stimulated emission cross-section ($\sigma_e(800\text{nm}) \approx 4 \cdot 10^{-19}$W/cm^2). The gain from a single pass through the gain crystal is consequently small. This

is compensated by increasing the interaction length with the gain medium by passing the seed pulses multiple times through the amplifier crystal. The upper state lifetime of the gain crystal thus has to be long compared to the amplification process. For Ti:Sapphire the upper-state lifetime is 3.2 µs and therefore sufficient for such an amplification scheme.

The optical setup of the amplifier stage can either be a so-called regenerative amplifier or a multipass amplifier (a third approach is OPCPAs, which, however, falls out of the range of this introduction). While regenerative amplifiers (see Figure 5.5(c) top) consist of an optical cavity that the seed pulse is introduced into and coupled out by means of a Pockels cell and thin film polarizers, a multipass amplifier (see Figure 5.5(c) bottom) propagates the pulses through the crystal by reflection of a series of mirrors, meaning that the pulse usually passes the crystal under slightly differing angles ,i.e., no cavity effect is established.

The advantage of a regenerative amplifier are the good spatial beam profile owing to the pulse propagation inside a cavity. To avoid the excessive build up of amplified spontaneous emission, the gain inside a regenerative amplifier has to be kept, however, small. This necessitates a higher number of passes and therefore a higher amount of dispersion accumulated during the amplification process.

The beam profile of a multipass amplifier is usually less clean due to the imperfect spatial overlap with the pump beam. For the same reason the conversion efficiencies are usually lower as well. However, the gain can be larger and less passes are necessary, leading to a smaller amount of accumulated dispersion. For power amplifiers, which only have an amplification factor between 20 and 100, multipass amplifiers are the common choice. For amplification on the order of 10^5 - 10^6 often a sequence of both regenerative amplification and multipass amplification stages is used.

In the last step of CPA, the pulses are re-compressed (see Figure 5.5(d)) by compensating the combined dispersion of the stretcher and of the dispersive material inside the amplifier. The angle and distance of the gratings in the grating compressor can therefore differ from the settings in the grating stretcher in order to optimize the final 2nd and 3rd order dispersion. By using gratings with different grating numbers in the stretcher and compressor, one can sometimes achieve compensation of even the 4th order dispersion [273].

Using CPA approaches, laser systems with terawatt or even petawatt peak powers and pulse durations in the femtosecond regime are nowadays available [274]. Such pulses can subsequently be used for laser driven electron or ion acceleration or as mentioned in Section 2.1.1 for the generation of very intense attosecond pulses [275, 276].

5.3 Fundamentals on Carrier Envelope Phase

As pointed out in Section 2.1.1, the stabilization of the carrier envelope phase (CEP) in ultrashort laser pulses is essential for the generation of isolated attosecond pulses. At the beginning of attosecond science, it was assumed that carrier envelope phase stability was important only in the application of few-cycle laser pulses, where the peak electric field inside the pulses depends strongly on the CEP. In Section 2.5.1 it was shown, however, that also the generation of IAPs from long driving pulses requires the stabilization of the CEP.

In this section, the fundamentals of CEP, its measurement and its stabilization will be introduced. Ultrashort pulses with a stabilized wave form can be used in a range of applications. Especially CEP-stable oscillators are particularly used for frequency comb spectroscopy. Considering the development of a CEP-stable amplifier, the main focus in this introduction will, however, lie on the stabilization schemes for amplifiers which are mainly used in the context of attosecond science and pump-probe spectroscopy.

5.3.1 Description in the time and frequency domain

Already in Sections 5.2.1 and 5.2.3 the carrier envelope phase was mentioned in terms of a carrier envelope offset frequency and as the zeroth order dispersion term in the Taylor expansion of the spectral phase.

Starting from equation 5.9, the spectral phase $\phi(\omega)$ can be divided into a constant phase ϕ_0 at the carrier frequency ω_0 and the residual frequency-dependent phase evolution ϕ':

$$\begin{aligned} E(t) &= e^{-i\omega_0 t} \cdot \frac{1}{2\pi} \int \left[a(\omega_0 + \omega') e^{i(\phi_0 + \phi'(\omega_0+\omega'))} \right] e^{-i\omega' t} d\omega' \\ &= e^{-i(\omega_0 t - \phi_0)} \cdot \int \left[a(\omega_0 + \omega') e^{i\phi'(\omega_0+\omega')} \right] e^{-i\omega' t} d\omega' \ . \end{aligned} \tag{5.17}$$

After performing the Fourier transform, this yields the temporal evolution of the field as

$$E(t) = f'(t) \cdot e^{-i(\omega_0 t - \phi_0)} \ . \tag{5.18}$$

Assuming a flat spectral phase $\phi'(\omega_0 + \omega')$ and a spectrum that is symmetric around the carrier frequency, the temporal envelope $f'(t)$ will also be real and symmetric and the temporal evolution of the laser pulse can simply be written as

$$E(t) = A(t) cos(\omega_0 t + \phi_0) \ . \tag{5.19}$$

The term ϕ_0 thus describes a phase shift of the carrier wave relative to the electric field envelope with respect to time and space; $\phi_0 = 0$ hence defines a cosine shaped pulse.

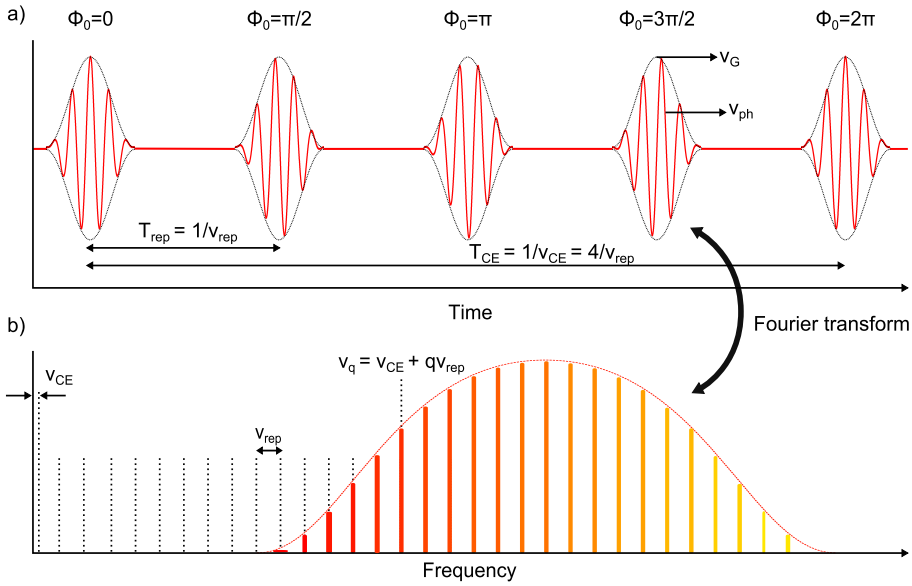

Figure 5.6: CEP phase in the time (a) and frequency (b) domain. In the time domain the relevant values are the oscillator round-trip time T_{rep} and the CEP period $T_{CE} = 1/\nu_{CE}$, which describes the time period between two pulses with identical CEP. In the specific illustrated case T_{rep} and T_{CE} are related by a factor of four, which results in a reproduction of the original pulse shape every fourth pulse; also signified by a CEP slip of $\pi/2$. In the frequency domain the complete frequency comb is defined by the CEO-frequency $\nu_{CE} = 1/T_{CE}$, the repetition rate $\nu_{rep} = 1/T_{rep}$, and in this case $\nu_{CE} = \nu_{rep}/4$. Both interpretations are equivalent and related via the Fourier transformation. Additionally, in the time domain image also the group and phase velocity are indicated.

The pulses emitted from a modelocked laser resonator in general are not identical, in the sense that their CEP is not the same from pulse to pulse. This is again due to the dispersive material inside the laser resonator. A detailed illustration of the following description can be found in Figure 5.6.
The group velocity v_G, defined by

$$v_G = \frac{dk(\omega)}{d\omega} = \frac{c}{n(\omega_0)} + \frac{c \cdot k(\omega_0)}{n^2(\omega_0)} \frac{dk}{dn} \ , \tag{5.20}$$

is the velocity of the pulse envelope, while the phase velocity v_{ph}, defined by

$$v_{ph} = \frac{\omega_0}{k(\omega_0)} = \frac{c}{n(\omega_0)} \ , \tag{5.21}$$

describes the velocity of the carrier frequency below the envelope (see Figure 5.6). Both are only equal in the absence of dispersion. Otherwise dispersion will give rise to a difference between the phase and the group velocity which translates into a phase shift between the peak of the envelope and the carrier wave. This phase shift then changes from pulse to pulse and will be referred to as the

carrier envelope phase slip $\Delta\phi_{CE}$. Further, this phase slip in the frequency domain is described by the carrier envelope offset (CEO) frequency ν_{CE} (introduced in Section 5.2.1 and equation 5.3). The phase difference between consecutive pulses can thus be expressed as

$$\Delta\phi_{CE} = 2\pi\frac{\nu_{CE}}{\nu_{rep}} \ . \tag{5.22}$$

For an illustration of ν_{CE} and ν_{rep} see Figure 5.1. If the CEO-frequency ν_{CE} now is an integer multiple of the repetition rate ν_{rep}

$$q \cdot \nu_{CE} = \nu_{rep} \ , \tag{5.23}$$

then every n-th pulse will have the same CEP. Accordingly if $\nu_{CE} = 0$, every pulse emitted from the oscillator will be exactly the same.

Assuming typical repetition rates of laser oscillators in the tens of Megahertz, both ν_{CE} and ν_{rep} will be in the microwave frequency range and are easily accessible using conventional electronics. If both frequencies can be stabilized against an external precision reference such as an atomic clock, then the precise spectral position of every single frequency component of the laser pulse is known. With these so-called frequency-combs, unknown optical frequencies can be measured with unprecedented resolution [277] (Nobel price 2005).

If, however, one only stabilizes the CEO-frequency with respect to the repetition rate of the laser resonator, only the CEP slip is fixed, however, not the repetition rate. Still, this is sufficient to control the electric field of the laser pulse on sub-femtosecond timescales (see also Section 2.3). If the CEO-frequency is an integer fraction $1/n$ of the repetition rate then every n-th pulse will have precisely the same field evolution.

5.3.2 Measurement of the relative CEP using f-2f interferometers

So far it is impossible to measure the absolute CEP with a simple optical setup. Some approaches that are able to extract the absolute phase of a laser pulse are shown in Section 2.2. Hence, when one speaks of CEP measurements, most often the measurement of the relative CEP phase slip in form of the CEO-frequency ν_{CE} is meant. Since the laser spectrum, does not reach all the way to zero frequency the CEO-frequency cannot be measured directly and needs to be extracted by other means.

The established tool do this is the f-2f interferometer [278–280], which exists in two different implementations that measure the CEP phase either in the frequency domain or in the time domain. The general working principle for both setups is, however, the same and will therefore be summarized first. A schematic illustration can also be found in Figure 5.7.

The f-2f principle relies on an octave spanning frequency comb, i.e., a spectrum containing both frequencies ν_q and $\nu_{2q} \sim 2{\cdot}\nu_q$. If the low frequency mode ν_q is doubled by second harmonic generation (SHG), applying equation 5.3 results in the frequency

$$2 \cdot \nu_q = 2 \cdot (\nu_{CE} + q \cdot \nu_{rep}) = 2 \cdot \nu_{CE} + 2 \cdot q \cdot \nu_{rep} \ . \tag{5.24}$$

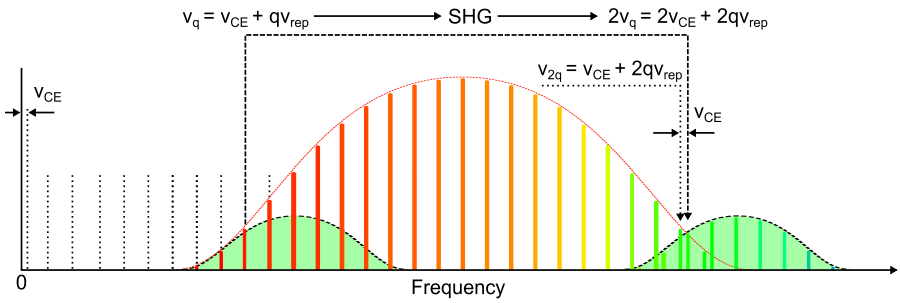

Figure 5.7: Graphical illustration of the f-2f interferometer principle. Longitudinal modes from the low frequency range of the laser spectrum are frequency doubled. The beat frequency between those doubled frequencies and the closest frequencies of the high frequency part of the spectrum is equal to the CEO-frequency. An octave spanning spectrum is thus a strict requirement.

This frequency can now be compared with the mode ν_{2q}

$$\nu_{2q} = \nu_{CE} + 2 \cdot q \cdot \nu_{rep} \ . \tag{5.25}$$

If these two frequencies are brought to interfere inside a spectrometer, they will create an interference signal with the beat frequency ν_{CE}, as can be seen from

$$2 \cdot \nu_q - \nu_{2q} = 2 \cdot \nu_{CE} + 2 \cdot q \cdot \nu_{rep} - \nu_{CE} + 2 \cdot q \cdot \nu_{rep} = \nu_{CE} \ . \tag{5.26}$$

It should be noted that the measured beat signal in an f-2f interferometer arises from a large number of frequency modes and not as might be insinuated from the equations only by a single one. Hence the signal-to-noise ratio is greatly enhanced.

Oscillators and amplifiers have repetition rates that commonly differ by several orders of magnitude. With repetition rates in the MHz regime, the beat signal can be directly measured on a photodiode, i.e., in the time domain. If the stabilized pulses are further amplified they can, however, pick up additional phase deviations, usual at a much slower rate though. Due to the low repetition rates of amplifiers, time domain detection is not suitable, and detection in the frequency range has been developed [281–283]. Both principles are explained in detail below.

f-2f interferometer and time domain detection

Measuring the beat signal in the time domain is usually done for oscillators, owing to their high repetition rate. However, pulse energies directly from an oscillator are usually only on the order of a couple nanojoules. Further,the optical spectra of common femtosecond oscillators (although such oscillators exist [284]) are not octave spanning as required by the f-2f principle. The

output of the laser thus has to be spectrally broadened before it can be used in the f-2f interferometer.

This is usually achieved in photonic crystal fibers (PCFs), which are fibers that possess an array of air filled micro-channels at their center. These fibers can be designed such, that the GDD becomes zero at a specific central wavelength and the pulse can be propagated over extended distances while maintaining a high peak intensity due to the spatial and temporal confinement. During this propagation the pulse spectrum is broadened via self-phase modulation, with the resultant spectra easily spanning a full octave.

Most time-domain f-2f interferometers are built up in a Mach-Zehnder geometry (see Figure 6.1). The two parts of the spectrum are separated using a dichroic beamsplitter and propagate on different paths until they are recombined spatially and temporally to interfere. In the low frequency arm the frequency is subsequently doubled by SHG either in a beta-barium borate (BBO) or periodically poled lithium niobate (PPLN) crystals. The delay between the two arms is then adjusted such that both pulses overlap temporally and the relative intensity is controlled using $\lambda/2$-plates and a polarizing beamsplitter cube.

Before the detection on a photodiode, the spectrum is confined to the part where interference takes place using spectral filters. The photodiode then detects the temporal modulation of the incident light intensity. The modulation is composed of harmonic multiples of the pulse repetition rate and the CEO-frequency ν_{CE}, while the latter can be filtered using low-pass or band-pass filters. The frequency of the resultant sinusoidal signal can be stabilized either to an external radio-frequency standard or to a fraction 1/n of the oscillator repetition rate, which is picked up with a second photodiode. In this case the CEP slip is adjusted such that every n-th pulse is emitted with the same CEP. In order to stabilize the CEO-frequency to zero some additional modifications to the f-2f scheme are necessary as explained in reference [285].

Using difference frequency generation between two laser pulses that share the same CEP also yields phase stable pulses at the full repetition rate without using an f-2f interferometer [286, 287]. Section 5.4 will, however, concentrate on stabilization techniques that use the error signal of f-2f interferometers to actively stabilize the CEP of modelocked oscillators and/or subsequent amplifiers.

f-2f interferometer and frequency domain detection

For more energetic pulses at low repetition rates (tens of Hertz to several Kilohertz) as they are produced in laser amplifiers, detection in the frequency domain is necessary [281–283]. The octave spanning spectrum in this case is usually realized by white-light generation inside a thin Sapphire plate or a noble gas filled hollow core fiber. Contrary to the Mach-Zehnder setup for the time-domain detection, the frequency approach relies on a common-path interferometer, i.e., the low and high frequency pulses usually propagate collinearly instead of spatially separated.

Assuming that the spectral phase of the white light is flat, both the high

(2ν) and the low (ν) frequency pulse will start out with the same CEP ϕ_0. Due to their difference in frequency and the material dispersion in the beampath, they will, however, experience different group delays τ_d as they propagate. This leads to a phase shift of the blue component with respect to the red component equal to $\omega_{2\nu} \cdot \tau_d$.

After frequency doubling of the red spectrum part inside a BBO or other doubling crystal, the frequency doubled pulse will gain an additional phase difference of $\pi/2$ [282]. The two pulses with now the same frequency 2ν are brought to interfere inside a spectrometer with the pulses having a resulting phase difference

$$\begin{aligned} \Delta\phi &= 2\phi_\nu - \phi_{2\nu} \\ &= (2\phi_0 + \pi/2) - (\omega_{2\nu}\tau_d + \phi_0) \\ &= \omega_{2\nu}\tau_d + \phi_0 + \pi/2 \ . \end{aligned} \tag{5.27}$$

The recorded spectral interference pattern will therefore have the shape

$$I(\omega) \propto I(\omega_{2\nu}) + I(2\omega_\nu) + 2\sqrt{I(\omega_{2\nu}) \cdot I(2\omega_\nu)} \cdot cos(\omega_{2\nu}\tau_d + \phi_0 + \pi/2) \tag{5.28}$$

Due to the group-delay difference $\Delta t_{\nu-2\nu}$ between the two pulses, the recorded spectrum will show a strong modulation over the bandwidth, where the two wavelengths overlap. The modulation period on the wavelength scale around spectral overlap is given by $\Delta\lambda = \lambda/c\tau_d$. One can further see that the spectral position of the fringes depends on the CEP if the group delay difference τ_d is constant.

In the more realistic case that the incoming pulse is not transform limited, i.e., that the spectral phase is non-zero, the difference phase (equation 5.27) will have an additional unknown but frequency independent shift. Due to this shift it is impossible to extract the absolute phase ϕ_0, however, one can measure the relative phase slip between consecutive pulses. This information can then be used as an error signal to stabilize the CEP phase slip to zero, making sure that every pulse emitted from the amplifier will have the same, though unknown absolute CEP.

The bandwidth of phase noise that this type of f-2f interferometer can detect is usually limited by the read-out speed of the CCD detector inside the spectrometer. If the signal is not strong enough to be detected in a single pulse acquisition, it is often necessary to acquire over several laser shots, which then yields an averaged CEP value. If the phase noise during the acquisition of multiple pulses is, however, too high, the fringes will wash out. Such a system can therefore only be used for pre-stabilized systems with only slow temporal modulations of the CEP value.

Another problem is that with most spectrometers the measurement cannot be performed at the full repetition rate of the system. Higher frequency noise might therefore be hidden in the measurement. A recent development by Koke and coworkers [288] overcomes this limitation by using an analog detection scheme, which is able to perform CEP measurements at the full repetition rate

of a kHz amplifier system. They revealed that the phase noise if measured at the full repetition rate can be up to a factor 2 larger than measured in a digital system with slower read out rates.

5.4 Stabilization of the CEP in oscillators and amplifiers

5.4.1 Oscillator stabilization

As derived in equation 5.22, the CEP slip between consecutive pulses is defined by the ratio between the CEO-frequency and the repetition rate of the resonator. Therefore, stabilizing either both frequencies or the ratio of the two frequencies to a known value will produce a fixed and known pulse-to-pulse CEP slip. The beat signal, which is measured with an f-2f interferometer, can be used in a phase locked loop (PLL), whose output signal can be fed back to control a laser parameter that influences the CEO-frequency inside the laser resonator.

It is, however, important that the reference signal of the PLL is coherently related to the repetition rate of the oscillator to be stabilized. This can either be achieved using common external references both repetition rate as well as CEO-frequency are stabilized to. This approach is, however, more common for frequency comb applications, where also the repetition rate of the resonator has to be known and stable. In the case of pure CEP-stabilization, the reference signal can be the repetition rate itself, picked up by an additional photodiode. Hence only the ratio ν_{CE}/ν_{rep} is stabilized.

The presented stabilization techniques are given in the order of decreasing residual phase jitter, i.e., increasing CEP-stability.

Tilt mirror The first implementations of CEP-stabilization in modelocked Ti:Sapphire oscillators relied on piezo actuated tilt mirrors behind a prism sequence [279, 289]. Also the stabilization of the source oscillator for the amplifier setup presented in this work relies on this technique.

In order to achieve ultrashort laser pulses from a modelocked oscillator it is essential to compensate the dispersion accumulated inside the laser cavity. This can either be done using chirped mirrors or prism compressors. As described in Section 5.2.4, after the second prism of a prism compressor the spectrum is spatially dispersed over and incident on a folding mirror. If the prism compressor lies inside a laser cavity, this folding mirror usually is at the same time one of the end-mirrors. If this mirror is positioned perfectly perpendicular with respect to the incoming beam, it will not have any effect on the pulse. If the mirror is, however, tilted slightly it provides a linear phase change over the complete spectrum. A linear spectral phase describes the group delay (as described in Section 5.2.3, equation 5.12) [290] and controlling the mirror angle therefore gives access to the CEO-frequency ν_{CE}, which is defined by the difference between group and phase velocity of the circulating laser pulse.

Mounting the end-mirror in the Fourier-plane of the prism compressor on a piezoelectric transducer allows the realization of very high feedback frequencies ($\sim$ 10 kHz). The necessary angles for the CEP-stabilization are much smaller than the beam divergence and therefore do not lead to a misalignment of the cavity. An additional translation of the mirror along the propagation direction of the laser beam can additionally be used to stabilize the repetition rate of the oscillator.

It has been shown [291], however, that prism based oscillators are inherently more prone to translate intra-cavity intensity fluctuations into phase fluctuations than resonator designs that do not involve prism sequences [292]. This can result in a up to one order of magnitude higher phase noise in prism based resonators compared to prism-less oscillators. The responsible mechanism is a combination of non-linear beam steering inside the Ti:Sapphire crystal and the sensitivity of the prism sequence to the resulting beam pointing instability.

Pump power modulation For laser resonators that rely on chirped mirror dispersion control the tilting mirror approach is obsolete as it needs the spatially dispersed beam. Early on, however, it was shown empirically that the energy concentrated inside the laser cavity has a more or less linear effect on the CEP [293]. The proposed mechanisms that cause this behavior include phase shifts caused by Kerr effect induced dispersion changes (see also Section 5.2.1 and equation 5.5) [294] and non-linear Raman spectral shifts. In this way, small changes in the intra-cavity pulse energy are translated into large CEP changes. Consequently, controlling the pump-power of a laser resonator by placing an acousto-optic (AOM) or electro-optic modulator in the pump-path has been proven to be an efficient way of CEP control [292, 295].

From this analysis it is also clear that the most constant pulse energy inside the resonator will lead to the best CEP-stability, assuming other parameters to be stable. The external phase control via the pump power modulation therefore also acts as a stabilization of the emitted pulse energy. Resonators whose CEP is stabilized with this approach therefore often also show an improved energy stability of the generated pulse train [296].

The benefits of the stabilization by pump-power modulation are the already mentioned energy stabilization but especially also the achievable stabilization bandwidth, which is considerably higher than in the tilting mirror approach. Generally the feedback rate for this stabilization approach is only limited by the upper state lifetime of Ti:Sapphire crystals of 3.2 µs. Most of the de-phasing dynamics, however, happen on longer time-scales.

Acousto-optic frequency shifter One of the newest developments in the CEP-stabilization of laser resonators is a simple but extremely robust feed forward scheme. It nevertheless also relies on a self-referenced measurement of the CEO-frequency in an f-2f interferometer [297].

In this approach the emitted frequency comb of a modelocked femtosecond resonator is diffracted into a zero-order and first-order beam by the refractive index grating of an acousto-optic frequency shifter (AOFS). The frequency

modes of the zeroth order pass the AOFS undisturbed while the first order frequencies are shifted by the value of the frequency applied to the AOFS.

Hence a feed-forward stabilization scheme becomes possible. The value of the CEO-frequency is measured in the zeroth order using a conventional f-2f interferometer. This frequency is then directly applied to the AOFS which shifts the frequency modes in the first order beam by an equivalent negative amount. The CEO-frequency in the first order beam thus becomes zero, meaning that every single pulse in this beam shows the same CEP. By adjusting the frequency which is applied to the AOFS it is also possible to generate CEP slips of arbitrary value.

There are a number of strong arguments that make this stabilization scheme very attractive. The efficiency with which the index grating diffracts energy into the first order, the stabilized beam, is on the order of 60 - 70%. The amount of energy that is used to measure the CEO-frequency is thus the same as in the other presented stabilization techniques.

The major difference with respect to the before mentioned schemes is the implementation of the stabilization outside the laser cavity. The laser oscillator is hence free-running and does not experience any disturbances introduced by the usual feedback mechanisms. The new scheme further does not need any complicated locking electronics and can work at much fast update rates then the common approaches.

The achieved residual phase jitter has been shown to be only limited by detection noise for a bandwidth from 30 Hz to 2.5 MHz, including the otherwise critical regions for acoustic noise between 100 - 1000 Hz and the region around 100 kHz, which usually shows influences of the multi-mode pump lasers [297]. It is therefore significantly more stable than other so far demonstrated techniques.

5.4.2 Amplifier stabilization

One common approach to compensate the slow phase drifts accumulated in amplifiers is to add the slow feedback signal to the fast signal of the oscillator stabilization and thus pre-compensate these slow fluctuations already inside the oscillator cavity [55]. This, however, forces the oscillator stabilization loop to handle much larger phase excursions, which subsequently can influence the stability of the oscillator CEP locking. There have therefore been a number of other approaches developed that aim at compensating the amplifier phase drifts inside the amplifier independently of the oscillator loop. These are addressed in the following paragraphs.

Glass wedges The most straightforward way to actively stabilize the CEP of amplifiers, but also of oscillators, is the controlled introduction of additional dispersive material into the beam path in the form of glass wedges. This can either happen inside a laser cavity [298] or outside the laser cavity. In the latter case glass wedges are either used to actively stabilize the pulse-to-pulse phase slip or, more commonly, to fine-tune and scan the absolute CEP [66, 299] in an experiment. The pathlength in any given material that changes the CEP

by 2π is related to the difference in the group and phase velocity of the laser pulse and can be written as

$$L_{2\pi} = \frac{2\pi}{\omega_0} \cdot \frac{1}{[v_G(\omega_0)]^{-1} - [v_{ph}(\omega_0)]^{-1}} = \left(\left. \frac{dn}{d\lambda} \right|_{\lambda_0} \right)^{-1} . \tag{5.29}$$

Typical values of $L_{2\pi}$ for a common range of optical materials can be found in reference [283].

The use in amplifiers to compensate slow phase drifts is more common than the use in oscillators nowadays. Especially for very broadband spectra, however, glass wedges can introduce additional dispersion which is hard to compensate at a later stage. Other techniques have therefore been developed which overcome this problem.

Modulation of grating separation Most of the first chirped pulse amplifiers were based on stretching the pulses prior to amplification with glass blocks and subsequent compression in prism sequences. With the scaling to higher final pulse energies, the use of grating compressors and stretchers became more common. Some initial studies soon showed that, contrary to expectations, also these amplifiers could allow CEP-stable operation [250, 300, 301].

As it turns out the CEP slip can be controlled by adjusting the grating separation in either the grating stretcher or compressor. In reference [302] it was first shown that the CEP slip related to a change in the grating distance can be written as

$$\Delta\phi_{CE} = 4\pi \cdot \frac{\Delta G}{d} \cdot tan(\gamma - \theta(\omega_0)) , \tag{5.30}$$

where ΔG is the change in grating separation, d is the grating constant and γ and $\theta(\omega_0)$ are the incidence angle and the diffraction angle of the central wavelength, respectively. Assuming that γ is close to the Littrow-angle of the grating, the equation can further be simplified to

$$\Delta\phi_{CE} \approx 4\pi \cdot \frac{\Delta G}{d} \cdot tan(\gamma) . \tag{5.31}$$

A change in the grating separation equal to half the groove distance of the grating (0.4 µm for a 1200 line grating) therefore causes a phase change of $\sim 2\pi$, assuming a incidence angle of $\sim 45°$. Separation changes on this order are easily achieved with piezo electric transducers. For the same reason interferometric stability of the grating mounts both in the compressor and stretcher is a mandatory prerequisite to achieve CEP-stable operation in grating based CPA systems. Such a setup also makes possible the easy scanning and fine adjustment of CEP values by choosing a different stabilization point without the need for additional glass wedges or similar.

The implementation of this approach has been successfully demonstrated in a number of setups, modulating either the grating distance in the stretcher

[303, 304] or the compressor [102]. The technique is also used in the setup described in this work for stabilization of both the first stage kHz amplifier as well as of the TW 50-Hz amplifier. Depending on the size and weight of the optic to be moved, the bandwidth of the noise frequencies that can be compensated is limited. For the slow phase drifts inside an amplifier, it is, however, mostly sufficient. A good overview of grating based CEP-stable amplifiers can be found in reference [305].

AOPDFs and other fast options The last feedback technique that is presented here is based on an acousto-optic programmable dispersive filter (AOPDFs) and therefore is very similar to both the dispersion control technique discussed in Section 5.2.4 and the phase shifter approach for the oscillator stabilization described in the Section 5.4.1.

As mentioned earlier the AOPDF induces a longitudinal interaction between the optical and acoustic beams [270], which can efficiently control the spectral phase as well as the spectral amplitude of the incident pulse. If proper phase matching between the optical and acoustic wave is established, the following CEP conversion law applies:

$$\phi_{out} + \phi_{in} - \phi_{acc} = \pi/2 \ . \tag{5.32}$$

In this case ϕ_{in} is the CEP of the incoming beam, while ϕ_{out} is the phase of the diffracted beam and ϕ_{acc} is the phase of the applied acoustic wave. The CEP of the outgoing beam can therefore be controlled by adjusting the phase of the acoustic wave accordingly. This approach is applied in a closed loop [253, 306], which ensures that the phase slip between consecutive pulses is kept at zero.

The advantage is that there are no moving parts involved that could introduce mechanical vibration. Also the update rate with which arbitrary phases can be reached is almost instantaneous. The low diffraction efficiency of $\sim$ 30 %, however, make the position before the actual amplifier necessary. Also, temporal jitter between the acoustic wave and the incident laser pulse can introduce additional phase jitter, which, however, is only on the order of $\pi/200$ [306].

One of the newest developments in the field of fast non-disturbing CEP control was recently demonstrated [307, 308]. They used the linear electro-optical effect to control the CEP of amplified laser pulses. The system consists of a Pockels cell with the voltage applied transversally to the beam propagation direction. Note that in the usual pulse picker Pockels cell, the voltage is applied longitudinally. The advantage of such a setup are similar to those of the acousto-optic devices, however, the costs can be considerably lower, while the implementation is straight forward.

6 Carrier envelope phase stabilized terawatt amplifier

6.1 Description of the phase-stable source system

The task of the project described in this chapter was to build an amplifier, which supplies femtosecond pulses with peak powers in the TW regime, while maintaining a stable CEP from pulse to pulse. For supplying the seed pulses, the existing commercial laser system[1] was to be used as a first amplification stage. This commercial system has been purchased as an already phase-stabilized laser[2] system in 2007. The challenge of the development was to maintain this CEP stability also during amplification up to the TW level in the new power amplifier.

In the following sections, first the source system made up of the phase-stable oscillator and kHz amplifier will be described. The subsequent section will focus first on the design and then technical implementation of the new amplifier and the achieved laser parameters. The implementation and results concerning specifically the CEP control will be discussed separately in the last sections.

6.1.1 The seed oscillator

The laser oscillator, which supplies the initial femtosecond pulses, is based on a Ti:Sapphire crystal as the gain medium. Modelocking is achieved via Kerr-lensing inside the gain medium and a soft aperture formed by the pump size inside the Ti:Sapphire crystal. The dispersion is compensated with an intra-cavity prism compressor folded at the symmetry axis by one of the end mirrors.

The system is pumped with 5.5 W of 532 nm light from a diode-pumped continuous wave frequency-doubled Nd:YVO laser[3]. This laser has established its position as the most commonly used pump-laser for CEP-stable oscillators due to its extremely low rms-noise of <0.02 % (10 Hz - 1 GHz) [309].

[1] Oscillator: KMLabs Griffin; kHz-Amplifier: KMLabs Dragon

[2] Oscillator stabilization: Menlo XPS800 + Menlo PLL electronics; kHz-Amplifier stabilization: Menlo APS800

[3] Coherent Verdi V6

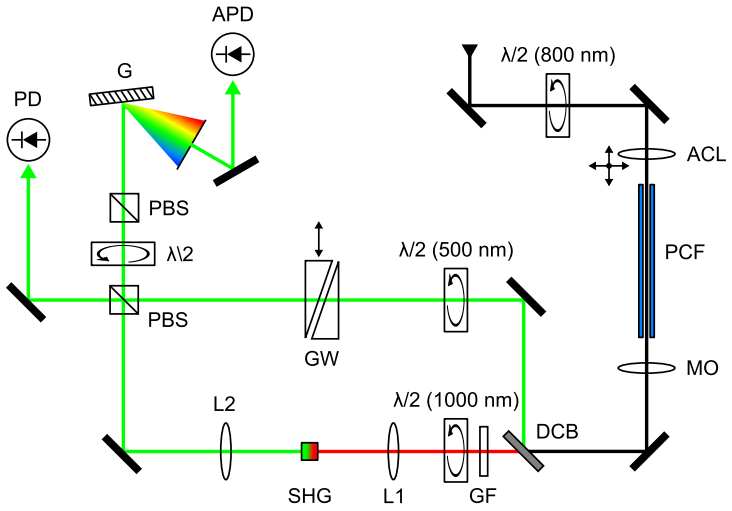

Figure 6.1: Schematic illustration of the f-2f interferometer used in this work. λ/2: Waveplates at the given wavelength; ACL: achromatic lens; PCF: photonic crystal fiber with zero dispersion length of 765 nm; MO: microscope objective; DCB: dichroic beamsplitter, high reflectivity 532 nm, high transmission (HT) 1064 nm; GF: Glass-filter, HT >715 nm; SHG: potassium niobate crystal for frequency doubling; GW: glass wedges for delay adjustment; PBS: polarizing beam splitter; G: 2100 line/mm grating; PD: photodiode for reference frequency; APD: avalanche photodiode for beat signal detection. For a more detailed explanation, please refer to Section 5.3.2.

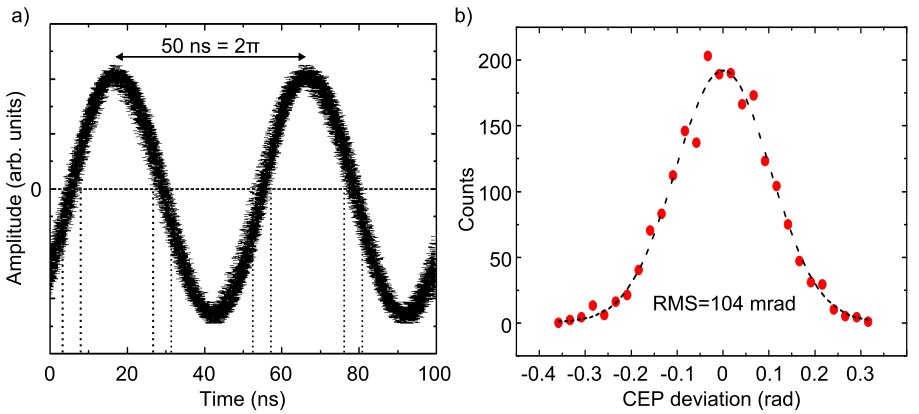

Figure 6.2: Measurement of the oscillator CEP stability. (a) shows 2000 traces of the f-2f beat signal recorded over a time interval of 40 ms. Since the beat signal is stabilized to a quarter of the repetition rate (80 MHz), the period of the signal is 50 ns. To estimate the residual phase jitter a histogram of the phase values at the zero transitions of this trace was taken. (b) The result is plotted as a function of phase. The resultant rms value of the residual phase jitter is 104 ± 2 mrad.

Pulses with a bandwidth of $\sim$ 60 nm centered at 785 nm are emitted at a repetition rate of 80 MHz. The Fourier limited pulse duration of these pulses is approximately 15 fs. To achieve these values, the insertion of both prisms can be changed, which allows precise control of both the central wavelength and bandwidth of the laser spectrum. In every day operation the average power of the emitted pulse train lies between 550 mW and 600 mW. The energy per pulse therefore is approximately 7 nJ. Since the pulses are intended for amplification they are not re-compressed after the output coupler and therefore can have much longer pulse durations than the transform limited pulse durations. This will be compensated, however, at a later stage in the amplifier.

For achieving phase-stability of the oscillator, approximately 30 % of the emitted pulse energy is split off after the output coupler, compressed with several bounces on a chirped mirror pair and sent into an f-2f interferometer with time detection. The working principle of such an f-2f has been discussed in Section 5.3.2. The f-2f interferometer and its parts used for the CEO measurement of the oscillator are illustrated in detail in Figure 6.1.

A digital phase counter then compares the beat signal of the CEO frequency to the repetition rate of the oscillator frequency divided by a factor of four. A signal, which is proportional to the phase slip, is passed on to an electronic PID[4] controller, which closes the feedback loop by driving a piezo-actuated tilt-mirror at the end of the prism-sequence (for details see Section 5.4.1).

The residual phase-jitter was measured directly with an oscilloscope by recording the CEO phase jitter with respect to the repetition rate of the oscillator itself. 2000 traces of the CEO signal were recorded over a time interval of 40 ms with a bandwidth of 8 MHz (see Figure 6.2). The temporal distribution of the phase jitter at the zero crossing was used to estimate the CEP jitter of 104 $\pm$ 2 mrad. Taking into account that this jitter was recorded over a very short time interval (limited by the internal memory of the oscilloscope), the rms value for longer acquisition times might well be higher. The high phase noise is an inherent problem of prism based oscillators as is described in Section 5.4.1 and reference [292].

Once phase-stability is achieved, the CEP can be locked over hours, only disturbed with intervals of higher noise on the error signal. The pulse energy which bypasses the f-2f interferometer and is subsequently amplified is 4 - 5 nJ. Amplification of these pulses in the first amplification stage is explained in the following section.

6.1.2 The kHz-amplifier

The amplification of the oscillator pulses is performed with the CPA technique, explained in Section 5.2.5. For this the duration of the pulses is increased to approximately 200 ps in a grating based stretcher. The stretch factor and therefore the reduction in peak power is consequently more than four orders of magnitude. The stretcher consists of a single 1200 line/mm grating and is set up in a folded 4-f geometry. Compared to other stretcher designs such as the

[4] proportional-integral-derivative

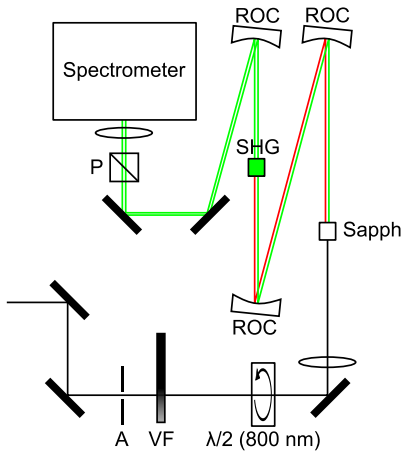

Figure 6.3: Schematic illustration of the f-2f interferometer used for measurement of the CEP slip of the amplified pulses. A: aperture; VF: variable neutral density filter; λ/2: 800nm waveplate; Sapph: 2 mm Sapphire plate for white light generation; ROC: concave silver mirrors, f = 10 cm; SHG: 1mm BBO crystal for frequency doubling at 1064 nm; P: polarizer. The dispersion could be controlled by inserting additional material after the Sapphire plate. In practice the setup was run without additional material in the beam path.

Öffner-geometry [310], this stretcher setup is comparatively compact (ca. 20 cm x 40 cm) and the necessary optics are relatively small. This is beneficial for the phase-stable operation of the amplifier, as the setup is less prone to pick up mechanical vibrations.

Subsequently the beam size is adjusted in a telescope and propagated to the pulse-picker. The pulse-picker decreases the repetition rate of the incoming pulse train to the chosen repetition rate of the amplifier. The amplifier is designed to support repetition rates between 1-4 kHz. The trigger and timing of the Pockels cell signal as well as all other relevant timing information are derived from digital timing cards, which use the oscillator repetition rate as a master clock. During the division of the repetition rate to the amplifier repetition rate it is ensured, that only pulses with identical CEP are picked and further amplified.

After passing through the stretching and pulse picking optics the energy of the pulses is reduced to approximately 2 nJ. These pulses are then amplified in a single stage multipass amplifier[5] to an output energy of 3.5 - 4 mJ. To achieve such a high final energy, the pulses are propagated 13 times through the amplifier crystal. To prevent thermal lensing and ensure a good spatial profile of the amplified beam, the amplifier crystal[6] is cryogenically cooled to temperatures around 70 K.

The crystal is optically pumped using a diode-pumped Nd:YLF Q-switched

[5]The gain factor thus lies on the order of $1.5 - 1.9 \cdot 10^6$ and an energy conversion efficiency of 15 %. This is close to the limit of what is achievable in a single stage multipass amplifier.

[6]Ti:Sapphire 6 mm Brewster cut

laser[7], which emits pulses at 527 nm with a duration of $\sim$ 200 ns. The average output power is 75 - 80 W and the pulse energy depending on the repetition rate is approximately 25 mJ. For the work presented in this chapter the amplifier was run at a pulse repetition rate of 3 kHz, which allowed a pulse energy after amplification of 3.8 mJ.

After the last pass through the amplifier crystal, the beam is coupled out with a mirror, propagated through a beam expanding telescope before finally reaching the grating compressor. The compressor consists of two gold coated gratings with 1200 lines/mm on a copper substrate for good heat conduction. The efficiency of the grating compressor is 66 % when the gratings are clean. The pulse energy that is available for experiments therefore is 2.5 mJ.

Due to gain narrowing, the spectral bandwidth after amplification is reduced to 30 nm at full width half maximum (FWHM). This results in a transform limited pulse duration of 29 fs. The pulse duration after the compressor was $\sim$ 31 fs, measured with a spectral phase interferometry for direct field reconstruction (SPIDER) setup. This setup was built up during this thesis work. A summary of the properties of the dragon amplifier which are relevant to the design of subsequent power amplifier is given in Table 6.1.

Table 6.1: Relevant properties for the subsequent amplification of the Dragon pulses

Parameter	Value
repetition rate	1 - 4 kHz (currently 3 kHz)
pulse energy after amplifier	3.5 mJ
stretched pulse duration	$\sim$ 200 ps
pulse duration after compression	31 fs
spectral bandwidth	30 nm
beam diameter after amplifier	$\sim$ 2 mm
B-integral	$3 \cdot 10^{-3}$
residual CEP error (rms)	266 - 500 mrad

Phase stabilization of the kHz-amplifier was achieved by measuring the slow drifts with a second f-2f interferometer based on frequency detection (see Section 5.3.2). The optical setup is illustrated in Figure 6.3. To run the f-2f interferometer, the leak of the first steering mirror after the amplifier output was used. The measured phase slip between consecutive pulses is used to supply a PID feedback control[8]. The control software originally supplied a -10 - 10 V control signal via a digital-to-analog converter (DAC) and was then reshaped in a small electronic circuit to be shifted to a center voltage of 5 V with a

[7] Photonics Industries DM60

[8] Originally the commercial setup Menlo APS800 in combination with Menlo software was used. The optical setup was rebuilt to allow an easier alignment. At a later point also the control software was replaced by an own development. This is described in more detail in Section 6.3.3

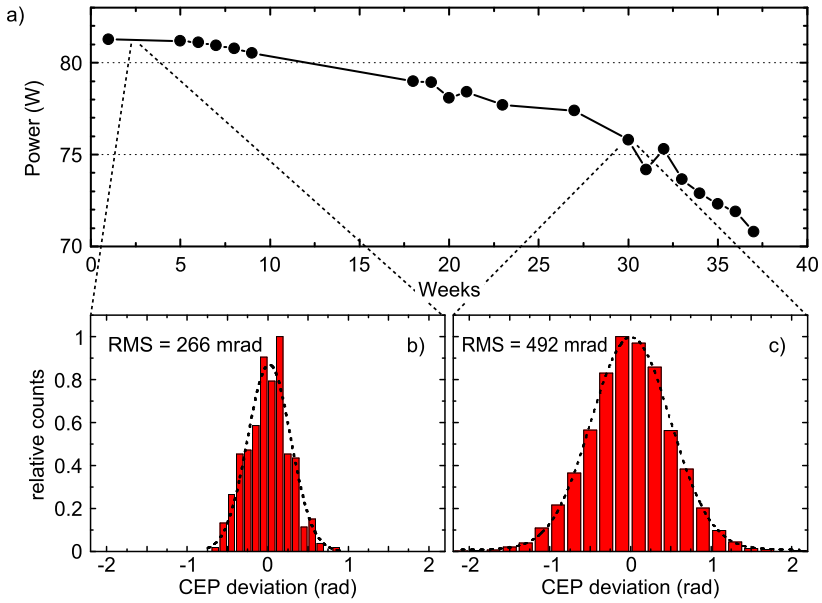

Figure 6.4: Performance of the pump-laser and its possible relation to the CEP stability of the system. (a) shows the pump power development over a course of 37 weeks after the last servicing. (b) shows a measurement of the residual phase jitter at the beginning of this period revealing an rms value of 266 mrad. In (c) the same measurement was performed approximately 30 weeks after installation of the pump-laser, showing a significantly larger rms value of the residual phase jitter.

controllable modulation from 0 V to +10 V. This signal was then used to drive a piezo controller with an amplification factor of 10 to control the grating separation with a piezo-electric transducer. For details of the stabilization mechanism, the reader is referred to Section 5.4.2.

In order to increase the stability of the amplifier, several special measures were taken in its constructions. This includes high stability mounts and posts for all optics and especially the grating stretcher and compressor. To eliminate vibration from the cryo-head, the crystal and vacuum chamber are mechanically decoupled from the cold head using flexible copper leaflets and edge-welded bellows. Additionally, the vacuum chamber is supported by vibration damping material on the breadboard, while the cold head is held by an aluminum gallows construction connected to the floor of the laboratory. To prevent coupling of vibrations into the floor and back to the table, the hollow aluminum post is filled with sand for additional damping. All other vibration prone equipment is decoupled from the optical table using thick sorbothane sheets.

The relative CEP of the amplifier pulses can be stabilized to an rms residual phase jitter of ~ 270 mrad. One problem which was encountered multiple times in the course of this thesis work was a slow degradation of the output power of the amplifier pump-laser as depicted in Figure 6.4 (a). In several cases, it

was observed that this power drop was accompanied with an instability in the spatial mode of the pump beam, which also translated into instabilities of the spatial profile of the amplified pulse. If the slow pump power degradation was also accompanied by a change of the pulse-to-pulse energy was not measured at the time. Nevertheless, this behavior could hint at a correlation between the general operating condition of the pump-laser and an observed degradation in the CEP-stability measured after the kHz-amplifier (shown in Figures 6.4 (b+c)).

Even though the difference in the two exemplary CEP measurements presented in Figure 6.4 could be related to a number of different effects, including CEP-stability of the seed oscillator and / or general amplifier performance related to the quality of alignment, the general degradation of CEP-performance has been persistent over multiple independent measurements. This rules out a possible influence of the amplifier alignment which has generally been changed between different measurements, while the CEP-stability of the oscillator was also not observed to be slowly changing. Further, the two presented CEP-measurements show that the noise distribution has changed from a slightly lopsided distribution (b) to an almost perfect Gaussian distribution in (c). This can further indicate that the CEP measurement in the second case is limited by shot noise generated in the white-light generation process, which consequently could be caused by instability of the amplified pulse energy, or instabilities in beam profile of the amplified pulses. While this behavior could be attributed to the performance of the pump-laser, a definitive conclusion can only be drawn after further systematic measurements.

6.2 Design of the CEP stable terawatt amplifier

The ambition for the development of the power amplifier was to achieve a pulse energy of 80 mJ at repetition rates of 25 - 50 Hz after the amplifier while maintaining a pulse duration of around 30 fs. One of the main challenges was to achieve phase-stability of the amplified pulses, even at these high energies and low repetition rates.

Based on the pulse properties after the Dragon amplifier, which are summarized in Table 6.1, the necessary setup to achieve these objectives was designed.

6.2.1 Design of the power amplifier

In the first design phase, the necessary parameters of the amplifier were modeled using the approach of LeBlanc and coworkers [311], which calculates the amplification process including the effects of gain narrowing and shifting. The model itself is based on the Frantz-Nodvik description of laser amplification [312], which makes two assumptions. First, the laser pulse duration is long enough such that the laser rate equations can be applied [260] and second that the upper state life-time is long compared to the duration of the pulses to be amplified. The relaxation of the laser-state during the amplification process can then be neglected. The output fluence (units are Joules per square

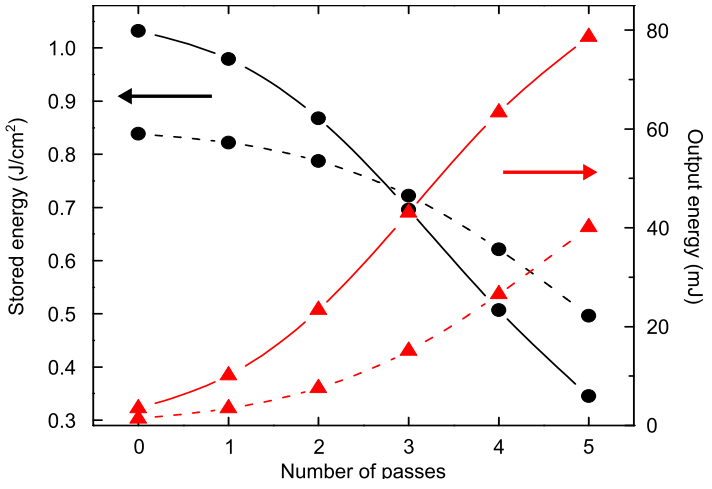

Figure 6.5: Calculated energy dependence during the amplification process. Plotted are the energy evolution of the amplified pulse (red triangles) as well as the stored energy in the amplifier medium (black circles) after each pass. The solid lines depict the situation with perfect seed laser parameters (E_{pump}=300 mJ, E_{in}=3.5 mJ, bandwidth: ∼ 30 nm). Dashed lines show the result for realistic input values (E_{pump}=260 mJ, E_{seed}=1.4 mJ, bandwidth: ∼ 33 nm) of the pump-laser and the seed pulses, while assuming an unchanged amplifier configuration. The reason for the change in input values is explained in the text.

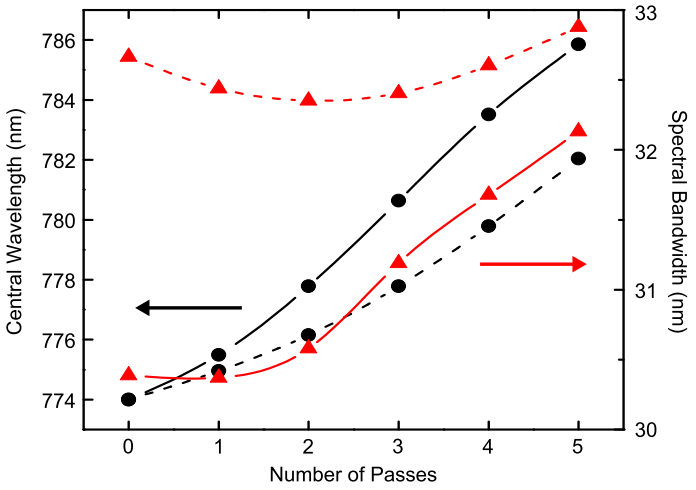

Figure 6.6: Evolution of the central wavelength (black circles) and bandwidth (red triangles) of the amplified pulse for each pass through the amplifier medium. Solid lines show the results for the initial design parameters (E_{pump}=300 mJ, E_{seed}=3.5 mJ, bandwidth: ∼ 30 nm). The results for the realistic seed pulse parameters (E_{pump}=260 mJ, E_{seed}=1.4 mJ, bandwidth: ∼ 33 nm), when amplified in the same amplifier configuration, are plotted as dashed lines.

centimeter) after pass n trough the gain medium can thus be described by

$$J_{out,n} = J_{sat}\left[1 + G_n(e^{J_{in,n}/J_{sat}} - 1)\right] \qquad \text{(Frantz – Nodvik equation).} \quad (6.1)$$

Here $J_{sat} = (h\nu)/(\sigma_e)$ is the saturation fluence. $J_{in,n}$ is the input fluence, which for successive amplification steps is equal to the output fluence of the previous pass multiplied by a loss factor. The small signal gain G is given by

$$G = e^{J_s/J_{sat}} \ , \quad (6.2)$$

where J_s is the energy which is stored in the gain crystal. J_s depends on the amount of absorbed energy from the pump-laser and the quantum defect described by the ratio λ_p/λ_s between the pump wavelength and seed wavelength. Both J_{sat} and therefore also the small signal gain G are dependent on the wavelength via the emission cross-section $\sigma_e(\lambda)$.

Assuming a strongly chirped pulse, instant frequency and time of the laser pulse can be related by $\omega(t) = \omega_0 + Kt$, with K being the chirp coefficient measured in 1/fs. This fact finds especially implementation in the calculation of the gain shifting, which is caused by a depletion of the instantaneous gain by the preceding frequencies in a chirped pulse. Following frequencies consequently will see a reduced gain, resulting in a net shift of the central frequencies towards frequencies that arrive earlier in the temporal pulse profile.

The results of the initial calculations are shown in Figure 6.5. Starting from experience values, a conversion efficiency of 25 - 30 % from pump energy to amplified pulse energy was assumed, which leads to a choice of the pump

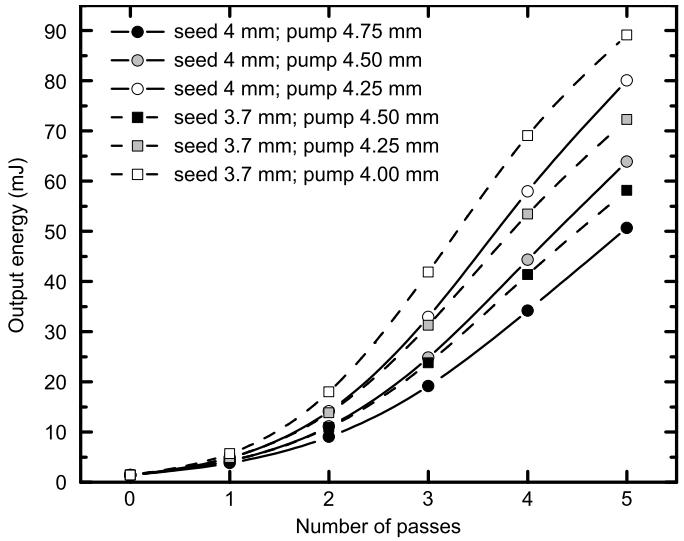

Figure 6.7: Evolution of the output pulse energy for different amplifier configurations using realistic pump and seed energies of 260 mJ and 1.4 mJ, respectively. For smaller beam diameters of both pump and seed the amplifier start to reach saturation levels.

energy of 300 mJ. The beam size of the pump beam was chosen to 5 mm such that the fluence on each face of the crystal would not exceed 1 J/cm^2, which is the damage threshold of the crystal anti-reflection coating including a safety factor. A slightly smaller beam size of 4 mm for the seed beam size ensures good overlap with the pump beam even at slightly differing angles between pump and seed. After five passes in this configuration, the seed beam is amplified to a final energy of 78 mJ. The stored energy is consequently depleted as the seed pulse gains energy, which is nicely visible in Figure 6.5.

In Figure 6.6, the calculated spectral evolution of the pulse during the amplification process is plotted. It shows that the carrier wavelength of the laser pulses is shifted by 10 nm to longer wavelength while the spectral bandwidth will increase by approximately 2 nm.

With the installation of the laser system it became clear that the input beam needed spatial cleaning, which reduced the input energy from 3.5 mJ to 1.4 mJ while the input spectral bandwidth had changed slightly from 30 nm to 33 nm. Additionally, the pump-lasers were not able to maintain the initial pump energy of 300 mJ; the more realistic pump energy at this point is 260 mJ. The result of these changes, when maintaining the initial amplifier configuration, are as well plotted in Figures 6.5 and 6.6. Using the new input parameters would result in a final pulse energy reduction of ~ 50 %.

This loss can be compensated by adjusting the beam sizes of both pump beam and seed beam inside the gain crystal. The results of a systematic study are shown in Figure 6.7. By reducing the pump size, the original output energy can be recovered. When the spot-size of the seed beam is reduced as well, the amplifier can be pushed more into saturation, while maintaining pump

fluences below the damage threshold of the Ti:Sapphire crystal. In the end a configuration was chosen which brings us closest to an output power of 80 mJ. At this configuration the accumulated B-integral in the power amplifier is 0.043. The total B-integral of both kHz-amplifier (see Table 6.1) and power-amplifier therefore stays safely far below critical values (see Section 5.2.5).

6.2.2 Design of the compressor

To find the optimum compression of the amplified pulses, the configuration of the new compressor is mainly dictated by the existing stretcher (see Section 6.1.2) and material dispersion in the kHz-amplifier. Taking into account the dispersion accumulated in this stretcher and material dispersion of the both the kHz amplifier and power amplifier, the settings for the new amplifier were optimized numerically.

The refractive indices for the relevant optical materials were calculated using the Sellmeyer equations, while the final combined dispersion induced by material, the grating stretcher and compressor were derived from the formulas given in Section 5.2.3 and in references [262–264].

As mentioned in Section 5.2.4, the fourth-order dispersion can sometimes be compensated when using different grating line numbers for stretcher and compressor. The calculations were therefore performed for gratings with 1200 lines / mm and 1500 lines / mm respectively.

The resulting pulse duration after the compressor are 32 fs for the 1200 line grating and 31 fs for the 1500 line grating. Thus, the 1500 line grating indeed yields a better compression as well as will decrease any pedestals to the laser pulse caused by the 4-th order dispersion (see also Figure 5.3). However, this comes at the cost of a rather large incident angle of 69°, which would result in

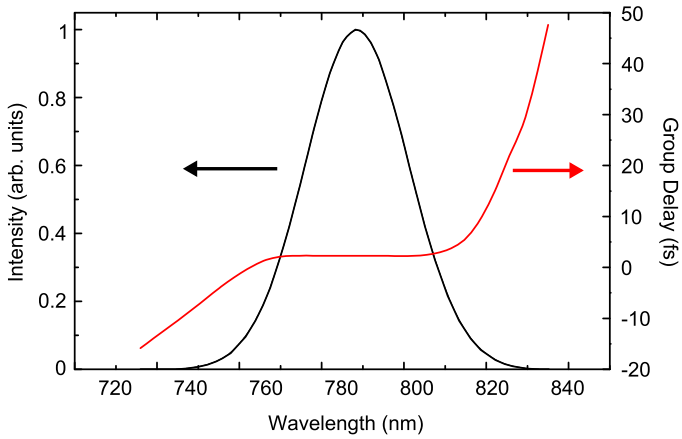

Figure 6.8: Simulation of the spectral phase after the compressor setup including the anticipated spectrum centered at 785 nm after the amplification. The resultant pulses are compressed to a duration of 32 fs. The calculations were performed for compressor gratings with 1200 lines / mm.

poor efficiency and the need of a very large second grating. The use of 1500 line / mm gratings was thus concluded to be not feasible. In the final setup the grating configuration using the 1200 line grating was therefore chosen. The assumed spectrum and resulting spectral phase are plotted in Figure 6.8.

6.3 Practical implementation

6.3.1 Installation of the TW-amplifier

In the following paragraphs, the practical implementation of the sub-parts that make up the TW-amplifier and the respective relevance to the stabilization of the CEP will be discussed individually. Implementation of the active CEP-stabilization will be discussed in the following Section 6.3.3.

The 50 Hz pulse-picker

The TW amplifier is running at a repetition rate of 50 Hz while the first stage amplifier runs at 3 kHz. The development of the TW amplifier was intended to be performed in a way that allows in parallel the continuation of experiments with the residual pulses of the kHz amplifier.

The pulse-picker was therefore constructed such that both arms can still be used simultaneously. As explained in Section 6.1.2, the timing signals for the kHz-amplifier are derived from the repetition rate of the oscillator via a digital timing card[9] housed in the control computer for the kHz-setup. For generating the timing signal for the TW-amplifier, a second timing card was introduced[10], which can be slaved to the already existing card. The benefit of the second card is, that it possesses a so-called modulo counter. With this modulo counter it is possible to configure the card such that it only puts out a trigger signal every n-th trigger of the master card; e.g., if the master card is configured to give a trigger signal at 3028 Hz, then the modulo counter of the second card can be set to 61 such that the card puts out a trigger signal for every 61st trigger that it receives from the master card. The resulting repetition rate used for the TW-amplifier is then 49.6 Hz. This signal is used to trigger the pulse-picker, pump-lasers, and spectrometer of the f-2f interferometer (see Section 6.3.3). Despite the small deviation of the 50 Hz repetition rate, this arm of the amplifier setup will for the rest of this text still be referred to as the 50 Hz arm.

The pulse-picker consists of a Pockels cell[11] followed by two thin film polarizers (TFPs). The first TFP is optimized for high polarization efficiency for the transmitted pulse, while the pulses at 50 Hz are reflected on the surface. This configuration is essential as the transmitted pulses are further propagated to the original kHz-compressor and are used in experiments. The kHz-beamline then has an effective repetition rate of ~ 2978.4 Hz, in the sense that every 61st

[9] Bergmann SG02 timing card
[10] Bergmann SG-05 timing card
[11] KMLabs Eclipse Pockels Cell including Pockels Cell driver and power-supply

pulse in the pulse train is missing. The reflected pulses at 50 Hz are cleaned with a second TFP used in reflection. In order to fulfill the polarization conditions of the two TFPs, the polarization of the pulses that enter the Pockels cell after the first amplification stage had to be changed to horizontal. Additionally the timing window of the Pockels cell is chosen such that it efficiently cleans most of the amplified spontaneous emission which might exist in the original pulses after the first amplification stage.

The pulse-picker is set up on a separate compact bread board, as the space on the original breadboard of the 3 kHz amplifier is limited. Before the beam is propagated to the breadboard of the TW amplifier, it is expanded in a telescope to the necessary beam size for the power amplifier. The transmitted kHz pulse train experiences only small losses and the pulse energy is maintained at over 2.3 mJ. Also the phase-stability of neither the kHz-amplifier or TW-amplifier is influenced by the additional pulse-picker.

The pump-lasers

With respect to the anticipated CEP stability of the TW amplifier, great care was taken in the selection of the pump-lasers. Pulse-to-pulse energy fluctuations of the pump-laser and thus also of the amplified pulses can easily translate into additional noise in the f-2f interferometer measurement [313, 314]. Usually this happens during the non-linear process of the white-light generation. The energy stability of available pumps lasers therefore was one of the major selection criteria in the purchase of an appropriate laser system.

For laser amplifiers running at repetition rates in the kHz regime, usually Q-switched solid state lasers that are pumped by continuous wave laser diodes are chosen, due to their high energy stability, low power consumption and long life-times. When reaching into repetition rates of a few ten to hundreds of Hertz this approach is, however, not feasible. Even though there are diode-pumped lasers at lower repetition rates available, their energy stability is not necessarily higher than what is nowadays reached with conventional flashlamp-pumped lasers. As a matter of fact, in all approaches where diode modules are used to pump low repetition rate lasers, the diode module will not be run in a continuous mode, but cycled at the repetition rate of the pumped laser.

The most cost-performance effective choice and eventually selected laser system consisted of two flashlamp-pumped Nd:YAG lasers, supplied by a single power supply and control unit[12]. Each laser head emits pulses of $\sim$ 10 ns duration with an energy of 160 mJ in multi-mode operation. The multi-mode operation comes at the cost of a bad M^2- value, however, ensures a good beam homogeneity in the spatial profile, and thus reduces the risk of damaging the amplifier optics and crystal. The measured rms energy stability of the two lasers is 0.56 %. To reach optimal lasing condition the Q-switch and flashlamps are triggered at separate delays. Since the trigger of the flashlamps has to come several microseconds before the actual output of the pulse, the trigger has to be chosen such that the pump pulse of the trigger coincides with the seed

[12]Litron NanoTRL 320-50 custom dual head version

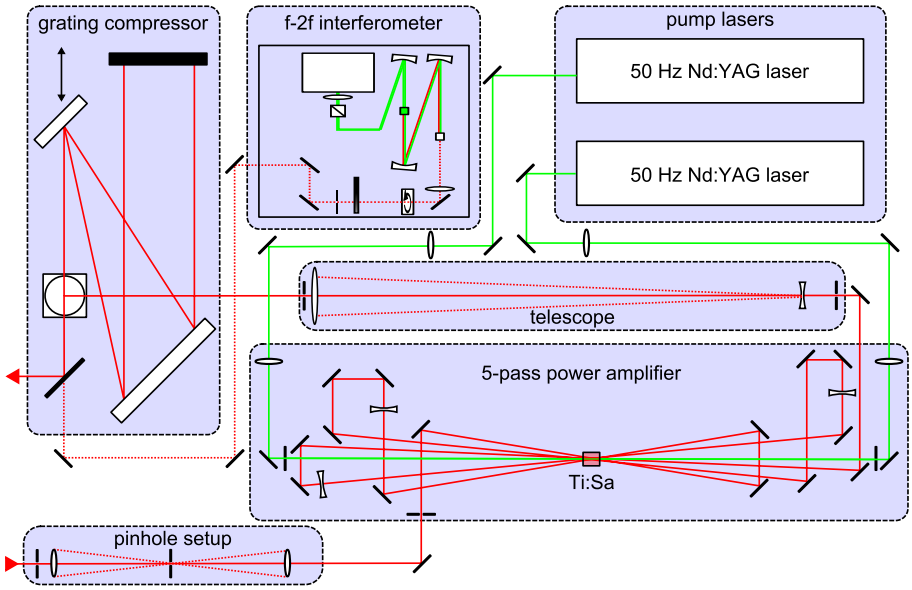

Figure 6.9: Schematic illustration of the TW-amplifier setup.

pulse of the next trigger point. Since the time-range of the digital timing cards is limited to 330 µs, while the pulses in the TW amplifier have a temporal distance of close to 20 ms, the trigger signal of the timing card was used to trigger a second digital delay generator[13], which possesses multiple outputs. This second delay generator is subsequently used to trigger both the flashlamp as well as the Q-switch of the two laser heads and can further be used to flexibly trigger any subsequent experiments.

The power amplifier

The power amplifier was set up in a traditional bow-tie configuration with 5 passes through the amplifier crystal. The incident radiation is chosen to be in s-polarization to benefit from the better efficiency of the reflecting optics. A breadboard[14] houses the complete amplifier setup, consisting of the amplifier itself, the grating compressor as well as the two pump-lasers and the f-2f interferometer for the CEP measurement (see Figure 6.9). To reach a higher mechanical stability, the beam height was chosen lower than in the original kHz-amplifier, e.g., 11.3 cm in the kHz-amplifier and 50 mm in the TW-amplifier.

The Ti:Sapphire crystal, which was used as the gain medium, has a cylindrical shape with flat AR-coated faces, a length of 15 mm and a diameter of 12 mm. It absorbs 93 % of the incident pump light, and the leaked pump light is additionally recycled into the crystal with a second pair of mirrors. To

[13]Stanford Research Systems, DG535 Digital delay generator
[14]size: 1800 mm x 900 mm x 50mm

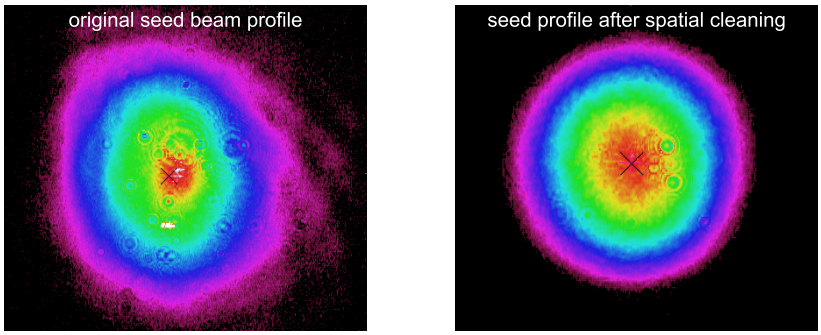

Figure 6.10: Spatial intensity distribution of the seed beam before (left) and after (right) spatial cleaning using a 120 µm pinhole in combination with a 1-to-1 telescope consisting of two 30 cm lenses.

counteract the effects of the induced thermal lens, the crystal is directly water-cooled, i.e. the cooling water flows directly around the crystal sides, while the seal towards the crystal faces is achieved with two O-rings.

The beam-sizes inside the amplifier crystal were first chosen to match the configuration calculated in the simulations described in Section 6.2.1. The thermal lens after each pass is compensated by placing long focal length diverging lenses inside the laser path. The lenses were chosen such that a stable beam-size of the seed beam was maintained for every pass. The size of the pump-laser is adjusted using a converging lens in combination with a cylindrical lens to ensure a symmetric beam profile on the crystal faces. Fine tuning of the gain and the final output energy was achieved by finely adjusting the position of the two pump focusing lenses.

Additionally, it turned out that the beam-profile of the seed-beam was not sufficient to allow good pump extraction as well as reach a clean beam profile after the power amplifier. This might be partially due to the pure multipass approach in the first amplification stage and / or to imperfect polarization optics. Before entering the amplifier setup, the beam was therefore spatially cleaned using a high power resistant pinhole. The initial and final beam profile are depicted in Figure 6.10. Due to the spatial cleaning the input pulse energy was reduced from 3.5 mJ to 1.4 mJ; the final extraction efficiency was, however, increased, eventually yielding a higher final output power.

The compressor

For the compressor a conventional grating setup was chosen. The calculated settings predicted an incidence angle of 40.23 °(in comparison the incidence angle on the kHz-line compressor is 38°), and a grating separation of 329 mm. The center wavelength of 785 nm is then diffracted by an angle of 17°. To prevent damage to the gratings the incident beam was expanded to a $1/e^2$ beam diameter of 30 mm.

The beam height for the grating compressor is adjusted using a polarization changing periscope. The incident beam enters the grating compressor at the

top and is down reflected with a roof mirror at the end of the compressor. The exiting beam has a beam height of $\sim$ 11 cm above the breadboard.

All mounts were designed to be extremely rigid. The periscope is attached to 1.5" thick pedestals with high stability mirror mounts, while the gratings are supported by home built mounts, which allow adjustment of the yaw and tilt angles as well as the grating angle along the vertical grating axis. The longitudinal position of the gratings can be adjusted with two stainless steel translation stages.

The throughput efficiency of the grating compressor is rather low with a value below 45 %. This is due to the low reflectivity of the individual gratings[15] of 80 - 82 %. Replacing these gratings for better efficiency gratings should easily yield a common compressor throughput of better than 60 %.

The fine tuning of the grating compressor to achieve the shortest pulse duration was done by measuring the pulse duration using spectral phase interferometry for direct electric field reconstruction (SPIDER) [138]. The SPIDER setup was built up at the beginning of this PhD work and is based on a design by Stibenz and Steinmeyer [315]. It is based on creating the two replica pulses with a thin etalon, while the auxiliary pulse is stretched by multiple passes in a highly dispersive glass block. The setup can easily be adjusted to measure either short ($<$ 10 fs) or longer ($\sim$ 30 fs) pulses by replacing the dispersive glass block and thus adjusting the spectral shear of the two replica pulses. Using this setup the residual dispersion after the compressor could be optimized up to the third order.

6.3.2 Amplifier performance

In everyday operation the power amplifier is seeded with pulses of 1.4 mJ energy and pumped with 10 ns pulses of 260 mJ energy at 532 nm. In this configuration the beam sizes of both pump and seed beam were adjusted to reach an output energy of around 82 mJ while maintaining a good beam profile of the amplified beam.

As predicted by the calculations in Section 6.2.1, the central wavelength of the spectrum after amplification is red shifted from 774 nm to 785 nm and the spectral bandwidth is enlarged from 33 nm to 37 nm. The results are plotted in Figure 6.11 a). Additionally the output spectrum was simulated using the gain profile of Ti:Sapphire and simply assuming a gain factor of 80. The calculation was performed twice. First the gain spectrum was approximated by a Lorentz-profile [316], which is described by

$$g(\omega) = \frac{\gamma/2\pi}{(\omega - \omega_0)^2 + (\gamma/2)^2} \ . \tag{6.3}$$

In this case ω_0 gives the central frequency of the Ti:Sapphire gain profile and $\gamma = 2\pi \cdot 98$ THz is its FWHM. In a second calculation the actual gain

[15] Grating 1: Spectrogon 1200 lines / mm compressor grating (64 mm x 64 mm); Grating 2: Spectrogon 1200 lines / mm compressor grating (120 mm x140 mm)

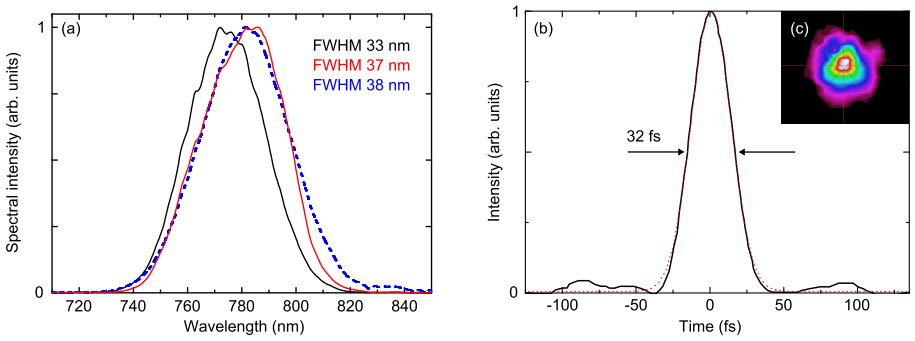

Figure 6.11: In (a) the seed spectrum (black) as well as the experimentally measured amplifier spectrum (red) are plotted. Additionally the spectrum of the amplifier pulse was simulated (blue dash) using the gain profile of Ti:Sapphire and assuming an amplification factor of 80. In (b) the temporal pulse profile as measured with SPIDER is plotted including a Gaussian fit (red dashed line) yielding a pulse duration of 32 fs. In (c) the farfield profile of the amplified pulse is plotted at the focal position of a $f = 1$ m lens. The profile shows a slight non-Gaussian distribution.

profile of Ti:Sapphire as stated in reference [258] was used. Both times the results were comparable. Plotted is the calculation using the experimental Ti:Sapphire gain spectrum.

Even though this approach does not take into account the spectral chirp of the incoming pulse, the resultant spectrum reproduces the experimentally measured distribution well on the lower wavelength side, whereas on the long wavelength side, the calculation slightly overestimates the spectral wings. It is questionable if this is due to the already mentioned shortcomings of the calculations, or if it is a real effect of the experiment, i.e. due to the bandwidth of the mirrors used. Taking into account the efficiency curve of the mirror did not change the results significantly.

The duration of the output pulses after compressor optimization was 32 fs. This agrees well with the predicted pulse duration from the compressor calculations. Even though the spectral bandwidth can support transform limited pulse durations of 27 fs, higher order terms of dispersion are likely to be the source of the residual imperfect compression.

Due to the poor compressor efficiency the final output energy of the TW-amplifier system is 35 mJ, which subsequently can be supplied to experiments. This is equivalent to a peak power of 1.1 TW. If the compressor gratings were to be replaced for gratings with efficiencies around 90 %, a final output energy of > 50 mJ and peak powers of up to 1.65 TW should be achievable. The energy stability of the laser output showed an rms stability of 0.6 % with fluctuations depending on the warm-up time of the laser and especially the extraction efficiency (see also Section 6.3.3).

In a first building phase of the amplifier, a Ti:Sapphire crystal with a diameter of only 8 mm was used. This caused a diffraction pattern on the amplified beam profile, which redistributed a significant amount of energy from the beam center to the wings. The beam profile was substantially improved when the

amplifier crystal was replaced by a crystal with 12 mm diameter. In this case the beam profile does not show any significant inhomogeneities. A preliminary farfield distribution is shown in Figure 6.11 c), however, using the first amplifier crystal. An initial M^2 measurement with the larger crystal revealed spatial chirp from imperfect alignment of the compressor gratings. A second measurement of the M^2 value could not be performed anymore due to a breakdown of one of the pump-lasers. However, from visual examination of the beam-profile good values are to be expected.

The pointing stability of the amplified beam was measured by imaging the beam with a 1 m focal length lens onto a CCD chip. The lens was positioned approximately 1 m behind the final output mirror inside the amplifier housing. Subsequently the focal position was recorded over a time interval of 10 min. The position trace revealed a slow global drift which is linear in time with a drift rate of 1.17 µm/min in the horizontal and 2.55 µm/min in the vertical direction. On top of this slow drift, the fast pointing fluctuations amount to an rms value of the focal position jitter of 3 µm in both the vertical and horizontal direction.

6.3.3 Phase stabilization of the TW-amplifier

To gain control over the waveform of the emitted pulses of the TW-amplifier, a number of measures had to be taken. Some have already been mentioned in the last section; further relevant developments and the path towards the final results will be laid out in this section.

The f-2f interferometer

In order to measure the phase slip between consecutive pulses of the TW-amplifier, an f-2f interferometer was set-up, which is equivalent to that used for the CEP measurement of the kHz-amplifier (see Section 6.1.2 and Figure 6.3). The system was built up on a separate small breadboard, to keep the positioning of the interferometer inside the amplifier system flexible.

To run the interferometer, the leak of the backside polished out-coupling mirror after the compressor was used. The beam is subsequently focused using a f = 10 cm lens inside a 2 mm sapphire plate. The intensity of the pulses inside the Sapphire plate can be adjusted using an adjustable aperture and variable neutral density filter to generate a stable white light, characterized by a stable white spot encircled with one or multiple concentric rings of red and green radiation. The divergent white light is collimated using a concave silver mirror with focal length 10 cm. The collimated beam is propagated to a next f = 10 cm concave silver mirror which focuses the beam into a 1 mm thick BBO crystal to generate the second harmonic of the long wavelength part of the white-light. The crystal is cut for a phase matching wavelength of 960 nm. After second harmonic generation the two copropagating 2f pulses are projected onto a common axis using a rotatable polarizing beamsplitter cube.

For detection the beam is focused directly onto the 20 µm entrance slit of

a compact Czerny-Turner spectrometer[16], which has a spectral resolution of better than 0.5 nm at 435 nm and a signal to noise ratio of 2000:1. This allows the detection also of very weak interference signals. The read-out rate of this spectrometer is limited to 100 Hz[17], sufficient to allow single shot acquisition at the full repetition rate of the TW-amplifier. When used in a triggered mode, which was always the case for the 50 Hz system, it was, however, observed that signal with intensities of less than 40 - 50 % of the peak signal was cut off. This, however, seems to be an inherent problem of the functioning of the spectrometer and could not be further addressed in the software.

Judging from the measured fringe-spacing of 4 nm the temporal delay between the two consecutive pulses was 186 fs. By inserting additional glass wedges into the beampath, before SHG takes place, this delay could be adjusted to larger values, i.e., smaller fringe spacing. Considering the phase-matching band width of $\sim$ 20 nm, still 5 - 6 fringes could be resolved. Due to the large fringe spacing this setup could ideally be used in combination with the detection scheme presented in reference [288], which is based on a metal prism to separate the valley and peak of two consecutive fringes and detection on two photo-multiplier tubes. The benefits of this scheme will be discussed at a later point in this chapter.

Control of the CEP

The complete laser system including oscillator, kHz-amplifier and TW-amplifier is divided into independent feed-back loops, each driven by a separate f-2f interferometer and CEP control system. This is illustrated in Figure 6.12. To close the feedback loop of the TW-amplifier the same approach as in the kHz-amplifier was chosen (see Section 6.1.2). However, in the TW-amplifier the combined phase excursions accumulated in both the kHz-amplifier and the power amplifier have to be compensated.

To control the separation of the two gratings in the grating compressor (see Section 5.4.2) a small piezo-stack[18] was inserted into the translation stage of the first grating. The translation direction of the stage is oriented to move the grating parallel to the propagation direction of the incoming laser beam. This configuration ensures that movement of the grating for the purpose of CEP stabilization will not translate into instabilities of the beam position. The piezoelectric actuator is driven by an open-loop control unit[19]. The control unit can be accessed either via an analog 0 - 10 V input voltage or via a serial RS232 interface.

In the maximum displacement of 9.1 µm (at 150 V) of the piezo stack, the grating separation is effectively changed by 11.9 µm. According to equation 5.30 this leads to an effective CEP modulation range of 24.2π rad. To be able to

[16]Thorlabs Compact CCD spectrometer CCS100

[17]For the kHz system a Thorlabs SP3 spectrometer was used. In the triggered mode, single shot acquisition was possible at a read-out rate of 100 - 120 Hz.

[18]Thorlabs Piezoelectric Actuator, max. displacement 9.1 µm at 150 V, 3.5mm x 4.5 mm x 10 mm

[19]Thorlabs, MDT694A Single Axis Open Loop Piezo Control

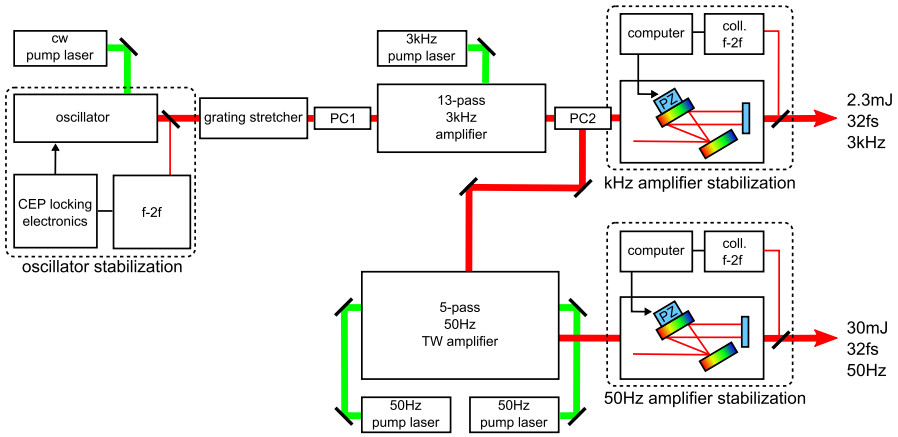

Figure 6.12: Schematic drawing of the complete laser system including the elements for CEP stabilization. The oscillator is stabilized using a piezo-actuated tilt mirror in combination with Menlo XPS f-2f interferometer and Menlo PLL-electronics. The output of both amplifier stages is stabilized by controlling the grating separation in the grating compressors. The second amplification stage amplifies pulses at 50 Hz to the TW level while maintaining the same residual phase error as in the kHz-arm.

adjust both positive and negative CEP excursions, the piezo is kept at a constant offset voltage of 75 V. This is implemented in the stabilization software which is described in the following paragraph.

The Stabilization software

To read out the data of the spectrometer and generate a feedback signal for the CEP stabilization loop a Labview based stabilization software was written. This software retrieves the spectrometer data at the highest possible readout rate. Subsequently, the data is Fourier-transformed into the time-domain, which yields an array of complex numbers. When the absolute value is plotted over the resultant time axis, a prominent peak reveals the value of the temporal delay between the two 2f pulses. The Fourier phase at this temporal position presents the desired phase value, which will be stabilized (see also Section 5.3.2).

In the program the user can select the spectral region, where the interference pattern is visible to perform the Fourier transformation on. The time value at which the phase will be extracted is set manually by the user and the resultant phase value is compared to the set-point phase and if necessary forwarded to a PID-control loop. At the same time the current phase value is displayed on the graphical user interface, as are the current rms-value and the Fourier transformation of the CEP noise and the signal strength. This allows the online detection of instabilities of the CEP up to frequencies equal to half the repetition rate of the system. Additionally, the number of samples, over which the CEP value and the respective rms values are calculated, can individually be set. Commonly the averaging for the acquisition is set to one

to show the single shot results.

The PID loop can be adjusted to arbitrary set values of the CEP. Additionally the program provides the possibility to be interfaced from other Labview programs, which in the future will allow the external steering of CEP scans for the purpose of experiments. The instantaneous stability is constantly monitored and given out to the same interface in order to pause acquisition of an interfacing program during times of CEP instabilities. After the systems detects excessive instabilities, a delay can be set before the interface system returns back to the acquisition procedure.

The new set-values of the PID loop are translated directly into the necessary voltage values, which are subsequently written via the RS232 interface to the piezo controller. This allows update rates of the piezo grating position which can be much higher than in the original Menlo software approach used in the kHz-amplifier. In practice there is a value of the update rate which yields the best stability of the system, also the bandwidth of the feedback is limited by the mechanical inertia of the gratings. If the set repetition rate is to high, the fast update rates can cause undesired mechanical instabilities in the actuated compressor grating. Also if the feedback bandwidth is set higher than the limit at which the CEP detection is limited by shot noise, the feedback can introduce additional CEP noise, i.e. reduce the achievable CEP stability. The feedback rate thus has to be chosen based on the performance of the laser system and the f-2f interferometer. To avoid sudden large movements when a phase jump is detected, the voltage values from the PID loop are limited by an adjustable maximum step size. This additionally ensures a smooth moving of the compressor grating.

The new stabilization software thus has several advantages compared to the commercial software originally used in the kHz-arm. The online display of single shot data allows a much better direct analysis of the amplifier stability. The increased flexibility of the analysis parameters additionally enables a better fine-tuning of the stabilization loop. One major difference is the increased feedback rate and the direct interfacing of the piezo controllers. The original setup is described in more detail in Section 6.1.2.

6.3.4 CEP-stabilization results

The first step to implement the CEP-stabilization of the 50 Hz-amplifier was to measure the isolated impact of the newly set up grating compressor [300], bypassing the 50 Hz power-amplifier and only running the oscillator CEP-stabilization. The recorded phase after the 50 Hz-compressor was compared against the phase measured after the original kHz-compressor. The fast phase jitter was comparable after both compressors, however, the slow phase drifts measured behind the kHz-compressor were not visible in the measurements behind the 50 Hz compressor. We conclude therefore that most of the slow phase drifts of the kHz-system are accumulated only in the compressor setup, whereas the stretcher has no measurable effect on the slow drift of the CEP. We suspect that this is due to thermal fluctuations as well as direct thermal load on the kHz-compressor. The fluctuations are not visible in the 50 Hz-compressor

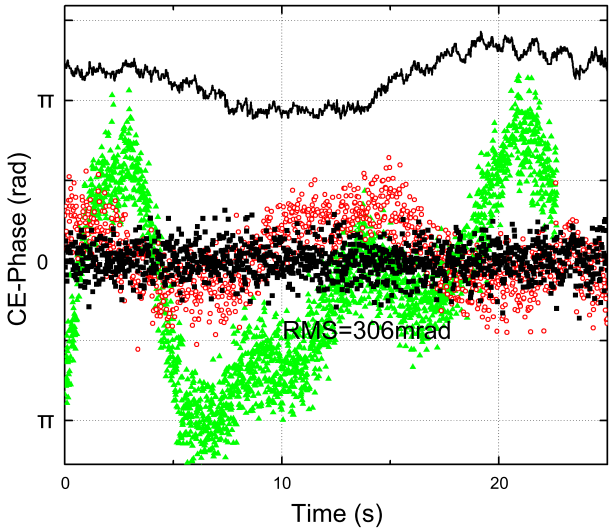

Figure 6.13: Short term measurements of the CEP drift in the stabilized case (black dots) and the corresponding compensating phase (black line) that is introduced in the grating compressor. For comparison, typical cases of the free-running CEP evolution in the kHz-arm (green triangles) and in the 50 Hz-arm (red circles) are depicted as well. These measurements were not taken simultaneously and therefore one cannot draw any conclusions on correlation between the free running evolution in the two arms.

as the thermal load without pumping is negligible.

Taking into account the influence of thermal drifts introduced by the amplifier and the pump-lasers, the 50 Hz-amplifier was set up in such a way as to leave ample room in between the individual components. Additionally, compressor and f-2f interferometer were separated by vertical metal walls inside the amplifier housing and all walls were covered with foam to prevent acoustic noise from coupling into the CEP. The two pump-lasers were effectively decoupled from the breadboard by placing 25 mm thick sorbothane sheets beneath them. However, it turned out that the pump-lasers initially introduced strong thermal fluctuations causing CEP jumps, which could not be compensated by the slow feedback loop. Accordingly the pump-lasers were as well separated with metal walls from the amplifier section and it was ensured that there was enough air circulation in the pump-laser section to remove the excess heat from the rest of the breadboard housing.

Figure 6.13 shows the CEP-drift for the amplified 50 Hz-arm in the stabilized case (black squares) and in the free-running case (red circles). For comparison a trace of the kHz-arm is plotted also in the free running case (green triangles). In both free-running cases, only the oscillator CEP-stabilization is active. In agreement with the before mentioned observation, the 50 Hz-arm shows a slow drift with significantly lower amplitude compared to the kHz-arm. This is due to the direct thermal load on the compressor gratings. In the kHz-compressor the dissipated heat is by a factor 2 - 3 higher than in the com-

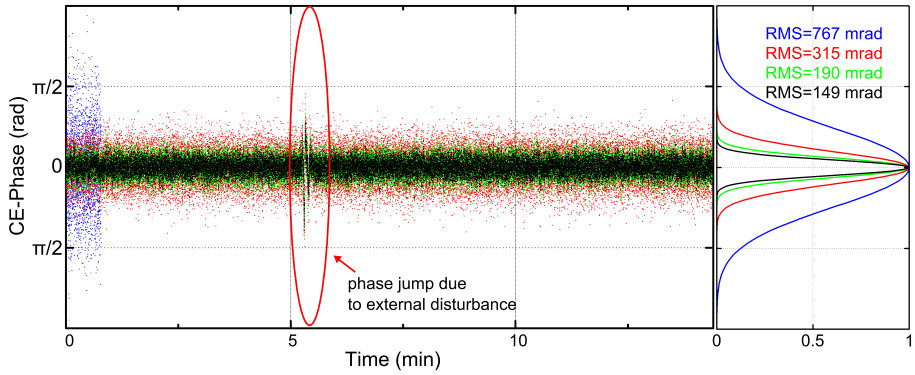

Figure 6.14: Measurement of the CEP-stability over an extended time interval. The red curve shows the single pulse CEP measurements of the 50 Hz TW-amplifier in the optimal configuration. The dots in green and black show the same measurement when averaging over three pulses and five pulses respectively. Histograms for all three cases are shown on the right with the respective rms-error values of 315 mrad, 190 mrad and 149 mrad. For comparison, a short measurement of the phase jitter is included in the case of low extraction efficiency (21%) (blue dots). The respective rms value in this case was 767 mrad.

pressor after the TW-amplifier. Additionally the thermal expansion coefficient of the copper grating substrates used in the kHz-compressor ($17 \cdot 10^{-6}/°C$) is significantly higher than those of the BK-7 gratings ($7 \cdot 10^{-6}/°C$) used in the TW-compressor.

In the first amplification attempts, the optical efficiency was rather low with values of around 20-25%. As a result the pulse-to-pulse energy fluctuations of the amplified pulses were large. This can easily translate into instabilities in the CEP measurement mostly during the strongly non-linear white-light generation process. As a result, the measured CEP-stability only reached values of above 700 mrad (see Figure 6.14 blue curve). In order to achieve a better stability of the pulse energy and therefore also of the CEP measurement, we adjusted the amplifier to be operated at higher saturation levels as described in Section 6.2.1. At efficiency levels of 31 %, the phase-jitter is reduced by a factor of more than two to values around 300 mrad in single pulse measurements. Results of a long term measurement are shown in Figure 6.14. The rms-stability of both pump-lasers is 0.56% and of the amplified pulse in this configuration is 0.6%.

Nonetheless, even at this value the achievable CEP stability appears to be limited by shot noise resulting from the low photon numbers in the relevant spectral ranges produced in white-light generation process in the Sapphire plate. This assumption is supported by two facts: First the histograms plotted in Figure 6.14 and the resultant rms-values follow almost perfectly a Gaussian statistic, indicative for white noise limitation. If, however, the oscillator would be a limiting factor at this point, one would expect a non-Gaussian statistic [317]. Second, the analysis of the frequency spectra of the residual phase error,

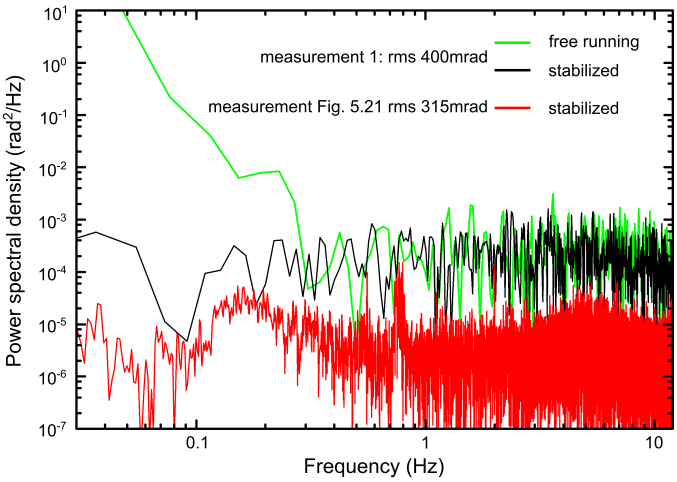

Figure 6.15: Power spectral density of the phase noise for three measurements. The top two graphs (green and black) show the frequency spectrum of the TWA amplifier in the free running (green) and stabilized (black) case. Due to somewhat lower energy extraction from the amplifier crystal, the rms value of this measurement in the stabilized case was 400 mrad. The frequency spectrum of the residual phase noise of the measurement in Figure 6.14 is plotted in red. In both stabilized cases the measurement is limited by shot noise in the f-2f interferometer. The strong peak in the red trace at a frequency of 0.76 Hz is due to a cooling cycle in the chiller in the kHz pump-laser. By changing the set-temperature of the chiller this disturbance could be eliminated.

plotted in Figure 6.15, reveals similar indications. Power spectral densities of the residual phase noise for three different measurements are plotted. In the first two measurements the influence of the stabilization loop is shown. A clear reduction of the slow modulations up to a frequency of 0.3 Hz is visible. Higher frequencies are already at the level of the shot noise for this measurement. In the third plot the frequency spectrum for the phase noise of the measurement in Figure 6.14 is shown. The shot noise level in this case lies almost two orders of magnitude lower than in the previous measurements, however, the stabilized frequencies are still covered by the average shot noise level.

The high shot noise level finds its origin in the extremely low spectral densities in the 2f arm of the interferometer. Considering that the white-light generation in the Sapphire plate is limited to only a few microjoule of input energy, the effective photon number N in the frequency-doubled part of the spectrum might be as low as 10^4, taking into account conversion efficiency into the IR, the doubling efficiency, losses in the spectrometer and the quantum efficiency of the detector. The achievable phase resolution between consecutive laser pulses is then limited to a value of $\Delta\phi_{CE} = \pi/(N/2)^{1/2}$ [288], e.g. values between 40 - 50 mrad. These numbers, however, hold only for a perfect detection system. In the case of a fast CCD chip, the resultant value could be higher by up to one order of magnitude [317] and thus lie at similar levels as

those measured in our f-2f setup.

The situation could be tremendously improved by increasing the photon numbers in the relevant frequency range. Using super-continuum generation in noble gases would allow input energies in the mJ range with high conversion efficiencies in the super-continuum generation process. A realistic increase in the relevant photon number by a factor of 10 or more would improve the shot noise by more than one order of magnitude. With the laser system presented in this chapter, the pulse energies to run a noble gas filled fiber setup, which would generate the necessary white-light, only amounts to 2 - 3 % of the total output energy of the system.

There have been hints that the stability of the residual phase noise of the oscillator might also be a limitation [288]. This should be easily measurable by simultaneously recording the oscillator stability and amplifier stability and subsequently plotting the correlation of the phase noise values. This measurement could not be performed anymore during the available time in the laboratory, but should be repeated at a given time.

Even at shot noise limitations, the final CEP-stability of the system is still strongly dependent on external environmental influences. Especially mechanical vibrations seem to play a major role, i.e. the difference of rms-error values of the CEP can be as high as 150 mrad when comparing measurements taken during the day and after working hours. Since the laser systems are supplying experimental setups that are not connected to the optical table, floating the table is not an option. We expect that the rms value of the system could still improve when moving to a more stable environment. Additionally, there have been techniques developed that actively stabilize the output energy of laser pulses after an amplifier setup [318]. This could be a way to achieve better CEP measurements, however, is rather involved to implement.

Many commercial suppliers of CEP-stabilized laser systems only state rms-error values for averaged measurements. As was shown by Koke and coworkers [288], single pulse measurements at the full repetition rate of the laser system are necessary to determine the real phase-stability of a system. All measurements for the 50 Hz-arm presented in this chapter are single pulse data taken at the full repetition rate of the amplifier. Measurements of the kHz-arm are usually taken at 100-120 Hz. To make the results comparable with other published data, the long term single-pulse measurement shown in Figure 6.14 is also plotted for cases when a moving average over three and five pulses respectively was applied. As expected, the rms-value of the phase jitter in these cases is reduced dramatically to 190 mrad and 149 mrad respectively.

Further improvements of the results could be achieved with a non-prism based femtosecond oscillator for the source and / or implementing the frequency shifter approach for the oscillator stabilization [297] (also described in Section 6.2). An improved detection system for the collinear f-2f interferometer for the amplifier stabilization based on photo multiplier tubes [288], which offer a much higher quantum efficiency and signal to noise ratio than commonly used CCD chips, could also bring a significant improvement of the stabilization results.

6.3.5 Conclusion

In this Chapter the CEP-stabilization of an amplifier producing 32 fs pulses with a peak-power of 1.1 TW at 50 Hz repetition rate was demonstrated. It was shown that CEP-stabilization in CPA systems can be achieved even at low pulse repetition rates. Doing so, the phase-stability of the original kHz-system was fully maintained and the measured CEP values rank among the best values published so far.

The presented results are the highest pulse energy reached for CEP-stabilized femtosecond pulses to this point, and open up the possibility of the controlled generation of IAPs with unprecedented photon fluxes (see Section 2.5). This is an important step towards experimental conditions that allow experimental researchers to perform XUV-XUV pump-probe experiments, as described in Section 2.4.

Further it paves the way towards even more energetic driver pulses with stable CEP. Nowadays CPA systems with repetition rates in the 10 Hz regime and several Joules of pulse energy are commercially available (see Section 5.2.5). From the demonstrated measurements we conclude that scaling to higher energies should be straight forward, as long as the pulse repetition period is short compared to the slow thermal fluctuations introduced in the compressor and the pulse-to-pulse energy instabilities can be maintained at a low level.

The availability of high pulse energies might additionally promote the use of super-continuum generation in fibers for the use with f-2f interferometers. This could potentially allow a significant increase in the phase sensitivity in the f-2f measurement scheme and therefore should be further investigated in the future use of the laser system.

References

[1] Aristotle. *Physics, Chapter IV 10-14* (around 350 BC).

[2] R. J. Collins, D. F. Nelson, A. L. Schawlow, W. Bond, C. G. B. Garrett and W. Kaiser. *Coherence, Narrowing, Directionality, and Relaxation Oscillations in the Light Emission from Ruby.* Physical Review Letters, **5**, 303–305 (1960).

[3] T. Maiman. *Stimulated Optical Radiation in Ruby.* Nature, **187**, 493–494 (1960).

[4] F. J. McClung and R. W. Hellwarth. *Giant Optical Pulsations from Ruby.* Applied Optics, **1**, 103–105 (1962).

[5] L. Hargrove, R. Fork and M. Pollack. *Locking of He-Ne Laser Modes Induced by Synchronous Intracavity Modulation.* Applied Physics Letters, **5**, 4–5 (1964).

[6] A. DeMaria, J. Glenn, W.H., M. Brienza and M. Mack. *Picosecond laser pulses.* Proceedings of the IEEE, **57**, 2 – 25 (1969).

[7] P. Smith, M. Duguay and E. Ippen. *Mode-locking of lasers.* Progress in Quantum Electronics, **3**, 107 – 229 (1974).

[8] A. Rundquist, C. Durfee, Z. Chang, G. Taft, E. Zeek, S. Backus, M. M. Murnane, H. C. Kapteyn, I. Christov and V. Stoev. *Ultrafast laser and amplifier sources.* Applied Physics B-Lasers and Optics, **65**, 161–174 (1997).

[9] A. H. Zewail. *Femtochemistry: Atomic-scale dynamics of the chemical bond.* Journal of Physical Chemistry A, **104**, 5660–5694 (2000).

[10] P. M. Paul, E. S. Toma, P. Breger, G. Mullot, F. Auge, P. Balcou, H. G. Muller and P. Agostini. *Observation of a train of attosecond pulses from high harmonic generation.* Science, **292**, 1689–1692 (2001).

[11] M. Hentschel, R. Kienberger, C. Spielmann, G. A. Reider, N. Milosevic, T. Brabec, P. Corkum, U. Heinzmann, M. Drescher and F. Krausz. *Attosecond metrology.* Nature, **414**, 509–513 (2001).

[12] F. Kelkensberg. *Capturing Atomic and Electronic Motion with High Harmonic Generation Light Pulses.* Ph.D. thesis, FOM Institute AMOLF (2011).

[13] W. K. Siu. *Probing Molecular Dynamics Using Novel Light Sources.* Ph.D. thesis, FOM Institute AMOLF (2011).

[14] P. A. Franken, A. E. Hill, C. W. Peters and G. Weinreich. *Generation of Optical Harmonics.* Physical Review Letters, **7**, 118–119 (1961).

[15] G. H. C. New and J. F. Ward. *Optical Third-Harmonic Generation in Gases.* Physical Review Letters, **19**, 556–559 (1967).

[16] J. F. Reintjes. *Nonlinear Optical Parametric Processes in Liquids and Gases.* Quantum Electronics, Principles and Application, Academic Press (1984).

[17] A. McPherson, G. Gibson, H. Jara, U. Johann, T. S. Luk, I. A. McIntyre, K. Boyer and C. K. Rhodes. *Studies of multiphoton production of vacuum-ultraviolet radiation in the rare gases.* Journal of the Optical Society of America B, **4**, 595–601 (1987).

[18] M. Ferray and et al. *Multiple-harmonic conversion of 1064 nm radiation in rare gases.* Journal of Physics B: Atomic, Molecular and Optical Physics, **21**, L31 (1988).

[19] K. J. Schafer, B. Yang, L. F. DiMauro and K. C. Kulander. *Above threshold ionization beyond the high harmonic cutoff.* Physical Review Letters, **70**, 1599 (1993).

[20] P. B. Corkum. *Plasma Perspective on Strong-Field Multiphoton Ionization.* Physical Review Letters, **71**, 1994–1997 (1993).

[21] A. L'Huillier, M. Lewenstein, P. Salieres, P. Balcou, M. Y. Ivanov, J. Larsson and C. G. Wahlstrom. *High-Order Harmonic-Generation Cutoff.* Physical Review A, **48**, R3433–R3436 (1993).

[22] M. Lewenstein, P. Balcou, M. Y. Ivanov, A. L'Huillier and P. B. Corkum. *Theory of High-Harmonic Generation by Low-Frequency Laser Fields.* Physical Review A, **49**, 2117–2132 (1994).

[23] L. V. Keldysh. *Ionization in the Field of a Strong Electromagnetic Wave.* Zh. Eksp. Teor. Fiz., **47**, 1945–1957 (1964). [Sov. Phys. JETP **20**, 1307 (1965)].

[24] L. V. Keldysh. *Translation: Ionization in the Field of a Strong Electromagnetic Wave.* Soviet Physics JETP, **20**, 1307–1314 (1965).

[25] K. S. Budil, P. Salières, M. D. Perry and A. L'Huillier. *Influence of ellipticity on harmonic generation.* Physical Review A, **48**, R3437–R3440 (1993).

[26] N. H. Burnett, C. Kan and P. B. Corkum. *Ellipticity and polarization effects in harmonic generation in ionizing neon.* Physical Review A, **51**, R3418–R3421 (1995).

[27] P. Antoine, D. B. Milosevic, A. L'Huillier, M. B. Gaarde, P. Salieres and M. Lewenstein. *Generation of attosecond pulses in macroscopic media.* Physical Review A, **56**, 4960–4969 (1997).

[28] A. M. Zheltikov, A. L'Huillier and K. F. *Springer Handbook of Lasers and Optics: Nonlinear Optics.* Springer New York (2007).

[29] T. Popmintchev, M.-C. Chen, P. Arpin, M. M. Murnane and H. C. Kapteyn. *The attosecond nonlinear optics of bright coherent X-ray generation.* Nature Photonics, **4**, 822–832 (2010).

[30] M. B. Gaarde, J. L. Tate and K. J. Schafer. *Macroscopic aspects of attosecond pulse generation.* Journal of Physics B-Atomic Molecular and Optical Physics, **41**, 132001 (2008).

[31] A. Rundquist, C. G. Durfee, Z. H. Chang, C. Herne, S. Backus, M. M. Murnane and H. C. Kapteyn. *Phase-matched generation of coherent soft X-rays.* Science, **280**, 1412–1415 (1998).

[32] C. G. Durfee, A. R. Rundquist, S. Backus, C. Herne, M. M. Murnane and H. C. Kapteyn. *Phase matching of high-order harmonics in hollow waveguides.* Physical Review Letters, **83**, 2187–2190 (1999).

[33] E. Constant, D. Garzella, P. Breger, E. Mevel, C. Dorrer, C. Le Blanc, F. Salin and P. Agostini. *Optimizing high harmonic generation in absorbing gases: Model and experiment.* Physical Review Letters, **82**, 1668–1671 (1999).

[34] P. Balcou, C. Cornaggia, A. S. L. Gomes, L. A. Lompre and A. L'Huillier. *Optimizing high-order harmonic generation in strong fields.* Journal of Physics B: Atomic, Molecular and Optical Physics, **25**, 4467 (1992).

[35] T. Ditmire, E. T. Gumbrell, R. A. Smith, J. W. G. Tisch, D. D. Meyerhofer and M. H. R. Hutchinson. *Spatial coherence measurement of soft x-ray radiation produced by high order harmonic generation.* Physical Review Letters, **77**, 4756–4759 (1996).

[36] A. Bouhal, R. Evans, G. Grillon, A. Mysyrowicz, P. Breger, P. Agostini, R. C. Constantinescu, H. G. Muller and D. von der Linde. *Cross-correlation measurement of femtosecond noncollinear high-order harmonics.* Journal of the Optical Society of America B, **14**, 950–956 (1997).

[37] E. S. Toma, H. G. Muller, P. M. Paul, P. Breger, M. Cheret, P. Agostini, C. Le Blanc, G. Mullot and G. Cheriaux. *Ponderomotive streaking of the ionization potential as a method for measuring pulse durations in the XUV domain with fs resolution.* Physical Review A, **6206**, 061801.1–4(R) (2000).

[38] G. Farkas and C. Toth. *Proposal for Attosecond Light-Pulse Generation Using Laser-Induced Multiple-Harmonic Conversion Processes in Rare-Gases.* Physics Letters A, **168**, 447–450 (1992).

[39] S. E. Harris, J. J. Macklin and T. W. Hansch. *Atomic-Scale Temporal Structure Inherent to High-Order Harmonic-Generation.* Optics Communications, **100**, 487–490 (1993).

[40] P. Antoine, A. L'Huillier and M. Lewenstein. *Attosecond pulse trains using high-order harmonics.* Physical Review Letters, **77**, 1234–1237 (1996).

[41] P. B. Corkum, N. H. Burnett and M. Y. Ivanov. *Subfemtosecond Pulses.* Optics Letters, **19**, 1870–1872 (1994).

[42] M. Ivanov, P. B. Corkum, T. Zuo and A. Bandrauk. *Routes to Control of Intense-Field Atomic Polarizability.* Physical Review Letters, **74**, 2933–2936 (1995).

[43] I. J. Sola *et al. Controlling attosecond electron dynamics by phase-stabilized polarization gating.* Nature Physics, **2**, 319–322 (2006).

[44] I. J. Sola *et al. Temporal and spectral studies of high-order harmonics generated by polarization-modulated infrared fields.* Physical Review A, **74**, 013810.1–8 (2006).

[45] G. Sansone *et al. Isolated single-cycle attosecond pulses.* Science, **314**, 443–446 (2006).

[46] K. Varju, P. Johnsson, J. Mauritsson, A. L'Huillier and R. Lopez-Martens. *Physics of attosecond pulses produced via high harmonic generation.* American Journal of Physics, **77**, 389–395 (2009).

[47] H. G. Muller. *Reconstruction of attosecond harmonic beating by interference of two-photon transitions.* Applied Physics B-Lasers and Optics, **74**, S17–S21 (2002).

[48] D. H. Ko, K. T. Kim, J. Park, J. hwan Lee and C. H. Nam. *Attosecond chirp compensation over broadband high-order harmonics to generate near transform-limited 63 as pulses.* New Journal of Physics, **12**, 063008 (2010).

[49] K. J. Schafer and K. C. Kulander. *High harmonic generation from ultrafast pump lasers.* Physical Review Letters, **78**, 638–641 (1997).

[50] I. P. Christov, M. M. Murnane and H. C. Kapteyn. *High-harmonic generation of attosecond pulses in the "single-cycle" regime.* Physical Review Letters, **78**, 1251–1254 (1997).

[51] C. Kan, N. H. Burnett, C. E. Capjack and R. Rankin. *Coherent XUV Generation from Gases Ionized by Several Cycle Optical Pulses.* Physical Review Letters, **79**, 2971–2974 (1997).

[52] M. Drescher, M. Hentschel, R. Kienberger, G. Tempea, C. Spielmann, G. A. Reider, P. B. Corkum and F. Krausz. *X-ray pulses approaching the attosecond frontier.* Science, **291**, 1923–1927 (2001).

[53] J. Itatani, F. Quere, G. L. Yudin, M. Y. Ivanov, F. Krausz and P. B. Corkum. *Attosecond streak camera.* Physical Review Letters, **88**, 173903 (2002).

[54] F. Krausz and M. Ivanov. *Attosecond physics.* Reviews of Modern Physics, **81**, 163–234 (2009).

[55] A. Baltuska *et al. Attosecond control of electronic processes by intense light fields.* Nature, **421**, 611–615 (2003).

[56] E. Goulielmakis *et al. Single-cycle nonlinear optics.* Science, **320**, 1614–1617 (2008).

[57] R. Kienberger *et al. Steering attosecond electron wave packets with light.* Science, **297**, 1144–1148 (2002).

[58] F. Kienberger, H. Mueller, V. Pastushenko and P. Hinterdorfer. *Following single antibody binding to purple membranes in real time.* EMBO Rep, **5**, 579–583 (2004).

[59] M. Schultze, E. Goulielmakis, M. Uiberacker, M. Hofstetter, J. Kim, D. Kim, F. Krausz and U. Kleineberg. *Powerful 170-attosecond XUV pulses generated with few-cycle laser pulses and broadband multilayer optics.* New Journal of Physics, **9**, 243 (2007).

[60] L. C. Dinu, H. G. Muller, S. Kazamias, G. Mullot, F. Auge, P. Balcou, P. M. Paul, M. Kovacev, P. Breger and P. Agostini. *Measurement of the subcycle timing of attosecond XUV bursts in high-harmonic generation.* Physical Review Letters, **91**, 063901 (2003).

[61] J. Norin *et al. Time-frequency characterization of femtosecond extreme ultraviolet pulses.* Physical Review Letters, **88**, 193901 (2002).

[62] A. D. Bandrauk, S. Chelkowski and N. H. Shon. *Measuring the electric field of few-cycle laser pulses by attosecond cross correlation.* Physical Review Letters, **89**, 283903 (2002).

[63] G. G. Paulus, F. Lindner, H. Walther, A. Baltuska, E. Goulielmakis, M. Lezius and F. Krausz. *Measurement of the phase of few-cycle laser pulses.* Physical Review Letters, **91**, 253004 (2003).

[64] E. Goulielmakis *et al. Direct Measurement of Light Waves.* Science, **305**, 1267–1269 (2004).

[65] P. H. Bucksbaum. *The Future of Attosecond Spectroscopy.* Science, **317**, 766–769 (2007).

[66] G. G. Paulus, F. Grasbon and H. Walther. *Interference effects in above-threshold ionization.* Journal of Modern Optics, **50**, 343–352 (2003).

[67] S. A. Aseyev, Y. Ni, L. J. Frasinski, H. G. Muller and M. J. J. Vrakking. *Attosecond angle-resolved photoelectron spectroscopy.* Physical Review Letters, **91**, – (2003).

[68] Y. Mairesse *et al. Attosecond synchronization of high-harmonic soft x-rays.* Science, **302**, 1540–1543 (2003).

[69] P. Agostini and L. F. DiMauro. *The physics of attosecond light pulses.* Reports on Progress in Physics, **67**, 813–855 (2004).

[70] M. F. Kling and M. J. J. Vrakking. *Attosecond electron dynamics.* Annual Review of Physical Chemistry, **59**, 463–492 (2008).

[71] M. Uiberacker *et al. Attosecond real-time observation of electron tunnelling in atoms.* Nature, **446**, 627–632 (2007).

[72] J. Mauritsson *et al. Attosecond Electron Spectroscopy Using a Novel Interferometric Pump-Probe Technique.* Physical Review Letters, **105**, 053001 (2010).

[73] A. L. Cavalieri *et al. Attosecond spectroscopy in condensed matter.* Nature, **449**, 1029–1032 (2007).

[74] M. Schultze *et al. Delay in Photoemission.* Science, **328**, 1658–1662 (2010).

[75] M. Drescher, M. Hentschel, R. Kienberger, M. Uiberacker, V. Yakoviev, A. Scrinzi, T. Westerwalbesloh, U. Kleineberg, U. Heinzmann and F. Krausz. *Time-resolved inner shell spectroscopy.* Nature, **419**, 803 (2002).

[76] S. Gilbertson, M. Chini, X. Feng, S. Khan, Y. Wu and Z. Chang. *Monitoring and Controlling the Electron Dynamics in Helium with Isolated Attosecond Pulses.* Physical Review Letters, **105**, 263003 (2010).

[77] E. Goulielmakis *et al. Real-time observation of valence electron motion.* Nature, **466**, 739–743 (2010).

[78] M. Holler, F. Schapper, L. Gallmann and U. Keller. *Attosecond Electron Wave-Packet Interference Observed by Transient Absorption.* Physical Review Letters, **106**, 123601 (2011).

[79] G. Gademann, F. Kelkensberg, W. K. Siu, P. Johnsson, M. B. Gaarde, K. J. Schafer and M. J. J. Vrakking. *Attosecond control of electronion recollision in high harmonic generation.* New Journal of Physics, **13**, 033002 (2011).

[80] H. Wang, M. Chini, S. Chen, C.-H. Zhang, F. He, Y. Cheng, Y. Wu, U. Thumm and Z. Chang. *Attosecond Time-Resolved Autoionization of Argon.* Physical Review Letters, **105**, 143002 (2010).

[81] P. Johnsson, J. Mauritsson, T. Remetter, A. L'Huillier and K. J. Schafer. *Attosecond Control of Ionization by Wave-packet Interference.* Physical Review Letters, **99**, 233001.1–4 (2007).

[82] P. Ranitovic *et al. IR-assisted ionization of helium by attosecond extreme ultraviolet radiation.* New Journal of Physics, **12**, 013008 (2010).

[83] K. Klünder *et al. Probing Single-Photon Ionization on the Attosecond Time Scale.* Physical Review Letters, **106**, 143002 (2011).

[84] P. Johnsson *et al. Attosecond electron wave packet dynamics in strong laser fields.* Physical Review Letters, **95**, 013001 (2005).

[85] T. Remetter *et al. Attosecond electron wave packet interferometry.* Nature Physics, **2**, 323–326 (2006).

[86] J. Mauritsson, P. Johnsson, E. Mansten, M. Swoboda, T. Ruchon, A. L'Huillier and K. J. Schafer. *Coherent Electron scattering Captured by an Attosecond Quantum Stroboscope.* Physical Review Letters, **100**, 073003 (2008).

[87] G. Sansone *et al. Electron Localization following Attosecond Molecular Photoionization.* Nature, **465**, 763–766 (2010).

[88] F. Kelkensberg *et al. Attosecond Control in Photoionization of Hydrogen Molecules.* Physical Review Letters, **107**, 043002 (2011).

[89] K. P. Singh *et al. Control of Electron Localization in Deuterium Molecular Ions using an Attosecond Pulse Train and a Many-Cycle Infrared Pulse.* Physical Review Letters, **104**, 023001 (2010).

[90] W. K. Siu *et al. Attosecond control of disociative ionization of* O_2 *molecules.* to be published (2011).

[91] S. X. Hu and L. A. Collins. *Attosecond pump probe: Exploring ultrafast electron motion inside an atom.* Physical Review Letters, **96**, – (2006).

[92] F. Remacle and R. D. Levine. *An electronic time scale in chemistry.* Proceedings of the National Academy of Sciences of the United States of America, **103**, 6793–6798 (2006).

[93] A. I. Kuleff and L. S. Cederbaum. *Charge migration in different conformers of glycine: The role of nuclear geometry.* Chemical Physics, **338**, 320 – 328 (2007).

[94] O. Smirnova, Y. Mairesse, S. Patchkovskii, N. Dudovich, D. Villeneuve, P. Corkum and M. Y. Ivanov. *High harmonic interferometry of multi-electron dynamics in molecules.* Nature, **460**, 972–977 (2009).

[95] Y. Mairesse *et al. High Harmonic Spectroscopy of Multichannel Dynamics in Strong-Field Ionization.* Physical Review Letters, **104**, 213601 (2010).

[96] H. Soifer, P. Botheron, D. Shafir, A. Diner, O. Raz, B. D. Bruner, Y. Mairesse, B. Pons and N. Dudovich. *Near-Threshold High-Order Harmonic Spectroscopy with Aligned Molecules.* Physical Review Letters, **105**, 143904 (2010).

[97] A. D. Shiner, B. E. Schmidt, C. Trallero-Herrero, H. J. Worner, S. Patchkovskii, P. B. Corkum, J. C. Kieffer, F. Legare and D. M. Villeneuve. *Probing collective multi-electron dynamics in xenon with high-harmonic spectroscopy.* Nature Physics, **7**, 464–467 (2011).

[98] J. Itatani, J. Levesque, D. Zeidler, H. Niikura, H. Pepin, J. C. Kieffer, P. B. Corkum and D. M. Villeneuve. *Tomographic imaging of molecular orbitals.* Nature, **432**, 867–871 (2004).

[99] B. K. McFarland, J. P. Farrell, P. H. Bucksbaum and M. Guhr. *High Harmonic Generation from Multiple Orbitals in N-2.* Science, **322**, 1232–1235 (2008).

[100] D. Shafir, Y. Mairesse, D. M. Villeneuve, P. B. Corkum and N. Dudovich. *Atomic wavefunctions probed through strong-field light-matter interaction.* Nature Physics, **5**, 412–416 (2009).

[101] S. Baker, J. S. Robinson, C. A. Haworth, H. Teng, R. A. Smith, C. C. Chirila, M. Lein, J. W. G. Tisch and J. P. Marangos. *Probing proton dynamics in molecules on an attosecond time scale.* Science, **312**, 424–427 (2006).

[102] C. Li, H. Mashiko, H. Wang, E. Moon, S. Gilbertson and Z. Chang. *Carrier-envelope phase stabilization by controlling compressor grating separation.* Applied Physics Letters, **92**, 191114 (2008).

[103] S. Baker *et al. Dynamic Two-Center Interference in High-Order Harmonic Generation from Molecules with Attosecond Nuclear Motion.* Physical Review Letters, **101**, 053901 (2008).

[104] A. I. Kuleff and L. S. Cederbaum. *Tracing ultrafast interatomic electronic decay processes in real time and space.* Physical Review Letters, **98**, 083201 (2007).

[105] M. F. Kling *et al. Control of electron localization in molecular dissociation.* Science, **312**, 246–248 (2006).

[106] O. Smirnova. *Spectroscopy: Attosecond prints of electrons.* Nature, **466**, 700–702 (2010).

[107] J. Breidbach and L. S. Cederbaum. *Universal Attosecond Response to the Removal of an Electron.* Physical Review Letters, **94**, 033901 (2005).

[108] H. Hennig, J. Breidbach and L. S. Cederbaum. *Electron correlation as the driving force for charge transfer: Charge migration following ionization in N-methyl acetamide.* Journal of Physical Chemistry A, **109**, 409–414 (2005).

[109] F. Remacle, R. Kienberger, F. Krausz and R. D. Levine. *On the feasibility of an ultrafast purely electronic reorganization in lithium hydride.* Chemical Physics, **338**, 342–347 (2007).

[110] R. Weinkauf, E. W. Schlag, T. J. Martinez and R. D. Levine. *Nonstationary Electronic States and Site-Selective Reactivity.* The Journal of Physical Chemistry A, **101**, 7702–7710 (1997).

[111] S. Pabst, L. Greenman, P. J. Ho, D. A. Mazziotti and R. Santra. *Decoherence in Attosecond Photoionization.* Physical Review Letters, **106**, 053003 (2011).

[112] J. Breidbach and L. S. Cederbaum. *Migration of holes: Formalism, mechanisms, and illustrative applications.* Journal of Chemical Physics, **118**, 3983–3996 (2003).

[113] A. I. Kuleff, S. Lünnemann and L. S. Cederbaum. *Ultrafast Charge Migration Following Valence Ionization of 4-Methylphenol: Jumping over the Aromatic Ring.* The Journal of Physical Chemistry A, **114**, 8676–8679 (2010).

[114] S. Zherebtsov *et al. Controlled near-field enhanced electron acceleration from dielectric nanospheres with intense few-cycle laser fields.* Nature Physics (2011).

[115] P. Dietrich, F. Krausz and P. B. Corkum. *Determining the absolute carrier phase of a few-cycle laser pulse.* Optics Letters, **25**, 16–18 (2000).

[116] P. Eckle, M. Smolarski, P. Schlup, J. Biegert, A. Staudte, M. Schoffler, H. G. Muller, R. Dorner and U. Keller. *Attosecond angular streaking.* Nature Physics, **4**, 565–570 (2008).

[117] P. Eckle, A. N. Pfeiffer, C. Cirelli, A. Staudte, R. Dorner, H. G. Muller, M. Buttiker and U. Keller. *Attosecond Ionization and Tunneling Delay Time Measurements in Helium.* Science, **322**, 1525–1529 (2008).

[118] A. N. Pfeiffer, C. Cirelli, M. Smolarski, R. Dörner and U. Keller. *Timing the release in sequential double ionization.* Nature Physics, **7**, 428–433 (2011).

[119] S. Haessler *et al. Attosecond imaging of molecular electronic wavepackets.* Nature Physics, **6**, 200–206 (2010).

[120] W. Boutu *et al. Coherent control of attosecond emission from aligned molecules.* Nature Physics, **4**, 545–549 (2008).

[121] G. L. Yudin, S. Chelkowski, J. Itatani, A. D. Bandrauk and P. B. Corkum. *Attosecond photoionization of coherently coupled electronic states.* Physical Review A, **72**, – (2005).

[122] J. Hu, K. L. Han and G. Z. He. *Correlation quantum dynamics between an electron and D_2^+ molecule with attosecond resolution - Reply.* Physical Review Letters, **97**, 073004 (2006).

[123] T. Morishita, S. Watanabe and C. D. Lin. *Attosecond Light Pulses for Probing Two-Electron Dynamics of Helium in the Time Domain.* Physical Review Letters, **98**, 083003 (2007).

[124] Y. Kobayashi, T. Sekikawa, Y. Nabekawa and S. Watanabe. *27-fs extreme ultraviolet pulse generation by high-order harmonics.* Optics Letters, **23**, 64–66 (1998).

[125] P. Tzallas, D. Charalambidis, N. A. Papadogiannis, K. Witte and G. D. Tsakiris. *Direct observation of attosecond light bunching.* Nature, **426**, 267–271 (2003).

[126] Y. Nabekawa, H. Hasegawa, E. J. Takahashi and K. Midorikawa. *Production of doubly charged helium ions by two-photon absorption of an intense sub-10-fs soft x-ray pulse at 42 eV photon energy.* Physical Review Letters, **94**, 043001 (2005).

[127] H. Hasegawa, E. J. Takahashi, Y. Nabekawa, K. L. Ishikawa and K. Midorikawa. *Multiphoton ionization of He by using intense high-order harmonics in the soft-x-ray region.* Physical Review A, **71**, 023407 (2005).

[128] Y. Nabekawa, T. Shimizu, T. Okino, K. Furusawa, H. Hasegawa, K. Yamanouchi and K. Midorikawa. *Conclusive evidence of an attosecond pulse train observed with the mode-resolved autocorrelation technique.* Physical Review Letters, **96**, 083901 (2006).

[129] P. Tzallas, E. Skantzakis, L. A. A. Nikolopoulos, G. D. Tsakiris and D. Charalambidis. *Extreme-ultraviolet pump-probe studies of one femtosecond scale electron dynamics.* Nature Physics, **published online** (2011).

[130] Y. Nabekawa, T. Shimizu, Y. Furukawa, E. J. Takahashi and K. Midorikawa. *Interferometry of Attosecond Pulse Trains in the Extreme Ultraviolet Wavelength Region.* Physical Review Letters, **102**, 213904 (2009).

[131] T. Kobayashi, J. H. Geng and M. Takami. *Electric-field-enhanced predissociation of the NO molecule studied by the two-color resonant four-wave mixing spectroscopy.* Chemical Physics Letters, **284**, 195–199 (1998).

[132] T. Sekikawa, A. Kosuge, T. Kanai and S. Watanabe. *Nonlinear optics in the extreme ultraviolet.* Nature, **432**, 605–608 (2004).

[133] L. A. A. Nikolopoulos, E. P. Benis, P. Tzallas, D. Charalambidis, K. Witte and G. D. Tsakiris. *Second order autocorrelation of an XUV attosecond pulse train.* Physical Review Letters, **94**, 113905 (2005).

[134] Y. Nabekawa, T. Shimizu, T. Okino, K. Furusawa, H. Hasegawa, K. Yamanouchi and K. Midorikawa. *Interferometric autocorrelation of an attosecond pulse train in the single-cycle regime.* Physical Review Letters, **97**, 153904 (2006).

[135] D. J. Kane and R. Trebino. *Single-Shot Measurement of the Intensity and Phase of an Arbitrary Ultrashort Pulse by Using Frequency-Resolved Optical Gating.* Optics Letters, **18**, 823–825 (1993).

[136] Y. Mairesse and F. Quere. *Frequency-resolved optical gating for complete reconstruction of attosecond bursts.* Physical Review A, **71**, – (2005).

[137] A. Kosuge, T. Sekikawa, X. Zhou, T. Kanai, S. Adachi and S. Watanabe. *Frequency-resolved optical gating of isolated attosecond pulses in the extreme ultraviolet.* Physical Review Letters, **97**, 263901 (2006).

[138] C. Iaconis and I. A. Walmsley. *Self-referencing spectral interferometry for measuring ultrashort optical pulses.* Ieee Journal of Quantum Electronics, **35**, 501–509 (1999).

[139] Y. Mairesse, O. Gobert, P. Breger, H. Merdji, P. Meynadier, P. Monchicourt, M. Perdrix, P. Salieres and B. Carre. *High harmonic XUV spectral phase interferometry for direct electric-field reconstruction.* Physical Review Letters, **94**, 173903 (2005).

[140] J. Chen, R. Itakura and T. Nakajima. *Characterization of attosecond XUV pulses utilizing a broadband UV VUV pumping.* Optics Express, **18**, 2020–2035 (2010).

[141] N. Miyamoto, M. Kamei, D. Yoshitomi, T. Kanai, T. Sekikawa, T. Nakajima and S. Watanabe. *Observation of two-photon above-threshold ionization of rare gases by xuv harmonic photons.* Physical Review Letters, **93**, 083903 (2004).

[142] T. Okino, K. Yamanouchi, T. Shimizu, K. Furusawa, H. Hasegawa, Y. Nabekawa and K. Midorikawa. *Attosecond molecular Coulomb explosion.* Chemical Physics Letters, **432**, 68–73 (2006).

[143] Y. H. Jiang *et al. Temporal coherence effects in multiple ionization of* $N2$ *via XUV pump-probe autocorrelation.* Physical Review A, **82**, 041403 (2010).

[144] Y. H. Jiang *et al. Investigating two-photon double ionization of D-2 by XUV-pump-XUV-probe experiments.* Physical Review A, **81**, 051402 (2010).

[145] Y. H. Jiang *et al. Ultrafast Extreme Ultraviolet Induced Isomerization of Acetylene Cations.* Physical Review Letters, **105**, 263002 (2010).

[146] A. Peralta Conde, J. Kruse, O. Faucher, P. Tzallas, E. P. Benis and D. Charalambidis. *Realization of time-resolved two-vacuum-ultraviolet-photon ionization.* Physical Review A, **79**, 061405 (2009).

[147] E. Skantzakis, P. Tzallas, J. E. Kruse, C. Kalpouzos, O. Faucher, G. D. Tsakiris and D. Charalambidis. *Tracking Autoionizing-Wave-Packet Dynamics at the 1-fs Temporal Scale.* Physical Review Letters, **105**, 043902 (2010).

[148] X. Chen, L. Canova, A. Malvache, A. Jullien, R. Lopez-Martens, C. Durfee, D. Papadopoulos and F. Druon. *1-mJ, sub-5-fs carrier-envelope phase-locked pulses.* Applied Physics B-Lasers and Optics, **99**, 149–157 (2010).

[149] C. P. Hauri, W. Kornelis, F. W. Helbing, A. Heinrich, A. Couairon, A. Mysyrowicz, J. Biegert and U. Keller. *Generation of intense, carrier-envelope phase-locked few-cycle laser pulses through filamentation.* Applied Physics B-Lasers and Optics, **79**, 673–677 (2004).

[150] H. Mashiko, S. Gilbertson, C. Q. Li, S. D. Khan, M. M. Shakya, E. Moon and Z. H. Chang. *Double optical gating of high-order harmonic generation with carrier-envelope phase stabilized lasers.* Physical Review Letters, **100**, 103906 (2008).

[151] H. Mashiko, S. Gilbertson, C. Li, E. Moon and Z. Chang. *Optimizing the photon flux of double optical gated high-order harmonic spectra.* Physical Review A, **77**, 063423 (2008).

[152] X. M. Feng, S. Gilbertson, H. Mashiko, H. Wang, S. D. Khan, M. Chini, Y. Wu, K. Zhao and Z. H. Chang. *Generation of Isolated Attosecond Pulses with 20 to 28 Femtosecond Lasers.* Physical Review Letters, **103**, 183901 (2009).

[153] S. Gilbertson, Y. Wu, S. D. Khan, M. Chini, K. Zhao, X. Feng and Z. Chang. *Isolated attosecond pulse generation using multicycle pulses directly from a laser amplifier.* Physical Review A, **81**, 043810 (2010).

[154] C. Siedschlag, H. G. Mller and M. J. J. Vrakking. *Generation of Isolated Attosecond Pulses by Two-Color Laser Fields.* Laser Physics, **15**, 916–925 (2005).

[155] T. Pfeifer, L. Gallmann, M. J. Abel, P. M. Nagel, D. M. Neumark and S. R. Leone. *Heterodyne Mixing of Laser Fields for Temporal Gating of High-Order Harmonic Generation.* Physical Review Letters, **97**, 163901 (2006).

[156] E. J. Takahashi, P. Lan, O. D. Mücke, Y. Nabekawa and K. Midorikawa. *Infrared Two-Color Multicycle Laser Field Synthesis for Generating an Intense Attosecond Pulse.* Physical Review Letters, **104**, 233901 (2010).

[157] E. Takahashi, Y. Nabekawa, T. Otsuka, M. Obara and K. Midorikawa. *Generation of highly coherent submicrojoule soft x rays by high-order harmonics.* Physical Review A, **66**, 021802 (2002).

[158] E. Takahashi, Y. Nabekawa and K. Midorikawa. *Generation of 10- μJ coherent extreme-ultraviolet light by use of high-order harmonics.* Optics Letters, **27**, 1920–1922 (2002).

[159] G. D. Tsakiris, K. Eidmann, J. Meyer-ter Vehn and F. Krausz. *Route to intense single attosecond pulses.* New Journal of Physics, **8**, – (2006).

[160] N. M. Naumova, J. A. Nees, I. V. Sokolov, B. Hou and G. A. Mourou. *Relativistic Generation of Isolated Attosecond Pulses in a λ^3 Focal Volume.* Physical Review Letters, **92**, 063902 (2004).

[161] S. V. Bulanov, N. M. Naumova and F. Pegoraro. *Interaction of an ultrashort, relativistically strong laser pulse with an overdense plasma.* Physics of Plasmas, **1**, 745–757 (1994).

[162] R. Lichters, Meyer and A. Pukhov. *Short-pulse laser harmonics from oscillating plasma surfaces driven at relativistic intensity.* Physics of Plasmas, **3**, 3425–3437 (1996).

[163] L. Plaja, L. Roso, K. Rzazewski and M. Lewenstein. *Generation of attosecond pulse trains during the reflection of a very intense laser on a solid surface.* Journal of the Optical Society of America B, **15**, 1904–1911 (1998).

[164] A. Tarasevitch, A. Orisch, D. von der Linde, P. Balcou, G. Rey, J.-P. Chambaret, U. Teubner, D. Klöpfel and W. Theobald. *Generation of high-order spatially coherent harmonics from solid targets by femtosecond laser pulses.* Physical Review A, **62**, 023816 (2000).

[165] F. Quéré, C. Thaury, P. Monot, S. Dobosz, P. Martin, J.-P. Geindre and P. Audebert. *Coherent Wake Emission of High-Order Harmonics from Overdense Plasmas.* Physical Review Letters, **96**, 125004 (2006).

[166] B. Dromey *et al. High harmonic generation in the relativistic limit.* Nature Physics, **2**, 456–459 (2006).

[167] B. Dromey *et al. Bright Multi-keV Harmonic Generation from Relativistically Oscillating Plasma Surfaces.* Physical Review Letters, **99**, 085001 (2007).

[168] C. Thaury *et al. Plasma mirrors for ultrahigh-intensity optics.* Nature Physics, **3**, 424–429 (2007).

[169] Y. Nomura *et al. Attosecond phase locking of harmonics emitted from laser-produced plasmas.* Nature Physics, **5**, 124–128 (2009).

[170] L. B. E. Bom, S. Haessler, O. Gobert, M. Perdrix, F. Lepetit, J.-F. Hergott, B. Carré, T. Ozaki and P. Salières. *Attosecond emission from chromium plasma.* Optics Express, **19**, 3677–3685 (2011).

[171] T. Baeva, S. Gordienko and A. Pukhov. *Relativistic plasma control for single attosecond x-ray burst generation.* Physical Review E, **74**, 065401 (2006).

[172] S. G. Rykovanov, M. Geissler, J. M. ter Vehn and G. D. Tsakiris. *Intense single attosecond pulses from surface harmonics using the polarization gating technique.* New Journal of Physics, **10**, 025025 (2008).

[173] P. Heissler *et al. Toward single attosecond pulses using harmonic emission fromsolid-density plasmas.* Applied Physics B: Lasers and Optics, **101**, 511–521 (2010).

[174] Y. Tamaki, J. Itatani, Y. Nagata, M. Obara and K. Midorikawa. *Highly Efficient, Phase-Matched High-Harmonic Generation by a Self-Guided Laser Beam.* Physical Review Letters, **82**, 1422–1425 (1999).

[175] R. Bartels, S. Backus, E. Zeek, L. Misoguti, G. Vdovin, I. P. Christov, M. M. Murnane and H. C. Kapteyn. *Shaped-pulse optimization of coherent emission of high-harmonic soft X-rays.* Nature, **406**, 164–166 (2000).

[176] E. Takahashi, Y. Nabekawa, H. Mashiko, H. Hasegawa, A. Suda and K. Midorikawa. *Generation of strong optical field in soft X-ray region by using high-order harmonics.* Selected Topics in Quantum Electronics, IEEE Journal of, **10**, 1315 – 1328 (2004).

[177] S. Kazamias, D. Douillet, F. Weihe, C. Valentin, A. Rousse, S. Sebban, G. Grillon, F. Augé, D. Hulin and P. Balcou. *Global Optimization of High Harmonic Generation.* Physical Review Letters, **90**, 193901 (2003).

[178] K. Midorikawa, Y. Nabekawa and A. Suda. *XUV multiphoton processes with intense high-order harmonics.* Progress in Quantum Electronics, **32**, 43 – 88 (2008).

[179] J. F. Hergott, M. Kovacev, H. Merdji, C. Hubert, Y. Mairesse, E. Jean, P. Breger, P. Agostini, B. Carre and P. Salieres. *Extreme-ultraviolet high-order harmonic pulses in the microjoule range.* Physical Review A, **66**, 021801(R) (2002).

[180] E. J. Takahashi, H. Hasegawa, Y. Nabekawa and K. Midorikawa. *High-throughput, high-damage-threshold broadband beam splitter for high-order harmonics in the extreme-ultraviolet region.* Optics Letters, **29**, 507–509 (2004).

[181] O. Ghafur, W. Siu, P. Johnsson, M. F. Kling, M. Drescher and M. J. J. Vrakking. *A velocity map imaging detector with an integrated gas injection system.* Review of Scientific Instruments, **80**, 033110 (2009).

[182] J. L. Sanz-Vicario, H. Bachau and F. Martin. *Time-dependent theoretical description of molecular autoionization produced by femtosecond xuv laser pulses.* Physical Review A, **73**, 033410 (2006).

[183] A. Lafosse, J. C. Brenot, A. V. Golovin, P. M. Guyon, K. Hoejrup, J. C. Houver, M. Lebech and D. Dowek. *Vector correlations in dissociative photoionization of O_2 in the 20 - 28 eV range. I. Electron-ion kinetic energy correlations.* The Journal of Chemical Physics, **114**, 6605–6617 (2001).

[184] Y. Lu, Z. X. He, J. N. Cutler, S. H. Southworth, W. C. Stolte and J. A. R. Samson. *Dissociative photoionization study of* O_2. J Electron spectrosc. Relat. Phenom., **94**, 135–147 (1998).

[185] J. Parker and C. R. Stroud. *Coherence and decay of Rydberg wave Packets.* Physical Review Letters, **56**, 716–719 (1986).

[186] H. Ihee, V. A. Lobastov, U. M. Gomez, B. M. Goodson, R. Srinivasan, C. Y. Ruan and A. H. Zewail. *Direct imaging of transient molecular structures with ultrafast diffraction.* Science, **291**, 458–462 (2001).

[187] B. J. Siwick, J. R. Dwyer, R. E. Jordan and R. J. D. Miller. *An atomic-level view of melting using femtosecond electron diffraction.* Science, **302**, 1382–1385 (2003).

[188] N. Gedik, D. S. Yang, G. Logvenov, I. Bozovic and A. H. Zewail. *Nonequilibrium phase transitions in cuprates observed by ultrafast electron crystallography.* Science, **316**, 425–429 (2007).

[189] F. Krasniqi, B. Najjari, L. Struder, D. Rolles, A. Voitkiv and J. Ullrich. *Imaging molecules from within: Ultrafast angstrom-scale structure determination of molecules via photoelectron holography using free-electron lasers.* Physical Review A, **81**, 033411 (2010).

[190] S. X. Hu, L. A. Collins and B. I. Schneider. *Attosecond photoelectron microscopy of* H_2^+. Physical Review A, **80**, 023426 (2009).

[191] R. Neutze, R. Wouts, D. van der Spoel, E. Weckert and J. Hajdu. *Potential for biomolecular imaging with femtosecond X-ray pulses.* Nature, **406**, 752–757 (2000).

[192] H. N. Chapman, A. Barty, M. J. Bogan, S. Boutet, M. Frank, S. P. Hau-Riege, S. Marchesini, B. W. Woods, S. Bajt and W. H. Benner. *Femtosecond diffractive imaging with a soft-X-ray free-electron laser.* Nature Physics, **2**, 839 (2006).

[193] A. Landers *et al. Photoelectron diffraction mapping: Molecules illuminated from within.* Physical Review Letters, **8701**, 013002 (2001).

[194] W. Ackermann, G. Asova, V. Ayvazyan, A. Azima, N. Baboi, J. Bähr, V. Balandin, B. Beutner, A. Brandt and A. Bolzmann. *Operation of a free-electron laser from the extreme ultraviolet to the water window.* Nature Photonics, **1**, 336 (2007).

[195] P. Emma *et al. First lasing and operation of an angstrom-wavelength free-electron laser.* Nature Photonics, **4**, 641–647 (2010).

[196] H. Stapelfeldt. *Alignment of molecules by strong laser pulses.* European Physical Journal D, **26**, 15–19 (2003).

[197] F. Rosca-Pruna and M. J. J. Vrakking. *Experimental observation of revival structures in picosecond laser-induced alignment of* I_2. Physical Review Letters, **87**, 153902 (2001).

[198] O. Ghafur, A. Rouzee, A. Gijsbertsen, W. K. Siu, S. Stolte and M. J. J. Vrakking. *Impulsive orientation and alignment of quantum-state-selected NO molecules.* Nature Physics, **5**, 289–293 (2009).

[199] P. Johnsson *et al. Field-free molecular alignment probed by the free electron laser in Hamburg (FLASH).* Journal of Physics B-Atomic Molecular and Optical Physics, **42**, 134017 (2009).

[200] R. R. Lucchese, D. K. Watson and V. McKoy. *Iterative approach to the Schwinger variational principle for electron-molecule collisions.* Physical Review A, **22**, 421–426 (1980).

[201] R. E. Stratmann, R. W. Zurales and R. R. Lucchese. *Multiplet-specific multichannel electron-correlation effects in the photoionization of NO.* The Journal of Chemical Physics, **104**, 8989–9000 (1996).

[202] R. E. Stratmann and R. R. Lucchese. *A graphical unitary group approach to study multiplet specific multichannel electron correlation effects in the photoionization of* O_2. The Journal of Chemical Physics, **102**, 8493–8505 (1995).

[203] R. Guillemin *et al. Nondipolar electron angular distributions from fixed-in-space molecules.* Physical Review Letters, **89**, 033002 (2002).

[204] H. Niikura, F. Legare, R. Hasbani, A. D. Bandrauk, M. Y. Ivanov, D. M. Villeneuve and P. B. Corkum. *Sub-laser-cycle electron pulses for probing molecular dynamics.* Nature, **417**, 917–922 (2002).

[205] T. Kanai, S. Minemoto and H. Sakai. *Quantum interference during high-order harmonic generation from aligned molecules.* Nature, **435**, 470–474 (2005).

[206] J. Mauritsson, P. Johnsson, E. Gustafsson, A. L'Huillier, K. J. Schafer and M. B. Gaarde. *Attosecond pulse trains generated using two color laser fields.* Physical Review Letters, **97**, 013001 (2006).

[207] K. J. Schafer, M. B. Gaarde, A. Heinrich, J. Biegert and U. Keller. *Strong Field Quantum Path Control Using Attosecond Pulse Trains.* Physical Review Letters, **92**, 023003 (2004).

[208] J. Biegert, A. Heinrich, C. Hauri, W. Kornelis, P. Schlup, M. Anscombe, K. J. Schafer, M. B. Gaarde and U. Keller. *Enhancement of High-order harmonic emission using attosecond pulse trains.* Laser Physics, **15**, 899–902 (2005).

[209] P. Salieres *et al. Feynman's path-integral approach for intense-laser-atom interactions.* Science, **292**, 902–905 (2001).

[210] J. A. Hostetter, J. L. Tate, K. J. Schafer and M. B. Gaarde. *Semiclassical approaches to below-threshold harmonics.* Physical Review A, **82**, 023401 (2010).

[211] C. Nicole, I. Sluimer, F. Rosca-Pruna, M. Warntjes, M. Vrakking, C. Bordas, F. Texier and F. Robicheaux. *Slow photoelectron imaging.* Physical Review Letters, **85**, 4024–4027 (2000).

[212] D. W. Chandler and P. L. Houston. *Two-dimensional imaging of state selected photodissociation products detected by multiphoton ionization.* Journal of Chemical Physics, **87**, 1445–1447 (1987).

[213] A. J. R. Heck and D. W. Chandler. *Imaging Techniques for the study of chemical reaction dynamics.* Annual Review of Physical Chemistry, **46**, 335–372 (1995).

[214] A. Eppink and D. Parker. *Velocity Map Imaging of ions and electron using electostatic lenses: Application in photoelectron and photofragment ion imaging of molecular oxygen.* Review of Scientific Instruments, **68**, 3447–3484 (1997).

[215] V. Papadakis and T. Kitsopoulos. *Slice Imaging and velocity mapping using a single field.* Review of Scientific Instruments, **77**, 083101 (2006).

[216] R. Moshammer, M. Unverzagt, W. Schmitt, J. Ullrich and H. Schmidt-Böcking. *A 4π recoil ion electron momentum analyzer: A high resolution 'microscope' for the investigation of the dynamics of atomic and molecular and nuclear reactions.* Nuclear Instruments and Methods in Physics Research B, **108**, 425–445 (1996).

[217] J. Ullrich, R. Moshammer, A. Dorn, L. Schmidt and H. Schmidt-Böcking. *Recoil-ion and electron momentum spectroscopy: reaction-microscopes.* Reports on Progress in Physics, **66**, 1463–1545 (2003).

[218] D. de Bruijn and J. Los. *Time and position-sensitive detector for dissociative processes in fast ion beams.* Review of Scientific Instruments, **53**, 1020–1026 (1982).

[219] B.-Y. Chang, R. Hoetzlein, J. Mueller, J. Geiser and P. Houston. *Improved two-dimensional product imaging: The real-time ion-counting method.* Review of Scientific Instruments, **69**, 1665–1670 (1998).

[220] R. Dörner, V. Mergel, O. Jagutzki, L. Spielberger, J. Ullrich, R. Moshammer and H. Schmidt-Böcking. *Cold target recoil ion momentum spectroscopy: a 'momentum microscope' to view atomic collision dynamics.* Physics Reports, **330**, 95–192 (2000).

[221] RoentDek Handels GmbH. Kelkheim-Ruppertshain, Germany.

[222] V. Mergel, O. Jagutzki, L. Spielberger, K. Ullmann-Pfleger, R. Dörner and H. Schmidt-Böcking. *Particle and UV-imaging with position sensitive MCP-detectors - three dimensional momentum space imaging.* Materials Research Society Symposium Proceedings 1998, **502**, 171–176 (1998).

[223] J. Vallerga, J. McPhate, A. Tremsin and O. Siegmund. *The current and future capabilities of MCP based UV detectors.* Astrophysics and Space Science, **320**, 247–250 (2009).

[224] J. Lapington. *A Comparison of readout techniques for high resolution imaging with microchannel plate detectors.* Nuclear Instruments and Methods in Physics Research A, **525**, 361–365 (2004).

[225] *www.cern.ch/medipix.* (homepage of the Medipix collaboration).

[226] X. Llopart, M. Campbell, R. Dinapoli, D. S. Segundo and E. Pernigotti. *Medipix2, a 64k pixel readout chip with 55micron square elements working in single photon counting mode.* IEEE Transactions on Nuclear Science, **49**, 2279–2283 (2002).

[227] X. Llopart and M. Campbell. *First test measurements of a 64k pixel reaout chip working in single photon counting mode.* Nuclear Instruments and Methods in Physics Research Section A, **509**, 157–163 (2003).

[228] G. McMullan, D. Cattermole, S. Chen, R. Henderson, X. Llopart, C. Summerfield, L. Tlustos and A. Faruqi. *Electron imaging with Medipix2 hybrid pixel detector.* Ultramicroscopy, **107**, 401–413 (2007).

[229] A. Faruqi, R. Henderson and L. Tlustos. *Noiseless direct detection of electrons in Medipix2 for Electron Microscopy.* Nuclear Instruments and Methods in Physics Research A, **546**, 160–163 (2005).

[230] *aladdin.utef.cvut.cz/ofat/others/Pixelman/index.* (Pixelman software homepage by the Czech Technical University of Prague, IEAP).

[231] T. Holy, J. Jakubek, S. Pospisil, J. Uher, D. Vavrik and Z. Vykydal. *Data acquisition and processung software package for Medipix2.* Nuclear Instruments and Methods in Physics Research A, **563**, 254–258 (2006).

[232] *alladin.utef.cvut.cz/ofat/others/USB_interface/index.html.* (Medipix-Timepix Interface homepage by the Czech Technical University of Prague, IEAP).

[233] Z. Vykydal, J. Jakubek and S. Pospisil. *USB interface for Medipix2 pixel device enabling energy and position detection of heavy charged particles.* Nuclear Instruments and Methods in Physics Research A, **563**, 112–115 (2006).

[234] *www.nikhef.nl/pub/experiments/medipix/muros.html.* (MUROS-interface project homepage by the National Institute for Sub-Atomic Physics (Nikhef)).

[235] D. S. Segundo, M. van Beuzekom, P. Jansweijer, H. Verkooijen and J. Visschers. *An interface board for the control and data acquisition of the Medipix2 chip.* Nuclear Instruments and Methods in Physics Research A, **509**, 164–170 (2003).

[236] H. d. Graaf, J. Timmermans, J. Visschers, M. Campbell and P. Colas. *www.nikhef.nl/pub/experiments/medipix/TimePix.pdf* (2004). (Timepix Proposal).

[237] J. Vallerga, J. McPhate, A. Tremsin, O. Siegmund, B. Mikulec and A. Clark. *Optically sensitive Medipix2 detector for adaptive optics wavefront sensing.* Nuclear Instruments and Methods in Physics Research A, **546**, 263–269 (2005).

[238] B. Mikulec *et al. A noiseless kilohertz frame rate imaging detector based on microchannel plates read out with the Medipix CMOS pixel chip.* Nuclear Instruments and Methods in Physics Research Section A, **567**, 110–113 (2006).

[239] X. Llopart, R. Ballabriga, M. Campbell, L. Tlustos and W. Wong. *Timepix a 65k programmablepixel readout chip for arrival time, energy and/or photon counting measurement NIM-A.* Nuclear Instruments and Methods in Physics Research Section A, **581**, 485–494 (2007).

[240] Z. Vykydal, J. Visschers, D. S. Tezcan, K. D. Munck, T. Borgers, W. Ruythooren and P. D. Moor. *The RELAXd project: Development of four-side tilable photon-counting imagers.* Nuclear Instruments and Methods in Physics Research Section A: Accelerators, Spectrometers, Detectors and Associated Equipment, **591**, 241 – 244 (2008). Radiation Imaging Detectors 2007 - Proceedings of the 9th International Workshop on Radiation Imaging Detectors.

[241] *medipix.web.cern.ch/MEDIPIX/Medipix3/homeMP3.htm.* (Medipix3 project homepage by the Medipix Collaboration).

[242] M. Lipciuc, J. Buijs and M. H. M. Janssen. *High resolution slice imaging of a molecular speed distribution.* Physical Chemistry Chemical Physics, **8**, 219–223 (2006).

[243] P. Kruit, J. Kimman, H. Muller and M. van der Wiel. *Electron spectra from multiphoton ionization of xenon at 1064, 532 and 355nm.* Physical Review A, **28**, 248–255 (1983).

[244] M. Chmeissani, M. Maiorino, G. Blanchot, G. Pellegrini, J. Garcia, M. Lozano, R. Martinez, C. Puigdengoles and M. Ullan. *Charge Sharing measurements of pixelated CdTe using Medipix-II chip.* IMTC 2004 - Instrumentation and Measurement Technology Conference (2004).

[245] M. Campbell *et al. Study of the charge sharing in a silicon pixel detector by means of α-particles interacting with a Medipix2 device.* Nuclear

Instruments and Methods in Physics Research Section A, **591**, 38–41 (2008).

[246] A. Jablonski, F. Salvat and C. Powell. *NIST electron elastic-scattering cross-section database, Version 3.1.* Standard Reference Data Program Database 64 (National Institute of Standards and Technology).

[247] J. H. Jungmann, A. Gijsbertsen, J. Visser, J. Visschers, R. M. A. Heeren and M. J. J. Vrakking. *A new imaging method for understanding chemical dynamics: Efficient slice imaging using an in-vacuum pixel detector.* Review of Scientific Instruments, **81**, 103112 (2010).

[248] J. H. Jungmann, L. MacAleese, R. Buijs, F. Giskes, A. de Snaijer, J. Visser, J. Visschers, M. J. Vrakking and R. M. Heeren. *Fast, High Resolution Mass Spectrometry Imaging Using a Medipix Pixelated Detector.* Journal of the American Society for Mass Spectrometry, **21**, 2023 – 2030 (2010).

[249] M. Campbell. *10 years of the Medipix2 Collaboration.* Nuclear Instruments and Methods in Physics Research A, **633 Suppl. 1**, S1–S10 (2011).

[250] M. Kakehata *et al. Carrier-envelope-phase stabilized chirped-pulse amplification system scalable to higher pulse energies.* Optics Express, **12**, 2070–2080 (2004).

[251] T. Imran, Y. S. Lee, C. H. Nam, K. H. Hong, T. J. Yu and J. H. Sung. *Stabilization and control of the carrier-envelope phase of high-power femtosecond laser pulses using the direct locking technique.* Optics Express, **15**, 104–112 (2007).

[252] S. Adachi, N. Ishii, T. Kanai, A. Kosuge, J. Itatani, Y. Kobayashi, D. Yoshitomi, K. Torizuka and S. Watanabe. *5-fs, multi-mJ, CEP-locked parametric chirped-pulse amplifier pumped by a 450-nm source at 1 kHz.* Optics Express, **16**, 14341–14352 (2008).

[253] L. Canova, X. W. Chen, A. Trisorio, A. Jullien, A. Assion, G. Tempea, N. Forget, T. Oksenhendler and R. Lopez-Martens. *Carrier-envelope phase stabilization and control using a transmission grating compressor and an AOPDF.* Optics Letters, **34**, 1333–1335 (2009).

[254] T. Fordell, M. Miranda, A. Persson and A. L'Huillier. *Carrier-envelope phase stabilization of a multi-millijoule, regenerative-amplifier-based chirped-pulse amplifier system.* Optics Express, **17**, 21091–21097 (2009).

[255] S. Rausch, T. Binhammer, A. Harth, J. Kim, R. Ell, F. X. Kartner and U. Morgner. *Controlled waveforms on the single-cycle scale from a femtosecond oscillator.* Optics Express, **16**, 9739–9745 (2008).

[256] U. Keller, K. J. Weingarten, F. X. Kartner, D. Kopf, B. Braun, I. D. Jung, R. Fluck, C. Honninger, N. Matuschek and J. Aus der Au. *Semiconductor saturable absorber mirrors (SESAM's) for femtosecond to nanosecond pulse generation in solid-state lasers.* Ieee Journal of Selected Topics in Quantum Electronics, **2**, 435–453 (1996).

[257] D. E. Spence, P. N. Kean and W. Sibbett. *60-fsec pulse generation from a self-mode-locked Ti:sapphire laser.* Optics Letters, **16**, 42–44 (1991).

[258] P. F. Moulton. *Spectroscopic and laser characteristics of Ti:Al2O3.* Journal of the Optical Society of America B, **3**, 125–133 (1986).

[259] B. Saleh and M. Teich. *Fundamentals of Photonics.* John Wiley and Sons, Inc, (1991).

[260] J. C. Diels and W. Rudolph. *Ultrashort Laser Pulse Phenomena.* Academic Press, New York, 2nd. ed. (2006).

[261] S. Hooker and C. Webb. *Laser Physics.* Oxford University Press (2010).

[262] E. B. Treacy. *Optical Pulse Compression With Diffraction Gratings.* Ieee Journal of Quantum Electronics, **5**, 454–460 (1969).

[263] S. Backus, C. G. Durfee, M. M. Murnane and H. C. Kapteyn. *High power ultrafast lasers.* Review of Scientific Instruments, **69**, 1207–1223 (1998).

[264] F. Rosca-Pruna. *Alignment of diatomic molecules induced by intense laser fields.* Ph.D. thesis, FOM Institute AMOLF (2001).

[265] R. L. Fork, O. E. Martinez and J. P. Gordon. *Negative dispersion using pairs of prisms.* Optics Letters, **9**, 150–152 (1984).

[266] J. P. Gordon and R. L. Fork. *Optical resonator with negative dispersion.* Optics Letters, **9**, 153–155 (1984).

[267] R. Szipöcs, K. Ferencz, C. Spielmann and F. Krausz. *Chirped multilayer coatings for broadband dispersion control in femtosecond lasers.* Optics Letters, **19**, 201–203 (1994).

[268] C. Dorrer, F. Salin, F. Verluise and J. P. Huignard. *Programmable phase control of femtosecond pulses by use of a nonpixelated spatial light modulator.* Optics Letters, **23**, 709–711 (1998).

[269] E. Zeek, K. Maginnis, S. Backus, U. Russek, M. Murnane, G. Mourou, H. Kapteyn and G. Vdovin. *Pulse compression by use of deformable mirrors.* Optics Letters, **24**, 493–495 (1999).

[270] F. Verluise, V. Laude, Z. Cheng, C. Spielmann and P. Tournois. *Amplitude and phase control of ultrashort pulses by use of an acousto-optic programmable dispersive filter: pulse compression and shaping.* Optics Letters, **25**, 575–577 (2000).

[271] A. Major, F. Yoshino, I. Nikolakakos, J. S. Aitchison and P. W. E. Smith. *Dispersion of the nonlinear refractive index in sapphire.* Optics Letters, **29**, 602–604 (2004).

[272] P. Maine, D. Strickland, P. Bado, M. Pessot and G. Mourou. *Generation of ultrahigh peak power pulses by chirped pulse amplification.* Quantum Electronics, IEEE Journal of, **24**, 398 –403 (1988).

[273] I. Walmsley, L. Waxer and C. Dorrer. *The role of dispersion in ultrafast optics.* Review of Scientific Instruments, **72**, 1–29 (2001).

[274] D. Clery. *Taking Laser Science to the Extreme.* Science, **328**, 806–807 (2010).

[275] A. V. Korzhimanov, A. A. Gonoskov, E. A. Khazanov and A. M. Sergeev. *Horizons of petawatt laser technology.* Physics-Uspekhi, **54**, 9 (2011).

[276] G. Mourou, A. Sergeev, A. Korzhimanov, A. Gonoskov and E. Khazanov. *Extreme light fields and their fundamental applications.* Herald of the Russian Academy of Sciences, **81**, 211–217 (2011).

[277] T. Udem, R. Holzwarth and T. W. Hansch. *Optical frequency metrology.* Nature, **416**, 233–237 (2002).

[278] H. R. Telle, G. Steinmeyer, A. E. Dunlop, J. Stenger, D. H. Sutter and U. Keller. *Carrier-envelope offset phase control: A novel concept for absolute optical frequency measurement and ultrashort pulse generation.* Applied Physics B-Lasers and Optics, **69**, 327–332 (1999).

[279] D. J. Jones, S. A. Diddams, J. K. Ranka, A. Stentz, R. S. Windeler, J. L. Hall and S. T. Cundiff. *Carrier-envelope phase control of femtosecond mode-locked lasers and direct optical frequency synthesis.* Science, **288**, 635–639 (2000).

[280] R. Holzwarth, T. Udem, T. W. Hänsch, J. C. Knight, W. J. Wadsworth and P. S. J. Russell. *Optical Frequency Synthesizer for Precision Spectroscopy.* Physical Review Letters, **85**, 2264–2267 (2000).

[281] M. Mehendale, S. A. Mitchell, J. P. Likforman, D. M. Villeneuve and P. B. Corkum. *Method for single-shot measurement of the carrier envelope phase of a few-cycle laser pulse.* Optics Letters, **25**, 1672–1674 (2000).

[282] M. Kakehata, H. Takada, Y. Kobayashi, K. Torizuka, Y. Fujihira, T. Homma and H. Takahashi. *Single-shot measurement of carrier-envelope phase changes by spectral interferometry.* Optics Letters, **26**, 1436–1438 (2001).

[283] M. Kakehata, Y. Fujihira, H. Takada, Y. Kobayashi, K. Torizuka, T. Homma and H. Takahashi. *Measurements of carrier-envelope phase changes of 100-Hz amplified laser pulses.* Applied Physics B: Lasers and Optics, **74**, s43–s50 (2002).

[284] R. Ell *et al. Generation of 5-fs pulses and octave-spanning spectra directly from a Ti:sapphire laser.* Optics Letters, **26**, 373–375 (2001).

[285] T. M. Fortier, D. J. Jones, J. Ye, S. T. Cundiff and R. S. Windeler. *Long-term carrier-envelope phase coherence.* Optics Letters, **27**, 1436–1438 (2002).

[286] A. Baltuska, T. Fuji and T. Kobayashi. *Controlling the carrier-envelope phase of ultrashort light pulses with optical parametric amplifiers.* Physical Review Letters, **88**, 133901 (2002).

[287] T. Fuji, A. Apolonski and F. Krausz. *Self-stabilization of carrier-envelope offset phase by use of difference-frequency generation.* Optics Letters, **29**, 632–634 (2004).

[288] S. Koke, C. Grebing, B. Manschwetus and G. Steinmeyer. *Fast f-to-2f interferometer for a direct measurement of the carrier-envelope phase drift of ultrashort amplified laser pulses.* Optics Letters, **33**, 2545–2547 (2008).

[289] J. Reichert, R. Holzwarth, T. Udem and T. W. Hansch. *Measuring the frequency of light with mode-locked lasers.* Optics Communications, **172**, 59–68 (1999).

[290] K. F. Kwong, D. Yankelevich, K. C. Chu, J. P. Heritage and A. Dienes. *400-Hz mechanical scanning optical delay line.* Optics Letters, **18**, 558–560 (1993).

[291] F. W. Helbing, G. Steinmeyer, U. Keller, R. S. Windeler, J. Stenger and H. R. Telle. *Carrier-envelope offset dynamics of mode-locked lasers.* Optics Letters, **27**, 194–196 (2002).

[292] A. Poppe, R. Holzwarth, A. Apolonski, G. Tempea, C. Spielmann, T. Hnsch and F. Krausz. *Few-cycle optical waveform synthesis.* Applied Physics B: Lasers and Optics, **72**, 373–376 (2001).

[293] L. Xu, C. Spielmann, A. Poppe, T. Brabec, F. Krausz and T. W. Hansch. *Route to phase control of ultrashort light pulses.* Optics Letters, **21**, 2008–2010 (1996).

[294] P. M. Goorjian and S. T. Cundiff. *Nonlinear effects on the carrier-envelope phase.* Optics Letters, **29**, 1363–1365 (2004).

[295] F. Helbing, G. Steinmeyer, J. Stenger, H. Telle and U. Keller. *Carrier-envelope-offset dynamics and stabilization of femtosecond pulses.* Applied Physics B: Lasers and Optics, **74**, s35–s42 (2002).

[296] A. Poppe, A. Holzwarth, A. Apolonski, G. Tempea, C. Spielmann, P. Hnsch and F. Krausz. *Erratum: Appl. Phys. B , 373-376 (2001).* Applied Physics B: Lasers and Optics, **72**, 977–977 (2001).

[297] S. Koke, C. Grebing, H. Frei, A. Anderson, A. Assion and G. Steinmeyer. *Direct frequency comb synthesis with arbitrary offset and shot-noise-limited phase noise.* Nat Photon, **4**, 462–465 (2010).

[298] A. Apolonski, A. Poppe, G. Tempea, C. Spielmann, T. Udem, R. Holzwarth, T. W. Hansch and F. Krausz. *Controlling the phase evolution of few-cycle light pulses.* Physical Review Letters, **85**, 740–743 (2000).

[299] P. Dombi *et al. Direct measurement and analysis of the carrier-envelope phase in light pulses approaching the single-cycle regime.* New Journal of Physics, **6**, 39 (2004).

[300] I. Thomann, E. Gagnon, R. J. Jones, A. S. Sandhu, A. Lytle, R. Anderson, J. Ye, M. Murnane and H. Kapteyn. *Investigation of a grating-based stretcher/compressor for carrier-envelope phase stabilized fs pulses.* Optics Express, **12**, 3493–3499 (2004).

[301] E. Gagnon, I. Thomann, A. Paul, A. L. Lytle, S. Backus, M. M. Murnane, H. C. Kapteyn and A. S. Sandhu. *Long-term carrier-envelope phase stability from a grating-based, chirped pulse amplifier.* Optics Letters, **31**, 1866–1868 (2006).

[302] Z. Chang. *Carrier-envelope phase shift caused by grating-based stretchers and compressors.* Applied Optics, **45**, 8350–8353 (2006).

[303] C. Q. Li, E. Moon and Z. H. Chang. *Carrier-envelope phase shift caused by variation of grating separation.* Optics Letters, **31**, 3113–3115 (2006).

[304] C. Q. Li, E. Moon, H. Mashiko, C. M. Nakamura, P. Ranitovic, C. M. Maharjan, C. L. Cocke, Z. H. Chang and G. G. Paulus. *Precision control of carrier-envelope phase in grating based chirped pulse amplifiers.* Optics Express, **14**, 11468–11476 (2006).

[305] E. Moon, H. Wang, S. Gilbertson, H. Mashiko, M. Chini and Z. H. Chang. *Advances in carrier-envelope phase stabilization of grating-based chirped-pulse amplifiers.* Laser & Photonics Reviews, **4**, 160–177 (2010).

[306] N. Forget, L. Canova, X. Chen, A. Jullien and R. Lopez-Martens. *Closed-loop carrier-envelope phase stabilization with an acousto-optic programmable dispersive filter.* Optics Letters, **34**, 3647–3649 (2009).

[307] J.-F. Hergott *et al. Carrier-Envelope Phase stabilization of a 20 W, grating based, chirped-pulse amplified laser, using Electro-Optic effect in a LiNbO3 crystal.* Opt. Express, **19**, 19935–19941 (2011).

[308] O. Gobert, P. Paul, J. Hergott, O. Tcherbakoff, F. Lepetit, P. D. 'Oliveira, F. Viala and M. Comte. *Carrier-envelope phase control using linear electro-optic effect.* Opt. Express, **19**, 5410–5418 (2011).

[309] H. Gimpel. *Erzeugung und Anwendung intensiver ultrakurzer Lichtpulse mit stabiler Träger-Einhüllenden-Phase.* Ph.D. thesis, Ruprecht-Karls-Universität Heidelberg (2006).

[310] G. Cheriaux, P. Rousseau, F. Salin, J. P. Chambaret, B. Walker and L. F. Dimauro. *Aberration-free stretcher design for ultrashort-pulse amplification.* Optics Letters, **21**, 414–416 (1996).

[311] C. LeBlanc, P. Curley and F. Salin. *Gain-narrowing and gain-shifting of ultra-short pulses in Ti:sapphire amplifiers.* Optics Communications, **131**, 391–398 (1996).

[312] L. M. Frantz and J. S. Nodvik. *Theory of Pulse Propagation in a Laser Amplifier.* Journal of Applied Physics, **34**, 2346–2349 (1963).

[313] C. Li, E. Moon, H. Wang, H. Mashiko, C. M. Nakamura, J. Tackett and Z. Chang. *Determining the phase-energy coupling coefficient in carrier-envelope phase measurements.* Optics Letters, **32**, 796–798 (2007).

[314] C. Li, E. Moon, H. Mashiko, H. Wang, C. M. Nakamura, J. Tackett and Z. Chang. *Mechanism of phase-energy coupling in f-to-2f interferometry.* Applied Optics, **48**, 1303–1307 (2009).

[315] G. Stibenz and G. Steinmeyer. *Optimizing spectral phase interferometry for direct electric-field reconstruction.* Review of Scientific Instruments, **77**, 073105 (2006).

[316] W. Demtröder. *Laserspektroskopie.* Springer, Berlin (1993).

[317] G. Steinmeyer. *personal communication.*

[318] H. Wang, C. Li, J. Tackett, H. Mashiko, C. M. Nakamura, E. Moon and Z. Chang. *Power locking of high-repetition-rate chirped pulse amplifiers.* Applied Physics B: Lasers and Optics, **89**, 275–279 (2007).

Summary

The work described in this thesis aims at further developing experimental techniques as well as improving technological means to explore the motion of electrons in even greater detail than currently possible. The direct measurement of such dynamics in the last two decades has only been possible thanks to continuous technical developments in the fields of both detector and especially laser physics as well as to the creation of ever new experimental methods, which use the available technologies to their full extent.

Molecular dynamics evolve on timescales reaching from several picoseconds down to a few tens of femtoseconds (1 fs = 10^{-15} s). The shutter times of conventional cameras are many orders of magnitude to slow to measure such fast processes. Only with the development of laser sources, which allow the generation of ultrashort laser pulses, the time-resolved measurement of molecular phenomena became feasible. The field which emerged from these developments is known as femto-chemistry. The preferred experimental method in this field are so-called pump-probe experiments, where an initial femtosecond pulse spurs dynamics in the investigated molecules, which subsequently are probed by a second femtosecond pulse arriving at a variable delay.

Since the beginning of this millennium, the combined advances in strong field physics and ultrashort laser technology have made possible the controlled production of laser pulses whose field envelope evolves on timescales lasting a few hundred attoseconds (1 fs = 10^{-18} s) and less. This new technology established the growing field of attosecond science, which focuses mainly on the investigation of electronic motion occurring on few femtoseconds or even sub-femtosecond timescales. Additionally to the short duration of these pulses, the short wavelengths in the extreme ultraviolet range of the optical spectrum and consequently the high photon energies also allow new approaches to resolve nuclear dynamics in molecules.

While the achievable pulse energies of attosecond pulses up to now almost always restricted experimental researchers to investigate processes relying on the absorption of a single extreme ultraviolet-photon, the ultimate goal of attosecond science is to perform pump-probe experiments, where both pump and probe pulse are made up of attosecond pulses. Only in this fashion the ultimate time resolution possible with these pulses will be reached. Until the technology has advanced far enough to make possible such experiments, experimental scientists have been restricted to using two-color fields, consisting of a femtosecond IR laser pulse and an extreme ultraviolet attosecond pulse.

Following the described interconnectedness of technological advances and experimental progress, the work described in this thesis includes developments in both disciplines. The first part of this thesis focuses on new methods in the afore mentioned two-color experiments, while the second part is devoted

to advances in the technology, which will hopefully enable attosecond pump-attosecond probe experiments in the near future.

Two-color attosecond experiments

In the 1990s, fast progress in the field of strong-field light-matter interaction has led to the discovery of high harmonic generation. In a strongly non-linear process intense ultrashort laser pulses interact with an atomic medium. As a consequence, light which is composed of odd harmonics of the fundamental laser field is emitted, reaching wavelengths in the extreme ultraviolet or even soft x-ray regime. In the beginning of this millennium it was discovered that the temporal structure of this radiation under certain conditions could take the shape of bursts with attosecond durations, so-called attosecond pulses. These are the shortest achieved pulse durations so far.

As a consequence, a lively research field exploring the different possibilities to apply these extremely short pulses to measure electron dynamics has developed in the last few years. In **Chapter 2** an extended overview of this field is given, tracing the evolution of attosecond science in the sense of technical achievements and especially the successes in the application of these pulses to probe electron dynamics in a number of different host systems.

In relation to the development of a phase-stable terawatt amplifier in Part 2 of this thesis, the introductory chapter also includes a section which lays out the development in experiments relying on non-linear processes in the extreme ultraviolet spectral region. It focuses in particular on pump-probe experiments utilizing at the same time extreme ultraviolet pump and extreme ultraviolet probe-pulses. In the same context different techniques for the production of intense isolated attosecond pulses from energetic driver pulses are discussed.

In **Chapter 3** a number of two-color attosecond experiments is presented, which were performed in the course of the thesis. They stand in direct relation to the developments laid out in the introductory chapter.

In the first series of these experiments (**Chapter 3.1**) dissociative photoionization of small molecules in the presence of a moderately strong IR field was investigated using attosecond pulses trains as a probe. The measured data represents one of the first demonstrated results to apply attosecond pulses to the investigation of electron dynamics in molecules. The target systems were H_2, D_2 and O_2 molecules. Different fragmentation channels could be distinguished by measuring ion fragment kinetic energies as well as their angular distributions. Both yield as well as the angular distribution of the recorded ion fragments were observed to oscillate as a function of the delay between the IR field and the attosecond pulse train.

While in the case of H_2 and D_2, the yield oscillations could mechanistically be explained in terms of an IR induced coupling between two ionization continua, the interpretation of the results for O_2 proves slightly more difficult, because couplings to nuclear degrees of freedom as well as the existence of sequential processes cannot be ruled out. It was nonetheless possible to extract information on the participating electronic states by thorough analysis of the

ion yield oscillations and the respective delay dependent oscillations of the ion fragment angular distributions. In conclusion, it was shown that attosecond pulses can be used to probe electronic motion, and that ion yield as well as ion fragment angular distributions provide helpful observables for these type of measurements.

Chapter 3.2 presents the results of a new form of electron diffraction experiments, which could be used in the future to directly measure nuclear dynamics of molecules. Even though this experiment does not rely on the pulse duration of the attosecond pulses, it uses their photon energy to ionize electrons with a sufficiently short DeBroglie wavelength to allow scattering off the atomic centers as they leave the molecule. By recording the diffraction patterns, the position of the scattering centers, in this case the atoms, could potentially be extracted.

In order to successfully measure such diffraction signatures, it is necessary to measure the photo-electron angular distributions in the molecular frame. Field-free alignment techniques were used to achieve a high degree of alignment in CO_2 molecules at the moment of ionization through an extreme ultraviolet pulse. This allowed the measurements of the necessary molecular frame photo-electron angular distributions (MFADS). Comparison of the experimental results with theoretical calculations allowed the conclusion that onsets of both electronic as well as atomic structural information was imprinted in the MFADS. While at the moment this experiment only probed the static case, structural dynamics could easily be probed by introducing an additional pump pulse to the experiment.

The last experiment presented in **Chapter 3.3** shows the control of electron-ion recollision in the process of high harmonic generation. It therefore potentially forms an important tool for experiments, in which the recolliding electron is used as a probe to the generating system, allowing four-dimensional imaging with Ångström spatial and attosecond temporal resolution. The experimental principle relies on decoupling ionization and subsequent acceleration in a coincident infrared field by replacing the tunneling step in the semi-classical three-step model of high harmonic generation by a single-photon ionization via absorption of an extreme ultraviolet photon. These photons are provided at well defined points in time through an APT, which is synchronized to the accelerating IR field.

Measurements of the yield of high harmonic radiation generated in helium as a function of the delay between the attosecond pulse train and the infrared driving field show an oscillatory behavior with a maximum in generation efficiency achieved once per half-cycle of the fundamental infrared field. These results were well reproduced both in single atom as well as in macroscopic calculations and proved the working of the proposed control principle.

New technologies for the use in attosecond experiments

There is one inherent problem with the generation of isolated attosecond pulses via high harmonic generation in gas targets, which is the low conversion effi-

ciency from the driving photons to photons in the extreme ultraviolet region. While for the generation of attosecond pulse trains the conversion efficiencies are slightly higher, for isolated attosecond pulses they commonly lie only on the order of 10^{-7} - 10^{-5}, i.e., using driving laser fields in the millijoule range results in attosecond pulse energies in the pico- to nanojoule range.

Such low photon numbers lead to two main restrictions in attosecond experiments. First, the signal rates using isolated attosecond pulses can be restrictively low. Second, since the cross-section for non-linear processes in the extreme ultraviolet region is extremely small, pump-probe experiments with two isolated attosecond pulses, which always rely on such a non-linear processes, have so far not been demonstrated. In this sense the low photon numbers of current attosecond sources are a major limitation to the further progress of attosecond science.

The development presented in **Chapter 4** presents a solution to the first mentioned limitation of attosecond experiments: the low signal rates. Using common detection methods, which rely on the use of micro-channel plates, the background pressure in the experimental vacuum chambers is limited by the maximum operating pressure of the micro-channel plate to below 10^{-5} mbar. In order to increase the signal rates, background pressures which may exceed this limit become desirable.

The suggested solution lies in the application of a new in-vacuum pixel detector, which has the potential to circumvents the above formulated limitation. A detailed comparison between multiple aspects of different detector technologies was performed, which clearly indicates the benefits of the new detector technology for attosecond experiments. In a number of proof-of-principle experiments, using velocity map imaging to record photo-electron spectra of xenon atoms ionized by 355 nm light, it was determined that quantum efficiencies close to one can be reached. At the same time it was tested that correct operation of the detector was maintained for background pressures as high as 10^{-3} mbar. During all measurements the kinetic energies of the electrons were measured with an energy resolution $\Delta E/E$ of better than 0.07.

The second limitation, namely the low XUV intensities due to the low photon fluxes, can only be improved by new attosecond pulse generation approaches in combination with more energetic driver lasers. As discussed in Chapter 2, driving pulses for the generation of isolated attosecond pulses have to fulfill several conditions. Most importantly, their carrier-envelope phase has to be stable from pulse to pulse. The development of a terawatt amplifier system which fulfills these conditions is presented in **Chapters 5 and 6**. After a detailed introduction to the generation of ultrashort laser pulses, their amplification and particularly the stabilization of their carrier-envelope phase, the design followed by the practical implementation of the carrier-envelope stable terawatt amplifier is described.

The new laser amplifier emits pulses with a pulse duration of 32 fs at a repetition rate of 50 Hz. The achievable pulse energies after the amplifier are as high as 80 mJ. After compression pulse energies of 35 mJ were measured, however, values of > 50 mJ should be achievable using higher quality gratings

in the grating compressor. The demonstrated peak power lies at 1.1 TW, while at optimal conditions peak powers of 1.6 TW could be realistic. The phase stability of the new amplifier system is ensured by measuring the carrier-envelope phase slip using an f-2f interferometer and stabilizing the carrier envelope phase in a closed loop by controlling the grating separation in the compressor. The resultant phase stability can be maintained to a residual phase jitter of ~ 300 mrad. The developed laser system therefore provides the pulses with the highest energies reached so far, while maintaining excellent carrier-envelope phase stability of the system.

Acknowledgements

In the last four years, many people have asked me about the progress of my thesis. I have truthfully answered them that I probably would not be able to finish it if it was not for all the people that accompanied me both professionally and privately. These final pages, which at the same time also mark the end of these four years, give me the chance to honestly thank my colleagues, friends and family, who have been so essential for the coming about of this booklet.

First of all, I would like to thank my advisor Marc Vrakking for the trust imparted, when he chose me for this PhD position. What I began expecting would be mostly a laser project, ended up being a journey through almost the complete field of attosecond science. You gave me the opportunity to discover your field from every possible angles and although it might at times not have seemed like it, in retrospect I have very much appreciated exactly this fact. One point, which most other PhD students, that I know of, would envy me for, is that in the whole time of my PhD I have barely ever heard the word "impossible" from you, both in the financial as well in the general sense. You always were able to find a way to make things work out, which gave me a freedom to research and develop with most restraints taken off of me. Thank you for your support, confidence and general overview over the last four years.

The second group of people who I want to thank is the support staff at AMOLF. I could not imagine a better one anywhere else. Every single one of you always conveyed the atmosphere that you declared the goal of every PhD student to your own goal. This constructive environment, in my opinion, is absolutely essential for the success of AMOLF and every researcher working there. I am thankful that I had the privilege to work in such a positive and inspiring institute, made up of so many great individuals.

Rob, with your helping heart and helping hands, you were at the core of our group and also at the heart of my thesis. I wish you all the best for the time after your retirement, which you have earned dearly. I hope you will keep working with young people, I wish it for them. Hinco, even though you were not officially our group technician, you were always ready to give a helping hand, give advice and make time even if you did not have any. The same holds for Ad, a pity for our group that you left, I would often have appreciated a fellow laser buddy.

I always enjoyed the collaborations with the technical support staff. One of my great hobbies and balance to the physics work turned out to be the time that I spent in the mechanical workshop building and designing my own small mechanical parts. My thanks for all the help, hints, explaining of machines, and the patience when I would come in with yet another last minute job goes to Wim, Jan, Menno, Henk, Wouter, Niels and Ricardo as well as the great collaborations with Iliya.

The electronics department came up with the best solutions for all our requests in particular concerning laser safety and convenience. It was inspiring to see how much you got involved to find the best possible solutions to our problems. Thanks to Duncan, Ronald and Sjoerd, I believe there is not a second group in the world that has better designed and more elaborate laser shutter control system than our group. Also thank you for all the work and explanations on all the other electronics that you have built and repaired for me in the meantime.

There are further a number of support departments, which might not be involved as much in the everyday work of a PhD student, however, no PhD student at AMOLF would be able to work as freely as we do if there were not all the people that do all the background work for us. In my case this especially includes Wouter Harmsen, Tatiana and Michiel as well as the Johann and Arnelli.

Around half time of my PhD, we moved to the new building, which gave Freek and me the opportunity to design our own dream laboratory. The realization of this design would, however, not have been possible without the countless hours that Huub, Tarik and Iwan invested in our discussions, the organization and the final build of the lab.

The work presented in every single chapter of this thesis has only been possible thanks to the collaboration with some of the foremost experts in their respective fields. I thus want to thank Mette Gaarde and Kenneth Schafer on the theoretical work that they performed for the electron recollision experiments. For me this was the first attosecond experiment under my own responsibility. The discussions about the interpretation of the experimental and theoretical results gave me a deep insight in this area of attosecond science and fundamental research in general. The Medipix results have been achieved in close collaboration with the detector team at Nikhef. In particular I want to thank Jan Visschers, Jan Visser, Martin Fransen, Daan Boltje, Lukas Tomasek and the technical support from Joop Rovekamp.

The main and original thesis goal, when I started to work in the XUV group, was the development of the terawatt femtosecond amplifier. As life goes, the actual work on this project only started in the very last phase of my PhD. It gave me the opportunity to dwell upon my fascination for the technical challenge in the environment of an industrial partner. I thus want to thank the people from Amplitude Technologies, especially Pierre-Mary and Fabien, with whom I have spent several month both in Paris as well as in Amsterdam to develop and build up this laser system. At the same time, I probably would never have been so suited for this position, if it had not been for my diploma work under the supervision of Konstantin Simeonidis, whom I want to thank in particular for all the support and the frequent exchange that we kept up during the last years. Further, I would like to mention the help that I received from the complete team of KMLabs, who helped me solve all problems that arose with the original laser system in the course of my thesis.

I further would like to thank the members of my defense committee, especially Wim for heading the committee and committing to all the work related

with this position. My thank also goes to Günther Steinmeyer for his input and the great discussions on the interpretation of the amplifier results, as well as for being part of my defense committee. I further greatly appreciate the time of the other committee members Huib, Giuseppe and Jom that they have been willing to invest.

Probably the largest contribution to the success of this thesis I nonetheless attribute to the constant support and good company of my colleagues and friends in Amsterdam. With most of you I have formed a relationship in which we have shared a lot of laughs and good conversations over many lunches and dinners, fierce discussions, some fights, enough beers to do crazy things and photos that you don't want to see published, as well as some back patting if it was needed. All of this in my opinion is essential for what in the end has turned into good friendships. I have considered myself extremely lucky to work in a team which was made up of so many brilliant, diverse and all together good-natured characters.

Ymkje was the first person that I met when I started work at AMOLF and you really made the start in Amsterdam so much easier for me: Teaching me the basic Dutch to get everybody to lunch with, and also later enforcing my Dutch speaking as well as so much other help and genuine friendliness that I received from you. With both Wing Kiu and Freek I experienced some of the most exciting hours of experiments and time in the laboratory. But we also had many great hours outside the institute. Wing Kiu thanks for all the great dinners that you organized for the group and your organizational skills in general, which you always put to the best use for the group. Your compassion, when things were not going so great, and the good advice that you then always had were really appreciated. Freek, I think we had a great time designing and building up the lab together, doing experiments as well as sharing many fierce discussions, which spiced up the everyday work. You really pushed me with your ambition, always helped out with answering all my questions no matter if on physics, Matlab codes, Labview software or life in general. I really enjoyed the time with all of you, I hope we can keep up the friendship.

Julia and Aneta, you two are obviously named at the same time, since you made up the unbeatable girl duo of our group, introducing vast amounts of delicious cakes, female compassion and good travel stories. Fede, it was a great enrichment for me when you joined the group, both in the professional as well as in the social sense. Finally there was another person, who I could share my laser fun, and at the same time somebody that shared my interests for music and many other things. It was great to see you in Paris as well.

When I started my work in the group, we were still supported by three great post-docs. Per, it was inspiring to get to know your combination of technical skills and diligence, understanding of physics as well as great character and humor. I really enjoyed the time working together with you and also getting to know your family. Arjan, you were always the person to go to if there were unsolvable problems on the VMI setups or one just could not find signal. Also thank you for uncounted hints and tips for good concerts and good music. Arnaud, your frenchness was missed in the Amsterdam remains of our group

after you left for Berlin. Especially the amount and even more so the quality of our wine consumption plummeted once you left. Omair, it was great fun discovering the Amsterdam cultural scene together with you and sharing your great English/Scottish humor.

Last I want to mention, what I would call the next generation PhD students and Post-docs, consisting of Christian, Jesse, Chung-Hsin and Truong. It was great seeing how you took over the setup and all the work that you put into perfecting it. I wish you all the best, a lot of fun in discovering the new city and institute as well as a lot of success in the rest of your thesis works.

In spite of all the great people that I worked with professionally, I also had the great luck to always have had people outside physics and my work life, who have helped me tremendously throughout the time of my thesis. Thanks to them I have really learned to love Amsterdam, and it has become my home not only for the last four years, but also for a long time to come. Natalie, I have to thank you first of all, because you were one of the main advocates for applying for a PhD position in Amsterdam. Without you I probably would not have thought of coming here in the first place and I am really happy to have one of my best friends now living so close by again. The second fortunate coincidence was that I ended up in a language course, where I met Rainer and Nilgün, with whom and via whom I founded my great circle of friends here in Amsterdam. The plenty of dinners, boat tours, sailing trips, weekend tours and the many more things that we undertook together during the last four years really enriched my life enormously. Thank you for all that. Next I want to thank Karin, Kirsten, Yvonne, and Silke for being my ‚more or less weekly, climbing partners, for all the beers and frietjes that we shared at the Captein and all the good times in general. Let's keep that up also during the next four years. Dani I want to thank for putting so much effort into making Paris an attractive place to live for me. I really enjoyed all your visits to both Amsterdam and Paris as well as your good friendship and especially your company during my last stay in Paris.

Ich will außerdem meinen Eltern danken für das Vertrauen in meine Fähigkeiten, das Vertrauen in meine Entscheidungen und den unbedingten Rückhalt, den ich bei euch immer genossen habe. Eurer sowohl finanziellen aber mehr noch moralischen und familiären Unterstützung habe ich all das zu verdanken, was ich bisher erreicht habe. Katharina, jetzt da wir beide im Ausland leben, wohnen wir trotzdem so nah beisammen wie schon lange nicht mehr. Es war schön euch beide, Nicolas und dich, immer in der Nähe zu wissen. Maximilian, besonders schön war es immer dich hier in Amsterdam zu sehen, besonders bei der Vorbereitung zu Katharinas Hochzeit, und mitzuerleben wie gut du hier mit den unterschiedlichsten Menschen und in allen Kulturen zurecht kommst. Meiner Großmutter will ich danken, für all die Briefe zu Geburtstagen, Namenstage und allen anderen Ereignissen. Du verkörperst für mich den unglaublichen Familienzusammenhalt, in dem ich mich immer geborgen fühle, selbst während ich im Ausland und weit von dem Rest der Familie entfernt lebe.

Mein großer Dank geht an Silke, die mich in den letzten drei Jahren un-

unterbrochen begleitet hat. Du hast mich immer unterstützt, hast mir in den Hintern getreten, wenn es nötig war, hast mich aufgebaut, wenn ich nicht weiter wusste oder wollte, und mir all die Freiheiten gegeben die nötig war, um diese Doktorarbeit zum Abschluss zu bringen. In den letzten Monaten hast du mir Arbeit und Pflichten abgenommen, wo immer es dir möglich war und vielfach meine soziale Nabelschnur zur Außenwelt dargestellt. Das schönste Geschenk war, dass du mit mir nach Paris gekommen bist und mir hier die Zeit versüßt. Vielen Dank für alles, ich freue mich und bin gespannt auf was uns in den nächsten vier Jahren alles erwarten wird.

Georg Gademann, Paris, 12 October 2011

List of publications

This thesis is based on the following publications

Chapter 3 *Attosecond ionization of O_2 molecules in the presence of an IR laser field*,
W. Siu, F. Kelkensberg, G. Gademann, A. Rouzée, P. Johnsson, D. Dowek, M. Lucchini, F. Calegari, U. Giovanni, A. Rubio, R. R. Lucchese, H. Kono, F. Lépine and M. J. J. Vrakking, *submitted*

Attosecond control in photoionization of hydrogen molecules,
F. Kelkensberg, W. Siu, J. Pérez-Torres, F. Morales, G. Gademann, A. Rouzée, P. Johnsson, M. Lucchini, F. Calegari, J. L. Sanz-Vicario, F. Martín and M. J. J. Vrakking, Physical Review Letters **107**, 043002 (2011)

EUV Ionization of Aligned Molecules,
F. Kelkensberg, A. Rouzée, W. Siu, G. Gademann, P. Johnsson, M. Lucchini, R. R. Lucchese and M. J. J. Vrakking, *submitted*

Attosecond control of electron ion recollision in high harmonic generation,
G. Gademann, F. Kelkensberg, W. Siu, P. Johnsson, M. B. Gaarde, K. J. Schafer and M. J. J. Vrakking, New Journal of Physics **13**, 033002 (2011)

Chapter 4 *Velocity map imaging using an in-vacuum pixel detector*,
G. Gademann, Y. Huismans, A. Gijsbertsen, J. Jungmann, J. Visschers, and M. J. J. Vrakking, Review of Scientific Instruments **80**, 103105 (2009)

Ruisloos deeltjes detecteren,
R. van Gastel, S. J. van der Molen, I. Sikharulidze, G. Gademann, J. Jungmann, R.M.A. Heeren and M. J. J. Vrakking, Nederlandse Tijdschrift voor Natuurkunde **75-11**, 374-377 (2009)

Chapter 6 *Carrier-envelope phase stabilization of a terawatt level chirped pulse amplifier for generation of intense isolated attosecond pulses*,
G. Gademann, Fabien Ple, Pierre-Mary Paul and M. J. J. Vrakking, *Optics Express accepted*

not covered *Atomic vs. many-electron effects in ultrafast ionization of C_{60}*, Y. Huismans, E. Cormier, C. Cauchy, P.-A. Hervieux, G. Gademann, A. Gijsbertsen, O. Ghafur, P. Johnsson, P. Logman, C. Bordas, F. Lépine and M.J.J. Vrakking *manuscript in preparation*

Photoelectron kinetic and angular distributions for the ionization of aligned molecules using a HHG source, A. Rouzée, Freek Kelkensberg, Wing Kiu Siu, Georg Gademann, R. Lucchese and M.J.J. Vrakking *submitted*

About the author

Georg Gademann was born in Schweinfurt in 1983 and lived in Heidelberg until 1999. In this year, he left the local Kurfürst-Friedrich-Gymnasium to continue his school career in the boarding school Choate Rosemary Hall in Connecticut, USA, from which he graduated in 2001. His American high school diploma was fully recognized as a general qualification for university entrance in Germany. After his return from the USA, he carried out his mandatory military service in the German navy on the frigate "Brandenburg" with specialization in navigation. For the summer semester 2002 he returned to Heidelberg to start his physics studies at the Ruprecht-Karls-Universität Heidelberg. During this time he also did internships in the quality managment team of the IFA-Rotorion group (2003) as well as at the Proton Center of the Massachusetts General Hospital in Boston (2006). The research for his diploma thesis he conducted in the group of Prof. Joachim Ullrich at the Max-Planck-Institute for Nuclear Physics in Heidelberg, where he developed an optical pulse-compression stage based on filamentation and an adaptive-mirror compressor. He finished his studies in Heidelberg with the German physics diploma in 2007. In the same year he started his PhD research at the FOM Institute for Atomic and Molecular Physics (AMOLF) in Amsterdam under the supervision of Prof. Marc Vrakking. In the course of this PhD thesis, he worked on the application of attosecond pulses to investigate electron dynamics in atoms and molecules, tested novel detector designs, and developed a new laser amplifier to be used in the generation of intense attosecond pulses. Part of this work was conducted at the facilities of Amplitude Technologies in France in the framework of a European exchange program for academic and industrial partners.